

付録 B

Flare-Substorm/Space Weather Topics (Earth, Planets and Space, Vol. 61, No. 5, 2009)

“Flare-Substorm/Space Weather Topics” (Earth, Planets and Space, Vol. 61, No. 5, 2009) は、2007 年 3 月にアラスカで開催された「CAWSES Space Weather Workshop」(本報告書 88 ページを参照)の集録として出版されたものである。

掲載論文

- **Preface,**
Earth Planets Space, Vol. 61 (No. 5), pp. 553, 2009
- **A two-step scenario for both solar flares and magnetospheric substorms: Short duration energy storage,**
Bruce T. Tsurutani, Kazunari Shibata, Syun-Ichi Akasofu, and Mitsuo Oka,
Earth Planets Space, Vol. 61 (No. 5), pp. 555–559, 2009
- **Modeling of substorms and flares by the fast reconnection mechanism,**
M. Ugai, K. Kondoh, and T. Shimizu,
Earth Planets Space, Vol. 61 (No. 5), pp. 561–564, 2009
- **Coronal loops, flare ribbons and aurora during slip-running,**
Brigitte Schmieder, Guillaume Aulanier, Pascal Demoulin, and Etienne Pariat,
Earth Planets Space, Vol. 61 (No. 5), pp. 565–568, 2009
- **Three-dimensional non-linear instability of spontaneous fast magnetic reconnection,**
T. Shimizu, K. Kondoh, and M. Ugai,
Earth Planets Space, Vol. 61 (No. 5), pp. 569–572, 2009
- **Patchy reconnection in a Y-type current sheet,**
M. G. Linton, C. R. DeVore, and D. W. Longcope,
Earth Planets Space, Vol. 61 (No. 5), pp. 573–576, 2009
- **Flares and the chromosphere,**

Hugh S. Hudson and Lyndsay Fletcher,

Earth Planets Space, Vol. 61 (No. 5), pp. 577–580, 2009

- **Development of the global simulation model of the heliosphere,**

Satomi Kamei, Aoi Nakamizo, Takashi Tanaka, Takahiro Obara, and Hironori Shimazu,

Earth Planets Space, Vol. 61 (No. 5), pp. 581–584, 2009

- **The interplanetary magnetic decrease automatic detection (IMDAD) code,**

F. L. Guarnieri, B. T. Tsurutani, and E. Echer,

Earth Planets Space, Vol. 61 (No. 5), pp. 585–588, 2009

- **Impacts of torus model on studies of geometrical relationships between interplanetary magnetic clouds and their solar origins,**

Katsuhide Marubashi, Suk-Kyung Sung, Kyung-Suk Cho, and Ronald P. Lepping,

Earth Planets Space, Vol. 61 (No. 5), pp. 589–594, 2009

- **Halo coronal mass ejections and geomagnetic storms,**

Nat Gopalswamy,

Earth Planets Space, Vol. 61 (No. 5), pp. 595–597, 2009

- **Numerical simulations of the solar corona and Coronal Mass Ejections,**

Stefaan Poedts, Carla Jacobs, Bart van der Holst, Emmanuel Chane, and Rony Keppens,

Earth Planets Space, Vol. 61 (No. 5), pp. 599–602, 2009

- **Non-thermal electrons at the Earth's bow shock: A 'gradual' event,**

M. Oka, T. Terasawa, M. Fujimoto, H. Matsui, Y. Kasaba, Y. Saito, H. Kojima, H. Matsumoto, and T. Mukai,

Earth Planets Space, Vol. 61 (No. 5), pp. 603–606, 2009

- **Influence of the foreshock of the Earth's bow shock on the interplanetary shock propagation during their mutual interaction,**

Lubomír Přech, Zdeněk Němeček, and Jana Šafránková,

Earth Planets Space, Vol. 61 (No. 5), pp. 607–610, 2009

- **Three dimensional configuration of earthward fast plasma flow in the near-Earth plasma sheet,**

Koji Kondoh, Masayuki Ugai, and Tohru Shimizu,

Earth Planets Space, Vol. 61 (No. 5), pp. 611–614, 2009

- **Timing of substorm related auroral oscillations,**

P. Martin, N. E. Turner, and J. Wanliss,

Earth Planets Space, Vol. 61 (No. 5), pp. 615–619, 2009

- **Statistically predicting Dst without satellite data,**

A. S. Parnowski,

Earth Planets Space, Vol. 61 (No. 5), pp. 621–624, 2009

- **Properties of dayside nonlinear rising tone chorus emissions at large L observed by GEOTAIL,**

Olga P. Verkhoglyadova, Bruce T. Tsurutani, Y. Omura, and S. Yagitani,

Earth Planets Space, Vol. 61 (No. 5), pp. 625–628, 2009

- **Proxy for the ionospheric peak plasma density reduced by the solar zenith angle,**

T. L. Gulyaeva,

Earth Planets Space, Vol. 61 (No. 5), pp. 629–631, 2009

- **Investigation of ionospheric gradients for GAGAN application,**

K. Ravi Chandra, V. Satya Srinivas, and A. D. Sarma,

Earth Planets Space, Vol. 61 (No. 5), pp. 633–635, 2009

- **The total failures of GPS functioning caused by the powerful solar radio burst on December 13, 2006,**

E. L. Afraimovich, V. V. Demyanov, and G. Ya. Smolkov,

Earth Planets Space, Vol. 61 (No. 5), pp. 637–641, 2009

- **Aeronomomic effects of the solar flares in the topside ionosphere,**

L. A. Leonovich and A. V. Tashilin,

Earth Planets Space, Vol. 61 (No. 5), pp. 643–648, 2009

Preface

Under the sponsorship of CAWSES, a Workshop was held on the topic of solar flares, magnetospheric substorms (particularly the relationship between the two) and other space weather topics. The workshop was held under the sponsorship of the University of Alaska, Fairbanks from 18 to 20 March, 2007. This special issue is a result of this workshop. Auroras were observed nightly during the workshop interval. Many presentations given at the workshop showed detailed images of solar flares. This special issue includes, but is not limited to, papers presented at the Workshop. We hope that the following papers will be stimulating to the readership of *Earth, Planets and Space*.

Guest Editors: Bruce T. Tsurutani
Kazunari Shibata
Syun-Ichi Akasofu
Mitsuo Oka

A two-step scenario for both solar flares and magnetospheric substorms: Short duration energy storage

Bruce T. Tsurutani¹, Kazunari Shibata², Syun-Ichi Akasofu³, and Mitsuo Oka⁴

¹*Jet Propulsion Laboratory, California Institute of Technology, Pasadena, CA*

²*Kyoto University, Kyoto, Japan*

³*International Arctic Research Center (IARC), Univ. Alaska, Fairbanks, AK*

⁴*University of Alabama in Huntsville, Huntsville, AL*

(Received September 16, 2008; Revised February 25, 2009; Accepted March 12, 2009; Online published May 29, 2009)

The basic observations for magnetic storms and substorms at Earth and for flares at the Sun are reviewed for background. We present a common scenario of double magnetic reconnection for both substorms and flares based on previous interplanetary observations and substorm-triggering results. Central to the scenario is that the first magnetic reconnection phase is the source of energy loading for possible substorms and flares. The energy placed in the magnetotail or magnetosphere/at the sun lasts for only a short duration of time however. The energy gets dissipated away rapidly (in some less dramatic form). This scenario predicts that if the initial reconnection process is sufficiently intense and rapid, concomitant substorms and flares occur soon thereafter. If the energy input is less rapid, there may be lengthy delays for the onset of substorms and flares. If external influences (shocks, etc.) occur during the latter energy buildup, the “trigger” will cause a sudden release of this energy. The model also explains reconnection without subsequent substorms and flares. The model addresses the question why strong triggering events are sometimes ineffective.

Key words: Solar flares, substorms, magnetic storms, magnetic reconnection.

1. Introduction

It has been well established that major geomagnetic storms do not occur at Earth unless the upstream interplanetary magnetic field (IMF) is southward for durations of hours (Gonzalez and Tsurutani, 1987; Gonzalez *et al.*, 1994, 2007). There have been no exceptions to this rule found to date. On the other hand, if the upstream IMF is northward, the magnetosphere and auroras becomes very quiet (Tsurutani and Gonzalez, 1995). It can be assumed that the energy input into the magnetosphere/magnetotail does not occur during such intervals (or takes place at a much lower rate). The implication of both of these observations is that magnetic reconnection (Dungey, 1961) is the major mechanism for solar wind energy input into the magnetosphere (Echer *et al.*, 2008) and is a direct or indirect source of the energy powering magnetic storms.

Substorms are much smaller intensity geomagnetic events, and there the situation is less clear. Tsurutani and Meng (1972) and Meng *et al.* (1973) found that southward IMFs preceded substorms by ~10 to 40 min, and concluded that southward IMFs are both the ultimate energy source and trigger for the substorms that follow. Alternatively Lyons *et al.* (1997) have suggested that some substorms are “triggered” by northward IMF turnings due to braking of the magnetospheric convection process. Freeman and Morley (2004) have demonstrated that substorms

may occur spontaneously and may not be triggered at all. We will argue that all of these positions are correct and are not contradictory to each other.

The strongest external impact on the magnetosphere and potential substorm triggers are interplanetary fast forward shocks (Kennel *et al.*, 1985) impinging on the dayside magnetopause. The solar wind ram pressure can increase by an order of magnitude across a shock. Such pressure pulses will compress the magnetosphere in a dramatic fashion such that magnetic increases (sudden impulses or SIs) are detected on the ground (Araki, 1994). As the shock propagates further downstream, it will compress the magnetotail and thereby increase currents within and bounding the tail (Tsurutani *et al.*, 1986; Tsurutani and Zhou, 2003). Shock compression will also enhance field-aligned currents from the magnetosphere to the ionosphere (Araki, 1994). These shocks can immediately trigger substorms with little or no delay (Heppner, 1955; Kawasaki *et al.*, 1971; Kokubun *et al.*, 1977). However there are also times when they do not trigger substorms. What does this mean?

Zhou and Tsurutani (2001) and Tsurutani and Zhou (2003) have found that if the IMF is southward or ~zero nT a few hrs prior to shock impingement, a substorm will occur. If the IMF is northward, one will not. These observations have been somewhat of a mystery. The Earth’s magnetotail has enough stored magnetic energy to supply a dozen or more substorms. Why don’t shocks trigger substorms irrespective of preceding IMF directionality? A similar question can be asked about solar flares. The energy stored in the coronal loops is sufficient for many solar flares. Why

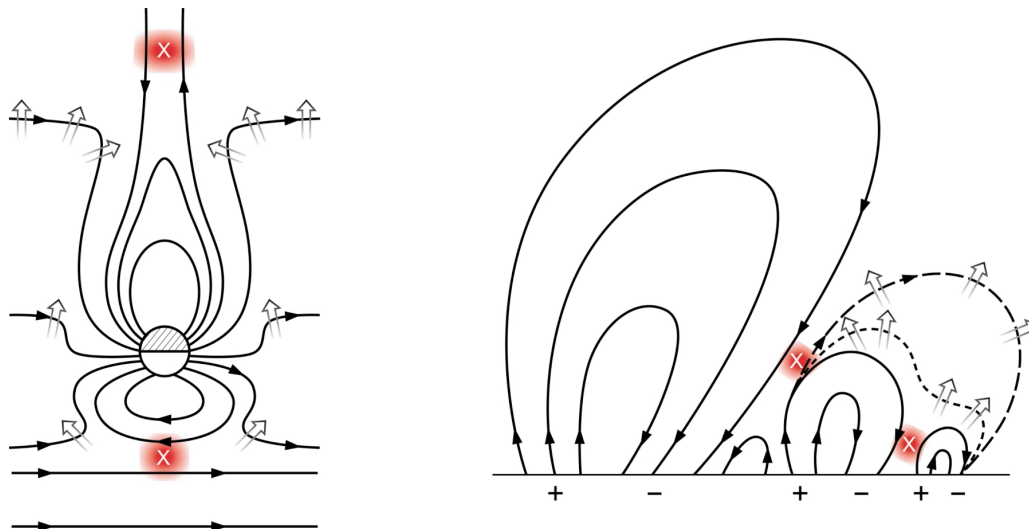


Fig. 1. A schematic of two-step reconnection at Earth (on left) and at the sun (on right). For the Earth's case the solar wind from the sun (at bottom out of the figure) convects interplanetary magnetic fields to the Earth. Magnetic reconnection at the magnetopause (indicated in red at the bottom) allows the transfer of solar wind energy to the ionosphere/magnetosphere/magnetotail. If this first reconnection process is intense enough, a substorm will occur. Magnetic reconnection in the tail (indicated in red at the top) may either drive the substorm or be a consequence of the substorm. This is currently being debated in the literature. An analogous solar flare schematic is shown on the right. An emerging flux region occurs on the far right of the figure. Magnetic reconnection between it and the neighboring (central) loop leads to an increase of magnetic stress between the central loop and the large loop at the left. Release of this stress occurs in the form of a solar flare.

don't flares occur continuously until the loop energy is exhausted? The loop configuration often looks remarkably similar before and after the flare.

We present a scenario of double magnetic reconnection for substorms and solar flares. Our scenario follows the above empirical findings that magnetic reconnection is the major process transferring solar wind energy into the magnetosphere. That is a standard, well-accepted concept (see Terasawa *et al.*, 2000 for a discussion of the similarities and differences between substorms and flares). However we also follow the Zhou and Tsurutani (2001) and Tsurutani and Zhou (2003) result that the energy stored in some form in the magnetosphere/magnetotail/ionosphere is being dissipated rapidly. If the energy is not released in the form of a substorm within several hrs, it gets released in a less dramatic manner. In this scenario, the quiet-time tail lobe energy does not play a prominent role. In this paper we explore the consequences of this idea, assuming that the same processes occur at the sun. We will hypothesize under what condition solar flares occur and when they do not.

2. Results

2.1 Substorms

Substorms were first identified and described by Akasofu (1964) (see also Akasofu and Chapman, 1972) by all sky images measured from the ground. Substorms are isolated midnight sector auroral zone ($\sim 60^\circ$ to 65° magnetic latitude) events. Akasofu (1964) found that a substorm was found to consist of the following sequence: 1) a brightening of the equatorward arc (the arc width typically is ~ 1 km), 2) a breakup of the arc, and then poleward, eastward and westward expansions of auroral forms. This sequence takes between ~ 10 and ~ 30 min to complete, with no definite time interval identified.

Auroral light is created by ~ 1 – 10 keV electrons pre-

cipitating into the upper atmosphere colliding with neutral atoms and molecules. The electrons lose their kinetic energies through electron-electron collisions resulting in the excitation of the atoms and molecules. The excited atoms and molecules relax to emit visible and UV photons. To a much lesser extent (~ 1 to 2% of the total radiated energy), the incoming energetic electrons are accelerated by interactions with atmospheric nuclei to form bremsstrahlung X-rays.

The processes accelerating the electrons to 1 – 10 keV occurs above the ionosphere. Electric fields with components aligned along the geomagnetic field (so called "parallel electric fields") have been detected at low altitudes by satellites such as FAST (Carlson *et al.*, 1998). These electric fields accelerate thermal electrons to monoenergetic beams of \sim keV kinetic energies (Evans, 1968). The causes of these electric fields are due to processes occurring in the magnetosphere, at higher altitudes still. The lack of sufficient current carrier densities is the cause of the parallel electric fields generated above the ionosphere (Carlson *et al.*, 1998).

Large scale convection of magnetotail (plasmashet) plasma also occurs simultaneous with auroral substorms. The plasmashet is convected inward towards the Earth, compressing (heating) the plasmashet plasma. Due to curvature and gradients in the magnetospheric magnetic field, the electrons drift from the midnight sector towards dawn and the ions from the midnight sector to dusk. The energies of these particles are ~ 10 to 100 keV. Through plasma instabilities and plasma wave growth, these magnetospheric particles are pitch-angle scattered and some precipitate into the ionosphere. This is the "diffuse" component of the aurora.

It is well documented that the energy for substorms ultimately comes from the solar wind Poynting flux (discussed previously). The magnetic field directionality serves as

an energy gate. If the interplanetary magnetic fields are oriented in a southward direction, opposite in direction to the magnetopause magnetic fields, reconnection will take place. A second site of reconnection occurs in the magnetotail. A schematic of this model is shown on the left-hand side of Fig. 1.

Although sufficient energy may be transferred into the magnetosphere/magnetotail system by the first reconnection process, substorms may not take place immediately or even at all. Our scenario is that if energy is supplied at a rapid enough rate, e.g., if the IMF is intensely southward, substorms will result (Tsurutani and Meng, 1972). If sufficient energy has recently been put into the magnetosphere and the IMF turns northward, this current disruption can cause a substorm (Lyons *et al.*, 1997). Or if there is energy being put into the magnetosphere/magnetotail continuously, substorms will occur sporadically (Freeman and Morley, 2004). However if the IMF is northwardly directed for hours prior to the “trigger” arriving at the magnetopause, neither IMF southward turnings, northward turnings nor shocks will trigger substorms. In our scenario, the important feature is the rate of energy input into the magnetosphere/magnetotail system. The “triggers” are less important.

In the above substorm scenario, there is less emphasis on the second reconnection event. It may occur as a byproduct of the substorm or may lead to the substorm. There are many ongoing debates of the timing of the events. In our point of view, it is the first reconnection event that is the important one. This leads to energy input from the solar wind to the ionosphere/magnetosphere/magnetotail.

2.2 Solar flares

Solar flares were first observed (1859) and reported independently by R. C. Carrington (1860) and R. Hodgson (1860) as localized brightenings in a sunspot group. The brightening lasted only ~ 5 min. No changes in the sunspot orientation or intensity was noted after the flare had occurred. This is similar to the case of substorms, viewed from a great distance. Differences in the magnetosphere before and after substorms would be difficult to discern from a viewing distance of 10^8 km.

Since the above 1859 observations, numerous flare events have been recorded by ground-based, balloon-borne and spacecraft telescopes. Today, a solar flare is defined as “a transient phenomenon showing a rapid increase followed by either a rapid or gradual decay” (Tajima and Shibata, 1997). The “rapid” time scale normally corresponds to 10 sec to 10 min, although it varies largely from event-to-event. It is often accompanied by quasi-periodic variations, or pulsations, with the time-scale as small as 20 msec. These observations are similar to those of substorms.

The wavelength of the electromagnetic emission covers radio wavelengths at the low end to γ -rays at the upper end. The γ -rays are produced by precipitating high energy ions, a feature far more energetic than that in substorms. The low end includes H α photons, a feature often used in flare diagnostics. Recent progress has come from spectral and imaging observations of X-rays (e.g., Svestka, 1976). Soft X-rays (SXR) are thought to be thermal emission from plasmas of 10^7 K temperature whereas hard X-rays are “non-

thermal”. The latter are bremsstrahlung emissions created by 10 keV to 1 MeV electron collisions with ions.

The whole duration of a flare depends on the type of flare. Long duration event (LDE) flares typically last more than 1 hr while impulsive flares are short-lived ones that last far less. The latter is characterized by impulsive hard X-ray emission whereas the former shows a softer X-ray spectrum.

Generally, the LDE flares have larger characteristic scale sizes of $\sim 10^5$ km. SXR observations show cusp-type loops associated with their rise and expansion motion (e.g., Tsuneta *et al.*, 1992). The temperature was found to be systematically higher in the outer loops. The loops gradually shrink with time (Forbes and Acton, 1996). Some other phenomenon such as plasmoid ejections (Hudson, 1994), downflows (McKenzie and Hudson, 1999; Asai *et al.*, 2004), and inflows (Yokoyama *et al.*, 2001) were also observed.

Impulsive flares, on the other hand, are relatively small with characteristic scales of $\sim 10^4$ km but occur much more frequently than LDE flares. A notable feature of these events is that they do not show clear cusp-shaped loop structures, so some researchers considered the two types of flares to be different phenomena. From the mid-1990s, however, many features similar to LDE flares were found in impulsive flares (e.g., see a review by Shibata, 1999). In 1994, a careful comparison between SXR and HXR images revealed an above-the-looptop HXR source so-called Masuda-type source (Masuda *et al.*, 1994). It was soon discovered, from the time-of-flight (TOF) analysis, that the acceleration site of energetic electrons is situated high above the Masuda type sources (Aschwanden *et al.*, 1996). Other important findings in impulsive flares are plasmoid ejections (Shibata *et al.*, 1995; Ohyama and Shibata, 1998), temperature distributions, upward and shrinking motions of SXR loops, and increasing footpoint/double-ribbon separation (Sakao, 1994; Fletcher and Hudson, 2001; Asai *et al.*, 2002). A detailed analysis of spatial distribution of the coronal sources has provided evidence of a large scale current sheet (Sui and Holman, 2003). It is only recently that the γ -ray line observations revitalized the discussion of the differences between ions and electrons in acceleration and/or propagation (Lin *et al.*, 2003).

In both types of flares, plasma heating and particle acceleration are primary processes of solar flares that take place in the solar corona (very recent observations by Hinode clarified many small-size flares not only in the solar corona but also in the chromosphere (e.g., Shibata *et al.*, 2007). The impact of such ubiquitous presence of flares, caused by reconnection, should be discussed in the future literature. During the peak time of flares, the accelerated particles and thermal conduction fronts propagate to and heat the chromosphere. The heated chromospheric plasma results in an upward flow or ‘chromospheric evaporation’. It is this phase that the highest energy emission such as HXR and γ -rays are prominently observed. In the later phase of flares, a cooling process dominates heating. The typical temporal variation of energy spectra shows the “soft-hard-soft” sequence (e.g. Fletcher and Hudson, 2002).

The magnetic field configuration for our solar flare model

is shown on the right-hand side of Fig. 1. Our model is a double reconnection event, similar to the process of reconnection at Earth (reconnection occurs first at the magnetopause and then in the tail). We note that double reconnection models for solar flares have been previously proposed by Wang and Shi (1993), Aulanier *et al.* (2000), Kusano *et al.* (2004) and Zhang *et al.* (2006). We include the tether cutting model (Moore and Roumeliotis, 1992) and the breakout model (Antiochos *et al.*, 1999) because in a broader sense, they are double reconnection models too (see review by Shibata, 2005). In this paper we build on this model to draw a schematic for solar flares that is similar to the magnetospheric case. The initial condition is two magnetic loops adjacent to each other. These are the large loops on the left and center. The source of the loops and their intrinsic magnetic energy is magnetic buoyancy.

The emergence of a new loop on the far right leads to energy transfer to the system (e.g., Chen and Shibata, 2000). This loop has a polarity that is conducive to magnetic reconnection (indicated by an “x”) between the emerging loop and the right-hand initial loop. This reconnection corresponds to the dayside reconnection in the Earth’s case. Reconnection between the small emerging loop and the central loop enlarges the initial right-hand loop and increases the magnetic stress between it and the left-hand loop. If significant stress builds up between the two loops, magnetic reconnection will take place between them and the energy will be abruptly released in the form of a flare. If on the other hand the stress build up is slow such that the magnetic stress is being dissipated more rapidly than increased, no sudden release of energy will occur.

If the rate of energy input (reconnection between the new loop and central loop) is rapid enough, a flare will occur with short delay. If the energy input is less rapid but the amount of accumulated energy is sufficient for a flare, coronal disturbances may “trigger” it. As one example, coronal shocks propagating from distant regions of the sun can trigger “sympathetic” flares, much in the way an interplanetary shock can trigger a substorm at Earth. If however the energy input is at a relatively low rate or there is no energy being added, even strong triggers may be ineffective.

3. Summary

We have developed a scenario for double reconnection involving three coronal loops at the sun which has an analog to the case of interplanetary magnetic reconnection at the Earth’s magnetosphere and reconnection in the magnetotail. Our scenario emphasizes short duration energy storage time scales in both the magnetosphere/ionosphere and at the sun. If the energy input is rapid, flares/substorms occur. This scenario is based on detailed observations made for storms and substorms at Earth.

At this time, the authors do not speculate on what specific form the resultant energy from the (first) magnetic reconnection process is stored at Earth and at the Sun. For the Earth’s case, energy storage in the magnetotail, magnetosphere and in the ionosphere have been suggested. The literature is extensive. For the solar case, Zirin and Tanaka (1973), Neidig (1979), Hagyard *et al.* (1983) and Moore *et al.* (2001) have suggested that shear in the magnetic field

is one mechanism. This may be the case for our model between the central and left-hand loop of Fig. 1. Kusano *et al.* (2002) have suggested flux emergence was an important feature for a November 1997 interval. Similarly Schrijver *et al.* (2008) have indicated that electrical currents associated with the emerging flux is important. In our model, the existence of the right-hand side emerging loop is such a feature.

All of the energy storage mechanisms mentioned above (and more) may occur to varying degrees, depending on the particular solar preconditions. It is possible that the path of energy storage and release may be different for different events.

4. Final Comments

We have proposed a double reconnection model that can be applied to both substorms at Earth and to solar flares. We emphasize that the rate of the first reconnection process is important to determine if the substorm/flare: 1) will occur immediately, 2) will occur with some delay, 3) could occur if there is an external “trigger” and 4) may not occur at all. Key to this scenario is that the energy input leaks away from the storage site (as implied from magnetospheric results) and the preexisting magnetotail/loop energy is not the main source for the substorm/flare. The ideas presented in this paper are readily testable.

One can envision obvious simple variations to this double reconnection model. Flux emergence enhancing the central loop will eliminate the need for the emergence of the small right-hand loop. Otherwise, the scenario is the same. Again, the rate of free energy input into the system will be critical for the occurrence/lack of occurrence of a flare.

Acknowledgments. Portions of this work were performed at the Jet Propulsion Laboratory, California Institute of Technology under contract with NASA. This work was supported by the Grant-in-Aid for Creative Scientific Research “The Basic Study of Space Weather Prediction” (17GS0208, Head Investigator: K. Shibata) from the Ministry of Education, Culture, Sports, Science, and Technology of Japan. Copyright 2009. All rights reserved.

References

- Akasofu, S.-I., The development of the auroral substorm, *Planet. Space Sci.*, **12**, 273, 1964.
- Akasofu, S.-I. and S. Chapman, *Solar Terr. Phys.*, Clarendon, Press, Oxford, 1972.
- Antiochos, S. K., C. R. DeVore, and J. A. Klimchuk, A model for solar coronal mass ejections, *Astrophys. J.*, **510**, 485, 1999.
- Araki, T., A physical model of geomagnetic sudden commencement, in *Solar Wind Sources of Magnetospheric Ultra-Low-Frequency Waves*, Geophys. Mon. 81, AGU, Wash. D.C., 183, 1994.
- Asai, A. *et al.*, Difference between spatial distributions of the H α kernels and hard X-Ray sources in a solar flare, *Astrophys. J.*, **578**, L91, 2002.
- Asai, A. *et al.*, Downflow motions associated with impulsive nonthermal emissions observed in the 2002 July 23 solar flare, *Astrophys. J.*, **605**, L77, 2004.
- Aschwanden, M. J. *et al.*, The scaling law between electron time-of-flight distances and loop lengths in solar flares, *Astrophys. J.*, **470**, 1198, 1996.
- Aulanier, G., E. E. DeLuca, S. K. Antiochos, R. A. McMullen, and L. Golub, The topology and evolution of the Bastille Day Flare, *Astrophys. J.*, **540**, 1126, 2000.
- Carlson, C. W., R. F. Pfaff, and J. G. Watzin, The Fast auroral snapshot (FAST) mission, *Geophys. Res. Lett.*, **25**, 2013, 1998.
- Carrington, R. C., Description of a singular appearance seen in the Sun on September 1, 1859, *Mon. Not. R. Astron. Soc.*, **XX**, 13, 1860.
- Chen, P. F. and K. Shibata, An emerging flux trigger mechanism for coronal mass ejections, *Astrophys. J.*, **545**, 524, 2000.

- Dungey, J. W., Interplanetary magnetic field and the auroral zones, *Phys. Rev. Lett.*, **6**, 47, 1961.
- Echer, E., W. D. Gonzalez, B. T. Tsurutani, and A. L. C. Gonzalez, Interplanetary conditions causing intense geomagnetic storms ($Dst \leq -100$ nT) during solar cycle 23 (1996-2006), *J. Geophys. Res.*, **113**, A05221, doi:10.1029/2007JA012744, 2008.
- Evans, D., The observation of a near mono-energetic flux of auroral electrons, *J. Geophys. Res.*, **73**, 2315, 1968.
- Fletcher, L. and H. Hudson, The magnetic structure and generation of EUV flare ribbons, *Sol. Phys.*, **204**, 69, 2001.
- Fletcher, L. and H. Hudson, Spectral and spatial variations of flare hard X-ray footpoints, *Sol. Phys.*, **210**, 307, 2002.
- Forbes, T. G. and L. W. Acton, Reconnection and field line shrinkage in solar flares, *Astrophys. J.*, **459**, 330, 1996.
- Freeman, M. P. and S. K. Morley, A minimal substorm model that explains the observed statistical distribution of times between substorms, *Geophys. Res. Lett.*, **31**, L12807, doi:10.1029/2004GL019989, 2004.
- Gonzalez, W. D. and B. T. Tsurutani, Criteria of interplanetary parameters causing intense magnetic storms ($Dst < -100$ nT), *Planet. Space Sci.*, **35**, 1101, 1987.
- Gonzalez, W. D., J. A. Joselyn, Y. Kamide, H. W. Kroehl, G. Rostoker, B. T. Tsurutani, and V. M. Vasyliunas, What is a geomagnetic storm?, *J. Geophys. Res.*, **99**, 5771, 1994.
- Gonzalez, W. D., E. Echer, A. L. C. Gonzalez, and B. T. Tsurutani, Interplanetary origin of intense geomagnetic storms ($Dst < -100$ nT) during solar cycle 23, *Geophys. Res. Lett.*, **34**, L06101, doi:10.1029/2006GL028879, 2007.
- Hagyard, M. J., D. Teuber, E. A. West, E. Tandberg-Hanssen, W. Henze Jr., J. M. Beckers, M. Bruner, C. L. Hyder, and B. E. Woodgate, Vertical gradients of sunspot magnetic fields, *Sol. Phys.*, **84**, 13, 1983.
- Hagyard, M. J., J. B. Smith, Jr., D. Teuber, and E. A. West, A quantitative study relating observed shear in photospheric magnetic fields to repeated flaring, *Sol. Phys.*, **91**, 115, 1984.
- Hepner, J. P., Note on the occurrence of world-wide SSCs during the onset of negative bays at College, Alaska, *J. Geophys. Res.*, **60**, 29, 1955.
- Hodgson, R., On a curious appearance seen in the Sun, *Mon. Not. R. Astron. Soc.*, **XX**, 15, 1860.
- Hudson, H. S., Thermal plasmas in the solar corona: The YOHKOH soft x-ray observations, in *Proc. Kofu Meeting*, edited by S. Enome and T. Hirayama, Nobeyama Radio Observatory, 1, 1994.
- Kawasaki, K., S.-I. Akasofu, F. Yasuhara, and C.-I. Meng, Storm sudden commencements and polar magnetic substorms, *J. Geophys. Res.*, **76**, 6781, 1971.
- Kennel, C. F., J. P. Edmiston, and T. Hada, A quarter century of collisionless shock research, in *Collisionless Shocks in the Heliosphere: A Tutorial Review*, edited by R. G. Stone and B. T. Tsurutani, AGU, Wash. D.C., 34, 1, 1985.
- Kokubun, S., R. L. McPherron, and C. T. Russell, Triggering of substorms by solar wind discontinuities, *J. Geophys. Res.*, **76**, 6781, 1977.
- Kusano, K., T. Maeshiro, T. Yokoyama, and T. Sakurai, Measurement of magnetic helicity injection and free energy loading into the solar corona, *Astrophys. J.*, **577**, 501, 2002.
- Kusano, K., T. Maeshiro, T. Yokoyama, and T. Sakurai, The trigger mechanism of solar flares in a coronal arcade with reversed magnetic shear, *Astrophys. J.*, **610**, 537, 2004.
- Lin, R. P., S. Krucker, G. J. Hurford, D. M. Smith, H. S. Hudson, G. D. Holman, R. A. Schwartz, B. R. Dennis, G. H. Share, R. J. Murphy, A. G. Emslie, C. Johns-Krull, and N. Vilmer, RHESSI observations of particle acceleration and energy release in an intense solar gamma-ray line flare, *Astrophys. J.*, **595**, L69, 2003.
- Lyons, L. R., G. T. Blanchard, J. C. Samson, R. P. Lepping, T. Yamamoto, and T. Moretto, Coordinated observations demonstrating external substorm triggering, *J. Geophys. Res.*, **102**, 27,039, 1997.
- Masuda, S., T. Kosugi, H. Hara, S. Tsuneta, and Y. Ogawara, A loop-top hard X-ray source in a compact solar flare as evidence for magnetic reconnection, *Nature*, **371**(6497), 495, 1994.
- McKenzie, D. E. and H. S. Hudson, X-ray observations of motions and structure above a solar flare arcade, *Astrophys. J.*, **519**, L93, 1999.
- Meng, C.-I., B. T. Tsurutani, K. Kawasaki, and S.-I. Akasofu, Cross-correlation analysis of the AE index and the interplanetary magnetic field Bz component, *J. Geophys. Res.*, **78**, 617, 1973.
- Moore, R. L. and G. Roumeliotis, Triggering of eruptive flares—Destabilization of the preflare magnetic field configuration, in *Eruptive Solar Flares*, edited by Z. Svestka, B. V. Jackson and M. E. Machado, Springer-Verlag, Berlin, 69, 1992.
- Moore, R. L., A. C. Sterling, H. S. Hudson, and J. R. Lemen, Onset of the magnetic explosion in solar flares and coronal mass ejections, *Astrophys. J.*, **552**, 833, 2001.
- Neidig, D. F., High resolution observations of fibril changes in a small flare, *Sol. Phys.*, **61**, 121, 1979.
- Ohyama, M. and K. Shibata, X-ray plasma ejection associated with an impulsive flare on 1992 October 5: Physical conditions of X-ray plasma ejection, *Astrophys. J.*, **499**, 934, 1998.
- Sakao, T., Characteristics of solar flare hard X-ray sources as revealed with the Hard X-ray Telescope aboard the Yohkoh satellite, PhD Thesis, University of Tokyo, 1994.
- Schrijver, C. J., M. L. DeRosa, T. Metcalf, G. Barnes, B. Lites, T. Tarbell, J. McTiernan, G. Valori, T. Wiegelmann, M. S. Wheatland, T. Amari, G. Aulanier, P. Démoulin, M. Fuhrmann, K. Kusano, S. Régnier, and J. K. Thalmann, Nonlinear force-free modeling of a solar active region around the time of a major flare and coronal mass ejection, *Astrophys. J.*, **675**, 1673, 2008.
- Shibata, K., Evidence of magnetic reconnection in solar flares and a unified model of flares, *Astrophys. Space Sci.*, **264**, 129, 1999.
- Shibata, K., in *Proc. IAU Symp. No. 226, Coronal and Stellar mass Ejections*, 241, 2005.
- Shibata, K., S. Masuda, M. Shimojo *et al.*, Hot plasma ejections associated with compact-loop solar flares, *Astrophys. J. Lett.*, **451**, L83, 1995.
- Shibata, K., T. Nakamura, T. Matsumoto *et al.*, Chromospheric anemone jets as evidence of ubiquitous magnetic reconnection, *Science*, **318**, 1591, 2007.
- Sui, L. and G. D. Holman, Evidence for the formation of a large-scale current sheet in a solar flare, *Astrophys. J.*, **596**, L251, 2003.
- Svestka, Z., *Solar Flares*, Reidel, Dordrecht, 1976.
- Tajima, T. and K. Shibata, Plasma astrophysics, in *Frontiers in Physics*, edited by David Pines, Perseus Publishing, Cambridge, Massachusetts, pp. 494, 1997.
- Terasawa, T., K. Shibata, and M. Scholer, Comparative study of flares and substorms, *Adv. Space Res.*, **26**(3), 573, 2000.
- Tsuneta, S., H. Hara, T. Shimizu, L. W. Acton, K. T. Strong, H. S. Hudson, and Y. Ogawara, Observation of a solar flare at the limb with the YOHKOH Soft X-ray Telescope, *PASJ*, **44**, L63, 1992.
- Tsurutani, B. T. and C.-I. Meng, Interplanetary magnetic field variations and substorm activity, *J. Geophys. Res.*, **77**, 2964, 1972.
- Tsurutani, B. T. and W. D. Gonzalez, Calculations of the efficiency of “viscous interaction” between the solar wind and the magnetosphere during intense northward IMF events, *Geophys. Res. Lett.*, **22**, 663, 1995.
- Tsurutani, B. T. and X.-Y. Zhou, Interplanetary shock triggering of substorms: WIND and POLAR, *Adv. Space Res.*, **31**, 1063, 2003.
- Tsurutani, B. T., B. E. Goldstein, M. E. Burton, and D. E. Jones, A review of the ISEE-3 GEOTAIL magnetic field results, *Planet. Space Sci.*, **34**(10), 931, 1986.
- Wang, J. and Z. Shi, The flare-associated magnetic changes in an active region. II - Flux emergence and cancellation, *Sol. Phys.*, **143**, 119, 1993.
- Yokoyama, T., K. Akita, T. Morimoto, K. Inoue, and J. Newmark, Clear evidence of reconnection inflow of a solar flare, *Astrophys. J. Lett.*, **436**, L197, 2001.
- Zhang, Y. Z., J. X. Wang, and Y. Q. Hu, Two-current-sheet reconnection model of interdependent flare and coronal mass ejection, *Astrophys. J.*, **641**, 572, 2006.
- Zirin, H. and K. Tanaka, The flare of August 1972, *Sol. Phys.*, **32**, 173, 1973.
- Zhou, X.-Y. and B. T. Tsurutani, Interplanetary shock triggering of night-side geomagnetic activity: Substorms, pseudobreakups and quiescent events, *J. Geophys. Res.*, **106**, 18,957, 2001.

Modeling of substorms and flares by the fast reconnection mechanism

M. Ugai, K. Kondoh, and T. Shimizu

Research Center for Space and Cosmic Evolution, Ehime University, Matsuyama 790-8577, Japan

(Received October 2, 2007; Revised March 29, 2008; Accepted June 4, 2008; Online published May 29, 2009)

The 3D spontaneous fast reconnection model is applied to well-known signatures of geomagnetic substorms and solar flares. First, it is applied to the traveling compression regions (TCRs) associated with plasmoids propagating down the tail plasma sheet, known as a definite signature of geomagnetic substorms, and the in-situ satellite observations can be precisely explained, both qualitatively and quantitatively. Then, it is demonstrated that the magnetospheric current wedge drastically evolves through field-aligned currents to link the tail current to the auroral electrojet. It is also found that the well-known morphological features of two-ribbon flares can be explained by the fast reconnection model. In particular, the joule heating, associated with the flare current wedge, is shown to be important for the two-ribbon heating. Therefore, it is suggested that both solar flares and geomagnetic substorms result from the same physical mechanism, i.e., the fast reconnection mechanism.

Key words: Fast reconnection, substorms, flares, TCR, current wedge.

The fast reconnection mechanism involving standing slow shocks should be most responsible for explosive events observed in space plasmas (Shibata, 1999). Then, question is how the fast reconnection mechanism is realized in space plasmas of extremely large magnetic Reynolds number. A possible fast reconnection configuration was first proposed by Petschek (1964), and it was suggested that the fast reconnection mechanism may be determined by external boundary conditions (Vasyliunas, 1975). However, it can be realized only when a localized resistivity is applied (Ugai and Tsuda, 1977), and we have proposed the spontaneous fast reconnection model and demonstrated by 2D and 3D MHD simulations that the fast reconnection mechanism can be realized as an eventual solution by the nonlinear instability due to positive feedback between current-driven anomalous resistivities and global reconnection flows (Ugai, 1984, 1986, 1992, 1999; Ugai and Zheng, 2005).

In general, the energy conversion principle can directly be derived from Maxwell Equations as

$$\frac{\partial}{\partial t} \left(\frac{\mathbf{B}^2}{2\mu_0} + \frac{\epsilon_0 \mathbf{E}^2}{2} \right) = -\nabla \cdot (\mathbf{E} \times \mathbf{B})/\mu_0 - \mathbf{E} \cdot \mathbf{J} \quad (1)$$

The electric energy is negligible for the Alfvén time scale, so that $\mathbf{E} \times \mathbf{B}$ indicates the magnetic energy flow, and $\mathbf{E} \cdot \mathbf{J}$ the rate of conversion between magnetic and plasma energies. Any fast reconnection process involves magnetic energy inflow $\mathbf{E} \times \mathbf{B}$ toward the diffusion region and hence requires the dissipation mechanism $\mathbf{E} \cdot \mathbf{J} > 0$ in the diffusion (reconnection) region. Hence, the reconnection electric field \mathbf{E} at the X reconnection point must be sustained by some dissipation mechanism. If there is no dissipation mechanism, the reconnection electric field should readily

be short-circuited by electrons in the small diffusion region of electron inertial length of c/ω_{pe} .

The generalized Ohm's law may be written as $\mathbf{E} + \mathbf{u} \times \mathbf{B} = \mathbf{R}$, where \mathbf{R} is composed of the resistivity term \mathbf{R}_η , the Hall term \mathbf{R}_H , the electron pressure-tensor term \mathbf{R}_p , and the electron inertial term \mathbf{R}_i . For the Hall term, $\mathbf{R}_H \cdot \mathbf{J} = 0$, so that it cannot have any direct influence on the reconnection process, since it has no dissipation mechanism. In the diffusion region ($\mathbf{u} \times \mathbf{B} \sim 0$), \mathbf{R} can be described as $\eta \mathbf{J}$ since $\mathbf{E} \cdot \mathbf{J} > 0$, where $\eta (> 0)$ is the effective resistivity. The effective resistivity, usually provided by Coulomb collisions, is extremely small in space plasmas, and if current densities are notably intensified, it may result from wave-particle collisions due to current-driven microinstabilities, such as ion acoustic, two-stream (Buneman), lower-hybrid drift instabilities (Lui, 2001). In fact, anomalous resistivities are detected in laboratory plasmas (Ono *et al.*, 2001).

First, let us examine the physical conditions for the fast reconnection evolution to be realized in actual 3D systems. Initially, we assume a current sheet system that contains antiparallel magnetic fields B_x and a sheet current in $|y| < 1$. Initiated by a small disturbance, all the phenomena grow by the self-consistent interaction between the reconnection flow and the effective resistivity. In order to examine how magnetic reconnection is influenced by the effective resistivity, we may assume the following resistivity models. For the current-driven anomalous resistivity model (A), $\eta(\mathbf{r}, t) = k_R [V_d(\mathbf{r}, t) - V_C]$ for $V_d > V_C$ ($V_d = |\mathbf{J}/\rho|$), where ρ is plasma density, and V_d the relative electron-ion drift velocity. For another anomalous resistivity model (B), $\eta(\mathbf{r}, t) = k_J [|\mathbf{J}(\mathbf{r}, t)| - J_C]$ for $|\mathbf{J}| > J_C$. For the model (C), the Spitzer resistivity is assumed as, $\eta(\mathbf{r}, t) = k_C [T(\mathbf{r}, t)/T_0]^{-3/2}$, where T is the temperature.

We find that for the anomalous resistivity model (A) or (B), if the threshold V_C or J_C is sufficiently large, the fast

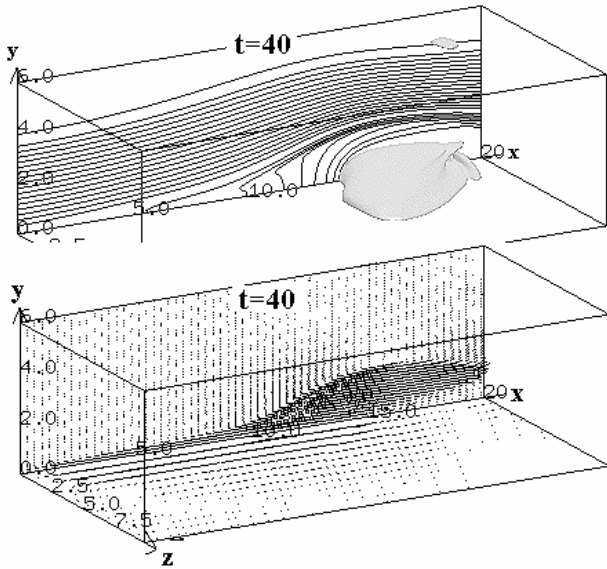


Fig. 1. (Upper) Magnetic field configuration with the isosurface of the plasma pressure P , and (lower) plasma flow vectors for the anomalous resistivity model (A), where the X neutral point is located at the origin.

reconnection mechanism fully evolves as a nonlinear instability because of the positive feedback, since the reconnection flows grow so as to enhance the current density at the X point by the pinch effect (Ugai, 1984, 1986, 1999). Figure 1 typically shows the resulting configuration for the anomalous resistivity model (A), where the fast reconnection mechanism involving slow shock builds up, and a large-scale plasmoid is formed ahead of the Alfvénic fast reconnection jet. Here, the simulation domain is a rectangular box, $0 \leq x \leq L_x = 20$, $0 \leq y \leq L_y = 6$, and $0 \leq z \leq L_z = 9.8$, with the mesh sizes $\Delta x = 0.04$, $\Delta y = 0.015$ and $\Delta z = 0.1$, and the conventional symmetry boundary conditions are assumed on the $z = 0$, $x = 0$, and $y = 0$ planes with the other outer planes being free boundaries. For the Spitzer resistivity model (C), no effective reconnection occurs because of the negative feedback, since the resistivity becomes reduced because of the increase in temperature T in the diffusion region (Ugai and Zheng, 2005). Note that magnetic reconnection is strongly influenced by the effective resistivity, and the fast reconnection mechanism can be realized for current-driven anomalous resistivities even in general three dimensions.

Next, let us apply the spontaneous fast reconnection model to substorm signatures observed by satellites. The so-called traveling compression regions (TCRs) have been clearly observed in the tail lobe of the Earth's magnetosphere, and they were qualitatively expected to result from the plasmoid bulge propagating down the central plasma sheet. The TCR signatures have been studied in detail (Slavin *et al.*, 1993), and Fig. 2 typically shows the observed magnetic field variations, which indicates the pulse-like compression of the earthward (B_x) field component as well as the northward to the southward tilting of the B_z field component. These fundamental features of TCR have been theoretically discussed by Birn (1992) and by Young and Hameiri (1992), but have not been verified in detail by nu-

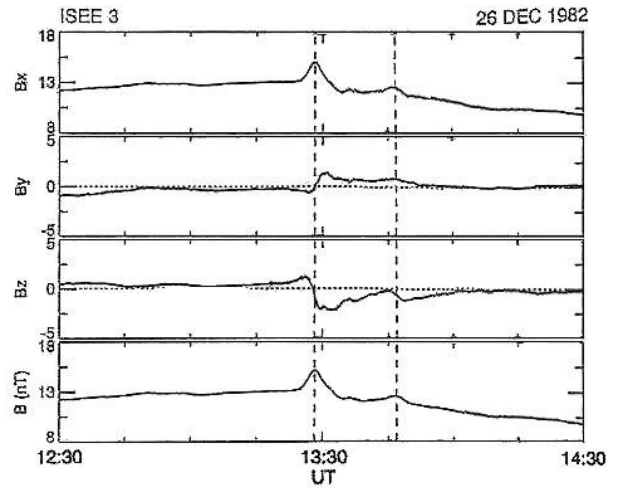


Fig. 2. ISEE 3 magnetic field observations taken in the north lobe of the tail at $x = -73R_e$ in GSM coordinates (after Slavin *et al.*, 1993).

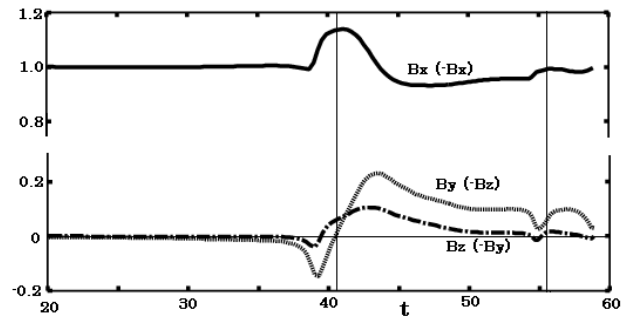


Fig. 3. Temporal variations of magnetic fields observed by virtual satellites located in the magnetic field (low- β) region, where B_x , B_y and B_z correspond to $-B_x$, $-B_z$ and $-B_y$ in GSM coordinates, respectively.

merical simulations.

In order to clarify the physical mechanism of TCR, 3D MHD simulations of the spontaneous fast reconnection model are performed with the same simulation model as in Fig. 1. It should be noted that unlike the traditional plasmoid, the resulting plasmoid contains no closed field lines and is caused and sustained by the Alfvénic fast reconnection jet. Then, in order to directly compare the simulation results with the satellite observations, virtual satellites are located in the magnetic field region outside the central plasma sheet in the simulation domain, which can readily measure the temporal variations of magnetic fields in accordance with the plasmoid propagation (Ugai and Zheng, 2006a). Figure 3 shows the field components, measured by the virtual satellites, which indicate the pulse-like field compression B_x with the bipolar changes in B_y and B_z . Then, another tearing suddenly occurs, leading to a small plasmoid propagating outward, so that a small TCR is observed at $t \sim 56$. These results are in good agreement with the actual satellite observations (Fig. 2) (Ugai and Zheng, 2006b).

Other well-known substorm signatures are the earthward jet and the magnetic field dipolarization. In particular, when a substorm builds up, the tail current sheet may suddenly

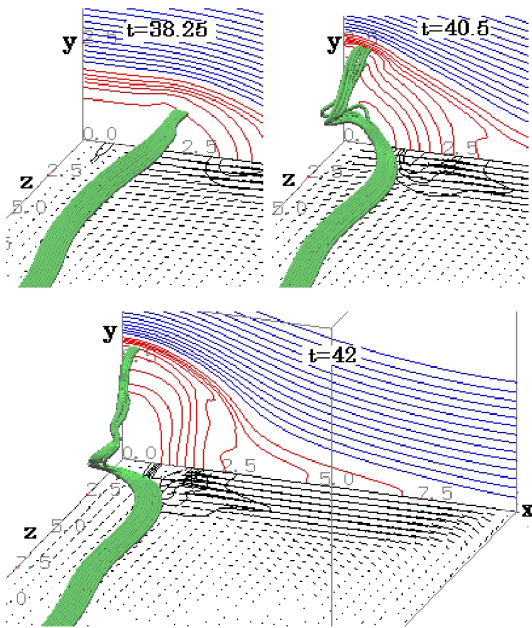


Fig. 4. (Color online) Current flow lines starting from the segment, $2.16 < x < 2.72$ at $y = 0.27$ and $z = 13$, at different times, where contour lines of the reconnected field component B_y and the flow velocity vectors \mathbf{u} in the (z, x) plane are also shown, where the X neutral point is located at $x = L_x = 10$.

be disrupted so that a substorm current wedge evolves to link the tail current to the auroral electrojet through field-aligned currents (McPherron *et al.*, 1973). The importance of current wedge has widely been recognized by satellite and ground observations, but this long-standing question has never been resolved theoretically. Recently, it is demonstrated on the basis of the 3D spontaneous fast reconnection model that when the fast reconnection jet collides with the closed field lines in the near-Earth magnetosphere, the drastic current wedge evolution can be realized (Ugai and Konoh, 2006).

We have also found that only when the east-west width of the tail current sheet is 3–4 times larger than its thickness, the 3D fast reconnection mechanism and the current wedge can fully be set up (Ugai and Shimizu, 1996; Ugai, 2007). For this case, Fig. 4 shows the resulting current flow lines, where the contour lines of the reconnected field component B_y and the flow velocity vectors \mathbf{u} in the (z, x) plane are also shown. In this model, magnetic reconnection is initiated at $x = L_x = 10$, and the $x = 10$ plane as well as the $x = 0$ plane is assumed to be the symmetry boundary. We readily see that when the closed field lines in the near-Earth magnetosphere is compressed by the 3D fast reconnection jet, the sheet current ($J_z < 0$) ahead of the closed field lines drastically turns its direction toward the foot points of close field lines through field-aligned currents. This is generally consistent with the predicted substorm current wedge.

In view of morphological similarities between flares and substorms, the spontaneous fast reconnection model may also be applied to two-ribbon flares. Unlike in-situ observations in the Earth's magnetosphere, magnetic fields can hardly be measured in the solar corona. In this sense, any theoretical model of solar flare is circumstantial, so that it is

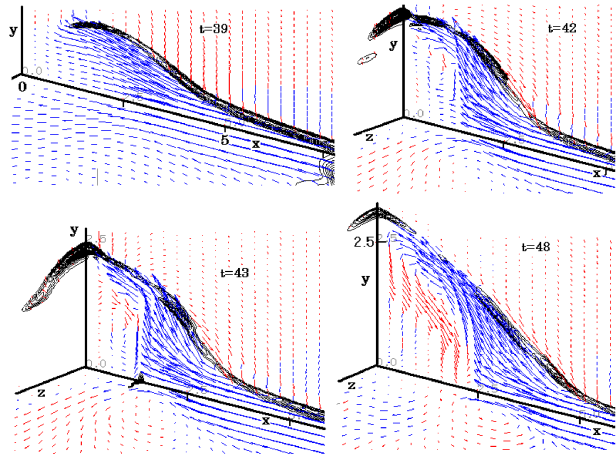


Fig. 5. (Color online) Plasma flow vectors and contour lines of the joule heating $\eta \mathbf{J}^2$, where the fast reconnection flow velocity $u_x < 0$ attains the Alfvén velocity, $V_A \sim -2.7$, measured in the low- β region.

essential to clarify the well-known morphological features that have been obtained from satellite observations. The previous theories were mostly based on the cartoon model based on the 2D Petschek reconnection configuration, and it was supposed that the chromospheric flare heating should be caused directly from the coronal plasma heated and accelerated by 2D reconnection shocks.

The solar surface is modeled as follows. An antiparallel magnetic field $\mathbf{B} = [B_x(y), 0, 0]$ is initially assumed as: $B_x(y) = \sin(\pi y/2)$ for $0 < y < 1$; $B_x = 1$ for $1 < y < 4$; $B_x = \cos[(y-4)\pi/1.2]$ for $4 < y < 4.6$; $B_x = 0$ for $y > 4.6$; also, $B_x(y) = -B_x(-y)$ for $y < 0$. Fluid velocity $\mathbf{u} = (0, 0, 0)$, and plasma pressure $P(y)$ satisfies the pressure-balance condition, $P + B_x^2 = 1 + \beta_0$, where $\beta_0 = 0.15$ is taken. Also, plasma density ρ initially satisfies $\rho(x, y) = [R_0 \exp[-(x/0.4)^4] + 1] P(y)/(1 + \beta_0)$, where $R_0 = 100$ is taken, so that $x = 0$ corresponds to the chromosphere, and the corona is for $x \gg 0.4$. In the chromosphere, placed in the $x = 0$ plane, the plasma density is assumed to be 100 times larger than in the corona for $x > 0.4$, so that the temperature in the corona is 100 times larger than in the chromosphere.

An initial disturbance is imposed at $x = L_x = 10$ on the initial configuration, and then the current-driven anomalous resistivity models are assumed. Figure 5 illustrates the resulting plasma flow vectors and contour lines of the joule heating $\eta \mathbf{J}^2$. The joule heating in the (x, y) plane mostly indicates the standing slow shock layer, across which the plasma is accelerated to the Alfvén velocity. The plasmoid, propagating in the negative x direction (at $t = 39$), collides with the chromosphere ($x = 0$) at $t \sim 42$, leading to sudden current wedge evolution, which may be called the flare current wedge by analogy with the substorm current wedge. For $t > 42$, distinct plasma downflows ($u_x < 0$) toward the chromosphere ($x = 0$) occur along the magnetic loop boundary.

The flare current wedge causes an extreme increase in the current density (hence an anomalous resistivity) in the chromosphere ($x = 0$). Hence, Fig. 5 indicates that re-

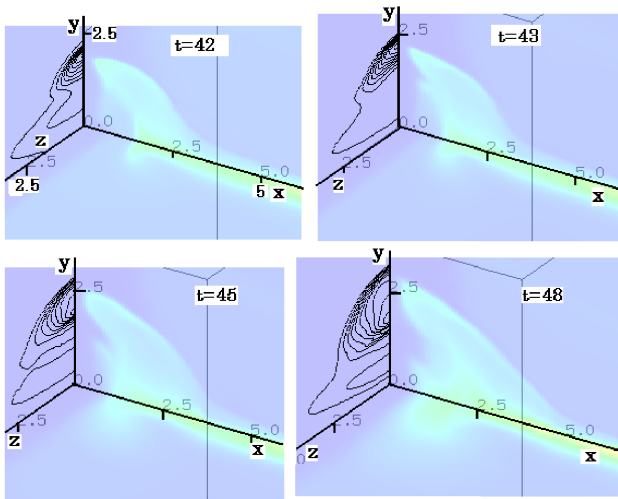


Fig. 6. (Color online) Temperature distributions, shown by contour lines at $x = 0$, where the maximum temperature becomes more than 20 times its initial value.

markable joule heating occurs along the thin layer in the chromosphere near the separatrix, which bounds the pre- and post-reconnection field lines. In particular, the strongest heating occurs impulsively at times $t = 42$ and 43 . Accordingly, Fig. 6 shows the resulting temperature distributions, and demonstrates that at $t = 42$ the temperature is suddenly enhanced distinctly in the chromospheric thin layer, which presents the two-ribbon structure because of the symmetry boundary conditions. Hence, the plasma pressure is notably enhanced in the chromosphere to cause distinct upward flows ($u_x > 0$) from the chromosphere at $t = 48$ inside the loop, which is consistent with the so-called chromospheric evaporation observed during flares. The joule heating layer moves in the positive y direction as the reconnected field lines are piled up, and the cusp-shaped flare loop expands outward. These results are consistent with the well-known morphological features of two-ribbon flares.

In summary, in-situ satellite observations of TCR signatures can exactly be explained by the 3D spontaneous fast reconnection model (Figs. 2 and 3). Also, the 3D fast reconnection jet causes drastic evolution of magnetospheric current wedge (Fig. 4). For this theoretical model, current-driven anomalous resistivities are essential, and the current disruption occurs just ahead of the closed field lines to form the current wedge (Fig. 4). Interestingly, these basic features are rather consistent with those of the current disruption model (Lui, 1996). In addition, it is demonstrated that the well-known morphological features of two-ribbon flares are pertinently explained by this theoretical model (Figs. 5 and 6). In particular, the drastic increase in the chromospheric temperature occurs in the shape of two ribbons, and the resulting coronal flare loop is expanding outward. Also, the definite chromospheric evaporation occurs. These re-

sults suggest that both solar flares and geomagnetic substorms result from the same physical mechanism, i.e., the fast reconnection mechanism.

Acknowledgments. This work was supported by Grant-in-Aids for Creative Scientific Research ‘The Basic Study of Space Weather Prediction’ (17GS0208, Head Investigator: K. Shibata) from the Ministry of Education in Japan, Mitsubishi Foundation, RISH of Kyoto University, and Solar-Terrestrial Environment Laboratory of Nagoya University.

References

- Birn, J., Quasi-steady current sheet structures with field-aligned flow, *J. Geophys. Res.*, **97**, 16,817–16,826, 1992.
- Lui, A. T. Y., Current disruption in the Earth’s magnetosphere: observations and models, *J. Geophys. Res.*, **101**, 13067–13088, 1996.
- Lui, A. T. Y., A multiscale model for substorms, *Space Sci. Rev.*, **95**, 325–345, 2001.
- McPherron, R. L., C. T. Russel, and M. P. Aurbry, Satellite studies of magnetospheric substorms on August 15, 1968. 9. Phenomenological model for substorms, *J. Geophys. Res.*, **78**, 3131–3149, 1973.
- Ono, Y. *et al.*, Fast compression of a current sheet during externally driven magnetic reconnection, *Earth Planets Space*, **53**, 521–526, 2001.
- Petschek, H. E., Magnetic field annihilation, in *AAS-NASA Symposium on the Physics of Solar Flares*, NASA Spec. Pub., SP-50, 425–439, 1964.
- Shibata, K., Evidence of magnetic reconnection in solar flares and a unified model of flares, *Astrophys. Space Sci.*, **264**, 129–144, 1999.
- Slavin, J. A. *et al.*, ISEE 3 observations of traveling compression regions in the Earth’s magnetotail, *J. Geophys. Res.*, **98**, 15425–15446, 1993.
- Ugai, M., Self-consistent development of fast magnetic reconnection with anomalous plasma resistivity, *Plasma Phys. Controlled Fusion*, **26**, 1549–1563, 1984.
- Ugai, M., Global dynamics and rapid collapse of an isolated current-sheet system enclosed by free boundaries, *Phys. Fluids*, **29**, 3659–3667, 1986.
- Ugai, M., Computer studies on development of the fast reconnection mechanism for different resistivity models, *Phys. Fluids B*, **4**, 2953–2963, 1992.
- Ugai, M., Computer studies on the spontaneous fast reconnection model as a nonlinear instability, *Phys. Plasmas*, **6**, 1522–1531, 1999.
- Ugai, M., Conditions for drastic evolution of magnetospheric current wedge, *Phys. Plasmas*, **14**, 062902, 2007.
- Ugai, M. and T. Tsuda, Magnetic field-line reconnection by localized enhancement of resistivity. Part 1. Evolution in a compressible MHD fluid, *J. Plasma Phys.*, **17**, 337–356, 1977.
- Ugai, M. and T. Shimizu, Computer studies on the spontaneous fast reconnection mechanism in three dimensions, *Phys. Plasmas*, **3**, 853–862, 1996.
- Ugai, M. and L. Zheng, Conditions for the fast reconnection mechanism in three dimensions, *Phys. Plasmas*, **12**, 092312, 2005.
- Ugai, M. and L. Zheng, Modeling of traveling compression regions in the Earth’s magnetotail by the spontaneous fast reconnection model, *Phys. Plasmas*, **3**, 032901, 2006a.
- Ugai, M. and L. Zheng, Parametric studies on traveling compression regions observed in the Earth’s magnetotail, *Phys. Plasmas*, **13**, 062906, 2006b.
- Ugai, M. and K. Kondoh, Evolution of magnetospheric current wedge by the spontaneous fast reconnection model, *Phys. Plasmas*, **13**, 102903, 2006.
- Vasyliunas, V. M., Theoretical models of magnetic field line merging, *Rev. Geophys. Space Phys.*, **13**, 303–336, 1975.
- Young, R. and E. Hameiri, Approximate magnetotail equilibria with parallel flow, *J. Geophys. Res.*, **97**, 16789–16802, 1992.

M. Ugai (e-mail: ugai@cosmos.ehime-u.ac.jp), K. Kondoh, and T. Shimizu

Coronal loops, flare ribbons and aurora during slip-running

Brigitte Schmieder¹, Guillaume Aulanier¹, Pascal Démoulin¹, and Etienne Pariat²

¹Observatoire de Paris, LESIA, 92195 Meudon, France

²NRL, Washington DC, USA

(Received September 12, 2007; Accepted August 16, 2008; Online published May 29, 2009)

Solar two ribbon flares are commonly explained by magnetic field reconnections in the low corona. During the reconnection energetic particles (electrons and protons) are accelerated from the reconnection site. These particles are following the magnetic field lines down to the chromosphere. As the plasma density is higher in these lower layers, there are collisions and emission of radiation. Thus bright ribbons are observed at both ends of flare loops. These ribbons are typically observed in H α and in EUV with SoHO and TRACE. As the time is going, these ribbons are expanding away of each other. In most studied models, the reconnection site is a separator line, where two magnetic separatrices intersect. They define four distinct connectivity domains, across which the magnetic connectivity changes discontinuously. In this paper, we present a generalization of this model to 3D complex magnetic topologies where there are no null points, but quasi-separatrices layers instead. In that case, while the ribbons spread away during reconnection, we show that magnetic field lines can quickly slip along them. We propose that this new phenomenon could explain fast extension of H α and TRACE 1600 Å ribbons, fast moving HXR footpoints along the ribbons as observed by RHESSI, and that it is observed in soft X rays with Hinode/XRT.

Key words: Sun: flares, magnetosphere: aurora.

1. Introduction

Eruptions occur at locations on the Sun where there is a build-up of a large amount of magnetic energy and when this energy is released via some reconnection process. Many models deal with how this energy release is accomplished; for example Forbes and Isenberg (1991), Lin *et al.* (1998) discuss on the convergence of magnetic flux below a flux tube situated along a magnetic polarity inversion line that leads to enhancement of the flux tube and eruption. Chen and Shibata (2000) presents a model where eruption results when the tension of the sheared arcade or flux tube field is weakened via reconnection between the main magnetic field and emerging flux (kind of “tether-cutting” mechanism). Antiochos *et al.* (1999) discuss instead disruption of field lines and reconnection above flux tubes. To determine which of the mechanism is predominantly responsible for eruptions it is necessary to observe the onset and the evolution of flares. The coronal plasma is frozen into the magnetic field almost everywhere except where current sheets can be formed and then dissipated. Current sheets develop along separatrices when the magnetic configuration evolves quasi-statically or dynamically. A very powerful tool to understand where the energy could be deposited is to study the magnetic topology of the active region, since it defines where magnetic reconnection is expected to occur (see reviews of Démoulin, 2005; Longcope, 2005; Schmieder, 2006).

In the first section, magnetic topology models are pre-

sented. In the second and third sections, we review eruptive and compact flares showing that their dynamics cannot be neglected to interpret the formation of long ribbons with evolving H α , UV brightenings and X-ray kernels. New simulations are briefly described. Slip-running reconnection simulation explains the fast motion of X-ray sources along flare.

2. Magnetic Topological Models

Coronal activities such as flares, eruptions and general heating are often attributed to the manner in which the coronal field responds to photospheric motion. The coronal plasma has a low resistivity and to release efficiently the free energy, small length scales have to be created. Coronal magnetic fields are forced to evolve continuously by slow photospheric velocities (0.1 km/s), faster velocities still lower to the typical Alfvén velocity (~ 1000 km/s) may exist during magnetic flux emergence. In this context magnetic configurations, with a slow evolution at the boundary leads to the formation of very thin current layers play a key role (review of Démoulin, 2006). Let us recall some classical definitions of magnetic configuration and reconnection. Separatrices are magnetic surfaces where the magnetic field line linkage is discontinuous, thus where the field lines can change abruptly of connectivity. In 2D configuration the reconnection occurs at a X-point (null point) where the magnetic vanishes, in 3D configuration the intersection of the field lines occur along the separator, intersection of the separatrices. Current sheet form along the whole separatrices when shearing flows are present in the photosphere. The flare ribbons are found at the intersections of the separatrices and the chromosphere.

Flare ribbons and loops evidence the locations where the stored energy is released. For testing the spatial localization of the energy release sites, it is needed to extrapolate the field lines in the corona using photospheric magnetograms as a boundary condition. When the magnetic field is no more represented by point charges but maintained continuously as observed, there are not necessarily separatrices to interpret the ribbons: a generalization of the concept of separatrices does provide an interpretation of 3D magnetic reconnection (Démoulin *et al.*, 1996a, 1997). This new concept is based on the existence of quasi-separatrice layers (QSL) for general magnetic fields anchored to a boundary. QSLs are defined as volumes where magnetic field lines can change of connectivity abruptly. There are no coronal null points in such configurations. Such topological properties are insensitive to detailed geometry of the magnetic field, and thereby create a very robust tool to understand the loci of flare energy release. The intersections of QSLs and the chromosphere are restricted to smaller regions than in the case of separatrices and match better the shape of the ribbons (Schmieder *et al.*, 1997).

3. Eruptive Flares

Firstly we investigated the regions of large flares, we called eruptive flares when a coronal mass ejection (CME) is related to the flare. In this frame, Chen and Shibata (2000) and Lin (2004) proposed unified models. As the magnetic field lines are reconnected, a plasmoid is escaping and forming the CME. During the reconnection, electrons are precipitated downwards to denser layers. They heat the plasma and form the so-called two bright ribbons in the chromosphere (visible in $H\alpha$, in Ca II H by Hinode/SOT, the 1600 Å continuum by TRACE), in the transition region (CDS, EIT and TRACE). Between the ribbons, loops are observed in different wavelengths: bright X ray loops, in coronal lines 171 Å and 195 Å and bright or dark in $H\alpha$ as they are cooling (Schmieder *et al.*, 1996; DelZanna *et al.*, 2006a). The loops form growing arcades with higher and higher hot loops while the reconnection point is rising. In the ribbons, kernels are the footpoints of loops (DelZanna *et al.*,

2006b). It was shown that the later arcades are less and less sheared (Su *et al.*, 2006). During cooling process the two ribbon distance is increasing. In complex active regions different systems of ribbons can be formed and developed in a fast time, of the order of few minutes (14 July 2000, 28 October 2003, 13 September 2005, 27 May 2003). In the event of 13 September 2005 a series of 10 flares occur within one day and even a series of 3 flares (X1.4, X 1.5, X1.7) in three hours. The concerned active regions are all complex containing a spot with constant new emerging field with fast moving polarities. It is difficult to identify the trigger of each flare of the series.

Nevertheless, we are able to find the locations where the magnetic reconnection is possible and produce flares by analyzing the topology either by lfff (linear-force-free field) extrapolation when the shear is weak enough, otherwise by nlfff (non linear-force-free field) methods of extrapolation have to be applied (Régnier and Canfield, 2007).

Many models of flare onset are developed based on tether-cutting or straining forces (Klimchuk, 2001). For large quadrupolar configuration, the breakout model proposed by Antiochos (1999) seems to be successful for some cases (Aulanier *et al.*, 2000). The existence of null point which was pointed out in the Antiochos model does not seem to be a necessary condition for breaking the overlying lines (Schmieder *et al.*, 2006; Mandrini *et al.*, 2006). Reconnection could occur in quasi separatrices layers with no null points (Li *et al.*, 2006; Schmieder *et al.*, 2007).

4. QSL Reconnection with Slippage of Magnetic Field Lines

In the previous section we have shown complex examples of flares with multiple ribbons formed at different places successively. Here we present a simple compact flare with no CME in order to study in details the dynamics of the ribbons, not the well known increasing distance of the ribbons versus time but the fast lateral extension of the ribbons. The flare occurs in a sheared active region at the location of a small emerging flux (Berlicki *et al.*, 2004). The observation in $H\alpha$ shows two ribbons, one of them is relatively

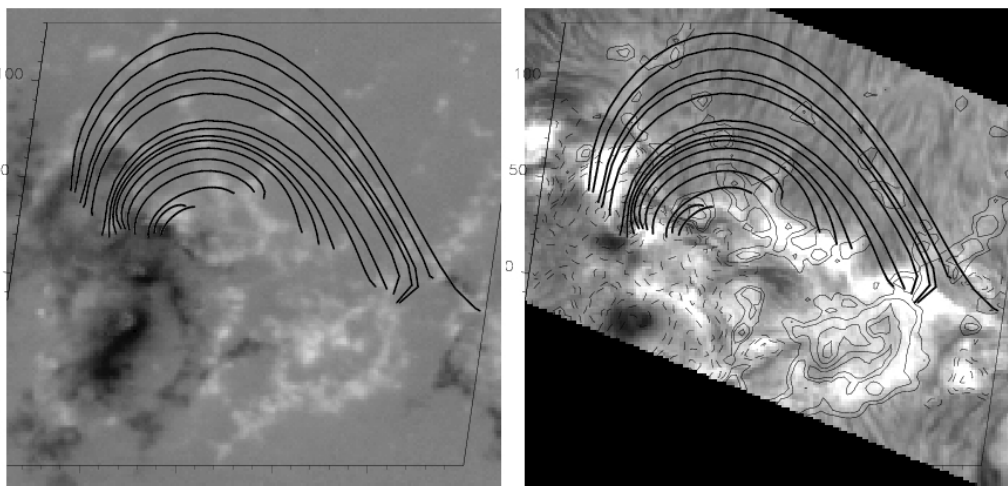


Fig. 1. Magnetic field lines extrapolated in a linear force free configuration and $H\alpha$ ribbons of the 22 October 2003 flare for two times observed with the VTT in Canarias showing the fast extension of the ribbons (Berlicki *et al.*, 2004).

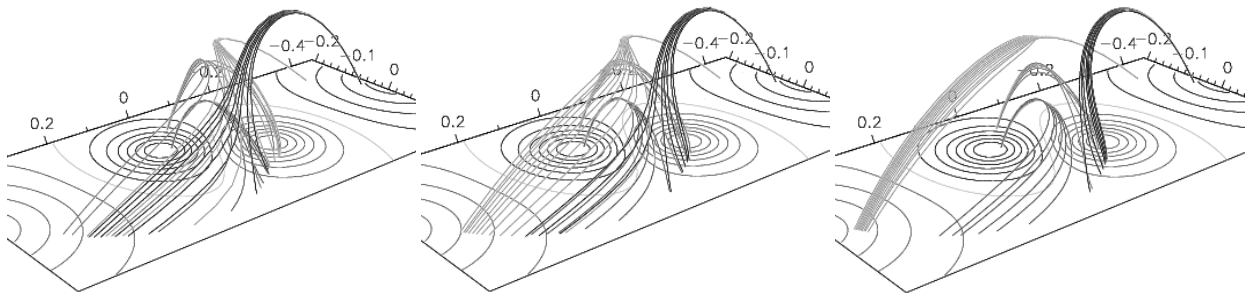


Fig. 2. Quadrupolar magnetic reconnection with slip-running field lines for three different times. The darker field lines have a fixed footpoint anchored in a fixed point in the right source, the other footpoint is slip-running continuously along the quasi-separatrix layer. During the reconnection, the plasma in the different field lines will be successively heated with footpoints visible as bright kernels. This behaviour explains the fast extension of ribbons (Aulanier *et al.*, 2006).

Auroral shapes & dynamics due to QSL slip-running reconnection

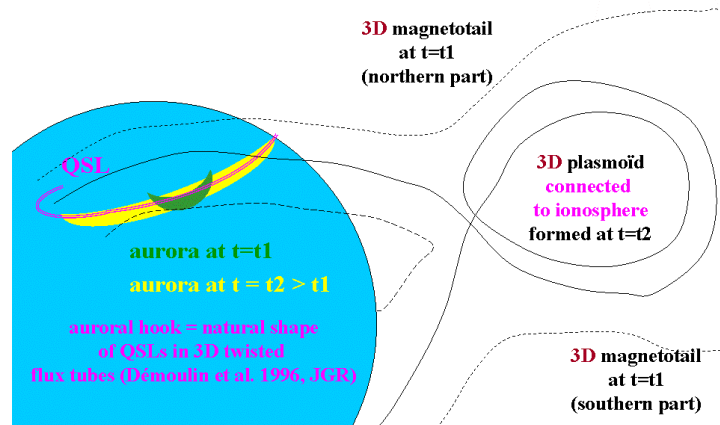


Fig. 3. Sketch of the formation of aurora due to magnetic reconnection in a QSL configuration.

short and stays short, the other one is developing an extension in a few minutes. The conclusion of the Berlicki *et al.* (2004)'s paper was that there was a series of reconnections in the corona. The question arises to know if this was really due to multiple reconnections. We performed a lfff extrapolation using the data base of FROMAGE and pointed out the existence of loop-like field lines growing with one fixed footpoint and the other footpoint was slip-running along the ribbon (Fig. 1).

Aulanier *et al.* (2006) propose a new idea with the slippage of the field lines along the QSLs (Fig. 2). Using time dependent MHD simulation it is shown the possibility of field lines to change connectivity in a continuously way and not abruptly like in the classical null point reconnection where field lines clearly connect by pair. This process can take place in many solar flares. Magnetic field configurations with fields weakly stressed by asymmetric line-tied twisting motions are considered. When the line-tied driving is suppressed, magnetic reconnection is solely due to the self-pinching and dissipation of current layers formed along QSLs. For thin QSLs and high resistivity, the field line footpoints slip-run at super-Alfvénic speeds along the intersection of the QSLs with the chromosphere. Since particles are probably accelerated in reconnection regions or

in the vicinity, slip-running reconnection could explain the fast extension of the ribbons in all the wavelengths, being the result of heat of the plasma as particles travel in denser plasma. Recently Hinode observed moving loops moving that have been interpreted as due to the slippage of magnetic field lines (Aulanier *et al.*, 2007).

5. Reconnection in the Magnetosphere in QSLs

Making an analogy between solar flares and magnetospheric substorms, we can conjecture that QSL reconnection may very well occur in the latter. Indeed, the geometry of the Earth magnetosphere can possibly make the appearance of real 3D null points impossible in the magneto-tail when it is stretched anti sunward. This does not preclude the development of rotational discontinuities in the tail, i.e. of 2D null points with an azimuthally guide field, as often reported in global models of the magnetosphere. But solar models teach us that the latter configurations can correspond to a hyperbolic flux tube (HFT), hence to QSLs when the system is viewed globally. Assuming that substorms correspond, on large scales, to the formation of a fully 3D twisted flux rope rooted in the ionosphere (and not a 2D plasmoid), we can transpose the solar Cartesian 3D model of Démoulin *et al.* (1996a) to the Earth spherical geome-

try, replacing the solar photosphere by the ionosphere and the solar corona by the magnetosphere. This topology naturally possesses QSLs between the flux rope and the outer fields, that intersect at a HFT located between the Earth and the flux rope, and whose footprints have J shapes. In this picture, polar auroras are the equivalent to chromospheric flare ribbons, i.e. they are due to the impact of particles accelerated from the reconnection site, i.e. the HFT.

Transposing our recent findings about slip running reconnection in the corona to the magnetosphere, we predict and interpret by the latter model the following evolution of aurorae: (1) the aurora starts to form a point-like brightening at the ionospheric footprint of the HFT, where QSL reconnection is the most efficient since that is where the strongest field aligned currents (i.e. parallel electric fields) naturally develop, according to Aulanier *et al.* (2005); (2) the aurora brightenings expand along the footprint of the J-shaped QSLs predicted by Démoulin *et al.* (1996b), azimuthally in the Earth case; this fast development is due to slip-running reconnection at the HFT (as described in Aulanier *et al.*, 2006) in the magneto-tail during the formation of the flux rope that it later ejected anti-sunward. We do not know whether these dynamics of polar aurorae are frequently observed or not, so we would like to encourage further studies to test our present transposition of solar slip-running reconnection models to magnetospheric models (Fig. 3).

6. Conclusion

Flares and eruptions are dynamical events which evolve with a fast speed. Past flare models were static in 2D and 3D. They provided good insight on the magnetic topology of active regions and the loci of possible deposit of energy.

We have shown that MHD simulations explain some particular aspects of the dynamics of flares. In one case we have shown how slip-running magnetic field lines in quasi-separatrix can mimic fast extension of $H\alpha$ and UV ribbons observed by THEMIS and TRACE and running XRT loops observed by Hinode. Finally, making an analogy between solar flares and magnetospheric substorms, we can conjecture that QSL reconnection may very well occur in the latter.

Acknowledgments. I would like to thank Dr. Akosufu and Dr. Shibata, the organizers of the CAWSES workshop in Alaska where I present this work.

References

- Antiochos, S. K., C. R. DeVore, and J. A. Klimchuk, A model for solar coronal mass ejections, *Astrophys. J.*, **510**, 485–493, 1999.
- Aulanier, G., E. E. DeLuca, S. K. Antiochos, A. McMullen, and L. Golub, The topology and evolution of the Bastille day flare, *Astrophys. J.*, **540**, 1126–1142, 2000.
- Aulanier, G., E. Pariat, and P. Démoulin, Current sheet formation in quasi-separatrix layers and hyperbolic flux tubes, *Astron. Astrophys.*, **444**, 961–976, 2005.
- Aulanier, G., E. Pariat, P. Démoulin, and DeVore, Slip-running reconnection in quasi-separatrix layers, *Sol. Phys.*, **238**, 347–376, 2006.
- Aulanier, G., L. Golub, E. W. DeLuca, J. W. Cirtain, R. Kano, L. L. Lundquist, N. Nakurage, T. Sakao, and M. Weber, *Science*, 2007 (submitted).
- Berlicki, A., B. Schmieder, N. Vilmer, G. Aulanier, and G. DeZanna, Evolution and magnetic topology of the M 1.0 flare of October 22, 2002, *Astron. Astrophys.*, **423**, 1119–1131, 2004.
- Chen, P. F. and K. Shibata, An emerging flux trigger mechanism for coronal mass ejections, *Astrophys. J.*, **545**, 524–531, 2000.
- DeZanna, G., B. Schmieder, H. Mason, A. Berlicki, and S. Bradshaw, The gradual phase of the X17 flare on October 28, 2003, *Sol. Phys.*, **239**, 173–191, 2006a.
- DeZanna, G., A. Berlicki, B. Schmieder, and H. Mason, A multi-wavelength study of the compact M1 flare on October 22, 2002, *Sol. Phys.*, **234**, 95–113, 2006b.
- Démoulin, P., Magnetic topologies: where will reconnection occur?, in *ESA SP*, edited by Innes, D., Lagg, A., and Solanki, S. A., **596**, 2005.
- Démoulin, P., Extending the concept of separatrixes to QSLs for magnetic reconnection, *Adv. Space Res.*, **37**, 1269–1282, 2006.
- Démoulin, P., J. C. Hénoux, E. R. Priest, and C. Mandrini, Quasi-Separatrix layers in solar flares. I. Method, *Astron. Astrophys.*, **308**, 643–655, 1996a.
- Démoulin, P., E. Priest, and D. Lonie, Three-dimensional magnetic reconnection without null points, *J. Geophys. Res.*, **101**, 7631–7646, 1996b.
- Démoulin, P., L. G. Bagala, C. Mandrini, J. C. Hénoux, and M. G. Rovira, Quasi-separatrix layers in solar flares. II. Observed magnetic configurations, *Astron. Astrophys.*, **325**, 305–317 1997.
- Forbes, T. G. and P. A. Isenberg, A catastrophe mechanism for coronal mass ejections, *ApJ*, **373**, 294–307, 1991.
- Klimchuk, J., Models of CMEs, *Geographical Monograph*, **125**, 143, 2001.
- Li, H., B. Schmieder, G. Aulanier, and A. Berlicki, Is pre-eruptive null point reconnection required for triggering eruptions?, *Sol. Phys.*, **237**, 85–100, 2006.
- Lin, J., T. G. Forbes, P. Isenberg, and P. Démoulin, The effect of curvature on flux-rope models of coronal mass ejections, *Astrophys. J.*, **504**, 1006–1009, 1998.
- Lin, J., Motions of flare ribbons and loops in various magnetic configurations, *Sol. Phys.*, **222**, 115–136, 2004.
- Longcope, D. W., Topological methods for the analysis of solar magnetic fields, *Living Rev. Sol. Phys.*, **2**, 1–25, 2005.
- Mandrini, C. H., P. Démoulin, B. Schmieder, E. E. DeLuca, E. Pariat, and W. Uddin, Companion event and precursor of the X17 flare on 28 October 2003, *Sol. Phys.*, **238**, 293–312, 2006.
- Régnier, S. and R. C. Canfield, Evolution of magnetic fields and energetics of flares in active region 8210, *Astron. Astrophys.*, **451**, 319–330, 2007.
- Schmieder, B., Magnetic source regions of coronal mass ejections, *J. Astrophys. Astron.*, **27**, 139–149, 2006.
- Schmieder, B., P. Heinzel, L. van Driel, and J. R. Lemen, Post-flare loops of 26 June 1992, II, *Sol. Phys.*, **165**, 303–328, 1996.
- Schmieder, B., G. Aulanier, P. Démoulin, L. van Driel, T. Roudier, N. Nitta, and G. Cauzzi, Magnetic reconnection driven by emergence of sheared magnetic field, *Astron. Astrophys.*, **325**, 1213–1225, 1997.
- Schmieder, B., C. H. Mandrini, P. Démoulin, E. Pariat, A. Berlicki, and E. DeLuca, Magnetic reconfiguration before the X 17 Solar flare of October 28 2003, *Adv. Space Res.*, **37**, 1313–1316, 2006.
- Schmieder, B., C. Mandrini, G. Aulanier, H. Li, and A. Berlicki, What is the role of magnetic null points in large flares?, *Adv. Space Res.*, **39**, 1840–1846, 2007.
- Su, Y. N., L. Golub, A. A. van Ballegooyen, and M. Gros, Analysis of magnetic shear in an X17 solar flare on October 28, 2003, *Sol. Phys.*, **236**, 325–349, 2006.

B. Schmieder (e-mail: brigitte.schmieder@obspm.fr), G. Aulanier, P. Démoulin, and E. Pariat

Three-dimensional non-linear instability of spontaneous fast magnetic reconnection

T. Shimizu, K. Kondoh, and M. Ugai

Department of Computer Science, Ehime University, Bunkyo town, Matsuyama City 790-8577, Japan

(Received November 2, 2007; Revised June 23, 2008; Accepted August 24, 2008; Online published May 29, 2009)

Three-dimensional instability of spontaneous fast magnetic reconnection is studied using MHD (magneto-hydro-dynamic) simulation. Previous two-dimensional MHD studies have demonstrated that, if a current-driven anomalous resistivity is assumed, two-dimensional fast magnetic reconnection occurs and two-dimensional large-scale magnetic loops, i.e., plasmoids, are ejected from the reconnection region. In most two-dimensional MHD studies, the structure of the current sheet is initially one-dimensional. On the other hand, in recent space plasma observations, fully three-dimensional magnetic loops frequently appear even in the almost one-dimensional current sheet. This suggests that the classical two-dimensional fast magnetic reconnection may be unstable to any three-dimensional perturbation, resulting in three-dimensional fast magnetic reconnection. In this paper, we show that a three-dimensional resistive perturbation destabilizes two-dimensional fast magnetic reconnection and results in three-dimensional fast magnetic reconnection. The resulting three-dimensional fast reconnection repeatedly ejects three-dimensional magnetic loops downstream. The obtained numerical results are similar to the pulsating downflows observed in solar flares. According to the Fourier analysis of the ejected magnetic loops, the time evolution of this three-dimensional instability is fully non-linear.

Key words: Magnetic reconnection, solar flare, MHD simulation.

1. Introduction

Fast magnetic reconnection provides a physical mechanism by which magnetic energy is explosively converted into plasma kinetic and thermal energies. This mechanism has been considered to play a crucial role in solar flares and geomagnetic substorms. Fast magnetic reconnection has been reported in many numerical magneto-hydro-dynamic (MHD) studies (e.g., Ugai and Tsuda, 1977). On the other hand, the plasma jets and magnetic loops associated with fast magnetic reconnection have been also reported in space satellite observations of solar flares (Masuda *et al.*, 1994; Shibata *et al.*, 1995; Shibata, 1996; Yokoyama *et al.*, 2001; Asai *et al.*, 2004). In particular, in some observation reports, the three-dimensional (3D) structure of fast magnetic reconnection was discussed (Shibata *et al.*, 1995; Asai *et al.*, 2004). Asai *et al.* (2004) reported that the intermittent plasma downflows observed in solar flares may be caused by fast magnetic reconnection in the high-altitude corona. In order to theoretically explain the observation data, they suggested that 3D fast magnetic reconnection may occur even in a uniform (1D) current sheet and, hence, the ejected 3D magnetic loops may be strongly localized in the current sheet direction. To explain the formation of impulsive plasma downflows, Linton and Longcope (2006) proposed a theoretical 3D model. However, it is still unclear how such a 3D fast magnetic reconnection process occurs in the 1D current sheet.

In this paper, the 2D spontaneous fast magnetic reconnection model proposed by Ugai is numerically developed to a 3D model. At this point, note that the study shown in this paper is basically different from the 3D studies reported by Ugai and colleagues (Ugai *et al.*, 2004, 2005). In the studies reported by Ugai, since the initial resistive disturbance is strongly localized in the sheet current direction, it directly results in a “single” 3D fast magnetic reconnection. In contrast, in the work presented here, the initial resistive disturbance is almost 2D but only includes a “very weak non-uniformity (perturbation)” in the sheet current direction, resulting in “multiple” 3D fast magnetic reconnection processes. In other words, this paper shows that the 2D fast reconnection process is basically unstable for a 3D perturbation. As a result, the destabilized 2D fast magnetic reconnection can be three-dimensionally localized even in a 1D current sheet. At the time, some 3D magnetic loops are repeatedly ejected from the reconnection region. These features of 3D fast reconnection seem to be consistent with the observation data of intermittent plasma downflows observed in solar flares.

2. Simulation Setup

In the spontaneous fast magnetic reconnection model, the reconnection process is initiated by a small resistive disturbance in the current sheet (Ugai and Shimizu, 1996; Ugai, 1999). After the initial disturbance is removed, fast reconnection spontaneously develops by a current-driven anomalous resistivity enhanced by the nonlinear tearing instability. Hence, no external driven mechanism is required to keep the reconnection process going.

The MHD simulation procedures are basically the same as in Ugai (1987), except for the initial resistive disturbance shown later, in this article i.e., Eq. (1). The 3D compressible MHD equations are used. The computational region is restricted to the first quadrant and set to be a rectangular box, ($0 \leq x \leq L_x$, $0 \leq y \leq L_y$, $0 \leq z \leq L_z$), because of the conventional symmetry boundary conditions with respect to the xz -plane at $y = 0$, yz -plane at $x = 0$, and xy -planes at $z = 0$ and L_z . On the other boundaries, free boundary conditions are assumed, where all the quantities are determined by the state of the inner region, so that the first derivatives of the quantities in the direction normal to the boundaries vanish (the normal component of \mathbf{B} is determined by the solenoidal condition). Because of the symmetry boundary conditions for xy -planes at $z = 0$ and L_z , the simulation box is closed in the z -direction. In other words, the simulation box may be considered to be periodic in the z -direction, where $2L_z$ is the maximum wave length for all the z -directional MHD waves. The computational region $L_x = 30$, $L_y = 10$, and $L_z = 20$ are taken with the mesh points $N_x = 880$, $N_y = 1000$, and $N_z = 100$.

3. Simulation Results

3.1 The initial stage

The simulation starts with $\beta_0 = 0.15$ in the magnetic field region, which consists of $B_{x0} = 1.0$ and $P_0 = 0.075$. Initially, every magnetic field line is exactly set up in the x -direction. The current sheet is initially formed on the xz -plane and the current is flowing in the negative z -direction. In the initial current sheet, B_x monotonously varies from B_{x0} at $y = +1$ to zero at $y = 0$. Then, $B_x = B_{x0}$ is set for $y > +1$. There is no initial plasma flow. The Alfvén speed V_A is unity in the initial upstream magnetic field region based on $B_{x0} = 1.0$, and the Alfvén transit time to pass the distance of $L_x = 30$ is set as $T = 30$ in the time scale.

The initial resistive disturbance shown below initiates a tearing instability in the current sheet during $0 < T < 4$, which is strongly localized around the z -axis.

$$\eta_0 = 0.04 \exp(-\alpha(x^2 + y^2)) \{1 + 0.01 \cos(\pi z/L_z)\} \quad (1)$$

where $\alpha = 0.01$. In this initial resistive disturbance, the magnetic Reynolds number is estimated to be 25 at the origin. Note that this resistive disturbance fluctuates only by 1% in the z -direction, which is the sheet current direction. Accordingly, the resulting reconnection process is expected to be nearly 2D. In fact, the magnetic loop ejected firstly from the reconnection region is almost 2D, as shown later in Fig. 1.

After $T = 4$, η_0 is removed and, instead, the current-driven anomalous resistivity η_1 shown below is switched on, which starts to drive the fast magnetic reconnection after about $T = 20$.

$$\eta_1 \begin{cases} = 0.002(V_d - V_c) & \text{for } V_d \geq V_c \\ = 0 & \text{for } V_d < V_c \end{cases} \quad (2)$$

$$(3)$$

where $V_d = |J|/\rho$ is the ion-electron drift velocity and $V_c = 4.0$ is set. The current density J is obtained from

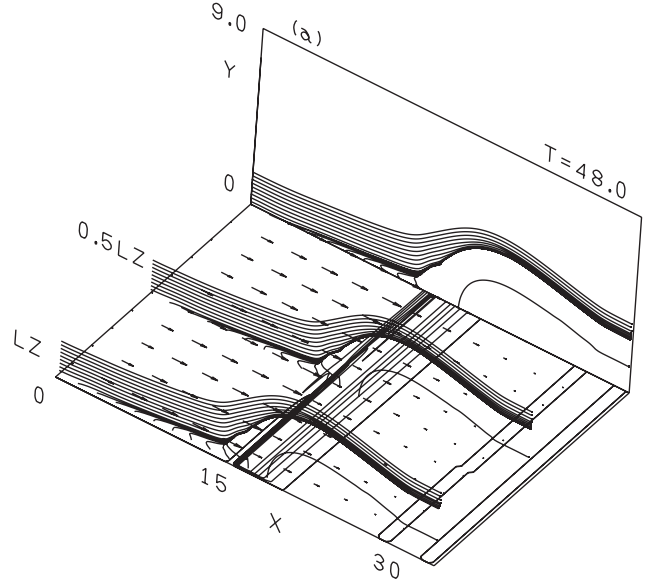


Fig. 1. Some of magnetic field lines, a contour map of B_y field intensity, and a pattern of flow velocity at $T = 48$.

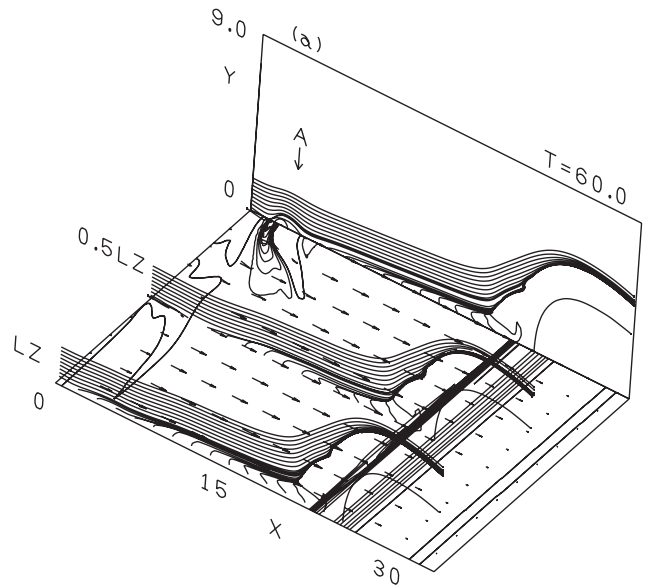
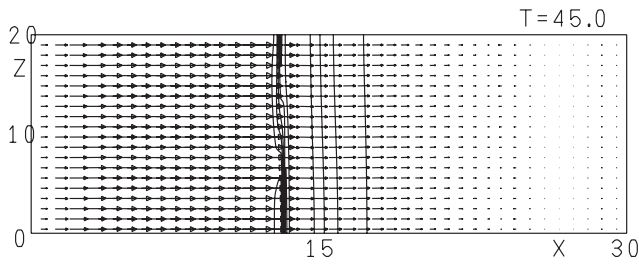
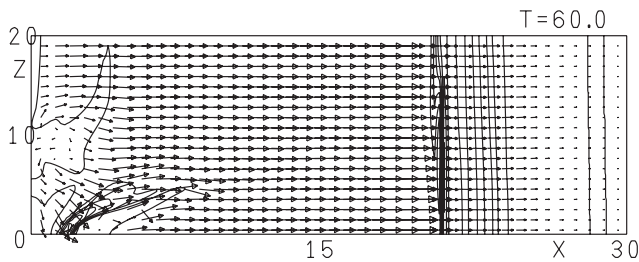
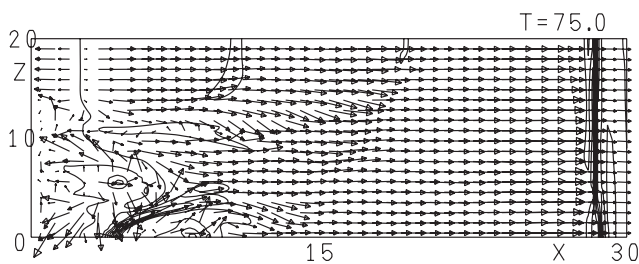
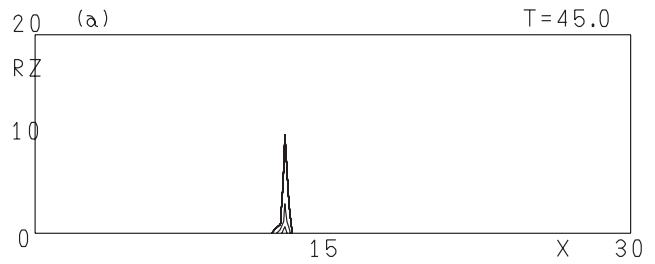
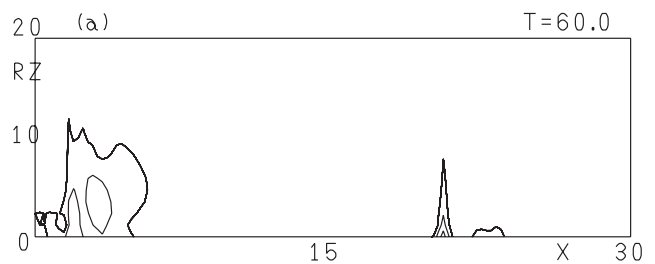
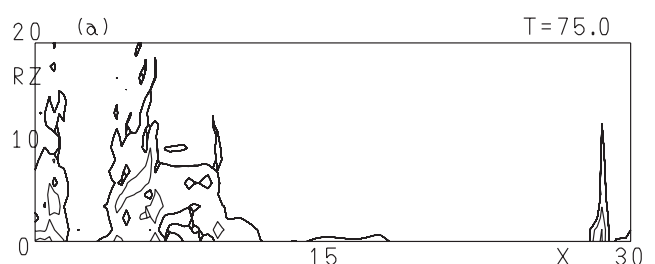


Fig. 2. The figure format is the same as Fig. 1 but at $T = 60$.

$\text{rot}\mathbf{B}$ and is unity at the center of the initial current sheet, i.e., $y = 0$. Also, the uniform plasma density ρ is initially set to be unity.

3.2 The first stage (2D fast reconnection)

Figure 1 shows magnetic field lines on three xy -planes for $z = 0$, $0.5L_z$, and L_z with a B_y contour map and plasma flow vectors on an xz -plane for $y = 0$ at $T = 48$. Along the z -axis, the magnetic neutral line for fast reconnection process is formed. The magnetic field lines in all three xy -planes are very similar. In addition, the B_y contour map and plasma flow vectors are almost uniform in the z -direction. Hence, at this time, the fast magnetic reconnection process is 2D, and a 2D large-scale magnetic loop is formed between $15 < x < 30$.

Fig. 3. B_y contour map on the xz -plane at $y = 0$ and $T = 45$.Fig. 4. B_y contour map at $T = 60$.Fig. 5. B_y contour map at $T = 75$.Fig. 6. Z -directional Fourier analysis of B_y contour map on xz -plane at $T = 45$.Fig. 7. Z -directional Fourier analysis at $T = 60$.Fig. 8. Z -directional Fourier analysis at $T = 75$.

3.3 The second stage (3D fast reconnection)

Figure 2 shows the numerical result similar to Fig. 1 but for $T = 60$. The 2D large-scale magnetic loop in $20 < x < 30$ corresponds to the one in $15 < x < 30$ of Fig. 1, so the loop is propagating with the reconnection jets. More exactly, the propagating speed is about $0.6V_A$ and is a little slower than the jet speed V_A . In addition, another small magnetic loop is observed in the vicinity of the origin, which is marked by “A” in Fig. 2. Since this magnetic loop is not observed in the magnetic field lines of $z = 0.5L_z$ and L_z , the loop structure is evidently 3D. This 3D magnetic loop is a result of the z -directional perturbation in the initial resistive disturbance Eq. (1). In Fig. 2, the B_y contour map on the xz -plane at $y = 0$ is also shown, which is the intensity of the reconnected magnetic field. Clearly, the 3D magnetic loop marked by “A” corresponds to a high-intensity island on the B_y contour map, which is a little extended in the z -direction and largely curved in the positive x -direction.

3.4 Time variation of B_y contour map

Figures 3, 4, and 5 show B_y contour maps on the xz -plane for $y = 0$ at $T = 45, 60$, and 75 . In Fig. 3, no 3D magnetic loop is observed and a 2D magnetic loop is only observed as vertical bands at $13 < x < 17$. This is consistent with Fig. 1. Figure 4 is exactly the same as the contour map in Fig. 2, where $L_z = 20$. In Fig. 4, a 3D magnetic

loop appears and then, in Fig. 5, slightly propagates in the positive x -direction. In addition, in Fig. 5, considering the symmetry boundary condition on the x -axis, i.e., $z = 0$, two 3D magnetic loops are also observed as small round-shape islands at $(x, z) = (5, 5)$ and $(7, 0)$.

3.5 z -directional Fourier analysis

Figures 6, 7, and 8 respectively show the z -directional Fourier analysis of Figs. 3, 4, and 5 as the contour map of the Fourier components. These figures show the time variation from $T = 45$ to 75 . The vertical axis R_z of these figures is scaled as the inverse of the z -directional wave length λ_z , where unity $R_z = (1/\lambda_z) = 1$ is equivalent to $1/(2L_z)$. Note that $2L_z$ corresponds to the wave length of the z -directional resistive perturbation in Eq. (1). In Fig. 6, the growth of the Fourier components $1 \leq R_z < 10$ related to the 2D magnetic loop is observed at $x = 13$. In Fig. 7, the Fourier components move to $x = 21$, and new Fourier components $1 \leq R_z < 10$ widely appear in the 3D magnetic loop region located in $2 < x < 5$. Next, in Fig. 8, the new Fourier components widely spread in the x -direction, because of the multiple formations of 3D magnetic loops in Fig. 5. Since the initial resistive disturbance Eq. (1) only has $R_z = 1$ component, the higher-order components $R_z \geq 2$ are generated by the non-linear instability of the fast magnetic reconnection. In Figs. 6 and 7, the 2D magnetic

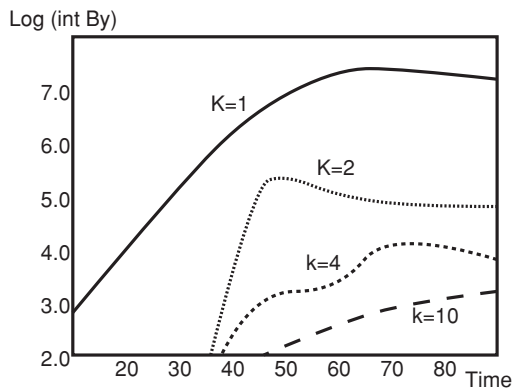


Fig. 9. Time variation of some z -directional Fourier components which are averaged over $0 < x < L_x$.

loop also generates the higher-order components $R_z \geq 2$. However, evidently, the higher-order Fourier components related to 3D magnetic loops are spread more widely than those of the 2D magnetic loop.

Figure 9 shows the time variation of four typical z -directional Fourier components for the B_y contour map, where $k = R_z$. On the 2D stage ($T < 50$), the $k = 1$ component that corresponds to the z -directional perturbation in Eq. (1) linearly grows up and, on the 3D stage ($50 < T$), almost saturates. As mentioned in Figs. 7 and 8, since Eq. (1) has no $R_z = k \geq 2$ components, such higher-order components should be created from the $k = 1$ component, due to the non-linear instability in the 3D fast magnetic reconnection. In fact, the higher-order components rapidly grow up after the linear growth of $k = 1$.

4. Summary

In this paper, we have shown that 2D fast magnetic reconnection caused by a current-driven anomalous resistivity is unstable to a 3D resistive perturbation. In fact, in this MHD model, the initial current sheet has exactly a 1D structure, and every setup is exactly prepared for 2D fast magnetic reconnection, except for the initial 3D resistive perturbation η_0 . At this point, note that the 3D fast reconnection process reported by Ugai (Ugai *et al.*, 2004, 2005) is largely different because the initial resistive disturbance employed in his papers includes a largely non-uniform component along the neutral line and, hence, the resulting fast reconnection processes is fully 3D even on the first stage. In contrast, as shown in Fig. 1, the fast reconnection studied in this paper is still 2D on the first stage. The 3D fast reconnection is spontaneously caused after the 2D fast reconnection has been established. In addition, as shown in the time variation of Fig. 9, the z -directional higher-order Fourier components generated by the 3D instability rapidly grows after the 2D stage. This means that the 3D instability shown here is fully non-linear.

As shown in Fig. 5, the appearance of the multiple 3D magnetic loops means that 3D fast reconnection process is pulsating. This may support the intermittent downflow reported by Asai *et al.* (2004), where 3D magnetic loops

may be repeatedly ejected even on the 1D current sheet, due to the fast magnetic reconnection.

In the next step of this study, the temporal dynamics of ejected magnetic loops must be studied. In the temporal dynamics, some of the ejected magnetic loops may merge into a magnetic loop in the downstream region. Finally, few large-scale magnetic loops can only survive. At this point, the 3D fast reconnection model shown in this paper may be closely related to the fractal and intermittent reconnection model that was proposed by Shibata and Tanuma (2001) to explain the solar flare observation data as a time-development from micro-reconnection processes to a macro-reconnection process. Since their basic concept is a 2D model, the 3D fast reconnection shown here should give a new view point to their model.

Acknowledgments. This work was supported by grant-in-aids of the Japanese education ministry; Ehime Univ. T. Shimizu, “Study of Multi-scale Plasma Simulation of Magnetic Reconnection” (15540475) and Kyoto Univ. K. Shibata, Creative Scientific Research, “The Basic Study of Space Weather Prediction” (17GS0208). In addition, this work is supported by Research Institute for Sustainable Humanosphere (RISH) of Kyoto University and Solar-Terrestrial Environment Laboratory (STEL) of Nagoya University. The numerical calculations were performed on the KDK computer system at RISH and FUJITSU HP2500 parallel computer system at Nagoya and Kyoto University Data Processing Centers.

References

- Asai, A., T. Yokoyama, M. Shimojo, and K. Shibata, Downflow motions associated with Impulsive nonthermal emissions observed in the 2002 July 23 Solar Flare, *Astrophys. J.*, **605**, L77, 2004.
- Linton, M. and D. Longcope, A Model for Patchy Reconnection in Three Dimensions, *Astrophys. J.*, **642**, 1177–1192, 2006.
- Masuda, S., T. Kosugi, H. Hara, S. Tsuneta, and Y. Ogawara, Loop-top impulsive hard X-ray source of a solar flare as evidence for magnetic reconnection, *Nature*, **371**, 495–497, 1994.
- Shibata, K., New Observational Facts about Solar Flares from Yohkoh Studies—Evidence of Magnetic Reconnection and a Unified Model of Flares, *Adv. Space Res.*, **17**, 9–18, 1996.
- Shibata, K. and S. Tanuma, Plasmoid-induced-reconnection and fractal reconnection, *Earth Planets Space*, **53**, 473–482, 2001.
- Shibata, K., S. Masuda, M. Shimojo, H. Hara, T. Yokoyama, S. Tsuneta, T. Kosugi, and Y. Ogawara, Hot plasma ejections associated with Compact-Loop solar flares, *Astrophys. J.*, **451**, L83, 1995.
- Ugai, M., Strong loop heating by the fast reconnection in a closed system, *Geophys. Res. Lett.*, **14**, 103–106, 1987.
- Ugai, M., Basic physical mechanism of reconnection development and magnetic loop dynamics, *J. Geophys. Res.*, **104**(A4), 6929–6939, 1999.
- Ugai, M. and T. Tsuda, Magnetic field-line reconnection by localized enhancement of resistivity, 1. Evolution in a compressible MHD fluid, *J. Plasma Phys.*, **17**, 337–351, 1977.
- Ugai, M. and T. Shimizu, Computer studies on the spontaneous fast reconnection mechanism in three dimensions, *Phys. Plasmas*, **3**, 853–862, 1996.
- Ugai, M., K. Kondoh, and T. Shimizu, Computer studies on the three-dimensional spontaneous fast reconnection model as a nonlinear instability, *Phys. Plasmas*, **11**, 1416–1423, 2004.
- Ugai, M., K. Kondoh, and T. Shimizu, Spontaneous fast reconnection in three dimensions, *Phys. Plasmas*, **12**, 042903, 2005.
- Yokoyama, Y., K. Akita, T. Morimoto, K. Inoue, and J. Newmark, Clear evidence of reconnection inflow of a solar flare, *Astrophys. J.*, **546**, L69, 2001.

Patchy reconnection in a Y-type current sheet

M. G. Linton¹, C. R. DeVore¹, and D. W. Longcope²

¹Naval Research Laboratory, Washington, DC, U.S.A.

²Montana State University, Bozeman, MT, U.S.A.

(Received November 21, 2007; Revised March 24, 2008; Accepted June 20, 2008; Online published May 29, 2009)

We study the evolution of the magnetic field in a Y-type current sheet subject to a brief, localized magnetic reconnection event. The reconnection produces up- and down-flowing reconnected flux tubes which rapidly decelerate when they hit the Y-lines and underlying magnetic arcade loops at the ends of the current sheet. This localized reconnection outflow followed by a rapid deceleration reproduces the observed behavior of post-CME downflowing coronal voids. These simulations support the hypothesis that these observed coronal downflows are the retraction of magnetic fields reconnected in localized patches in the high corona.

Key words: Solar, corona, flare, reconnection.

1. Introduction

Reconnection is believed to be a key process allowing the excitation of solar flares and coronal mass ejections (CMEs). The reconnection releases significant magnetic energy, leading to solar flare heating, and changes magnetic topologies, allowing CME magnetic fields to erupt and escape the solar corona into interplanetary space. Observations of the flaring which occurs behind recently erupted CMEs show downflowing voids (see, e.g., McKenzie and Hudson, 1999; Gallagher *et al.*, 2002; Innes *et al.*, 2003; Asai *et al.*, 2004; Sheeley *et al.*, 2004) which push their way through the heated flare plasma in the high corona. These downflowing voids, observed by TRACE, Yohkoh SXT, and Hinode XRT, have been shown to be evacuated structures. They are therefore not cool, dense plasma blobs being pulled down by gravity, but rather appear to be evacuated loops of magnetic field being pulled down by the magnetic tension force (McKenzie and Hudson, 1999). The three dimensional (3D) structure of these voids breaks up the two dimensional (2D) symmetry of the flare current sheet and arcade, implying that the reconnection which creates these voids occurs in localized 3D patches rather than uniformly along the current sheet. The reconnected field from this patchy reconnection takes the shape of individual 3D flux tubes rather than extended 2D sheets of field. In this letter, we study whether the formation of magnetic loops high in the corona via a 3D patch of reconnection creates structures consistent with the morphology and dynamics of these coronal voids.

In Linton and Longcope (2006), we showed that the shapes and evolutions of such magnetic loops in a one dimensional (1D) Harris type current sheet are consistent with observations of these downflowing loops. The cross sections of the simulated magnetic loops form teardrop shapes,

similar to that of the voids, while the 3D structure of the loops is similar to the structure of the coronal loops which appear below these voids, e.g., as seen by Sheeley *et al.* (2004).

However, there is a key aspect of the void dynamics which the initial 1D nature of the Harris current sheet cannot reproduce. This is the rapid deceleration of the voids once they reach the post-flare arcade loops in the low corona. Sheeley *et al.* (2004) have shown that the speeds of these voids through the high corona are relatively constant until they hit the coronal arcade, when they rapidly decelerate. As the Harris current sheet continues unchanged to the edge of the simulation, there is no arcade of loops at the base of such a current sheet with which the voids collide. To study this deceleration, we therefore now simulate this patchy reconnection in a Y-type current sheet (Green, 1965). The Y-type current sheet terminates at a set of magnetic arcade loops, as shown in Figs. 1(a) and 2(a). The intersections of the current sheet and the outermost of these arcade loops forms the two Y-lines, at $z = \pm L$ in Fig. 1(a). These arcades make the current sheet more representative of a post-CME coronal current sheet with underlying arcade fields. Note that these Y-lines are not Y-type nulls, as there is a uniform guide field in both the current sheet and the arcade, so the field strength does not go to zero at the Y-lines, even though the reconnection component of the field does go to zero here.

We study the effect of a localized reconnection event in this current sheet, focusing on the form of the reconnected field, and on whether it decelerates once it hits the Y-line and the coronal arcade below it. The current sheet configuration and the simulation setup are discussed in Section 2, the results are described in Section 3, and our conclusions are summarized in Section 4.

2. Simulations

The simulations were performed using the magneto-hydrodynamic (MHD) code ARMS (Adaptively Refined

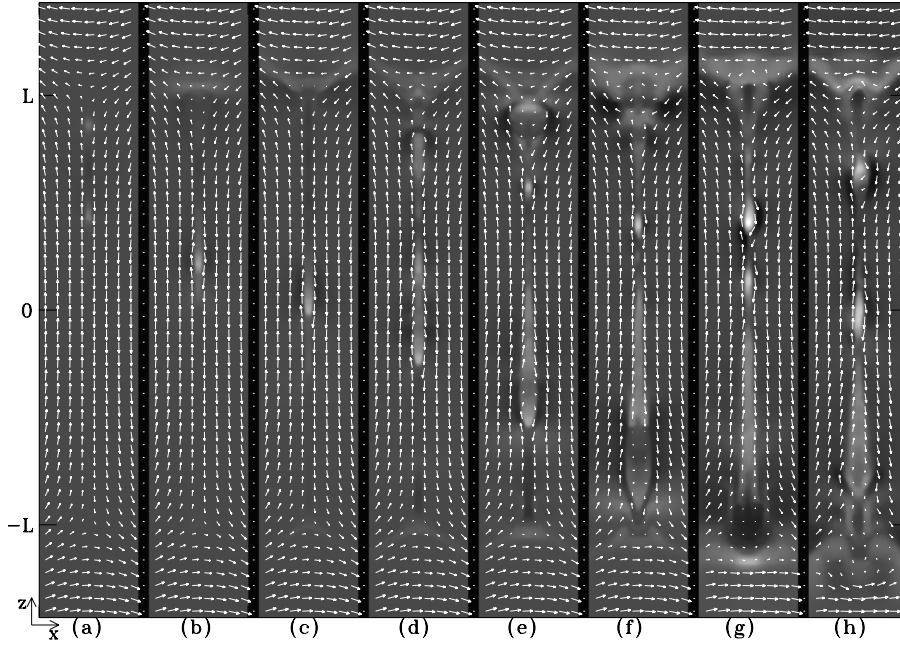


Fig. 1. Magnetic field of the Y-type current sheet in the $y = 0$ plane, with a magnetic reconnection patch imposed at $z = 2L/3$ for a time $tv_{A0}/L = 0.6$. The vectors show the magnetic field in the plane, while the greyscale shows the guide field component, with white representing maximum positive field. The panels show the simulation at times $tv_{A0}/L = [0.2, 0.7, 1.1, 1.6, 2.1, 2.6, 3.1, 3.5]$. The x boundaries of each panel shown are at $x = \pm 3L/4\pi$.

MHD Solver) on the Cray XD1 supercomputer at the Naval Research Laboratory. The code was used to solve the resistive MHD equations. See Welsch *et al.* (2005) for a discussion of the code, and a presentation of the equivalent ideal MHD equations. We include an explicit resistivity η in the induction equation, $\partial \mathbf{B}/\partial t = \nabla \times (\mathbf{v} \times \mathbf{B} - \eta \nabla \times \mathbf{B})$, and an ohmic heating term in the energy equation.

The Y-type magnetic field (e.g., Priest and Forbes, 2000) is

$$B_x + iB_z = -B_0 \sqrt{\omega^2/L^2 - 1}, \quad (1)$$

where i is the positive value of $\sqrt{-1}$, $\omega \equiv z + ix$, and L is the current sheet half-length. The guide field is uniform at $B_y = B_0/\pi$. Here $B_z(z = 0, x \sim 0) = B_0 = 44$ in units where the pressure is $p_0 = 20/3$. Due to the guide field, the magnetic fieldlines on either side of the current sheet form a half angle $\zeta = \arctan(B_z/B_y) \sim 2\pi/5$. The reconnection field strength $|B_z|$ decreases as $\sqrt{1 - z^2/L^2}$ along the current sheet, going to zero at the Y-lines at $z = \pm L, x = 0$. This magnetic configuration is force-free, so the density and gas pressure are initially set to be uniform at $\rho = \rho_0 = 1/2$ and $p = p_0$, which sets the ratio of plasma to magnetic pressure near the center of the current sheet at $\beta \equiv 8\pi p/|\mathbf{B}|^2 \sim 0.08$. The Alfvén speed used for normalization, $v_{A0} = |\mathbf{B}|/\sqrt{4\pi\rho}$, is measured near the center of the current sheet at $z = 0, x \sim 0$.

Extrapolative, zero gradient, open boundary conditions are imposed in the \hat{z} and \hat{x} directions, while periodic boundary conditions are imposed in the \hat{y} direction. The computational mesh is adaptively refined in areas of high current magnitude. This gives a resolution ranging from 64 to 512 cells in the \hat{y} , and \hat{z} directions $[-1.9L, 1.9L]$, and a resolution ranging from 32 to 256 cells in the \hat{x} direction $[-.95L, .95L]$. The current sheet is at the highest resolu-

tion, and it is effectively one cell wide, so its thickness is $l = 0.007L$.

The simulation is run with a uniform background resistivity η_0 . To initiate the reconnection, we impose a sphere of enhanced resistivity on the current sheet for the first $tv_{A0}/L = 0.6$ of the simulation. This resistive enhancement has the form $\eta = \eta_0 (1 + 99e^{-r^2/\delta^2})$, for $r = \sqrt{x^2 + y^2 + (z - 2L/3)^2} < 2\delta$, with $\delta/L = 0.087$. The Lundquist number of the background resistivity is $S_\eta \equiv \delta v_{A0}/\eta_0 = 5000$, while for the peak resistivity at the center of the reconnection region $S_\eta = 50$. Note that Ugai (2007) have found that reconnection induced by locally enhanced resistivity is inhibited if $\delta < 4l$. As $\delta \sim 10l$ here, the reconnection should not be inhibited by this mechanism.

3. Results

The effects of the magnetic reconnection event on the Y-type current sheet are shown in Figs. 1 and 2. Figure 1 shows a vector magnetogram view of the field in a plane perpendicular to the current sheet at $y = 0$. Figure 1(a) is taken soon after the reconnection event is turned on. The guide field, shown by the greyscale, is enhanced in two small spots on either side of the reconnection event at $z = 2L/3$. These spots are the cross sections of the two recently reconnected flux tubes flowing away from the reconnection site. The guide field is enhanced in these reconnected flux tubes because the reconnection component of the magnetic field has been annihilated, and the guide field must increase to make up for the lost magnetic pressure (see Hesse *et al.*, 1996).

Figure 2(a) shows the fieldlines on either side of this current sheet just before the reconnection starts. Three topologically distinct sets of fieldlines are shown. One set

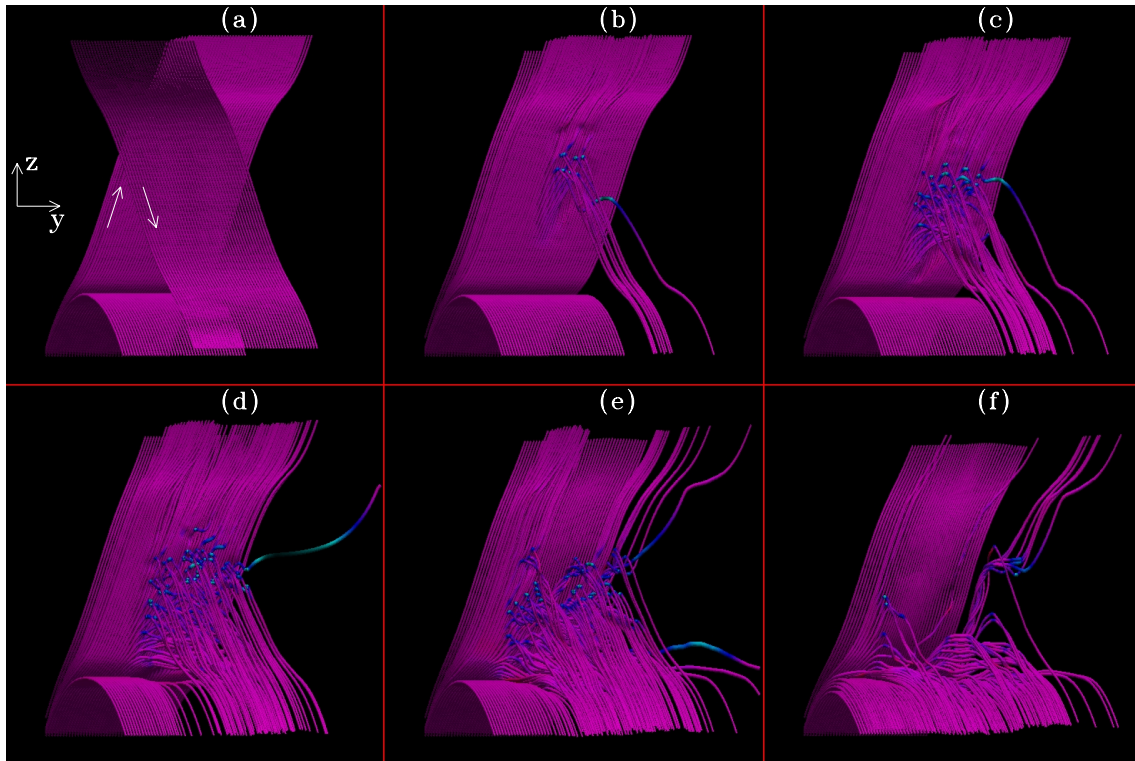


Fig. 2. Fieldlines of the reconnecting Y-type current sheet. The blue color shows where the electric current parallel to the magnetic field is strong. The panels show the simulation at times $t v_{A0}/L = [0.0, 1.3, 2.1, 2.8, 3.4, 3.9]$. Panel (a) shows fieldlines traced from both the front and back side of the current sheet, at the bottom boundary. The rest of the panels show only fieldlines traced from the back side of the current sheet, at the bottom boundary.

runs just behind the current sheet from the bottom to the top of the panel, while a second set runs in front of the current sheet from the top to the bottom of the panel, as marked by the arrows. The third set arches below the current sheet, running from the back of the simulation to the front, and coming close to the Y-line and the base of the current sheet at its apex. All three sets of fieldlines are canted gradually from left to right: this is the effect of the uniform guide field in the \hat{y} direction. The arched set of fieldlines represents the post-CME arcade loops while the two other sets of fieldlines represent the coronal current sheet fieldlines, which may still be connected to the CME above the second Y-line at the top of the simulation. For the remaining panels of Fig. 2, only the first and third sets of these fieldlines are traced, so that the second set, which lies in front of the current sheet, does not obscure the dynamics. Both of these sets of fieldlines are traced from the bottom boundary, behind the current sheet and arcade. Therefore, any section of a fieldline which appears in front of the current sheet above the arcade fieldlines is purely due to reconnection of front-side fieldlines with the back-side fieldlines.

The reconnection event was initiated very close to the upper Y-line, so the upflowing reconnected field quickly hits the Y-line, in Fig. 1(b). The corresponding upward retracting fieldlines are not shown in Fig. 2, since they are not connected to the lower boundary from which the fieldlines are traced. The upflow halts when it hits the upper Y-line and the arcade fieldlines lying above it. This is the equivalent of the upgoing fieldlines hitting and merging into the recently erupted CME, though this would only happen

if the CME were erupting at a slower rate than the fieldlines retract.

The downflowing part of the reconnected flux is displayed in Fig. 2(b) as the fieldlines which trace upwards with all the field on the back side of the current sheet, but then suddenly take a hairpin turn and trace back down to the bottom boundary on the front side of the current sheet. The blue color of the fieldlines at these hairpin turns shows that the parallel electric current is enhanced and therefore reconnection is strong there (see, e.g., Schindler *et al.*, 1988). The high placement of the initial reconnection region allows the cross section of the flux tube carrying this downflowing reconnected flux to fully take shape. Figures 1(b)–1(f) show how the cross section of the tube forms into an oblong shape, reminiscent of the coronal void observations, just as it did in the Harris sheet experiments of Linton and Longcope (2006). Note that the area of the downflowing flux tube cross section continues to grow as it absorbs more reconnected flux, even though the enhanced reconnection spot was turned off at $t v_{A0}/L = 0.6$, just before Fig. 1(b). Apparently the disturbance caused by the initial reconnection event spontaneously excites subsequent patchy reconnection events.

When this downflowing flux tube hits the Y-line and the arcade field below it, in Fig. 1(f), it decelerates and compresses the arcade field, in Fig. 1(g), and eventually joins the arcade, in Fig. 1(h). The reconnected flux which hits and joins the lower arcade is shown in Figs. 2(d)–2(f) as the fieldlines which now lie on top of the original arcade.

To illustrate the downflow and deceleration of the recon-

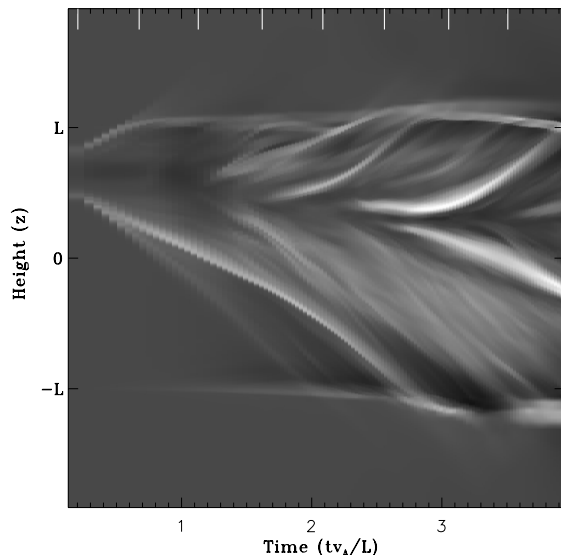


Fig. 3. Height-time plot of the guide field at $x = y = 0$. The white tickmarks at the top mark the times of the vector plots of Fig. 1.

nected flux tubes, we show a height-time plot of the guide field along the $x = y = 0$ line in Fig. 3. Here, the upward or downward propagating voids are displayed as diagonal white streaks of concentrated guide field. The first pair of up- and down-flowing streaks, starting at $tv_{A0}/R = 0$, are the tracks of the two initial reconnection voids. The up-flowing track rapidly hits the upper Y-line and decelerates, while the downflowing track starts off at about $v_{A0}/2$, accelerates as it passes the current sheet midpoint, and then also rapidly decelerates as it hits the lower Y-line. Guidoni and Longcope (2007) suggest that a reconnected flux should accelerate near $z = 0$ as seen here because the magnetic field strength, and thus the accelerating Lorentz force, peaks there.

After the reconnection is turned off at $tv_{A0}/L = 0.6$, no new tracks appear at the height of the initial reconnection site until about $tv_{A0}/L = 1.3$. Then patchy reconnection spontaneously sets in, as several reconnection outflow pairs appear in rapid sequence. This is supported by the more detailed views of Figs. 1 and 2. Figures 1(f)–1(h) show the corresponding newly reconnected flux tube cross sections flowing up and down at these times. Meanwhile, Figs. 2(c)–2(e) show the continual generation of newly reconnected fieldlines high up in the current sheet, well after the initial reconnection has been turned off and those reconnected fields have retracted. The source of this secondary patchy reconnection may be numerical resistivity due to the finite grid-scale of the simulation, in tandem with perturbations excited by the initial reconnection event, and will be explored in a future paper. Isobe *et al.* (2005) found a similar spontaneous patchy reconnection, but in their case it was due to an interchange instability, which cannot occur here. Interestingly, Fig. 1 also shows the reconnected fieldlines spreading in the \hat{y} direction along the current sheet, also in a patchy fashion, instead of remaining near the initial reconnection site. This is in contrast with the findings of Ugai *et al.* (2005) for a Harris current sheet without guide field. Their results show that initially localized reconnection does

not expand significantly in this direction. From these preliminary results, it appears that the guide field can play an important role in expanding the reconnection region along the current sheet.

4. Conclusions

We have studied the effect of a brief, localized burst of reconnection in a Y-type current sheet with guide field. The up- and down-flowing flux this creates decelerates rapidly when it hits the Y-lines and the arcade fields beyond them. This gives strong support to the theory that the downflowing post-CME voids observed by TRACE, Yohkoh, and Hinode are in fact downflowing reconnected magnetic flux loops. This model gives a clear mechanism to explain why downflowing post-CME voids decelerate rapidly when they reach the post-flare arcades, as observed by Sheeley *et al.* (2004). We also find that the velocities of the voids change as they propagate through regions of different magnetic field strength in the current sheet. Finally, we find that the perturbation created by the initial burst of reconnection is sufficient to excite spontaneous patchy reconnection events in the current sheet.

Acknowledgments. This work was funded by NASA and ONR, with a grant of computer time from the DoD High Performance Computing program.

References

- Asai, A., T. Yokoyama, M. Shimojo, and K. Shibata, Downflow motions associated with impulsive nonthermal emissions observed in the 2002 July 23 solar flare, *ApJL*, **605**, 77–80, 2004.
- Gallagher, P. T., B. R. Dennis, S. Krucker, R. A. Schwartz, and A. K. Tolbert, Rhesi and trace observations of the 21 April 2002 x1.5 flare, *Sol. Phys.*, **210**, 341–356, 2002.
- Green, J. M., Geometrical properties of three-dimensional reconnecting magnetic fields with nulls, in *Solar and Stellar Magnetic Fields*, edited by R. Lüst, 7 pp., North-Holland Publishing Co., Amsterdam, 1965.
- Guidoni, S. and D. Longcope, Dynamics of post-reconnected thin flux tubes, *Am. Astron. Soc. Meeting Abstracts*, **210**, #93.27, 2007.
- Hesse, M., J. Birn, M. M. Kuznetsova, and J. Dreher, A simple model of core field generation during plasmoid evolution, *J. Geophys. Res.*, **101**, 10797–10804, 1996.
- Innes, D. E., D. E. McKenzie, and T. Wang, SUMER spectral observations of post-flare supra-arcade inflows, *Sol. Phys.*, **217**, 247–265, 2003.
- Isobe, H., M. Takehiro, K. Shibata, and T. Yokoyama, Filamentary structure on the Sun from the magnetic Rayleigh-Taylor instability, *Nature*, **434**, 478–481, 2005.
- Linton, M. G. and D. W. Longcope, A model for patchy reconnection in three dimensions, *ApJ*, **642**, 1177–1192, 2006.
- McKenzie, D. E. and H. S. Hudson, X-ray observations of motions and structure above a solar flare arcade, *ApJL*, **519**, 93–96, 1999.
- Schindler, K., M. Hesse, and J. Birn, General magnetic reconnection, parallel electric fields, and helicity, *J. Geophys. Res.*, **93**, 5547–5557, 1988.
- Sheeley, N. R., H. P. Warren, and Y.-M. Wang, The origin of postflare loops, *ApJ*, **616**, 1224–1231, 2004.
- Priest, E. and T. Forbes, *Magnetic Reconnection, MHD Theory and Applications*, Cambridge University Press, Cambridge, UK, 2000.
- Ugai, M., Conditions for drastic evolution of magnetospheric current wedge, *Phys. Plasmas*, **14**, 062902.1–062902.8, 2007.
- Ugai, M., K. Kondoh, and T. Shimizu, Spontaneous fast reconnection model in three dimensions, *Phys. Plasmas*, **12**, 042903.1–042903.7, 2005.
- Welsch, B. T., C. R. DeVore, and S. K. Antiochos, Magnetic reconnection models of prominence formation, *ApJ*, **634**, 1395–1404, 2005.

Flares and the chromosphere

Hugh S. Hudson^{1,2} and Lyndsay Fletcher^{2,1}

¹SSL, UC Berkeley, CA 94720-7450, USA

²University of Glasgow, UK

(Received December 2, 2007; Revised August 24, 2008; Accepted August 31, 2008; Online published May 29, 2009)

The chromosphere (the link between the photosphere and the corona) plays a crucial role in flare and CME development. In analogies between flares and magnetic substorms, it is normally identified with the ionosphere, but we argue that the correspondence is not exact. Much of the important physics of this interesting region remains to be explored. We discuss chromospheric flares in the context of recent observations of white-light flares and hard X-rays as observed by TRACE and RHESSI, respectively. We interpret key features of these observations as results of the stepwise changes a flare produces in the photospheric magnetic field.

Key words: Solar flares, solar chromosphere, solar corona, Alfvén waves.

1. Introduction

The chromosphere historically has been the origin of much of what we understand about solar flares. The reason for this was the recognition, in the 19th and early 20th centuries, of the extreme sensitivity of $H\alpha$, a strong Fraunhofer absorption line formed in the chromosphere, to solar magnetic activity. Spectroscopic observations of this line and its imaging led to exciting discoveries regarding active prominences, ejecta, flare brightenings etc. (Hale, 1930). Eventually it was realized that the original flare observation of 1859 (Carrington, 1859) was simply the tip of the iceberg, and that the entire solar atmosphere was participating in events that have now come to be defined more by their coronal X-ray emission (the GOES classification) rather than their $H\alpha$ importance levels (Thomas and Teske, 1971). Research attention, indeed, has largely left the chromosphere layers in favor of coronal and even interplanetary effects (CMEs and ICMEs; see Schwenn, 2007, for a recent review).

Our understanding of the chromosphere, until recently, has been limited to the “semi-empirical” models, based on 1D radiative-transfer physics. Such an approach omits dynamics except for the “microturbulence” factor and much of the interesting plasma physics; for example these models assume $T_e = T_i$ everywhere. See Berlicki (2007) and Hudson (2007) for recent reviews about the flaring chromosphere, and for references to the abundant literature on this subject.

In the often-discussed but imperfect analogy between solar flares and auroral substorms, the chromosphere plays the role of the ionosphere, but these regions have substantially different properties and the detailed physics may not produce analogous effects (e.g., Haerendel, 2007). On the larger scale there is also no analog of the solar wind flow-

ing around an active-region field concentration in the solar corona, so that the convective ($\mathbf{v} \times \mathbf{B}$) electric field across the geotail does not have an appropriate analog. The presence of a highly conductive solar atmosphere *below* the chromosphere also distinguishes it from the ionosphere. Thus, although striking observational parallels between flares and aurorae have been noted by many authors (e.g., Obayashi, 1975), the basic physics may be quite different in regard to causation or the dynamical development of the phenomena. In this paper we touch on flare energetics (Section 2), energy build-up (Section 3), and energy release (Section 4), attempting to use magnetospheric concepts as a guide to understanding.

2. Chromospheric Flare Energetics

The radiative energy of a solar flare appears mainly in the optical and UV continuum, which form in the lower solar atmosphere, most probably the chromosphere (e.g. Allred *et al.*, 2005; Fletcher *et al.*, 2007). This is in spite of the fact that the chromosphere itself (for this purpose, all regions of the solar atmosphere between photospheric and coronal temperatures) cannot contain sufficient energy to power a flare (see Hudson, 2007, for discussion). For example, the gravitational energy contained in coronal filaments does not play a strong role in flare energization. The radiated flare energy appears in compact emission patches that our current observations do not resolve either in space or in time (Hudson *et al.*, 2006), and Fletcher *et al.* (2007) have confirmed that the immediate source of the radiated energy lies in the electrons accelerated in the impulsive phase of the flare. Of this energy the chromospheric $H\alpha$ component and the coronal soft X-ray component each comprise less than about 10% of the total (Thomas and Teske, 1971).

Zeeman-splitting observations (Wang, 1993; Sudol and Harvey, 2005) have shown convincingly that flares result in large-scale perturbations of the photospheric magnetic field (see Fig. 1). This would generally be expected from any model of energy release from the coronal magnetic field,

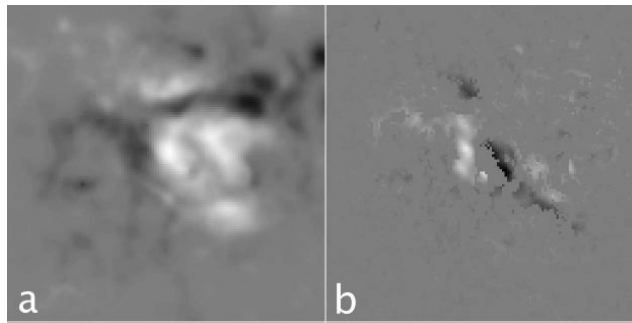


Fig. 1. GONG observations of the line-of-sight solar magnetic field prior to the X-class flare of 2003 October 29 (panel a); a difference map showing flare-related changes in the field (panel b); after Sudol and Harvey (2005). The field changes are of order 10% of the line-of-sight field and can be detected in essentially all X-class flares, according to Sudol and Harvey.

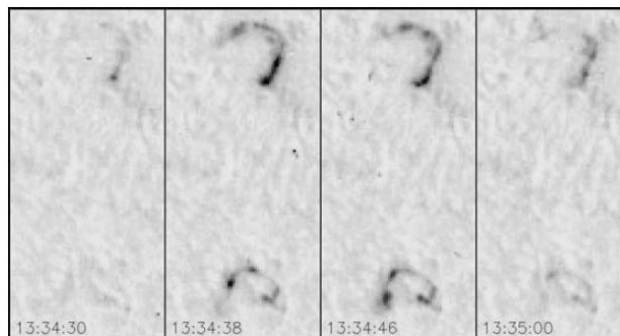


Fig. 2. Snapshots of TRACE observations (white light filter) of the C4.8 flare of 24 July 2004, showing the intermittency of the continuum emissions in both space and time. Spatial scale for each frame is $32'' \times 68''$; the times shown on the figure span 30 s (from Hudson *et al.*, 2006).

which will require restructuring in order to reduce the stored magnetic energy $\int (B^2/8\pi)dV$ (e.g., Hudson, 2000), as for example with large-scale magnetic reconnection. The main contribution to the coronal magnetic energy and its stress are concentrated strongly in the lower solar atmosphere (e.g., Régnier and Priest, 2007). Thus we need a theoretical understanding of how the coronal stored energy can flow to and focus itself into the chromospheric emission regions (see Fig. 2). Heretofore this coupling has been understood as the result of beams of electrons coming from an unknown coronal acceleration site, for which there are several possibilities (e.g., Miller *et al.*, 1997). These ideas underlie the “thick target” model for the impulsive phase of a flare, which envisions electron beams capable of transporting energy from the coronal storage site into the dissipation regions (Brown, 1971; Hudson, 1972). We do not know yet how the particle acceleration relates to the magnetic restructuring needed to release coronal energy.

3. Cross-field Currents

Another aspect of flare energetics and the chromosphere is the mapping of subphotospheric magnetic twist into coronal currents (Longcope and Welsch, 2000). This in principle involves the use of the full conductivity tensor, though there is little discussion of this yet in the solar literature (e.g., Kazeminezhad and Goodman, 2006; Arber *et al.*, 2007) at least as regards flares. Haerendel (2007) points out that the large ion-neutral coupling in the chromosphere makes the perpendicular conductivity is smaller than the parallel conductivity, at least for slowly-varying currents,

and yet cross-field current systems must develop slowly in such a way as to match the conflicting boundary conditions at the two independent footpoints of a coronal flux tube. Auroral models make use of ionospheric currents to close coronal current systems, but in the case of the Sun we believe that the significant currents are injected *through* the photosphere in a slowly-evolving manner, and that these currents serve to energize the non-potential fields in the corona. In this sense the chromosphere must play the roles of both the ionosphere and the magnetopause.

We can write the perpendicular conductivity as

$$\sigma_{\perp,x} = \frac{Ne^2}{m_e} \frac{\nu_{xn}}{\nu_{xn}^2 + \omega_{cx}^2} \quad (1)$$

with x representing either ions or electrons (Banks, 1966), where ω_{cx}^2 represents the Larmor frequency for particle species x and n denotes neutrals. The neutral collision frequencies ν_{xn} largely determine the perpendicular conductivity and it is not clear at present which particle species dominates the steady-state perpendicular current system. In any case for “normal” chromospheric and coronal conditions, as inferred from standard semi-empirical models, the Larmor frequencies greatly exceed the neutral collision frequencies so that the perpendicular conductivity is small relative to the parallel term. So far as we are aware, the questions posed by the requirement to establish slowly varying cross-field currents in the chromosphere have not been discussed in the literature, and we do not know the role that they play in energy storage or dissipation.

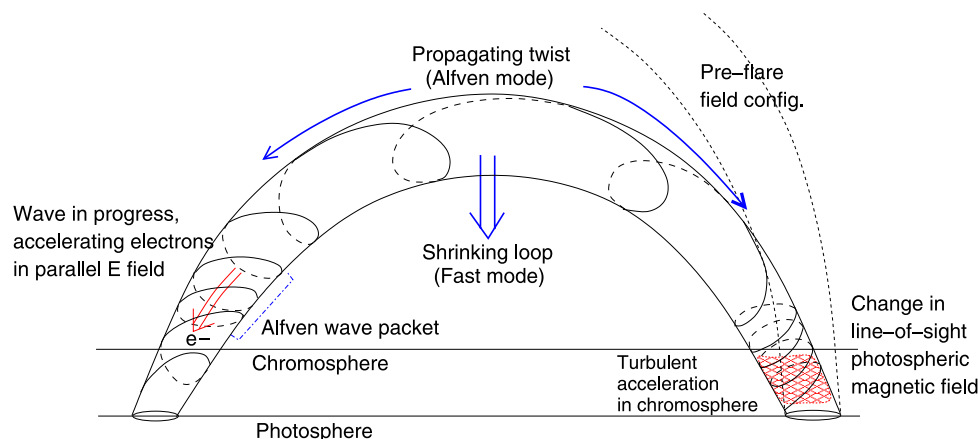


Fig. 3. Sketch of flare mechanisms as discussed in the text. Deformation of a flux tube results in Alfvén waves that transport energy into the footpoint regions via the Poynting flux. The wave deformation also perturbs the global structure to produce effects such as those seen in Fig. 1. Particle acceleration results either directly from parallel electric fields produced by the waves, or in turbulent cascades developing from their interactions.

4. Field Restructuring, Waves, and Energy Transport

Changes of the coronal magnetic structure imply the transport of energy via Poynting fluxes (Melrose, 1992). The observations indicate that coronal energy dissipates in the chromosphere, and the hard X-ray signature directly implicates weakly relativistic electrons. Thus the magnetic restructuring, and the energy transport it implies, must somehow result in the acceleration of electrons to non-thermal energies. We sketch how this may happen in Fig. 3 (Fletcher and Hudson, 2008). The sudden reconfiguration of the field, in the ideal MHD approximation, would launch Alfvén waves. Emslie and Sturrock (1982) argue that the suddenness of flare energy release requires that the Alfvén mode and the fast mode predominate in the partition of this energy. The Alfvén mode is particularly interesting in this context, because as a transverse wave its Poynting flux $\mathbf{E} \times \mathbf{B}$ must be strictly parallel to \mathbf{B} and thus be strongly ducted into the footpoint regions.

The mechanism for electron acceleration remains ill-understood. Because it is energetically so important (Kane and Donnelly, 1971; Lin and Hudson, 1971), its identification is fundamental to understanding the physics of solar flares. In the view of Fig. 3, the acceleration must happen as a result of the Alfvén-wave energy flux ducted along the arcade loops that result from the restructuring. This suggests several possible acceleration mechanisms, some of which have been recently reviewed by Miller *et al.* (1997).

Our scenario suggests additional acceleration mechanisms. Alfvén waves in the lower corona may propagate dispersively (e.g., Stasiewicz *et al.*, 2001), inducing parallel electric fields directly. If the plasma beta, $\beta = 2nkT/(B^2/8\pi)$, is smaller than m_e/m_i , where m_e/m_i is the electron/ion mass ratio, then the Alfvén mode can become dispersive in the form of a kinetic Alfvén wave and develop a parallel field directly. Fletcher and Hudson (2008) review how this happens. The waves may also cascade into forms of turbulence suitable for stochastic particle acceleration, and this cascade may develop promptly under some conditions. First-order Fermi acceleration and the betatron effect may also play roles in the “collapsing trap” (e.g., Veronig

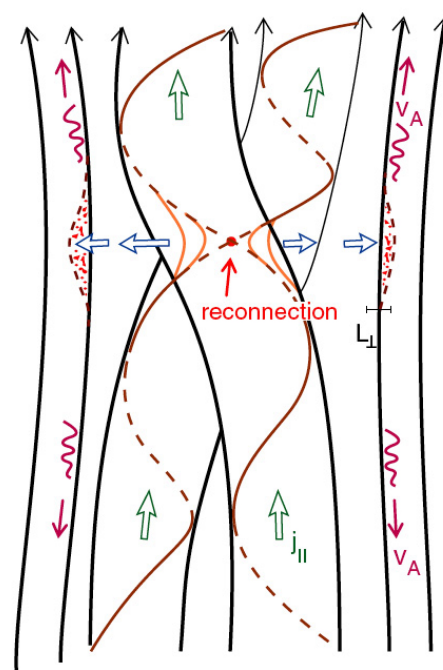


Fig. 4. Sketch showing how magnetic reconnection may excite Alfvén waves. From Haerendel (2007).

et al., 2006), and finally the disruption may create shock waves that may also accelerate particles.

Our preferred scenario (Fig. 3) has the virtue of linking the observed magnetic-field variations with the powerful energy release seen in the visible and UV continua. The sketch by Haerendel (2007), reproduced in Fig. 4, illustrates the generation of Alfvén waves from the reconnection process. Particle acceleration, in this picture, could readily occur in the lower solar atmosphere, where the ambient electrons are numerous enough to overcome the “number problem” and concerns about electron beam dynamics. One weakness may be the apparent time-of-flight signature noted by Aschwanden (2002), which—though somewhat ambiguous—provides the main observational evidence for the existence of the intense coronal electron beams the

thick-target model requires. Type III radio bursts also require beams, but of significantly lesser intensity.

5. Conclusions

Research in solar flares and terrestrial aurorae has long been stimulated by the observational analogies one can draw between the phenomena (e.g., Obayashi, 1975). The analogous elements include ribbon-like optical emissions, electron acceleration to keV energies, and similar magnetic geometries. There are observational differences though, and theoretically there also are good reasons not to have a strict analogy. Nevertheless we feel it important to discuss the physics of chromospheric flares, both in the energy build-up and release stages, in ways that exploit some of ideas auroral physics offers to the understanding of solar problems. We interpret the observed photospheric magnetic field changes as the result of large-scale Alfvén waves created during coronal magnetic restructuring (Fletcher and Hudson, 2008). Particle acceleration, a key observable in solar flares because of hard X-ray and γ -ray emission, then becomes secondary to the transport of energy via the Poynting fluxes of the waves. There are different ways in which the necessary particle acceleration may happen, most directly if the waves become dispersive in nature, but the identification of the acceleration mechanism remains an open problem.

Consideration of wave transport of energy in solar flares and CMEs seems like a logical and necessary development for the advancement of theoretical ideas. Some large-scale manifestations of waves are readily observable, originally as type II bursts and Moreton waves (e.g., Uchida *et al.*, 1973), but now also at higher resolution in the EUV as the EIT waves (Thompson *et al.*, 1999). The EIT waves introduce new kinds of behavior not seen before and it has become clear that not all of the motions can be identified with the Moreton-wave phenomenon (Biesecker *et al.*, 2002). Small-scale waves such as those that could be directly responsible for particle acceleration are difficult to observe remotely, but their presence may be just as fundamental to solar-flare physics as comparable structures are in auroral physics. We therefore urge theoretical work involving the ideas discussed here.

Acknowledgments. This work was carried out at the University of California, Berkeley, during a sabbatical leave of LF from the University of Glasgow, as well as at the University of Glasgow where HSH is grateful for hospitality. We are grateful to K. Shibata and the organizers of the workshop in Fairbanks, Alaska, where this paper was originally presented. LF gratefully acknowledges financial support by the European Commission through the SOLAIRE Network (MTRN-CT-2006-035484) NASA provided support under grant NAG-5-12878 and contract NAS5-38099.

References

- Allred, J. C., S. L. Hawley, W. P. Abbett, and M. Carlsson, Radiative hydrodynamic models of the optical and ultraviolet emission from solar flares, *ApJ*, **630**, 573–586, 2005.
- Arber, T. D., M. Haynes, and J. E. Leake, Emergence of a flux tube through a partially ionized solar atmosphere, *ApJ*, **666**, 541, 2007.
- Aschwanden, M. J., Particle acceleration and kinematics in solar flares, *Space Sci. Rev.*, **101**, 1–227, 2002.
- Banks, P., Collision frequencies and energy transfer. ions, *Planet. Space Sci.*, **14**, 1105–1122, 1966.
- Berlicki, A., Observations and modeling of line asymmetries in chromospheric flares, in *The Physics of Chromospheric Plasmas*, edited by P. Heinzel, I. Dorotovič, and R. J. Rutten, 387–406, 2007.
- Biesecker, D. A., D. C. Myers, B. J. Thompson, D. M. Hammer, and A. Vourlidas, Solar phenomena associated with “EIT waves”, *ApJ*, **569**, 1009–1015, 2002.
- Brown, J. C., The deduction of energy spectra of non-thermal electrons in flares from the observed dynamic spectra of hard X-ray bursts, *Solar Phys.*, **18**, 489–502, 1971.
- Carrington, R. C., Description of a singular appearance seen in the Sun on September 1, 1859, *Mon. Not. R. Astr. Soc.*, **20**, 13–16, 1859.
- Emslie, A. G. and P. A. Sturrock, Temperature minimum heating in solar flares by resistive dissipation of Alfvén waves, *Solar Phys.*, **80**, 99–102, 1982.
- Fletcher, L. and H. S. Hudson, Flare energy transport by Alfvén waves in the impulsive phase, *ApJ*, **675**, 1645–1655, 2008.
- Fletcher, L., I. G. Hannah, H. S. Hudson, and T. A. Metcalf, A TRACE white light and RHESSI hard X-ray study of flare energetics, *ApJ*, **656**, 1187–1196, 2007.
- Hale, G. E., The spectrohelioscope and its work, *ApJ*, **71**, 73–101, 1930.
- Haerendel, G., Commonalities between ionosphere and chromosphere, *Space Sci. Rev.*, **124**, 317–331, 2007.
- Hudson, H. S., Thick-target processes and white-light flares, *Solar Phys.*, **24**, 414–428, 1972.
- Hudson, H. S., Implosions in coronal transients, *ApJ*, **531**, L75–L77, 2000.
- Hudson, H., Chromospheric flares, in *The Physics of Chromospheric Plasmas*, edited by P. Heinzel, I. Dorotovič, and R. J. Rutten, 365–386, 2007.
- Hudson, H. S., C. J. Wolfson, and T. R. Metcalf, White-light flares: a TRACE/RHESSI overview, *Solar Phys.*, **234**, 79–93, 2006.
- Kane, S. R. and R. F. Donnelly, Impulsive hard X-ray and ultraviolet emission during solar flares, *ApJ*, **164**, 151–163, 1971.
- Kazeminezhad, F. and M. Goodman, Magnetohydrodynamic simulations of solar chromospheric dynamics using a complete electrical conductivity tensor, *ApJ (Suppl.)*, **166**, 613–633, 2006.
- Lin, R. P. and H. S. Hudson, 10–100 keV electron acceleration and emission from solar flares, *Solar Phys.*, **17**, 412–435, 1971.
- Longcope, D. and B. T. Welsch, A model for the emergence of a twisted magnetic flux tube, *ApJ*, **545**, 1089–1100, 2000.
- Melrose, D. B., Energy propagation into a flare kernel during a solar flare, *ApJ*, **387**, 403–413, 1992.
- Miller, J. A., P. J. Cargill, A. G. Emslie, G. D. Holman, B. R. Dennis, T. N. LaRosa, R. M. Winglee, S. G. Benka, and S. Tsuneta, *J. Geophys. Res.*, **102**, 14,631–14,659, 1997.
- Obayashi, T., Energy build-up and release mechanisms in solar and auroral flares, *Solar Phys.*, **40**, 217–226, 1975.
- Régnier, S. and E. R. Priest, Nonlinear force-free models for the solar corona. I. Two active regions with very different structure, *Astron. Astrophys.*, **468**, 701–709, 2007.
- Schwenn, R., Space weather: The solar perspective, *Living Rev. Solar Phys.*, **3**(2), 2007.
- Stasiewicz, K. *et al.*, *Space Sci. Rev.*, **92**, 423–533, 2001.
- Sudol, J. J. and J. W. Harvey, Longitudinal magnetic field changes accompanying solar flares, *ApJ*, **635**, 647–658, 2005.
- Thomas, R. J. and R. G. Teske, Solar soft X-rays and solar activity. II: Soft X-ray emission during solar flares, *Solar Phys.*, **16**, 431–453, 1971.
- Thompson, B. J., J. B. Gurman, W. M. Neupert, J. S. Newmark, J.-P. Delaboudinière, O. C. St. Cyr, S. Stezelberger, K. P. Dere, R. A. Howard, and D. J. Michels, SOHO/EIT observations of the 1997 April 7 coronal transient: Possible evidence of coronal moreton waves, *ApJ*, **517**, L151–L154, 1999.
- Uchida, Y., M. D. Altschuler, and G. Newkirk, Jr., Flare-produced coronal MHD-fast-mode wavefronts and Moreton’s wave phenomenon, *Solar Phys.*, **28**, 495–516, 1973.
- Veronig, A. M., M. Karlický, B. Vršnak, M. Temmer, J. Magdalenic, B. R. Dennis, W. Otruba, and W. Pötzi, X-ray sources and magnetic reconnection in the X3.9 flare of 2003 November 3, *Astron. Astrophys.*, **446**, 675–690, 2006.
- Wang, H., Evolution of vector magnetic fields and the August 27 1990 X-3 flare, *Solar Phys.*, **140**, 85–98, 1993.

Development of the global simulation model of the heliosphere

Satomi Kamei^{1,4}, Aoi Nakamizo^{2,4}, Takashi Tanaka^{2,4}, Takahiro Obara^{3,4}, and Hironori Shimazu^{3,4}

¹Department of Earth and Planetary Sciences, Graduate School of Sciences, Kyushu University, 6-10-1 Higashi-ku, Fukuoka 812-8581, Japan

²Department of Earth and Planetary Sciences, Faculty of Sciences, Kyushu University, 6-10-1 Higashi-ku, Fukuoka 812-8581, Japan

³National Institute of Information and Communications Technology, 4-2-1 Koganei-shi, Tokyo 184-8795, Japan

⁴CREST, Japan Science and Technology Agency, Kawaguchi-shi, Saitama 332-0012, Japan

(Received September 28, 2007; Accepted February 7, 2008; Online published May 29, 2009)

The heliospheric structure ranging from the solar surface to the earth's orbit is self-consistently reproduced from a time-stationary three-dimensional (3D) magnetohydrodynamic (MHD) simulation. The simulation model incorporates gravity, Coriolis, and centrifugal forces into the momentum equation, and coronal heating and field-aligned thermal conduction into the energy equation. The heating term in the present model has its peak at 2.8 solar radius (R_s) and exponentially falls to zero at greater distance from the solar surface. The absolute value of heating depends on the topology of the solar magnetic field so as to be in inverse proportion with the magnetic expansion factor. The results of the simulation simultaneously reproduce the plasma-exit structure on the solar surface, the high-temperature region in the corona, the open- and closed-magnetic-field structures in the corona, the fast and slow streams of the solar wind, and the sector structure in the heliosphere.

Key words: Solar wind, MHD simulation, CIR.

1. Introduction

There is a long history associated with the development of sun-earth-system models that try to predict the changes in the terrestrial environment caused by the disturbances on the solar surface following propagation through the interplanetary space (Dryer, 1998). Many early studies applied the physics-based model. Among these, the pioneering Hakamada-Akasofu-Fry kinematic model (Hakamada and Akasofu, 1982) is still currently in use by the U.S. space weather system. Since the large-scale structure and dynamics of the solar corona is dominated by the magnetic field, the source surface current sheet model was developed as an observed magnetic field data-driven model for the corona. This model can predict not only the sector structure but also the solar wind speed from the expansion factor (Wang and Sheeley, 1990). By extending the results up to the earth's orbit, model outputs can be compared directly with satellite observations.

In recent years, increases in computing speed have enabled the development of first-principle-based models. The hybrid model developed by Detman *et al.* (2006) combined the source surface current sheet model for the corona with the MHD solar wind model to predict the MHD parameters at the earth's orbit. Full MHD models from the solar surface to the solar wind region have also been developed by several authors (Linker *et al.*, 1999; Riley *et al.*, 2001; Manchester *et al.*, 2004; Tóth *et al.*, 2005; Shen *et al.*, 2007). Although there are differences in the details for each model, these models can extrapolate the surface magnetic field together with self-consistently described plasma into the interplane-

tary space.

In this paper, we report an attempt to develop an improved MHD simulation that unitedly reproduces quasi-stationary heliosphere from the solar surface to the earth's orbit from the observed solar surface magnetic field. When we try to reproduce the heliosphere extending from the solar surface to the earth's orbit, we must calculate both the fine structure around the corona and a global structure from the sun to near the earth's orbit simultaneously. In the following part of this paper, we first show how these difficulties are solved in our simulation model, and then we present some calculation results for a typical solar rotation period.

2. Simulation Model

2.1 Basic equation

The basic equations of the simulations are the modified MHD equations written by dividing magnetic field \mathbf{B} as $\mathbf{B} = \mathbf{B}_0 + \mathbf{B}_1$ with \mathbf{B}_0 a fixed potential field and \mathbf{B}_1 deviation from \mathbf{B}_0 (Tanaka, 1994).

$$\frac{\partial \rho}{\partial t} + \nabla \cdot (\rho \mathbf{v}) = 0, \quad (1)$$

$$\begin{aligned} \frac{\partial (\rho \mathbf{v})}{\partial t} + \nabla \cdot \left(\rho \mathbf{v} \mathbf{v} + P \mathbf{I} + \frac{B^2 - B_0^2}{2\mu_0} \mathbf{I} - \frac{\mathbf{B} \mathbf{B} - \mathbf{B}_0 \mathbf{B}_0}{\mu_0} \right) \\ = \rho \mathbf{g} - 2\rho \Omega \times \mathbf{r} - \rho \Omega \times (\Omega \times \mathbf{r}), \end{aligned} \quad (2)$$

$$\frac{\partial \mathbf{B}_1}{\partial t} + \nabla \times (\mathbf{v} \times \mathbf{B}) = 0, \quad (3)$$

$$\begin{aligned} \frac{\partial U_1}{\partial t} + \nabla \cdot \left[\mathbf{v} \cdot \left(U_1 + P + \frac{B_1^2}{2\mu_0} \right) - \frac{\mathbf{B}_1 (\mathbf{v} \cdot \mathbf{B}_1)}{\mu_0} - \frac{\mathbf{B}_0 (\mathbf{v} \cdot \mathbf{B}_1)}{\mu_0} \right. \\ \left. + \frac{\mathbf{v} (\mathbf{B}_1 \cdot \mathbf{B}_0)}{\mu_0} \right] = Q - \rho \mathbf{v} \cdot \Omega \times (\Omega \times \mathbf{r}) + \rho \mathbf{v} \cdot \mathbf{g}, \end{aligned} \quad (4)$$

Table 1. Boundary conditions of the MHD and Poisson equations.

Distance from the Sun	$1R_s$	$200R_s$
Density	Fix	$\partial/\partial r = 0$
Velocity (parallel)	$\partial/\partial r = 0$	$\partial/\partial r = 0$
Velocity (perpendicular 1)	0	$\partial/\partial r = 0$
Velocity (perpendicular 2)	0	$\partial/\partial r = 0$
B_1 (radial)	0	$\partial/\partial r = 0$
B_1 (tangential 1)	$\partial/\partial r = 0$	$\partial/\partial r = 0$
B_1 (tangential 2)	$\partial/\partial r = 0$	$\partial/\partial r = 0$
U_1	Fix	Fix ($P \rightarrow 0$)
B_0 (line-of-sight)	observation	free
B_0 (perpendicular 1)	free	free
B_0 (perpendicular 2)	free	free

$$U_1 = \frac{\rho v^2}{2} + \frac{P}{\gamma - 1} + \frac{B_1^2}{2\mu_0}, \quad (5)$$

where ρ , \mathbf{v} , P , \mathbf{r} , μ_0 , \mathbf{g} , and γ are the density, velocity, plasma pressure, position vector, the vacuum magnetic permeability, acceleration of gravity, angular velocity of solar rotation and polytropic index set as 5/3, respectively. These equations are generally called as continuity equation (1), equation of motion (2), induction equation (3), and energy equation (4). The energy equation (4) written through the modified total energy of plasma U_1 (Tanaka, 1994) includes the heating term Q . The equations are written in the rotating system, and they include the Corioli's force as well as the centrifugal force and gravity force.

2.2 Boundary condition

The inner boundary of the heliosphere is set at coronal base, which is approximately assumed to be 1 solar Radii (R_s), and the outer boundary is set at the near earth's orbit at $200R_s$. On the inner boundary, the density and total energy of the plasma are fixed, and field perpendicular velocities are set to 0. The field parallel velocity is obtained from the Neumann condition. For the magnetic field, we put the observation data, which were obtained from Wilcox Solar Observatory, to the line-of sight component of \mathbf{B}_0 . For \mathbf{B}_1 , the radial component is set to 0. On the outer boundary, total energy of the plasma is set so as the pressure becomes a small value near 0. Other variables are solved under the Neumann condition. The boundary conditions of the MHD equation used for the present simulation are summarized in Table 1.

2.3 Coronal heating

To obtain a realistic solar wind with $\gamma = 5/3$, some additional energy input is required (Lionello *et al.*, 2001; Sittler *et al.*, 2002). For the purpose of accelerating the solar wind to a high enough speed, we included an additional heating term to the energy Eq. (4) as

$$Q = \rho q_0 (r - 1.0) e^{-r/L} + \nabla \cdot \left(\xi T^{2.5} \frac{\nabla T \cdot \mathbf{B}}{B^2} \right) \cdot \mathbf{B}, \quad (6)$$

where q_0 , L , and T are amplitude of heating, decay distance of heating (set to $1.8R_s$), and temperature (Sittler *et al.*, 2002). The first term of the right handed side shows the ad hoc heating, while the second term shows Spitzer's heat conduction term parallel to the magnetic field line. This heat conduction is applied only inside $10R_s$. From Eq. (6),

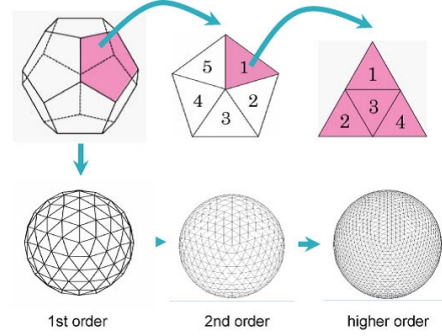


Fig. 1. Grid system made from a dodecahedron. One pentagon surface of regular dodecahedron is first divided into five right triangles, and then the generated triangles are divided into four smaller triangles.

it is clear that heating has its peak at $L + 1 = 2.8R_s$ and subsequently decreases with a distance from the sun.

The magnetic field topology of the solar surface is important for solar wind speed. Therefore, we consider the magnetic field topology into the calculation of heating amplitude q_0 . It is known that the flux tube expansion factor f_s , which is the ratio of the magnetic field intensity on the photosphere to that of respective points at extension along magnetic field, is inversely correlated with the velocity (Wang and Sheely, 1990). So, we set q_0 to be inversely proportional to f_s written in the form

$$f_s \equiv \left(\frac{r_s}{r_{s'}} \right)^2 \frac{B_{r_s}}{B_{r_{s'}}} = \left(\frac{r_s}{r_{s'}} \right) f_{s'}, \quad (7)$$

where r_s and B_{r_s} are $1R_s$ and field intensity at the photosphere, and $r_{s'}$ and $B_{r_{s'}}$ denote distance from the solar center and field intensity at $r_{s'}$. Given the magnetic field \mathbf{B} , the expansion factor f_s is calculated by solving $\nabla \cdot (\mathbf{n} f_{s'}) = 0$ ($\nabla \cdot (-\mathbf{n} f_{s'}) = 0$) with $\mathbf{n} = \mathbf{B}/|\mathbf{B}|$ along the away (toward) field lines, together with the boundary condition $f_s = 1.0$ on the inner boundary. In addition to this inverse correlation considered through Eq. (7), q_0 is additionally reduced in the place where temperature is higher than 2.8 million K.

2.4 Grid system and numerical scheme

When calculating a global system with a centrifugal configuration like the heliosphere, it is desirable to construct a spheroidal unstructured grid system having no apparent singularity. The grid system must also be tolerable for the calculation which treats both the fine structure around the center and wide-range structure extending the whole area simultaneously. To realize such a grid system, we first divide one pentagon surface of regular dodecahedron into five right triangles, adding a central point that inscribes a sphere. Next, we divide the generated triangles into four smaller triangles with all new points inscribing a sphere. Figure 1 shows this process of how we generate higher order splitting successively. By the fourth order splitting, 1922 grid points are generated. Stacking such spheres radially, a 3-D grid system is generated.

The control volume for the Finite Volume Method (FVM) calculation is hexagonal columns connecting the exocentric points of triangles on interfacing spheres. For each control volume, data for volume, area of interfacing surface, and normal and tangential vectors on the interfacing surface are

prepared for the FVM calculation.

The numerical scheme used in the present simulation for the time integration of the conservative MHD equation is the FVM total variation diminishing (TVD) scheme with the monotonic upstream scheme for conservation laws (MUSCL) method, and the Van Leer's differentiable limiter originally developed by Tanaka (1994). For details, see Tanaka (1994).

3. Numerical Results

Here, we show the simulation results for 3-D structures of the solar corona and the solar wind for a typical solar rotation period. We have calculated the period of Carrington Rotation (CR) 2028 (2005, March 25–April 21) and then compared it with the observation is made at the earth's orbit using the solar wind data obtained by ACE (OMNI web service).

Figure 2 shows a 3-D close up view of the solar surface and solar corona as viewed from the earth on 2005 March 29. In this figure, the contour surface shows an isothermperature surface at 2.8 and inside of it is higher than 2.8. This temperature value is normalized by the surface temperature 0.8×10^6 K. These high temperature regions correspond to the closed field regions, where the plasma is trapped. Red and blue lines show magnetic field lines. Here red (blue) lines show the away (toward) field lines. We can observe the origin of sector structure in the corona where toward and away sectors are separated by the high temperature region. Open field lines extending from one continuous region have a same color. The area of another-color open field lines is separated by the high-temperature region. These structures are a 3-D generalization of 2-D field, temperature and flow structures shown by Sittler *et al.* (2002).

Color shading on the solar surface shows plasma flux emitted from the solar surface. Yellow and red colors show the region from where solar wind plasma is supplied to the interplanetary space. Consequently, these regions can be looked upon as the coronal hole. Coronal holes are situated at the center of one continuous region having same-color field lines. Compared with SOHO extreme ultraviolet image observed during CR 2028, positions of these coronal holes estimated from the flux exiting region almost coincide with dark regions seen in X-ray images.

From Fig. 2, we can see that the calculation has reproduced the solar and coronal fine structures near the sun. The coronal hole, sector structure, and high temperature corona are organized as a combined structure. As will be shown in Fig. 3, sector and high-speed flow structures in the interplanetary space are the extension of this organized structure near the sun.

Figure 3 shows the global solar wind structure on the ecliptic plane from the solar surface to the earth's orbit. White lines show the start longitudes of each quarter which were face to face with the earth on March 25, April 1, April 15, and April 22. The shading and contour lines in Fig. 3 show the magnetic sector and solar wind speed in the interplanetary space. Velocity is shown by the contour lines after the conversion from the rotating (calculating) frame to the non-rotating (observing) frame. In Fig. 3, the interplanetary magnetic structure exhibits four sectors.

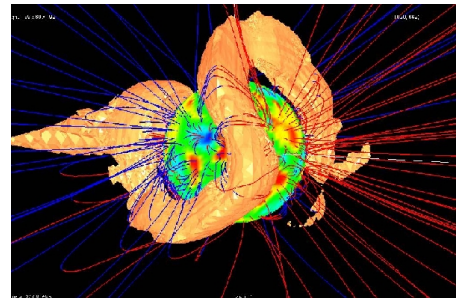


Fig. 2. A 3-D close up view of the solar surface and solar corona viewed from the earth on 2005 March 29. The contour surface shows an isothermperature surface at 2.8. Temperature value is normalized by the surface temperature 0.8×10^6 K. The coronal temperature outside the contour surface is about 1.7. Red lines show the away field lines and blue lines show the toward field lines. Color shading on the solar surface shows plasma flux emitted from the solar surface. The outward-flux area is indicated by warm colors.

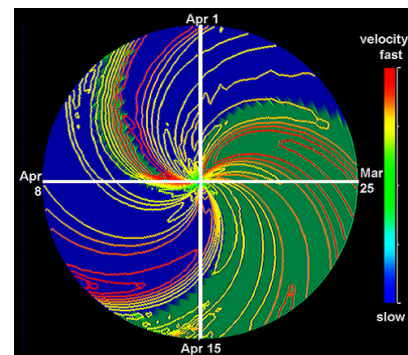


Fig. 3. The global solar wind structure in the ecliptic plane from the solar surface to near the earth's orbit. White lines show the start longitudes of each quarter which were face to face with the earth on March 25 (right), April 1 (top), April 8 (left), and April 15 (top). The shading and contour lines shows the magnetic sector (green-away, blue-toward) and solar wind speed (color bar: red-fast, blue-slow) in the interplanetary space.

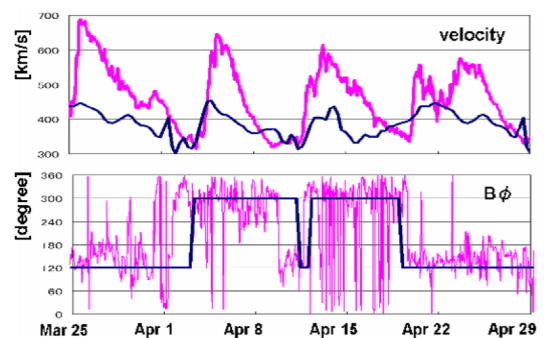


Fig. 4. Top panel shows observed (pink) and calculated result (navy) of solar wind speed and bottom shows B_ϕ for observed data and $B_r > 0$ (upper) or $B_r < 0$ (lower) for calculation result. Observed near-Earth solar wind speed and magnetic field data by OMNI (<http://omniweb.gsfc.nasa.gov>). From the observed data during CR2028, it seems to have three speed peaks and 4 sectors including one very narrow sector around Apr 10.

This four sector structure reflects, in the ecliptic plane, the sectors shown in 3D in Fig. 2. The away sector seen on the right of Fig. 2 corresponds to the first away sector in the first quarter of Fig. 3 that starts on March 25 at the earth,

as the beginning of CR 2028, and the toward sector seen on the left of Fig. 2 corresponds to the second toward sector in the second quarter of Fig. 3 that starts on April 1 at the earth. The third away sector seen in the third quarter at the earth is a very narrow away sector, and the fourth sector in the third and fourth quarter at the earth are both a toward sectors with a normal width.

Due to the solar rotation, the solar wind blows like a sprinkler seen in the non-rotating frame. In Fig. 3, three high-speed flows can be seen at the earth with their positions in the first away, second toward and fourth toward sectors. There is no high-speed flow in the third narrow away sector. In one sector, only one high-speed flow appears without consecutive high speed flows (Neugebauer *et al.*, 2004). These flow and sector structures can be quite reasonably understood from the coronal structure shown in Fig. 2. The time recognized on the earth for the increasing of wind speed is shorter than that for decreasing. This characteristic resembles the observed feature of solar wind variation in the increasing and decreasing of speed (Gosling and Pizzo, 1999). In Fig. 3, no shock is generated associated with the CIR. Actually, there may not be an obvious CIR formation in the interval treated in this paper. However, we cannot draw a firm conclusion, because grid spacing in the present model is still too sparse for the shock resolution.

Figure 4 shows observed and calculated results for variations in solar wind speed and sector near the earth's orbit. Comparing the calculation results with these observation data, it is clear that the four sectors and three high speed winds seen in calculation are also observable. A narrow third away sector in the third quarter is similarly seen both in the calculation and in the observation data. As for the relative position of the sector boundary and fast flow, similar features are seen in Figs. 2, 3 and 4. At the earth, fast flow starts after the sector boundary has been passed, and fast flow does not restart until the passage of the next sector boundary. However, some discrepancies are seen. However, provided that the calculated and observed magnitude of the low-speed solar wind is the same, the magnitude of the calculated high-speed solar wind value is lower than the observed value. In other words, the contrast between high- and low-speed flows is not sufficient in the calculated result. In addition, the decreasing speed of third fast flow is too rapid in the calculated than the observed data. These results suggest a further necessity for the improvement of the model. There are many uncertainties that prevent a model-observation coincidence. There may still be many unknown factors in heating term, expansion factor, radiation energy balance, and magnetic field observation.

4. Summary

We have succeeded in constructing an MHD model to reproduce the heliospheric structure extending from the solar surface to the earth's orbit using a uniform triangular grid system with no apparent singular point. The calculation results have reproduced both of the fine structure around the corona and global structure from the solar surface to the earth's orbit. The tendency of a rapid increase and slow decrease of velocity seen on the earth and the relative position of the sector boundary, including the narrow sector, have

been well reproduced in the model. Whereas three velocity peaks are seen at the earth's orbit in both the calculated and observed solar winds, the calculated results are still insufficient for the absolute speed of solar wind. This means that we need to improve this model further when using it for the real prediction of solar wind. For this purpose, we are going to continue variations and improvements of the model. In future research, we are going to adopt this model for the space weather prediction system operated in the National Institute of Information and Communication Technologies (NiCT), Japan.

Acknowledgments. Wilcox Solar Observatory data used in this study was obtained via the web site (<http://quake.stanford.edu/~wso>) courtesy of J. T. Hoeksema. The OMNI data were obtained from the GSFC/SPDF OMNIWeb interface at (<http://omniweb.gsfc.nasa.gov>).

References

- Brio, M. and C. C. Wu, An upwind differencing scheme for the equations of ideal magnetohydrodynamics, *J. Comput. Phys.*, **75**, 400–422, 1988.
- Detman, T., Z. Smith, M. Dryer, C. D. Fry, C. N. Arge, and V. Pizzo, A hybrid heliospheric modeling system: Background solar wind, *J. Geophys. Res.*, **111**, A07102, doi:10.1029/2005JA011430, 2006.
- Dryer, M., Multidimensional, magnetohydrodynamic simulation of solar-generated disturbances: space weather forecasting of geomagnetic storms, *AIAA J.*, **36**, 365–370, 1998.
- Gosling, J. T. and V. J. Pizzo, Formation of corotating interaction regions and their three dimensional structure, *Space Sci. Rev.*, **89**, 21–52, 1999.
- Hakamada, K. and S. Akasofu, Simulation of three-dimensional solar wind disturbances and resulting geomagnetic storms, *Space Sci. Rev.*, **31**, 3–70, 1982.
- Linker, J. A., Z. Mikic, D. A. Biesecker, R. J. Forsyth, S. E. Gibson, A. J. Lazarus, A. Lecinski, P. Riley, A. Szabo, and B. J. Thompson, Magnetohydrodynamic modeling of the solar corona during Whole Sun Month, *J. Geophys. Res.*, **104**, 9809–9830, 1999.
- Lionello, R., J. A. Linker, and Z. Mikic, Including the transition region in models of the large-scale solar corona, *Astrophys. J.*, **546**, 542–551, 2001.
- Manchester, W. B., T. I. Gombosi, I. Roussev, D. D. De Zeeuw, I. V. Sokolov, K. G. Powell, G. Toth, and M. Opher, Three-dimensional MHD simulation of a flux rope driven CME, *J. Geophys. Res.*, **109**, A01102, doi:10.1029/2002JA009672, 2004.
- Neugebauer, M., P. C. Liewer, B. E. Goldstein, X. Zhou, and J. T. Steinberg, Solar wind stream interaction regions without sector boundaries, *J. Geophys. Res.*, **109**, A10102, doi:10.1029/2004JA010456, 2004.
- Riley, P., J. A. Linker, and Z. Mikic, An empirically driven global MHD model of the solar corona and inner heliosphere, *J. Geophys. Res.*, **106**, 15,889–15,901, 2001.
- Shen, F., X. Feng, S. T. Wu, and C. Xiang, Three-dimensional MHD simulation of CMEs in three-dimensional background solar wind with the self-consistent structure on the source surface as input: Numerical simulation of the January 1997 Sun-Earth connection event, *J. Geophys. Res.*, **112**, A06109, doi:10.1029/2006JA012164, 2007.
- Sittler, Jr., E. C., L. Ofman, S. Gibson, M. Guhathakurta, J. Davila, R. Skoug, A. Fludra, and T. Holzer, Development of multidimensional MHD model for the solar corona and solar wind, *Solar wind 10*, 2002.
- Tanaka, T., Finite volume TVD scheme on an unstructured grid system for three-dimensional MHD simulation of inhomogeneous systems including strong background potential fields, *J. Comput. Phys.*, **111**, 381–389, 1994.
- Tóth, G., I. V. Sokolov, T. I. Gombosi, D. R. Chesney, C. R. Clauer, D. L. De Zeeuw, K. C. Hansen, K. J. Kane, W. Manchester, R. C. Oehmke, K. G. Powell, A. J. Ridley, I. I. Roussev, Q. F. Stout, O. Volberg, R. A. Wolf, S. Sazykin, A. Chan, B. Yu, and J. Kóta, Space Weather Modeling Framework: A new tool for the space science community, *J. Geophys. Res.*, **110**, A12226, doi:10.1029/2005JA011126, 2005.
- Wang, Y. M. and N. R. Sheely Jr., The solar wind speed and coronal flux-tube expansion, *Astrophys. J.*, **355**, 726–732, 1990.

The interplanetary magnetic decrease automatic detection (IMDAD) code

F. L. Guarnieri¹, B. T. Tsurutani², and E. Echer³

¹Universidade do Vale do Paraíba (UNIVAP), Sao José dos Campos, SP, Brazil

²Jet Propulsion Laboratory, California Institute of Technology, Pasadena, CA

³Instituto Nacional de Pesquisas Espaciais, INPE, Sao Jose dos Campos, SP, Brazil

(Received February 7, 2008; Revised April 15, 2008; Accepted May 5, 2008; Online published May 29, 2009)

A new code, called the interplanetary magnetic decrease (MD) automatic detection (IMDAD) code, has been developed to enable researchers in the field to rapidly identify MD events for further analyses. The criterion used for MD selection is $B_{\min} < XB_0$, where X is a variable value and B_0 is the ambient magnetic field magnitude. The code can be applied to data sets from different instruments/missions located in different space plasma environments in the heliosphere. The code has been tested during slow solar wind, fast solar wind and CIR intervals at ~ 5 AU (from November 28 to December 03, 1992). For this test, we used a sliding window with a width of 300 seconds applied to 1-second high-resolution magnetic field data. The events identified by the code have been confirmed by hand analyses. The routine was able to identify 57 of the 118 MDs identified by hand ($\sim 50\%$). The selection criteria for IMDAD and hand-analyses MDs were not exactly the same, accounting for the different rates of occurrence. What is particularly encouraging is that IMDAD did not falsely identify any events. The discrepancies between the two methods are discussed in the text. This code will be made available to the general public.

Key words: Interplanetary magnetic decreases, solar wind, Alfvén waves.

1. Introduction

Magnetic Decreases (MDs; Turner *et al.*, 1977) have been defined as $\sim 50\%$ decreases in the interplanetary magnetic field magnitude (Winterhalter *et al.*, 1994; Fränz *et al.*, 2000; Tsurutani *et al.*, 2003). These structures have been called a variety of names (magnetic holes, holes, magnetic dips, magnetic cavities, magnetic bubbles, etc.) due to their discovery at different times and in different locations of the heliosphere/Earth's magnetosphere (Sugiura *et al.*, 1969; Turner *et al.*, 1977; Luhr and Klockner, 1987; Winterhalter *et al.*, 1994; Fränz *et al.*, 2000). For events that have been examined to date, the magnetic pressure decreases have been supplanted by plasma thermal pressure increases, so that the entire structure is generally in pressure balance (Winterhalter *et al.*, 1995; Burlaga, 1995; Fränz *et al.*, 2000).

Most past studies have focused on large decreases of the magnetic field magnitude, events where the decrease magnitudes are larger than 0.5 times the ambient field. It is clear that this is an arbitrary threshold. Similar structures generated by the same mechanism, but lesser in intensity, are also present in the interplanetary medium. To allow the rapid detection of MDs of arbitrary intensity, a computer code called Interplanetary Magnetic Decrease Automatic Detection (IMDAD) has been developed for the space research. This code allows variable magnetic field decreases, variable inter-MD spacing, and can be applied to variable data rates. The code can be used to identify MDs of arbitrary length

by adjusting its window size (here we discuss only MDs of length up to 300 s to compare results to previous works). Although previous workers have developed routines to automatically identify MDs (Winterhalter *et al.*, 1994; Fränz *et al.*, 2000), those codes did not have the special features of IMDAD. The codes are also not available to the general public.

2. Method of Analyses

A general routine to identify MDs using high time resolution magnetometer data has been developed. The aim of the development of the IMDAD computer code is to be able to correctly identify MDs present in the data. In this paper, the routine will be described in detail. Pitfalls will also be discussed.

We have used the Ulysses high-resolution magnetometer data as our test sample. The data used for this test is nominally one-second (the Ulysses sampling rate varies) resolution magnetic field vector data for the interval from November 25 (day 330) to December 3 (day 338), 1992. Ulysses had recently encountered Jupiter (February, 1992) and was starting its first south polar pass. Ulysses was at $\sim -20^\circ$ and at 5.1 AU from the sun during the selected test data interval. This 9-day interval contained a variety of solar wind types. There are ~ 4 days of quiet solar wind, ~ 3 days of Corotating Interaction Region (CIR) solar wind, and ~ 1 day of non-CIR (pure) high speed stream solar wind.

IMDAD was tested on the above data interval. The MDs were identified by hand analyses and they were also independently identified by computer analyses. The MDs identified by hand but missed by computer were carefully examined to understand the reasons why.

The definition of a MD used in this test is a decrease of field magnitude of 50% of the ambient magnetic field strength ($0.5B_0$). This is the same general criterion used by Winterhalter *et al.* (1994). This criterion is kept so there will be continuity of methods used in the literature (however, we will later show that even with this simple definition, slightly different selection methods may yield significantly different results). We also hope to intercompare our results with those of others. It should also be noted by the reader that different decrease levels can be easily implemented. This program can be used by other scientists for analyses of MDs in the heliosphere and magnetosphere. Interested persons should contact F. L. Guarnieri at guarnieri@univap.br.

2.1 Details of the IMDAD routine

A sliding window of 300 seconds was used to calculate the average field magnitude (B_0) during the interval. All points that have values less than $0.5B_0$ are identified. The window is shifted by 1 second and the process repeated. This analysis is done for the entire data set. After the data has been initially processed in this manner, the same data points identified by different window placements and adjacent potential MD candidates are deleted (keeping only the beginning and end points). Single isolated points are also deleted, assuming that they are spurious data errors.

The window size of 300 seconds and the minimum MD separation of 30 seconds were empirically selected for this data set. We caution the reader that he/she might have to change these parameters for applications to different plasma regions. It would also be important that they empirically hand check the accuracy of the code as done in this paper.

A schematic showing the basics of the routine is indicated in Fig. 1. A nine-point interval with a sliding window size of three points is illustrated (only as an example) to give the reader a general idea of how the routine works. The sliding windows are represented by brackets A (black), B (blue), C (red), etc. For bracket A, the first 3 points are examined. The magnetic field average of the first three points is calculated. Any points that have values less than 50% of the average of the field are identified. In this case no points meet this criterion. Next, the window is slid by one point in time to give a new analysis subinterval (bracket B in the figure). The result of the subsequent calculation is that point 4 satisfies the MD criterion. A blue star is noted above the point (for visualization). For the subinterval bracket C, the average magnetic field is low, so no points are identified. The same is true for bracket D. For bracket E, point 5 will be detected as an MD. A yellow star is indicated above this point. After the entire interval has been analyzed, there are 2 points identified, points 4 and 5.

The program next considers single MD points. If there is only a single isolated MD point, this is discarded assuming that it is a spurious data spike. In the example shown above, two adjacent points were selected, so there are no such single point cases.

The next step of the routine is to consider cases where there are several adjacent points. Point 5 is adjacent to point 4 so the program considers the deletion of point 5. Next point 6 is examined. Since it is not identified as an MD, point 5 is retained and identified as the end of the MD. Thus, the program identifies point 4 as the beginning of the

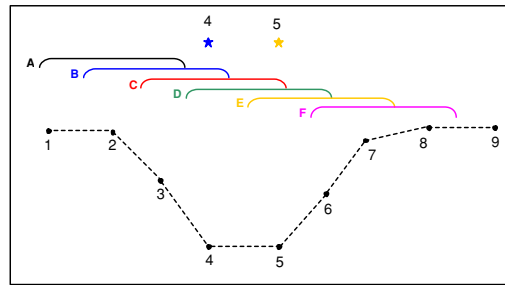


Fig. 1. Illustration of the general features of the routine. The stars over the brackets indicate the points that were identified as following the MDs criteria.

MD and point 5 as the end. This allows us to automatically determine the MD width.

The window width selected in our final analysis of the real Ulysses data was 300 seconds rather than 3 points, as shown in Fig. 1. The much shorter interval was chosen only to illustrate the general features of the program.

To be able to handle waves inside the MD or highly turbulent data, the program examines adjacent MDs that are closer than 30 seconds. Several different separation time scales, from 5 to 50 seconds were tested. The interval of 30 seconds was found to be the one with best correspondence to the hand-analyzed MD set, and it was selected for the present version of the program. If candidate MDs are closer together than 30 seconds, they are considered as a single MD. The two MDs are “merged” and the beginning of the first event and the end of the second become the boundaries of the new (merged) MD.

The MD duration indicated by the program is based only in the points that follow the MD criteria. The user would have to define what method he/she may find appropriate to identify the edges. Tsurutani *et al.* (1999), in their hand analyses of MDs, assumed an $1/e$ decay from the B_0 calculated outside the MD. This is the criteria used in this paper in order to check the IMDAD code. Although we have stated the method used here, we state this as only an example. Other users can select their own criteria for edge detection.

2.2 Hand analyses of MDs

To test the accuracy of IMDAD MD selection, the same 9-day Ulysses magnetic field interval was examined by visual inspection (without reference to the computer results). For a potential MD, a background field on both sides of the MD was estimated by drawing line “averages” on a data plot. These were determined by visual inspection. Of the two “background fields”, the higher value was used for the calculation. Next, the minimum field was determined by the same method. The $1/e$ value of the difference between the highest background field and minimum field was required to be greater than $0.5B_0$. This is the same method applied by Tsurutani *et al.* (1999).

3. Results of the Intercomparison Between Computer-selected Events and Hand-selected Events

Figure 2 shows the Ulysses data interval of the test. From top to bottom are the solar wind speed, proton density,

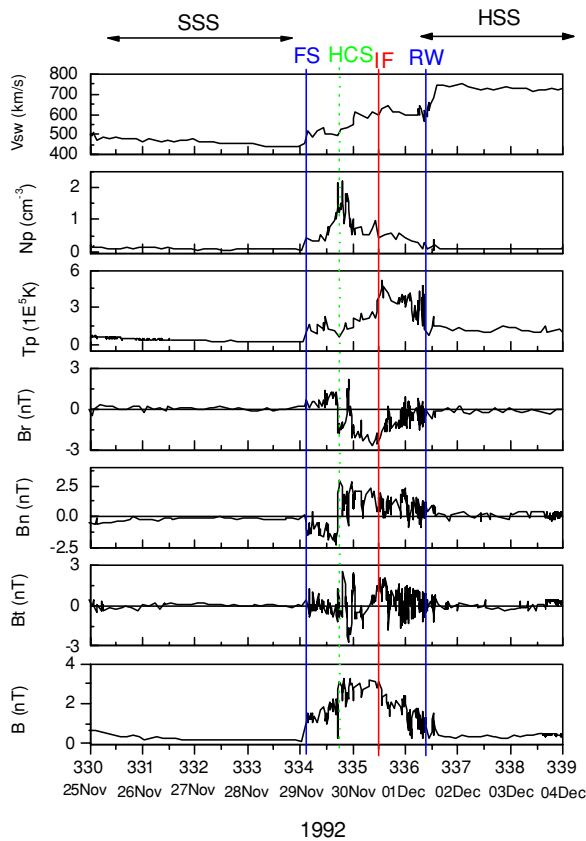


Fig. 2. Ulysses data interval (November 25 to December 3, 1992) used to test the routine. The panels are, from top to bottom, the solar wind speed, proton density, proton temperature, magnetic field components, R , T and N , and at the bottom, is the magnetic field magnitude. The slow speed stream is identified by SSS. The high speed stream is marked by HSS, and IF indicates the interface between the two regions. Present in the interval is a heliospheric current sheet, marked as HCS.

proton temperature, magnetic field components (in Solar Heliospheric R , T , and N coordinates), and at the bottom, the magnetic field magnitude. At the top of the figure, the slow speed stream (SSS) and high speed stream (HSS) intervals are indicated by horizontal arrows. The slow speed stream is present from November 25 to 29 and the high speed stream from December 2 through 3. The CIR is the region of interaction of the two types of streams proper. Some of the CIR structures are indicated for the interested reader. The CIR boundaries are a fast forward shock (FS, blue line) at the anti-solar direction boundary. A reverse wave (RW, blue line) is present at the solar direction boundary. The CIR occurs from 02:35 UT November 29 (day 334) to 11:30 UT December 1 (day 336). Several structures within the CIR are also indicated. There is an embedded heliospheric current sheet (HCS) indicated by a green line. The interface between the high speed stream and the slow speed stream is denoted by “IF” (for “interface”). The IF is indicated by a red line.

Figure 3 shows an example of a MD identified by the program. The panels are, from top to bottom, the magnetic field components B_R , B_T , and B_N , and the B magnitude. This MD event, clearly visible in the B magnitude panel, occurred on November 28, 1992 (DOY 333). The blue square

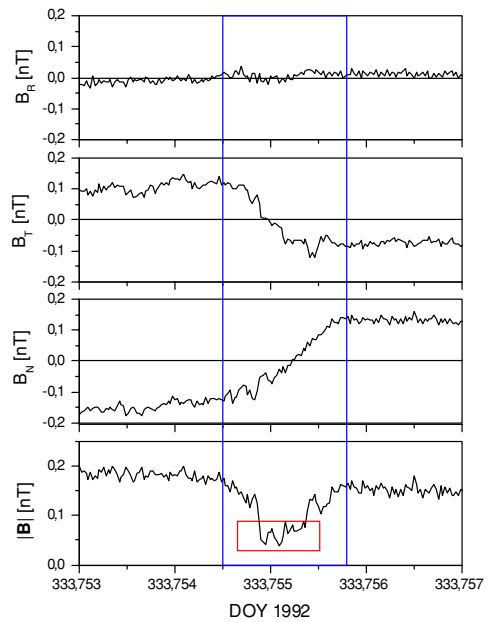


Fig. 3. Example of a MD identified by the program. The blue square marks the MD event, and the red box the MD identified by the program.

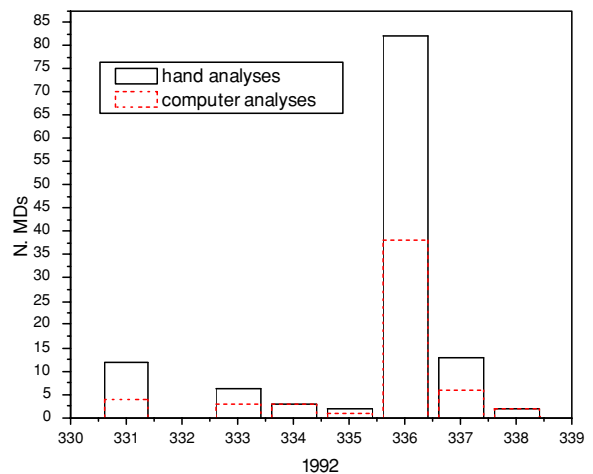


Fig. 4. MD occurrence rates using the two methods of analyses. The results from the computer analyses are plotted in dashed red and those from hand analyses are in solid black.

marks the MD event and the red box the MD identified by the program. There is a discontinuity in B_T and B_N components at the time of the MD occurrence. The B_T component changes from ~ 0.125 nT to ~ -0.1 nT across the discontinuity. The change in B_N is from ~ -0.125 nT to ~ 0.15 nT.

The MD identified by the computer routine (red box) has a shorter duration when compared with hand analysis due to different identification procedures. In the IMDAD identification, the edges are based only in the points following the criteria, while in the hand analysis the inspectors used the borders values as the reference field to identify the MDs (the same method previously applied by Tsurutani *et al.*, 1999).

The MD occurrence rates of the two methods of analyses are shown in Fig. 4. The top panel shows the number of MDs per day from the computer analyses in dashed red,

and for those from hand analyses in solid black. The reader should note that the number of events from hand analyses is always greater or equal to the number from computer analyses. Over the whole interval, there are 118 MDs identified by hand and 57 events identified by computer.

Each computer-selected event was compared with the events identified by hand. It is noted that **all 57 computer selected events were also identified by hand analyses**. This result gives confidence to the accuracy of the present program (and its internal parameters) used for this region of space, since no false positive MD was detected.

The causes for the code missing MDs were studied. It was found that the missed events fall into several categories. The two main causes were: 1) events where the magnetic field decrease is near the threshold of $-0.5B_0$, and 2) when there are rapid oscillations in the magnetic field magnitude (if these oscillations have amplitudes comparable to the MD decrease, they can change the reference value [B_0] for the window, while hand-analysis is not affected by these structures). In the first category there were 25 cases of “missed events” and in the second category there were 17 cases. Moreover, there are two minor causes of misidentification that we called “large MD” or “background contamination”. The “large MD” refers to MDs that are longer than the window size used. These MDs can be selected by hand inspection but they may be missed by the computer since their durations are close to the window size. The “background contamination” usually occurs when there are discontinuities or shocks around the MD that may affect the B_0 calculation for the window.

For the first category of “missed events”, the near “threshold” events, it is noted that the computer and hand analysis methods of determining the “background” field were slightly different. The hand analysis method used higher field values for the “background”, so this criterion was less strict than the computer criterion. The computer method often contains field values in the decreasing slopes of the MDs, lowering the calculated “background” fields, giving stricter limits than hand analyses. Here the background field on both sides of the MD was estimated by drawing line “averages” on a data plot. Of the two “background fields”, the higher value was used for the calculation (a more liberal assumption than the IMDAD code). Next, the minimum field was determined by the same method. The $1/e$ value of the difference between the highest background field and minimum field was required to be greater than $0.5B_0$. As the reader will readily note, although a simple condition of “ $0.5B_0$ ” was used, this is a different criterion still. The point that we wish to emphasize is that slightly different criteria will yield a different set of events. Thus, the method of implementation of the criterion is important to understand. On the other hand, it is felt that no one method is better than another. All methods will give equally valuable information.

It should be obvious that the IMDAD “missed events” are not really “missed”. Since hand-analyses and computer analyses will never have identical criteria, each is correct. It should be noted that the type of hand analyses done here and in Tsurutani and Ho (1999) is not exact and not 100% reproducible.

4. Summary and Discussion

A computer program has been written which identifies heliospheric MDs in the Ulysses magnetic field data at ~ 5 AU from the sun. The program works well in the slow solar wind, in the pure high speed stream solar wind, and in the compression regions at the interface between slow and high speed streams (CIRs). The routine was able to identify 57 of the 118 events identified by hand analysis, about 50% of the events (48.3%). However, all the 57 MDs identified by the program were also identified by hand analyses, giving confidence to the accuracy of the method. The events that were missed by the code were events that fell into two main categories: events that were slightly below the hand-technique threshold level of detection and events associated with “wave-like” intervals. For the first case, the slightly more liberal hand analyses method allowed the detection of these events. “Wave-like” events were generally found in hand analyses when the magnetic field magnitude was low. These events could possibly be compressional waves or small amplitude mirror mode (Tsurutani *et al.*, 1982) structures. These low field magnitude regions are generally low plasma beta (the ratio of magnetic pressure to plasma thermal pressure) regions. Thus they could also be due to magnetic noise or turbulent structures.

Acknowledgments. Portions of this work were done at the Jet Propulsion Laboratory, California Institute of Technology, Pasadena CA under contract with NASA. EE would like to thank to the Brazilian FAPESP (2007/52533-1) and CNPq (PQ-300104/2005-7 and 470706/2006-6) agencies for financial supports.

References

- Burlaga, L. F., *Interplanetary Magnetohydrodynamics*, Oxford University Press, New York, 1995.
- Fränz, M., D. Burgess, and T. S. Horbury, Magnetic depressions in the solar wind, *J. Geophys. Res.*, **105**, 12725, 2000.
- Luhr, H. and N. Klockner, AMPTE-IRM observations of magnetic cavities near the magnetopause, *Geophys. Res. Lett.*, **14**, 186, 1987.
- Sugiura, M., T. L. Skillman, B. Ledley, and J. P. Heppner, “Holes” in the magnetic field near the magnetopause, *EOS Trans. AGU*, **50**, 278, 1969.
- Tsurutani, B. T. and C. M. Ho, A review of discontinuities and Alfvén waves in interplanetary space: Ulysses results, *Rev. Geophys.*, **37**, 517, 1999.
- Tsurutani, B. T., E. J. Smith, R. R. Anderson, K. W. Ogilvie, J. D. Scudder, D. N. Baker, and S. J. Bame, Lion roars and non-oscillatory drift mirror waves in the magnetosheath, *J. Geophys. Res.*, **87**, 6060, 1982.
- Tsurutani, B. T., G. S. Lakhina, D. Winterhalter, J. K. Arballo, C. Galvan, and R. Sakurai, Energetic particle cross-field diffusion: Interaction with magnetic decreases (MDs), *Nonlin. Proc. Geophys.*, **6**, 235, 1999.
- Tsurutani, B. T., B. Dasgupta, J. K. Arballo, G. S. Lakhina, and J. S. Pickett, Magnetic field turbulence, electron heating, magnetic holes, proton cyclotron waves, and the onsets of bipolar pulse (electron hole) events: a possible unifying scenario, *Nonl. Proc. Geophys.*, **21**, 27, 2003.
- Turner, J. M., L. F. Burlaga, N. F. Ness, and J. F. Lemaire, Magnetic holes in the solar wind, *J. Geophys. Res.*, **82**, 1921, 1977.
- Winterhalter, D. H., M. Neugebauer, B. E. Goldstein, E. J. Smith, and S. J. Bame, and A. Balogh, Ulysses field and plasma observations of magnetic holes in the solar wind and their relation to mirror-mode structures, *J. Geophys. Res.*, **99**, 23372, 1994.
- Winterhalter, D., M. Neugebauer, B. E. Goldstein, E. J. Smith, B. T. Tsurutani, S. J. Bame, and A. Balogh, Magnetic holes in the solar wind and their relation to mirror-mode structures, *Space Sci. Rev.*, **72**, 201, 1995.

Impacts of torus model on studies of geometrical relationships between interplanetary magnetic clouds and their solar origins

Katsuhide Marubashi¹, Suk-Kyung Sung¹, Kyung-Suk Cho¹, and Ronald P. Lepping²

¹Space Science Division, Korea Astronomy and Space Science Institute, Daejeon 305-348, Korea

²Space Weather Laboratory, NASA-Goddard Space Flight Center, Greenbelt, MD 20771, USA

(Received December 14, 2007; Revised April 17, 2008; Accepted April 18, 2008; Online published May 29, 2009)

Our recent analysis of interplanetary magnetic clouds (MCs) showed that the orientations of MC axes determined by a model fitting with curvature of MCs taken into account (referred to as a torus model, hereafter) can be significantly different from those obtained from fittings with a straight cylinder model. Motivated by this finding, we re-examined geometrical relationships between magnetic field structures of MCs and their solar origins. This paper describes the results of the re-examination with special attention paid to two MC events, for which different orientations of MC axes were obtained from a torus model and a cylinder model. For both cases, it is shown that the torus models give the MC geometries of magnetic field structures in good agreement with those of coronal arcade structures which were formed in association with the launch of MCs along the magnetic field inversion lines. Summarizing the analysis results for 12 MCs investigated here, we conclude that: (1) the formation of coronal arcade structure is a good indication of MC formation; (2) MC geometries can be obtained that are consistent with the coronal arcades with respect to the axis orientation and the magnetic field structure including chirality, indicating that no significant direction changes occurred during the propagation of MCs through the interplanetary medium.

Key words: Interplanetary magnetic clouds, magnetic field structures, solar origins, geometrical relationships.

1. Introduction

The interplanetary magnetic cloud (MC) occupies the whole body or a significant part of a plasma cloud ejected into the solar wind in association with the coronal mass ejection (CME). The internal structure of a MC is characterized by the nested helical fields, which can be described as a magnetic flux rope (Goldstein, 1983; Marubashi, 1986; Burlaga, 1988). The geometrical relationship between magnetic structures of MCs and their solar source region is one of the key issues for understanding the mechanisms involved in the formation of MCs and their possible deformation during their propagation in interplanetary space. Most previous studies on this subject have shown that the orientations of MCs are roughly aligned with the inversion lines of photospheric longitudinal magnetic fields in the associated CME sites and that the chirality of MCs are of the same sign as the chirality of solar magnetic fields in the source regions (e.g., Marubashi, 1986, 1997; Bothmer and Schwenn, 1994; Bothmer and Rust, 1997; Yurchyshyn *et al.*, 2001). More recent studies, however, point out several cases in which the orientations of MCs do not agree with those of the associated filaments or solar magnetic inversion lines (Rust *et al.*, 2005; Wang *et al.*, 2006; Yurchyshyn *et al.*, 2007).

The purpose of this study is to re-examine the geometrical relationships between the MC magnetic fields and the solar magnetic fields with a new technique to determine

the orientations of MCs. In most studies on this subject, as mentioned above, the MC orientations were determined by fitting techniques with a straight cylinder model. Recently, Marubashi and Lepping (2007) analyzed the MC geometries using a torus-shaped flux rope model to take into account the curvature of the global configuration of MCs. Their comparison of the MC orientations determined from the torus and cylinder models revealed that there actually are such MC events for which observations can be as well explained by either of the models but that the obtained orientations are significantly different from each other. This finding impacts on our understanding the connection between MCs and CMEs and suggests that it may be possible to obtain a better agreement between the MC orientations and the solar magnetic inversion lines if the MC geometries are determined with a torus model.

The MC database for this study consists of the analysis results of 17 long-duration MCs (Marubashi and Lepping, 2007). We compared the MC geometries obtained from the torus and cylinder models with the magnetic field structures in the possible solar source regions of the MCs. We present here our analysis results, with a focus on two events for which the connection between the MC and related solar phenomena can be seen in a straightforward way. Similar connections are also seen for other MC events.

2. Analysis Results

Figure 1 shows the fitting results of the MC encountered on March 4, 1998, with solid lines for the torus model and dotted lines for the cylinder model, superposed on the ob-

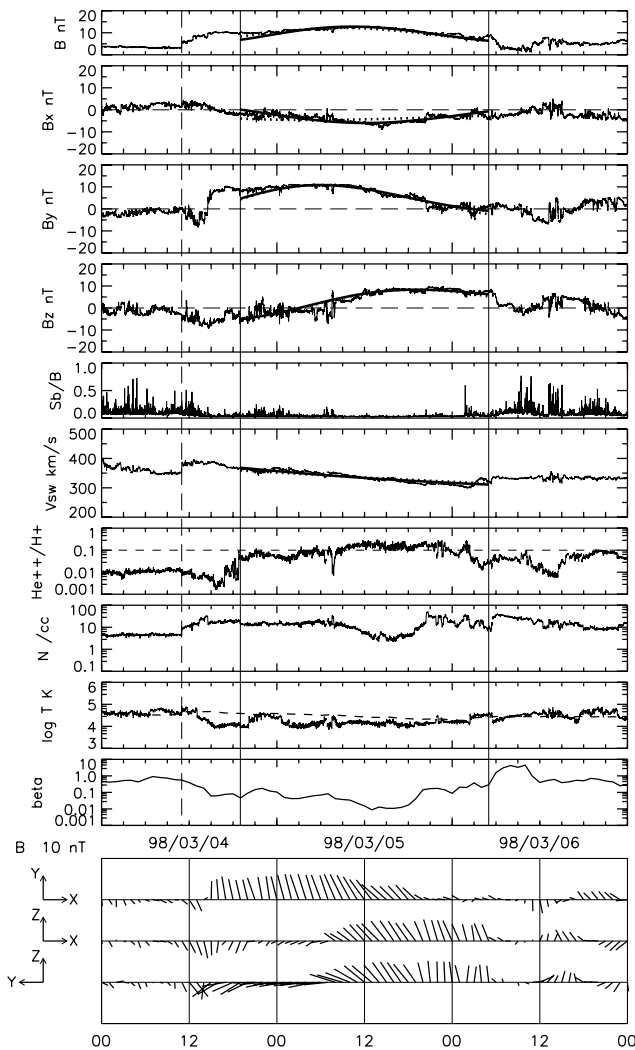


Fig. 1. Results of fitting the torus model (solid curve) and the cylinder model (dotted curve) to the magnetic cloud encountered on March 4, 1998. The bottom three panels show the projected magnetic field vectors onto three planes in GSE coordinates.

served variations of solar wind magnetic fields during a 3-day interval. Plotted from top to bottom are the magnetic field intensity, the X , Y , and Z components in GSE (geocentric solar ecliptic) coordinates, the ratio of standard deviations of high-resolution data to the average intensity, the solar wind speed, the number density ratio of $\text{He}^{++}/\text{H}^+$, the proton number density, the proton temperature, the plasma beta based on protons, and the magnetic field vectors projected on the X - Y , X - Z , and Y - Z planes of GSE coordinates. The dashed curve drawn along with the proton temperature shows the temperature statistically expected from the solar wind speed (Lopez, 1987). Two vertical solid lines indicate the MC boundaries as determined by such characteristics as the magnetic field rotation, the enhanced $\text{He}^{++}/\text{H}^+$ ratio, the relatively small magnetic field fluctuations, and the abnormally low proton temperature (Richardson and Cane, 1993). The vertical dashed line indicates the shock associated with this MC. The observed variations in magnetic field and solar wind speed are well reproduced by both the torus and cylinder models, so that the difference between the two fitted curves can be hardly distinguished in

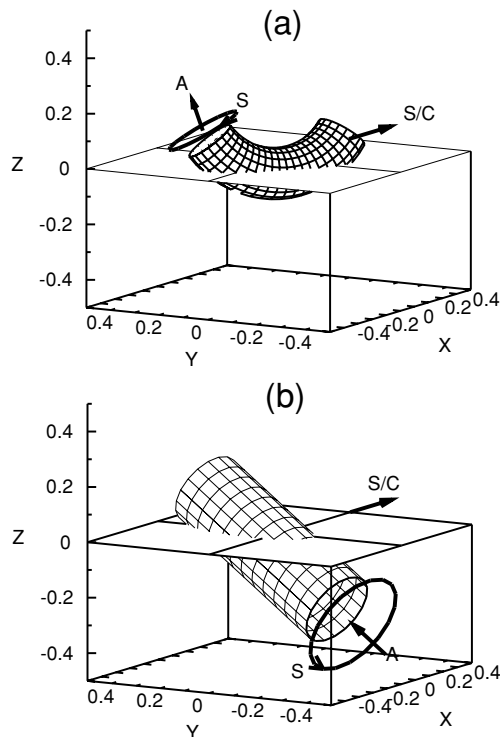


Fig. 2. Two geometries obtained for the magnetic cloud of March 4, 1998, from the fittings to the torus model (a) and to the cylinder model (b). Three directions are indicated: A, axial field; S, toroidal field on the surface; S/C, spacecraft trajectory relative to the magnetic cloud.

this presentation. However, the MC orientations obtained from the two models are substantially different from each other.

Figure 2 depicts the MC geometry obtained from the torus model (Fig. 2(a)) and that from the cylinder model (Fig. 2(b)), in which three arrows indicate the direction of the axial field of MC (A), the direction of magnetic field on the MC surface (S), and the direction of spacecraft trajectory (S/C). We can see that this MC has the left-handed magnetic chirality from the two arrows, A and S. At the location where the spacecraft traversed the MC, the approximate direction of the torus axial field is given by θ (latitude angle) = 17.4° and ϕ (longitudinal angle) = 136.9° , whereas the direction of the cylinder axis is given by $\theta = 29.3^\circ$, and $\phi = 76.7^\circ$ (for details of the fitted values, including other parameters, see Marubashi and Lepping, 2007).

In an attempt to identify the most plausible solar source event of this MC, we searched the LASCO CME catalog (Yashiro *et al.*, 2004; see also the website http://cdaw.gsfc.nasa.gov/CME_list) for candidate CMEs and related solar phenomena within a selected time window. For this purpose, we first estimate the launch time of the CME corresponding to this MC, assuming that the MC propagated at a constant speed. In accordance with three values for the typical speeds, 340 km/s (from the cylinder fitting), 350 km/s (from the torus fitting), and 365 km/s (the maximum speed within the MC), the launch time is estimated to be in the interval from 15:00 UT, February 27 to 01:00 UT, February 28, 1998. Thus, we select a time window from 03:00 UT,

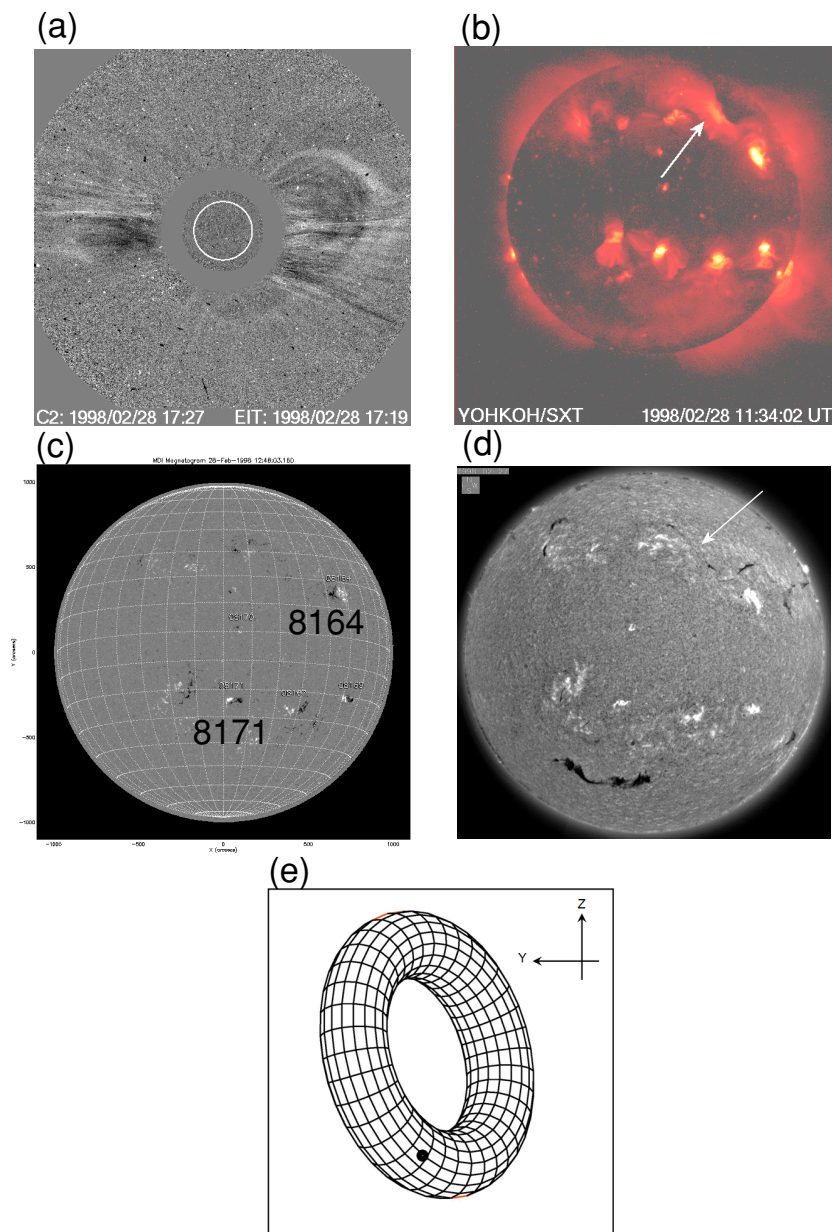


Fig. 3. Solar observations related to the March 4, 1998 MC: (a) LASCO C2 CME running difference image at 17:27 UT, February 28, 1998; (b) Yohkoh/SXT image at 11:34 UT; (c) SOHO/MDI image 12:48 UT, (d) BBSO H α image at 19:15 UT, February 27; (e) the torus MC inclination inferred from a local fit with a torus model.

February 27 to 13:00 UT, February 28, allowing an extra ± 12 h from the estimated launch time for searching the CME corresponding to the MC. The CME catalog shows that there were two CMEs with an angular width larger than 120° in this time window. The first one is a full halo CME which appeared in the LASCO C2 field of view first at 20:07 UT on February 27, 1998, and the second one is a partial halo CME with angular width of 169° that appeared at 12:48 UT on February 28, 1998. Of these two, the latter was identified as a solar source event of the March 4, 1998 MC by Gopalswamy *et al.* (2000, 2001), the speed of which is estimated to be approximately 300 km/s at 20 Rs. We adopt this selection and search for the solar source region of the CME for the purpose of comparing structures between the MC and solar magnetic fields.

Figure 3 shows images of solar observations relevant to

generation of the MC of March 4, 1998 (a: SOHO/LASCO C2 image; b: Yohkoh/SXT, c: SOHO/MDI; d: BBSO H α). The torus shape corresponding to the MC is also shown in Fig. 3(e) for the purpose of indicating the tilting angle of the fitted model. (It should be noted that the actual MC shape is just locally approximated by the torus.) During several hours before this CME (Fig. 2(a)) first appeared in the LASCO C2, we can see two kinds of prominent activities in the Yohkoh/SXT movie. One consists of small activities repeatedly observed in the AR 8171 (approx. 24° S, approx. 1° W), and the other is the formation of a soft X-ray arcade possibly associated with a filament eruption (Figs. 3(b, d)) along the neutral line extending from the north of AR 8164 towards the north-east in the region of weaker magnetic fields (see Figs. 3(c, d)), similar to the arcade formation exemplified by Tripathi *et al.* (2004). Although it is

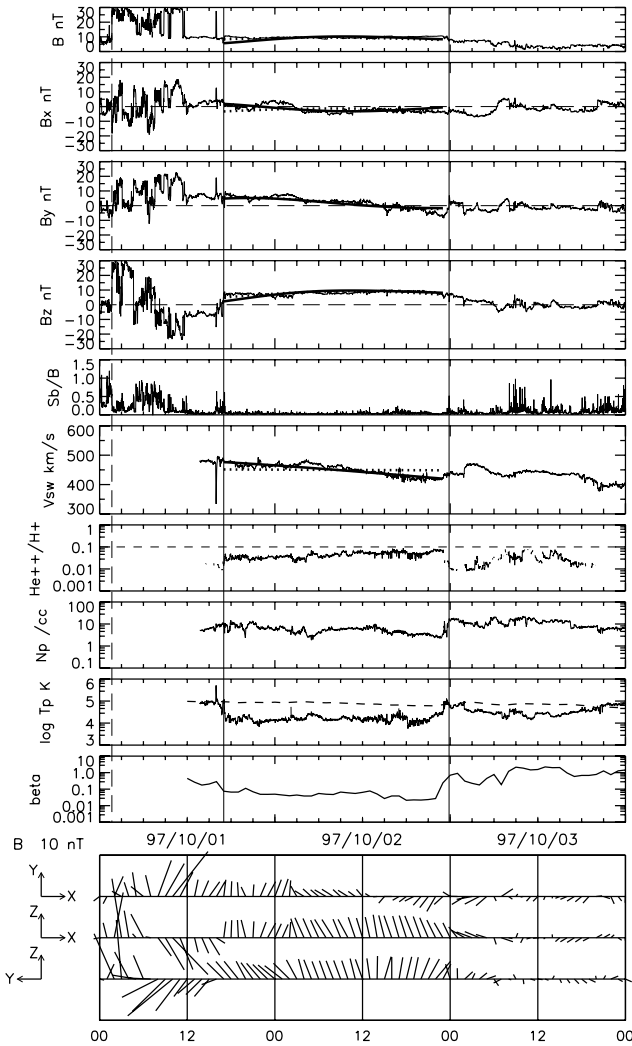


Fig. 4. Results of fitting the torus model (solid curve) and the cylinder model (dotted curve), respectively, to the magnetic cloud encountered on October 1, 1997. The bottom three panels show the projected magnetic field vectors.

difficult to rule out the association between the CME and some small activity in AR 8171, the arcade-formation event seems to be directly connected with the CME in Fig. 3(a). The latter association is more plausible based on several supporting pieces of evidence: (1) the orientation of the MC axis is close to the orientation of the arcade, as is evident by comparing Figs. 3(b, e); (2) the polarity of the magnetic field on the surface of the MC is consistent with the arcade magnetic field, as inferred from the MDI data; (3) the left-handed magnetic field chirality of MC agrees with the chirality of the coronal magnetic field expected from the inverse-S type sigmoid in this region (Rust and Kumar, 1996); (4) The chirality agrees with general tendency that the MCs with left-handed (right-handed) chirality are formed in association with the solar events in the northern (southern) hemisphere (Marubashi, 1986, 1997; Bothmer and Schwenn, 1994; Bothmer and Rust, 1997). Finally, it is possible to suppose from Fig. 3(a) that this CME was launched a little toward south, and that the ACE spacecraft passed the southern end of the MC loop as indicated by the dark dot in Fig. 3(e).

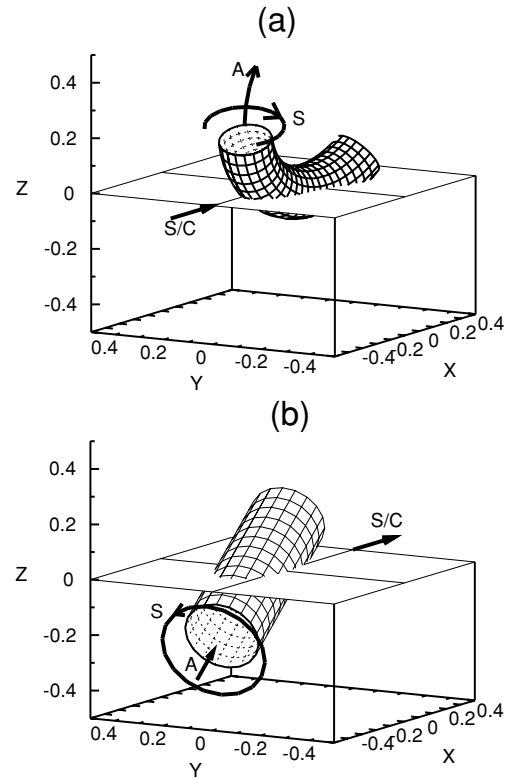


Fig. 5. Two geometries obtained for the magnetic cloud of October 1, 1997, from the fittings to the torus model (a) and to the cylinder model. Three directions are indicated: A, axial field; S, toroidal field on the surface; S/C, spacecraft trajectory relative to the magnetic cloud.

Figures 4 and 5 show the fitting results for another MC which was encountered on October 1, 1997, in the same format as Figs. 1 and 2. Again, both cylinder and torus models having the left-handed chirality reproduce the magnetic field variations agreeing well with the observation. It should be noted here that the torus parameters used here are different from original values presented in Marubashi and Lepping (2007). The orientation of the torus plane determined by the standard fitting method is given by $\theta_n = 35.1^\circ$, and $\phi_n = 65.0^\circ$, the latitude and longitude angles of a vector normal to the torus plane. This torus plane is tilted too much compared with the direction of the post-eruption arcade as will be seen later. Since our purpose is to examine a possibility to obtain the orientation of the MC axis which is close to the orientation of the inversion line of solar magnetic fields, we executed a least-squares method slightly modified from that applied in the previous work. We tried fitting with fixed ϕ_n , using different values around $\phi_n = 65.0^\circ$, and searched the parameter set which can reproduce the observed magnetic fields, and give geometries having the axis orientation as parallel to the inversion line as possible. Thus, we obtain a result shown in Fig. 4 for $\theta_n = 14.6^\circ$, and $\phi_n = 77.5^\circ$. The point is that we can get such an MC geometry by using a torus model.

As for the solar source of this MC, the CME catalog shows that there was only one CME with angular width greater than 120° within the time window from 08:00 UT on September 27 to 14:00 UT on September 28, 1997, that is, the halo CME that appeared in the LASCO C2 field of

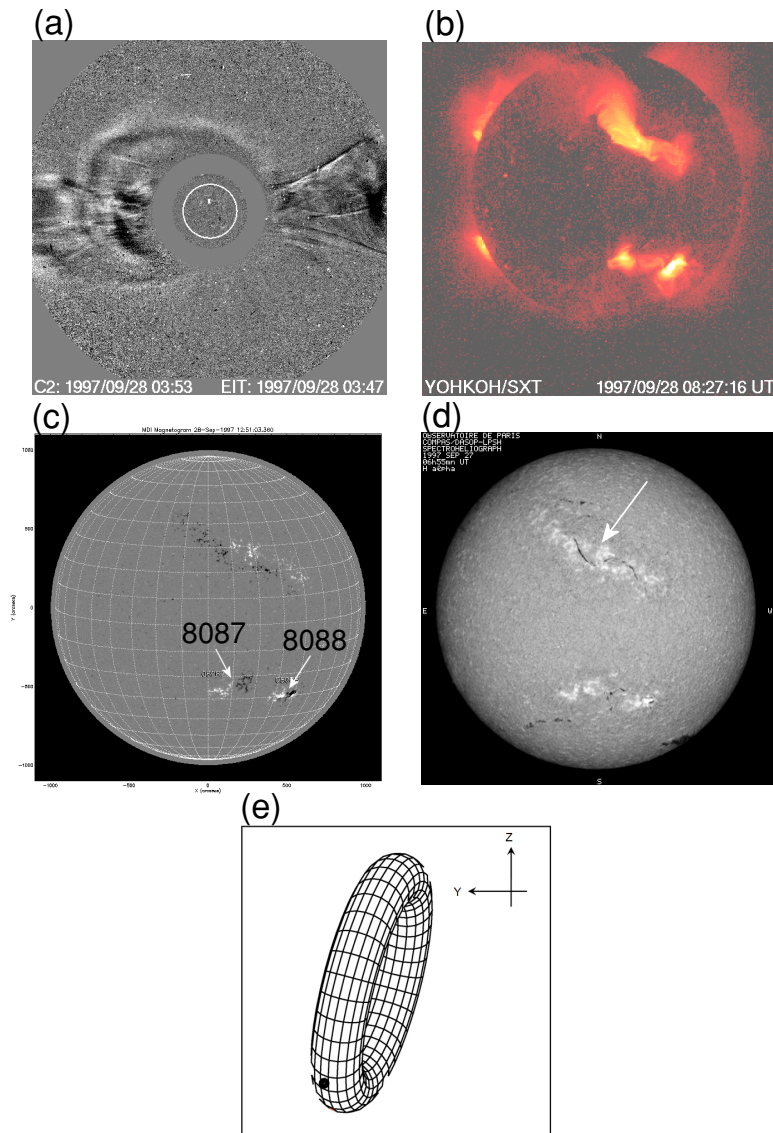


Fig. 6. Solar observations related to the October 1, 1997 MC: (a) LASCO C2 CME running difference image at 03:53 UT, September 28, 1997; (b) Yohkoh/SXT image at 08:27 UT; (c) SOHO/MDI image 12:51 UT, (d) Meudon H α image at 06:55 UT, September 27; (e) the torus MC inclination inferred from a local fit with a torus model.

view at 01:08 UT on September 28, 1997. Though there is a gap in the Yohkoh/SXT data from 22:39 UT September 27 to 08:23 UT September 28, we can see an arcade-formation activity which started around 22:12 UT on September 27 and developed rather slowly near the region surrounding the magnetic inversion line in the northern hemisphere. Gopalswamy *et al.* (2001) identified the solar source of the MC of October 1, 1977 to be this halo CME and associated it with the disappearing filament at 22°N, 05E. Figure 6 presents the images relevant to the generation of the MC, together with the torus tilt obtained from the fitting. Accepting this association, we see that the relationships between this interplanetary MC and the solar magnetic field are very much similar to the case of the March 4, 1998 MC. The MC with left-handed magnetic chirality was formed in association with the filament disappearance in the northern hemisphere, where an inverse-S type sigmoid had been observed. The orientation of the MC axis is nearly parallel to the neutral line or the erupted filament. The CME plasma

was launched slightly southward rather than radially, and hit the Earth with its southern end, as seen in Figs. 5(a) and 6(e).

Thus far we have seen the analysis results for two MC events with special attention being paid to the geometrical relationships between MCs and the magnetic field structures in their possible solar source regions. Here, we briefly summarize results of our analysis of the 17 long-duration MCs. This analysis was carried out for only 12 of these MCs because solar observation data were insufficient for the other five MCs (for reference, we present the same event numbers used in Marubashi and Lepping, 2007; #1, #2, #10, #16, and #17). We were able to find plausible solar source regions in six cases (#4, #5, #7, #12, #13, and #15), and for each of these, the magnetic inversion line on the Sun is consistent with the orientation of the MC axis determined by the torus fitting. We also found a formation of arcade-like structures along the magnetic inversion line within the solar source regions near the time of CME launch. For one

case (#14), no prominent solar activity was seen in the time window estimated by the MC observation. For the remaining five cases, more detailed analyses are needed both on the solar events and on the MC structures, although it is not impossible to find candidates as the solar sources.

3. Conclusions and Discussion

By analyzing the geometries of 12 long-duration MCs and their relationships with their solar origins, we have drawn the following conclusions.

- (1) The arcade formation in the corona is a good indication of the generation of an MC.
- (2) The magnetic field structure of a MC is consistent with the structure of a flux rope loop formed in the coronal region above the arcade, as various CME models commonly predict (see Forbes, 2000, for a review).

The above two findings are consistent with the view that MCs are expanding helical flux ropes formed in association with CME launch (Marubashi, 1997). The more comprehensive relation between the post-eruption arcades and flux rope structures in CMEs has been shown by Cremades and Bothmer (2004) and Tripathi *et al.* (2004).

- (3) Furthermore, for MCs of which the orientations obtained from cylinder fitting mismatch the above relationship, it is possible to obtain an MC orientation which is consistent with the above by using a torus. This suggests that no significant direction change of MCs is needed during the propagation through the interplanetary medium.

It is desirable to extend this study further to other MC events of shorter durations because our study is focused only on the long-duration MCs. Such a study is currently underway, but we can point out that two MCs analyzed by Ishibashi and Marubashi (2004) and Crooker and Webb (2006), respectively, are good examples of where good relationships are obtained using a torus model to explain the alignment between the MC axis and the inversion line of coronal magnetic fields.

Acknowledgments. We gratefully acknowledge the use of data from the WIND SWE instrument, provided by the National Space Science Center at the Goddard Space Flight Center, and ACE MAG and SWEPAM instruments provided by the ACE Science Center (<http://www.srl.caltech.edu/ACE/ASC/>). We also acknowledge the use of solar data from the SOHO LASCO and MDI instruments, YOHKOH SXT instruments, and H α images from Big Bear Solar Observatory and Meudon Observatory. We express our particular thanks to the many researchers involved in making and freeing providing the LASCO CME catalogs. This work was supported by the Development of Korean Space Weather Center, the project of KASI, and the KASI basic research fund.

References

Bothmer, V. and R. Schwenn, Eruptive prominences as sources of magnetic clouds in the solar wind, *Space Sci. Rev.*, **70**, 215–220, 1994.

- Bothmer, V. and D. M. Rust, The field configuration of magnetic clouds and the solar cycle, in *Coronal Mass Ejections, Geophys. Monogr. Ser.*, vol. 99, edited by N. Crooker, J. A. Joselyn, and J. Feynman, 139–146, AGU, Washington, D.C., 1997.
- Burlaga, L. F., Magnetic clouds and force-free fields with constant alpha, *J. Geophys. Res.*, **93**, 7217–7224, 1988.
- Cremades, H. and V. Bothmer, On the three-dimensional configuration of coronal mass ejections, *Astron. Astrophys.*, **422**, 307–322, 2004.
- Crooker, N. U. and D. F. Webb, Remote sensing of the solar site of interchange reconnection associated with the May 1977 magnetic cloud, *J. Geophys. Res.*, **111**, A08108, doi:10.1029/2006JA011649, 2006.
- Forbes, T. G., A review on the genesis of coronal mass ejections, *J. Geophys. Res.*, **105**, 23,153–23,165, 2000.
- Goldstein, H., On the field configuration in magnetic clouds, in *Solar Wind Five*, edited by M. Neugebauer, 731–733, NASA Conf. Publ., CP-2280, 1983.
- Gopalswamy, N., A. Lara, R. P. Lepping, M. L. Kaiser, D. Berdichevsky, and O. C. St. Cyr, Interplanetary acceleration of coronal mass ejections, *Geophys. Res. Lett.*, **27**, 145–148, 2000.
- Gopalswamy, N., A. Lara, M. L. Kaiser, and J.-L. Bougeret, Near-Sun and near-earth manifestations of solar eruptions, *J. Geophys. Res.*, **106**, 25,261–25,277, 2001.
- Ishibashi, H. and K. Marubashi, Structure of interplanetary magnetic cloud on April 16, 1999 and its origin estimated by fitting the torus-shaped flux rope model, *Geophys. Res. Lett.*, **31**, L21807, doi:10.1029/2004GL020702, 2004.
- Lopez, R., Solar cycle invariance in solar wind proton temperature relationships, *J. Geophys. Res.*, **92**, 11,189–11,194, 1987.
- Marubashi, K., Structure of interplanetary magnetic clouds and their solar origins, *Adv. Space Res.*, **6**(6), 335–338, 1986.
- Marubashi, K., Interplanetary magnetic flux rope and solar filaments, in *Coronal Mass Ejections, Geophys. Monogr. Ser.*, vol. 99, edited by N. Crooker, J. A. Joselyn, and J. Feynman, 147–156, AGU, Washington, D.C., 1997.
- Marubashi, K. and R. P. Lepping, Long-duration magnetic clouds: a comparison of analyses using torus- and cylinder-shaped flux rope models, *Ann. Geophys.*, **25**, 2453–2477, 2007.
- Richardson, I. G. and H. V. Cane, Signatures of shock drivers in the solar wind and their dependence on the solar source location, *J. Geophys. Res.*, **98**, 15,295–15,304, 1993.
- Rust, D. M. and A. Kumar, Helical magnetic fields in filaments, *Solar Phys.*, **155**, 69–97, 1996.
- Rust, D. M., B. J. Anderson, M. D. Andrews, M. H. Acuña, C. T. Russell, P. W. Schunk, and T. Mulligan, Comparison of interplanetary disturbances at the NEAR spacecraft with coronal mass ejections at the Sun, *Astrophys. J.*, **621**, 524–536, 2005.
- Tripathi, D., V. Bothmer, and H. Cremades, The basic characteristics of EUV post-eruptive arcades and their role as tracers of coronal mass ejection source regions, *Astron. Astrophys.*, **422**, 337–349, 2004.
- Wang, Y., G. Zhou, P. Ye, S. Wang, and J. Wang, A study of the orientation of interplanetary magnetic clouds and solar filaments, *Astrophys. J.*, **651**, 1245–1255, 2006.
- Yashiro, S., N. Gopalswamy, G. Michalek, O. C. St. Cyr, S. P. Plunkett, N. B. Rich, and R. A. Howard, A catalog of white light coronal mass ejections observed by the SOHO spacecraft, *J. Geophys. Res.*, **109**, A07105, doi:10.1029/2003JA010282, 2004.
- Yurchyshyn, V. B., H. Wang, P. R. Goode, and Y. Deng, Orientation of the magnetic fields in interplanetary flux ropes and solar filaments, *Astrophys. J.*, **563**, 381–388, 2001.
- Yurchyshyn, V., Q. Hu, R. P. Lepping, B. J. Lynch, and J. Krall, Orientations of LASCO halo CMEs and their connection to the flux rope structure of interplanetary CMEs, *Adv. Space Res.*, **40**, doi:10.1016/j.asr.2007.01.059, 2007.

K. Marubashi (e-mail: kmaru@kasi.re.kr), S.-K. Sung, K.-S. Cho, and R. P. Lepping

Halo coronal mass ejections and geomagnetic storms

Nat Gopalswamy

NASA Goddard Space Flight Center, Greenbelt, Maryland, U.S.A.

(Received June 21, 2008; Revised October 27, 2008; Accepted October 27, 2008; Online published May 29, 2009)

In this letter, I show that the discrepancies in the geoeffectiveness of halo coronal mass ejections (CMEs) reported in the literature arise due to the varied definitions of halo CMEs used by different authors. In particular, I show that the low geoeffectiveness rate is a direct consequence of including partial halo CMEs. The geoeffectiveness of partial halo CMEs is lower because they are of low speed and likely to make a glancing impact on Earth.

Key words: Coronal mass ejections, geomagnetic storms, geoeffectiveness, halo CMEs.

1. Introduction

Coronal mass ejections (CMEs) that appear to surround the occulting disk of the observing coronagraphs in sky-plane projection are known as halo CMEs (Howard *et al.*, 1982). Halo CMEs are fast and wide on the average and are associated with flares of greater X-ray importance because only energetic CMEs expand rapidly to appear above the occulting disk early in the event (Gopalswamy *et al.*, 2007). Extensive observations from the Solar and Heliospheric Observatory (SOHO) mission's Large Angle and Spectrometric Coronagraphs (LASCO) have shown that full halos constitute $\sim 3.6\%$ of all CMEs, while CMEs with width $\geq 120^\circ$ account for $\sim 11\%$ (Gopalswamy, 2004). Full halos have an apparent width (W) of 360° , while partial halos have $120^\circ \leq W < 360^\circ$. Halo CMEs are said to be front-sided if the site of eruption (also known as the solar source) can be identified on the visible disk usually identified as the location of H-alpha flares or filament eruptions. Details on how to identify the solar sources can be found in Gopalswamy *et al.* (2007). Halos with their sources within $\pm 45^\circ$ of the central meridian are known as disk halos, while those with a central meridian distance (CMD) beyond $\pm 45^\circ$ but not beyond $\pm 90^\circ$ are known as limb halos. Disk halos are likely to arrive at Earth and cause geomagnetic storms, while limb halos only impact Earth with their flanks and hence are less geoeffective (see Gopalswamy *et al.*, 2007).

Since CMEs propagate approximately radially from the Sun (except for a small eastward deflection due to solar rotation—see Gosling *et al.*, 1987), disk halos are likely hit Earth. Of course, the interplanetary counterpart of CMEs (ICMEs) must contain southward magnetic field component (B_s) to be geoeffective. It is well known that the intensity of the resulting magnetic storm depends on the magnitude of B_s and the speed V with which the CME impacts Earth's magnetosphere (see e.g., Gonzalez *et al.*, 1994; Tsurutani and Gonzalez, 1997). Halo CMEs are more energetic (av-

erage speed is ~ 1000 km/s compared to ~ 470 km/s for ordinary CMEs), so the V part is expected to be high. When CMEs are aimed directly at Earth, the ICMEs are likely to arrive at Earth as magnetic clouds (MCs), which are a subset of ICMEs that have flux rope structure. Since Earth passes through the nose of the MC, the chance of encountering B_s somewhere within the MC is high (except for unipolar MCs with north-pointing axis—see Yurchyshyn *et al.*, 2001). When the ICME is shock-driving, the sheath portion lying between the shock and the MC may also play a significant role in producing geomagnetic storms (see e.g., Gosling *et al.*, 1990). The sheath may have intervals of north and south-pointing magnetic fields, in addition to the varying field orientation in the MC portion. An Earth-directed halo CME leads to a situation whereby Earth passes through the nose of the shock, where the sheath field is most intense and may cause intense magnetic storm if south-pointing. Thus the ability of a halo CME in producing a geomagnetic storm depends on the structure of its interplanetary counterpart (the ICME event).

Since halos became common place in the SOHO era, there have been several attempts to characterize their geoeffectiveness (see e.g., Zhao and Webb, 2003; Yermolaev and Yermolaev, 2003; Kim *et al.*, 2005; Yermolaev *et al.*, 2005; Gopalswamy *et al.*, 2007). Using CMEs from the rise phase of solar cycle 23, St. Cyr *et al.* (2000) concluded that $\sim 75\%$ of the frontside CMEs are geoeffective. In most of the works discussed here, the geoeffectiveness is defined as the ability of a CME or an interplanetary structure to cause geomagnetic storms with intensity (D_{st}) ≤ -50 nT. While most of the intense storms are caused by CMEs, moderate storms (-100 nT $< D_{st} < -50$ nT) may also be caused by other structures such as corotating interaction regions. Zhao and Webb (2003) found an overall geoeffectiveness rate of $\sim 64\%$ for frontside halos detected up to the solar maximum in 2000. Yermolaev and Yermolaev (2003) used data from the period 1976–2000 and came up with a lower rate of 40–50%. Michalek *et al.* (2006) found that $\sim 56\%$ of frontside halos are geoeffective, but they did not use all the halos because of limitations in the method of obtaining

space speeds. Kim *et al.* (2005) reported that only about 40% of the frontside halos are geoeffective. Yermolaev *et al.* (2005) compiled published results and noted that the geoeffectiveness rate varied from <40% to >80%. Recently Gopalswamy *et al.* (2007) analyzed 378 halo CMEs covering almost whole of solar cycle 23 and found that ~71% of frontside halos are geoeffective. Zhao and Webb (2003) and Gopalswamy *et al.* (2007) used the same definition of halo CMEs ($W = 360^\circ$) and obtained similar geoeffectiveness rates. On the other hand, Kim *et al.* (2005) and Yermolaev and Yermolaev (2003) defined their halos as CMEs with $W \geq 120^\circ$ and obtained the lower geoeffectiveness rate. The purpose of this letter is to show that the discrepancy in the rate of geoeffectiveness can simply be explained by the different definition of halo CMEs used by these authors. We take Kim *et al.* (2005) and Gopalswamy *et al.* (2007) representing the low and high geoeffectiveness rates, respectively. Both these works have published their list of events and the study periods have maximum overlap. They also use data from the same instrument (SOHO/LASCO), so the comparison is straightforward. Finally, both works use the same definition of geoeffectiveness: the ability of a CME to produce a geomagnetic storm with $D_{st} \leq -50$ nT.

2. Geoeffectiveness of Partial Halo CMEs

Kim *et al.* (2005) investigated 305 CMEs (1997 to 2003) that included full ($W = 360^\circ$) and partial halos ($120^\circ < W < 360^\circ$) and found that 121 of them were geoeffective. On the other hand Gopalswamy *et al.* (2007) studied 378 full halos for the period 1996 to 2005. For making a proper comparison, we first separate the full and partial halos in Kim *et al.* (2005). We then use the geoeffectiveness of a subset of full halos from Gopalswamy *et al.* (2007) corresponding to the Kim *et al.* (2005) study period to estimate the geoeffectiveness of partial halo CMEs.

Among the 378 full halos reported by Gopalswamy *et al.* (2007), 168 occurred during the period 1997 to 2003 (the study period of Kim *et al.*, 2005). Many geomagnetic storms during the study period had multiple CME association, so we eliminate 68 such CMEs in estimating the geoeffectiveness rate. Sixty five of the remaining 100 frontside full halos (65%) were geoeffective. Note that this rate is close to the one obtained by Zhao and Webb (2003). Excluding the full halos from the CMEs in Kim *et al.* (2005), we get 205 partial halos (305 minus 100), out of which 56 (121 minus 65) were geoeffective. Thus we get a geoeffectiveness rate of 27% (56 out of 205) for the partial halos alone. The 40% geoeffectiveness rate obtained by Kim *et al.* (2005) is thus a consequence of combining highly geoeffective (65%) full halos and marginally geoeffective (27%) partial halos.

Note that we used the CME data for the period 1997–2003 in the above calculation. To extend this result to the whole study period (1996–2005) considered by Gopalswamy *et al.* (2007), we need to estimate the fraction of partial halos that are geoeffective. Since Gopalswamy *et al.* (2007) did not include partial halos in their study, we estimate the geoeffectiveness of partial halos by extrapolation. To do this, we make use of the fact that 3.5% of

all CMEs are full halos, while 11% are full + partial halos (Gopalswamy, 2004). Assuming that these fractions apply equally well to the front and backside CMEs and recalling that 229 full halos were front-sided, one can estimate the frontside wide CMEs as $(11\%/3.5\%) \times 229 = 720$. Therefore, $720 - 229 = 491$ is the likely number of partial halos. At the 27% geoeffectiveness rate estimated above, 134 of the 491 partial halos are expected to be geoeffective. Therefore, out of the 720 wide CMEs, 163 full halos and 134 partial halos (total of 297 or 41%) are geoeffective. This is virtually the same as the 40% rate obtained by Kim *et al.* (2005) and confirms that inclusion of partial halos lowers the overall geoeffectiveness rate. Note that the geoeffectiveness of halos varies with the phase of the solar cycle (see Gopalswamy *et al.*, 2007, figure 8; Zhao and Webb, 2003) and the way multiple halos associated with a given storm are treated. We estimate that these effects can account for an additional 10% variation.

2.1 Why are partial halos less geoeffective?

In studying the geoeffectiveness of CMEs as a function of source latitude, Gopalswamy *et al.* (2007) found that the strongly geoeffective ($D_{st} \leq -100$ nT) and moderately geoeffective ($-50 \geq D_{st} > -100$ nT) CMEs have average longitudes of W10 and E03, respectively. The non-geoeffective CMEs have an average longitude similar to the moderately geoeffective CMEs (E02). Furthermore, the fraction of limb halos steadily increases from 17% for strongly-geoeffective, to 31% for moderately geoeffective, and 37% for non-geoeffective CMEs. The average speeds also decrease in the same order (see figure 9 of Gopalswamy *et al.*, 2007). From these observations, Gopalswamy *et al.* (2007) concluded that non-geoeffective CMEs are relatively slower, originate predominantly from the eastern hemisphere, and have a greater central meridian distance. Partial halos generally have properties similar to the moderately geoeffective and non-geoeffective halos. Thus partial halos are less energetic and do not expand enough to fully surround the occulting disk within the LASCO field of view.

Gopalswamy *et al.* (2007) also reported that the geoeffectiveness rates of limb and disk halos as 60% and 75%, respectively. The geoeffectiveness of partial halos originating closer to the limb is expected to be even lower because they are slower and less likely to impact Earth. Thus, inclusion of partial halos reduces the overall geoeffectiveness rate of halo CMEs and hence correctly explains the lower geoeffectiveness rates reported in the literature.

3. Discussion and Conclusions

One of the important aspects of CME geoeffectiveness studies is to identify the solar source of CMEs. One might argue that the geoeffectiveness may be overestimated when front-sided CMEs are mistakenly classified as back-sided CMEs. This can happen only when front-sided halos have no disk signature. There may also be cases in which a fortuitous disk activity coincides with a backside CME and hence a backside CME gets classified as a frontside CME. Sometimes, one observes a full halo, which may be a combination of multiple CMEs occurring at different position angles. Such occurrences are generally rare and cannot ac-

count for the large discrepancies in the reported geoeffectiveness rate.

To clarify the identification of solar sources of halo CMEs, let us consider the association between CMEs and soft X-ray flares, one of the obvious indicators of disk activity. Whenever the eruption occurs on the frontside (CMD in the range 0 to 90°), we observe a soft X-ray flare. The halo CME appears asymmetric when the solar source has a larger CMD, typically beyond 45°. When the eruption is behind the limb, but not too far behind, we usually observe some EUV dimming above the concerned limb, but no soft X-ray flare is observed because the flare gets occulted by the solar limb. When a flare is partially occulted by a limb, the soft X-ray light curve tends to be very gradual and we observe the CME above the occulting limb. The extreme case is a backside CME whose associated flare is completely occulted, and we see no disk activity. In some of these cases one can see EUV dimming around most part of the solar disk, indicating a backside eruption. This kind of relationship between the soft X-ray flare and CMEs can be easily seen by tracking a large active region (AR) during its disk passage and eventual disappearance behind the west limb (e.g., AR 10486 reported in Gopalswamy *et al.*, 2005).

When one starts from geomagnetic storms and relate them to CMEs near the Sun, occasionally it becomes difficult to identify the CME. Zhang *et al.* (2007) were not able to identify wide CMEs or their solar sources for ~10% of large geomagnetic storms. Zhang *et al.* (2007) started with large geomagnetic storms and searched for CMEs and their solar sources. The solar and geomagnetic events were separated by more than a day to a few days. On the other hand, Gopalswamy *et al.* (2007) started with halo CMEs and identified their solar sources. Observations of the halo CME and the associated disk signature are nearly simultaneous. Halo CMEs are more energetic (see figure 4 of Gopalswamy *et al.*, 2007), so there is usually a prompt (and strong) disk signature if the halo is frontside. Thus, the solar source identification for geomagnetic storms and that for halo CMEs do not have the same level of difficulty. Furthermore, geomagnetic storms can also be caused by non-halo CMEs. If a CME originates close to the disk center and arrives at Earth with a southward magnetic field component, it will cause a geomagnetic storm. It is known that some magnetic clouds, which are interplanetary CMEs (ICMEs) with flux rope structure, are associated with non-halo CMEs. A recent statistical study (Gopalswamy *et al.*, 2008) finds that only ~63% of magnetic clouds are associated with full halos. The fraction increases to ~86% when full and partial halos are combined. The remaining 14% of magnetic clouds are associated with non-halo CMEs originating from close to the disk center. Since magnetic clouds constitute the most geoeffective subset of ICMEs, one expects that some magnetic clouds associated with non-halo CMEs are also geoeffective.

In conclusion, we confirm that the lower rate of geoeffectiveness obtained by some authors is due to the inclusion of partial halos. The reported variation in geoeffectiveness

rates can be readily explained by the different definition of halo CMEs used by different authors. Partial halos are less energetic and generally originate far from the disk center, so most of them behave similar to the nongeoeffective CMEs.

Acknowledgments. Work supported by NASA's LWS and TR&T programs.

References

- Gonzalez, W. D., J. A. Joselyn, Y. Kamide, H. W. Kroehl, G. Rostoker, B. T. Tsurutani, and V. M. Vasylunas, What is a geomagnetic storm?, *J. Geophys. Res.*, **99**, 5771, 1994.
- Gopalswamy, N., A global picture of CMEs in the inner heliosphere, in *The Sun and the Heliosphere as an Integrated System*, edited by G. Poletto and S. T. Suess, chap. 8, p. 201, Kluwer Acad., Boston, 2004.
- Gopalswamy, N., S. Yashiro, Y. Liu, G. Michalek, A. Vourlidas, M. L. Kaiser, and R. A. Howard, Coronal mass ejections and other extreme characteristics of the 2003 October–November solar eruptions, *J. Geophys. Res.*, **110**, A09S15, doi:10.1029/2004JA010958, 2005.
- Gopalswamy, N., S. Yashiro, and S. Akiyama, Geoeffectiveness of halo coronal mass ejections, *J. Geophys. Res.*, **112**, A06112, doi:10.1029/2006JA012149, 2007.
- Gopalswamy, N., S. Akiyama, S. Yashiro, G. Michalek, and R. P. Lepping, Solar sources and geospace consequences of interplanetary magnetic clouds observed during solar cycle 23, *J. Atm. Sol. Terr. Phys.*, **70**, 245, doi:10.1016/j.jastp.2007.08.070, 2008.
- Gosling, J. T., M. F. Thomsen, S. J. Bame, and R. D. Zwickl, The eastward deflection of fast coronal mass ejecta in interplanetary space, *J. Geophys. Res.*, **92**, 12399, 1987.
- Gosling, J. T., D. J. McComas, J. L. Phillips, and S. J. Bame, Coronal mass ejections and large geomagnetic storms, *Geophys. Res. Lett.*, **17**, 901, 1990.
- Howard, R. A., D. J. Michels, N. R. Sheeley, Jr., and M. J. Koomen, The observation of a coronal transient directed at earth, *Astrophys. J.*, **263**, L101, 1982.
- Kim, R.-S., K.-S. Cho, Y.-J. Moon, Y.-H. Kim, Y. Yi, M. Dryer, S.-C. Bong, and Y.-D. Park, Forecast evaluation of the coronal mass ejection (CME) geoeffectiveness using halo CMEs from 1997 to 2003, *J. Geophys. Res.*, **110**, A11104, doi:10.1029/2005JA011218, 2005.
- Michalek, G., N. Gopalswamy, A. Lara, and S. Yashiro, Properties and geoeffectiveness of halo CMEs, *Space Weather*, **4**, S10003, doi:10.1029/2005SW000218, 2006.
- St. Cyr, O. C. *et al.*, Properties of coronal mass ejections: SOHO LASCO observations from January 1996 to June 1998, *J. Geophys. Res.*, **105**, 18,169, 2000.
- Tsurutani, B. T. and W. D. Gonzalez, The interplanetary causes of magnetic storms: A review, in *Magnetic Storms*, edited by B. T. Tsurutani, W. D. Gonzalez, Y. Kamide, and J. K. Arballo, p. 77, AGU Monograph 98, AGU, Washington DC, 1997.
- Yermolaev, Yu. I. and M. Yu. Yermolaev, Statistical relationships between solar, interplanetary, and geomagnetic disturbances, 1976–2000: 3, *Cosmic Res.*, **41**, 539, 2003.
- Yermolaev, Yu. I., M. Yu. Yermolaev, G. N. Zastenker, L. M. Zelenyi, A. A. Petrukovich, and J.-A. Sauvaud, Statistical studies of geomagnetic storm dependencies on solar and interplanetary events: a review, *Planet. Space Sci.*, **53**(1–3), 189–196, 2005.
- Yurchyshyn, V. B., H. Wang, P. R. Goode, and Y. Deng, Orientation of the magnetic fields in interplanetary flux ropes and solar filaments, *Astrophys. J.*, **563**, 381, 2001.
- Zhang, J. *et al.*, Solar and interplanetary sources of major geomagnetic storms (Dst < -100 nT) during 1996–2005, *J. Geophys. Res.*, **112**, A10102, doi:10.1029/2007JA012321, 2007.
- Zhao, X. P. and D. F. Webb, Source regions and storm effectiveness of frontside full halo coronal mass ejections, *J. Geophys. Res.*, **108**(A6), 1234, doi:10.1029/2002JA009606, 2003.

Numerical simulations of the solar corona and Coronal Mass Ejections

Stefaan Poedts, Carla Jacobs, Bart van der Holst, Emmanuel Chané, and Rony Keppens

Centrum voor Plasma-Astrofysica, Katholieke Universiteit Leuven, Belgium

(Received October 31, 2007; Revised January 30, 2008; Accepted August 24, 2008; Online published May 29, 2009)

Numerical simulations of Coronal Mass Ejections (CMEs) can provide a deeper insight in the structure and propagation of these impressive solar events. In this work, we present our latest results of numerical simulations of the initial evolution of a fast CME. For this purpose, the equations of ideal MagnetoHydroDynamics (MHD) have been solved on a three-dimensional (3D) mesh by means of an explicit, finite volume solver, where the simulation domain ranges from the lower solar corona up to $30R_{\odot}$. In order to simulate the propagation of a CME throughout the heliosphere, a magnetic flux rope is superposed on top of a stationary background solar (MHD) wind with extra density added to the flux rope. The flux rope is launched by giving it an extra initial velocity in order to get a fast CME forming a 3D shock wave. The magnetic field inside the initial flux rope is described in terms of Bessel functions and possesses a high amount of twist.

Key words: Magnetohydrodynamics, numerical, coronal mass ejections.

1. Introduction

It is generally accepted that coronal mass ejections (CMEs) originate from the so-called ‘closed’ magnetic regions on the Sun, consisting of thousands of magnetic loops. Such ‘closed’ magnetic fields can be found in active regions, filaments, and transequatorial interconnection regions. The latter regions are most likely to appear during solar minimum, when the active regions are located, on average, much closer to the equator. Cremades and Bothmer (2004) studied 124 structured CME events and analysed the relation between the source region characteristics at the solar surface and the morphology of the corresponding CME observed with LASCO. They concluded that structured CMEs can be interpreted as three-dimensional magnetic field entities that arise in a self-similar manner from pre-existing small-scale loop systems. Jing *et al.* (2004) made a statistical study of more than 100 filament eruptions and found that 56% of the investigated events corresponded with a CME. Gilbert *et al.* (2000) performed also a statistical study of prominence activity and developed definitions of active and eruptive prominences. These authors came to the conclusion that eruptive prominences are more strongly associated to CMEs (viz. 94% of the investigated events) than active prominences (only 46%), and that probably all CMEs associated with eruptive prominences possess the three-part front-cavity-core structure. In general, filaments are believed to form in magnetic fields of the shape of sheared arcades and that the prominence material is suspended in the corona by concave upward magnetic fields, possibly possessing some twisted topology (e.g. Kippenhahn and Schlüter, 1957; Kuperus and Raadu, 1974; Manchester, 2001; Karpen *et al.*, 2001; Low and Zhang,

2004).

Axisymmetric (2.5D) MHD models can be used to numerically simulate CME propagation (e.g. Wu *et al.*, 1999). Chané *et al.* (2006) demonstrated that 2.5D simulations with a simple CME model, consisting of a high-density plasma blob including a magnetic flux rope, can predict the flow variables at 1 AU for a specific CME event reasonably well. Remark that Jacobs *et al.* (2007) made a detailed comparison of these 2.5D simulation results to a similar 3D simulation and showed that the 2.5D simulation yields acceptable results provided the momentum of the initial CME is chosen in a proper way. However, it is straightforward to see that the effect of the CME depends on the angular position of the observer and that the assumption of axial symmetry poses severe restrictions to the possible magnetic field configuration in the magnetic cloud. In the present paper, the three-dimensional (3D) extension of this 2.5D model is presented. The strategy followed for simulating a CME event is the same as in Chané *et al.* (2006), but in stead of launching a spherical plasma blob, a more advanced magnetic flux rope model, with an enhanced density, is flung into the interplanetary medium by giving it an initial velocity profile. The initial magnetic configuration in the flux rope is a modification of the Lundquist equilibrium for constant α force-free fields in cylinder geometry and will be presented in the next section.

2. Simulation Set-up

The ideal MHD equations have been solved in spherical coordinates (r, θ, φ) on a three-dimensional spherical mesh, covering a complete sphere, i.e. $\theta \in [0, \pi]$ and $\varphi \in [0, 2\pi]$. The magnetic field is kept divergence-free by using the vector potential on the nodal points. The computational domain covers the region between the lower corona and $30R_{\odot}$, using a grid resolution of $324 \times 95 \times 184$ cells, including two ghost cells at each boundary. The grid shows

an accumulation of cells both towards the solar surface and towards the solar equator, where the grid size varies from $\Delta r = 0.02R_\odot$ near the solar surface to $\Delta r = 0.25R_\odot$ at the outer boundary and from $\Delta\theta = 4^\circ$ near the poles to $\Delta\theta = 0.8^\circ$ at the equator. The grid was taken to be equidistant in the azimuthal direction. The simulation was executed on the VIC-cluster of the K.U.Leuven. To reach a time of $t = 10$ h in the code, 35 382 iterations were needed. The run was finalised in about 21.5 h by using 120 processors simultaneously.

In order to construct a background solar wind model, the full set of (ideal) MHD equations has been solved in a co-rotating frame along with an extra added gravitational force as well as an additional heating/cooling source term, very similar to the term that was used by Groth *et al.* (2000). This wind model shows no dependence on the azimuthal direction and provides a good approximation for the roughly axisymmetric wind occurring at solar minimum.

Romashets and Vandas (2003) present an expression for the magnetic field in toroidal geometry, reading:

$$B_{r'} = B_0 \frac{R_0 - 2r' \cos \theta'}{2\alpha R_0 (R_0 + r' \cos \theta')} J_0(\alpha r') \sin \theta', \quad (1)$$

$$B_{\phi'} = B_0 \left(1 - \frac{r'}{2R_0} \cos \theta'\right) J_0(\alpha r'), \quad (2)$$

$$B_{\theta'} = B_0 \frac{R_0 - 2r' \cos \theta'}{2\alpha R_0 (R_0 + r' \cos \theta')} J_0(\alpha r') \cos \theta' - B_0 \left(1 - \frac{r'}{2R_0} \cos \theta'\right) J_1(\alpha r'), \quad (3)$$

where (r', ϕ', θ') represent the toroidally curved cylindrical coordinates, J_0 and J_1 are Bessel functions of the first kind (of order 0 and 1, respectively), and R_0 denotes the major axis of the torus. The minor axis is indicated by $r' = r_0$ and the constant α is determined by $J_0(\alpha r_0) = 0$. In this way, the magnetic field lines are confined within the torus. This solution for the magnetic field satisfies the solenoidal constraint and approximates the force-free condition in the limit of a large aspect ratio, i.e. in the limit $R_0/r_0 \gg 1$. Next, the Romashets and Vandas solution is subjected to the transformation $r \rightarrow r - a$ (Gibson and Low, 1998), stretching space inward, towards the origin. The transformation deforms the shape of the original flux rope, resembling an already rising prominence. The stretch factor a is set to a value of $0.3R_\odot$ and the top of the flux rope is at a height of $0.7R_\odot$ above the solar surface. The transformed flux rope solution is then superposed on top of the stationary background wind model discussed above. To keep the analogy with previous work (e.g. Jacobs *et al.*, 2005; Chané *et al.*, 2006) some extra density and velocity is added to the flux rope. The additional density and velocity profiles are both dependent on the toroidal coordinates r' and ϕ' . In doing so, we have control over the added amount of mass, energy, and momentum, and as such over the propagation of the CME.

Prominences are always observed above photospheric regions where the magnetic field changes sign. Since in the applied (axisymmetric) background coronal model for solar minimum the only polarity inversion line coincides with the equator, the flux rope solution is placed above the so-

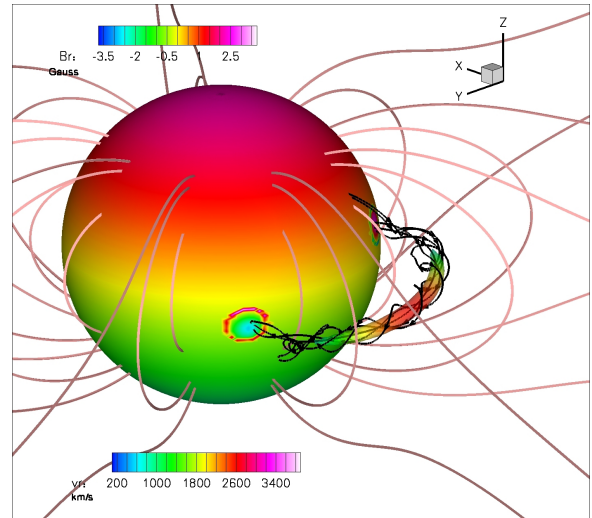


Fig. 1. Initial magnetic field configuration. The solar surface is coloured with the radial magnetic field strength. Inside the flux rope the isosurface of $\rho = 2\rho_*$ is plotted, with ρ_* the surface density. The isosurface is coloured with the radial velocity.

lar equator in the present simulation. From observations it is known that filaments lie in a highly sheared fashion over the inversion line, making an angle of $\sim 20^\circ$ (Leroy *et al.*, 1984). Also according to Leroy *et al.* (1984), most quiescent prominences are of inverse polarity. The initial configuration of the flux rope was taken such that the observational constraints were satisfied. The magnetic field strength in a quiescent prominence is typically between 5 and 40 Gauss. In the model, the value for the toroidal field in the centre of the flux rope was set to $B_0 = 1.44$ Gauss. This is lower than what is observed, but remember that the initial condition represents a prominence that is already erupting. The maximum velocity inside the flux rope was set to $v_{\text{cme}} = 4000$ km s $^{-1}$ and the total amount of mass added equals 4×10^{15} g. A visualisation of the initial state is shown in Fig. 1.

3. Results

Figure 2 shows contours of the radial velocity at $t = 15$ min after the onset of the CME event. The initially highly twisted magnetic field in the flux rope reconnects with the overlying magnetic field, but the magnetic field lines in the CME remain connected to the solar surface.

Figure 3 illustrates the longitudinal variation in the density and the velocity. This plot shows the density and radial velocity in the cross-section of three meridional planes and the equatorial plane. The three meridional planes are located at a constant azimuthal position of $\phi = 150^\circ$, $\phi = 165^\circ$, and $\phi = 180^\circ$. The velocity and density profile in the original undisturbed background solar wind are indicated on the plots with a dashed line. From these plots it is clear that a strong shock is propagating ahead of the CME. Since the CME is launched along the negative X -axis, the part of the CME in the plane $\phi = 180^\circ$ moves the fastest.

Gopalswamy *et al.* (2005) studied the arrival times of several historical fast events and these authors argue that

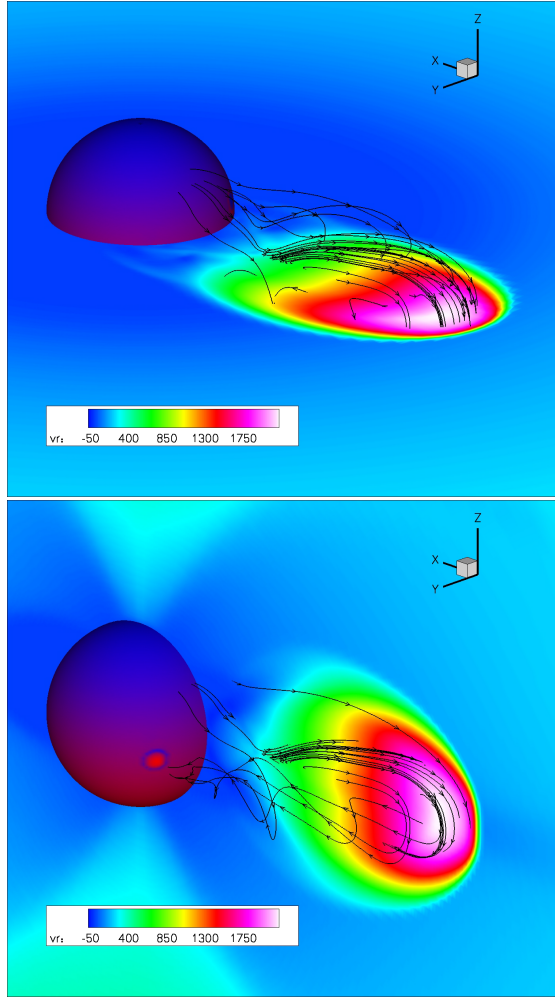


Fig. 2. Snapshot at $t = 15$ min showing the radial velocity contours (colour) and the magnetic field lines (black). The solar surface is coloured with the radial magnetic field strength. Top: velocity contours in the equatorial plane; bottom: velocity contours in the xz -plane.

the maximum initial speed of a CME may not be much higher than $\sim 3000 \text{ km s}^{-1}$. In the present simulation, the plasma blob was given an initial speed in order to mimic the eruption. Since no initiation mechanism was considered, also the mechanism for accelerating CMEs is not captured well in this simulation and the plasma cloud will experience a strong deceleration in the initial phase of the simulation. Therefore, the v_{cme} parameter is set to a quite high velocity of 4000 km s^{-1} . However, remark that this high velocity is only reached in one single point of the flux rope and the average amount of extra velocity added corresponds to a value of only $\sim 600 \text{ km s}^{-1}$. The deceleration of the CME is made clear in Fig. 4, where the position of the CME front in the equatorial plane is plotted versus time. The figure shows the height-time plots for the CME front in the three meridional planes discussed above. The plot shows also the height-time profile for the centre of mass, being defined as

$$\mathbf{r}_{\text{CRM}} = \frac{\int_V \mathbf{r} \bar{\rho}(\mathbf{r}) d^3 \mathbf{r}}{\int_V \bar{\rho}(\mathbf{r}) d^3 \mathbf{r}}.$$

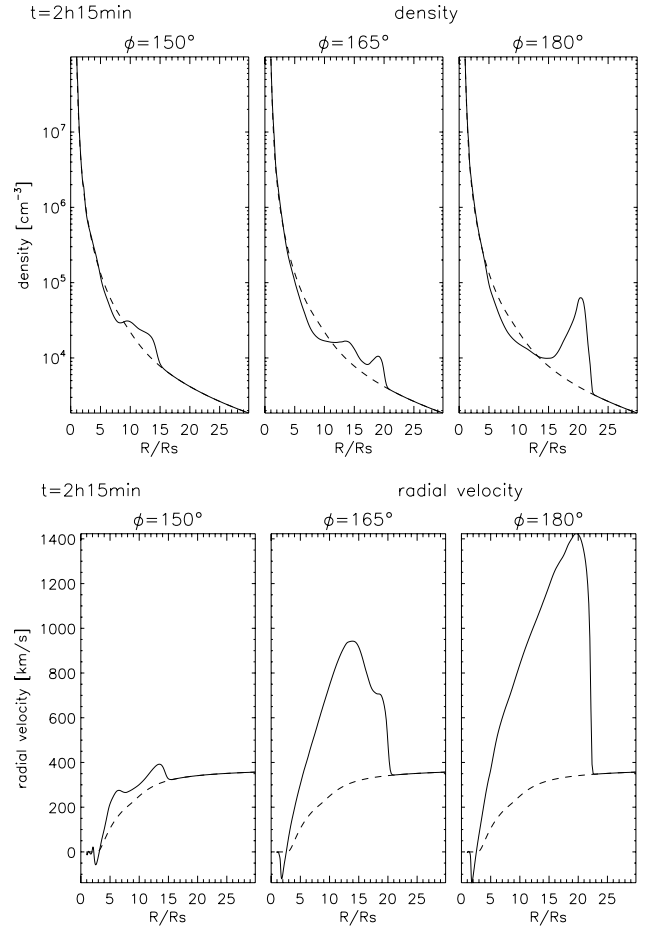


Fig. 3. Cut along the equator of the radial velocity (top) and the density (bottom) at three azimuthal positions, 2 h 15 min after the launch of the CME. The dashed line indicates the steady state wind value.

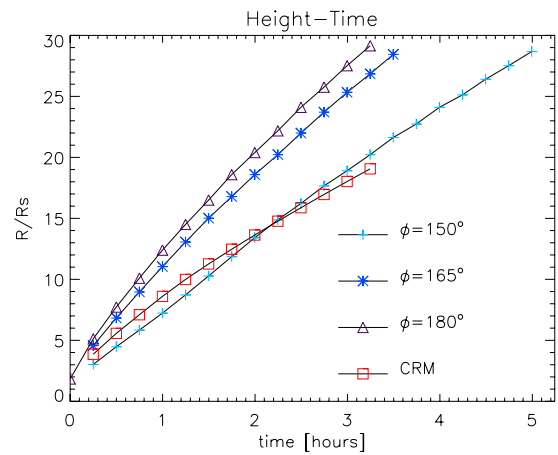


Fig. 4. Height-time curves for the position of the CME front along the equator in three meridional planes and for the centre of relative mass (CRM).

The centre of mass is calculated by using the relative density $\bar{\rho}$, which is a measure for the excess or depletion of the density with respect to the background solar wind density. Since a CME is defined as an outward motion of a new, discrete, bright, white light feature in the coronagraph field of view, only those locations with an enhancement in density

Table 1. Average velocity and acceleration of the CME front and of the centre of relative mass (CRM).

	$\varphi = 150^\circ$	$\varphi = 165^\circ$	$\varphi = 180^\circ$
$\langle v \rangle$	1059 km s ⁻¹	1411 km s ⁻¹	1594 km s ⁻¹
$\langle a \rangle$	-21.3 m s ⁻²	-48.5 m s ⁻²	-78.8 m s ⁻²

of at least 10% with respect to the background density were taken into account in the calculation of the centre of mass.

The height-time curves were fitted with first and second order polynomials to obtain the average velocity and acceleration. The measured quantities for the average velocity and acceleration are summarised in Table 1. The CME front (in the $\varphi = 180^\circ$ -plane) shows a strong deceleration of 79 m s⁻². The extensive statistical study of Yashiro *et al.* (2004) pointed out that, on average, the acceleration of CMEs with average velocity $\langle v \rangle \geq 900$ km s⁻¹ is -15 m s⁻². The strong deceleration of 79 m s⁻² of the CME front is rare, but not un-occurring.

4. Conclusions

A three-dimensional time dependent MHD simulation of a CME event has been performed, where the simulation domain ranged from the lower corona up to $30R_\odot$. The CME was mimicked by launching a high density flux rope in the solar wind, where the used model for the background wind represents solar minimum conditions. The magnetic field topology of the flux rope was the Romashets and Vandas (2003) solution in toroidal geometry. By applying the transformations of Gibson and Low (1998), the flux rope was stretched towards the solar surface, imitating a rising prominence. The simulation presented in this paper is the 3D generalisation of the 2.5D models described in earlier work (e.g. Jacobs *et al.*, 2005; Chané *et al.*, 2006). Three-dimensional CME simulations provide the ability to investigate the three-dimensional nature of CMEs. With the recent launch of the STEREO mission, it will become possible to check the outcome of the models with the multiple view point observations made by STEREO.

The model presented here is different from the simulations of e.g. Roussev *et al.* (2003) and Manchester *et al.* (2004) in the sense that we add an extra amount of momentum and energy to the flux rope, in order to have more control over its propagation. Roussev *et al.* (2003) used the flux rope model of Titov and Démoulin (1999) and by removing the overlying line current, the flux rope became unstable, causing an eruption. In case no extra density or velocity is added, the magnetic field of the flux rope in our model simply reconnects with the overlying coronal field, not causing a violent eruption. This might be due to the low magnetic field strength inside the flux rope and a higher magnetic field strength might be desirable. Another weakness of the simulation is the background wind model. The medium in which the CME is propagating influences the evolution of the CME. A more realistic wind model with input from magnetograms and/or empirical laws (e.g. Wang and Sheeley, 1990) for the solar wind is then also necessary if the model wants to be used to simulate specific CME events. For future studies it might be interesting to investigate the effect of the initial parameters like the amount of added ve-

locity, density, and magnetic field on the CME evolution.

Acknowledgments. These results were obtained in the framework of the projects GOA/2004/01 (K.U.Leuven), G.0304.07 (FWO-Vlaanderen) and C 90203 (ESA Prodex 8). Financial support by the European Commission through the SOLAIRE Network (MTRN-CT-2006-035484) is gratefully acknowledged. The numerical results were obtained on the HPC cluster VIC of the K.U.Leuven.

References

- Chané, E., B. van der Holst, C. Jacobs, S. Poedts, and D. Kimpe, Inverse and normal coronal mass ejections: evolution up to 1AU, *A&A*, **447**, 727–733, 2006.
- Cremades, H. and V. Bothmer, On the three-dimensional configuration of coronal mass ejections, *A&A*, **422**, 307–322, 2004.
- Gibson, S. E. and B. C. Low, A time-dependent three-dimensional magnetohydrodynamic model of the coronal mass ejection, *ApJ*, **493**, 460–473, 1998.
- Gilbert, H. R., T. E. Holzer, J. T. Burkepile, and A. J. Hundhausen, Active and eruptive prominences and their relationship to coronal mass ejections, *ApJ*, **537**, 503–515, 2000.
- Gopalswamy, N., S. Yashiro, Y. Liu, G. Michalek, A. Vourlidis, M. L. Kaiser, and R. A. Howard, Coronal mass ejections and other extreme characteristics of the 2003 October–November solar eruptions, *J. Geophys. Res.*, **110**, A09S15, 2005.
- Groth, C. P. T., D. L. De Zeeuw, T. I. Gombosi, and K. G. Powell, Global three-dimensional MHD simulation of a space weather event: CME formation, interplanetary propagation, and interaction with the magnetosphere, *J. Geophys. Res.*, **105**, 25053–25078, 2000.
- Jacobs, C., S. Poedts, B. van der Holst, and E. Chané, On the effect of the background wind on the evolution of interplanetary shocks, *A&A*, **430**, 1099–1107, 2005.
- Jacobs, C., B. van der Holst, and S. Poedts, Comparison between 2.5D and 3D simulations of coronal mass ejections, *A&A*, **470**, 359–365, 2007.
- Jing, J., V. B. Yurchyshyn, G. Yang, Y. Xu, and H. Wang, On the relation between filament eruptions, flares, and coronal mass ejections, *ApJ*, **614**, 1054–1062, 2004.
- Karpen, J. T., S. K. Antiochos, M. Hohensee, and J. A. Klimchuk, Are magnetic dips necessary for prominence formation?, *ApJ*, **553**, L85–L88, 2001.
- Kippenhahn, R. and A. Schlüter, Eine Theorie der solaren Filamente, *Z. Astrophys.*, **43**, 36–62, 1957.
- Kuperus, M. and M. A. Raadu, The support of prominences formed in neutral sheets, *A&A*, **31**, 189–193, 1974.
- Leroy, J. L., V. Bommier, and S. Sahal-Bréchet, New data on the magnetic structure of quiescent prominences, *A&A*, **131**, 33–44, 1984.
- Low, B. C. and M. Zhang, Magnetostatic structures of the solar corona III. Normal and inverse quiescent prominences, *ApJ*, **609**, 1098–1111, 2004.
- Manchester, W., The role of nonlinear Alfvén waves in shear formation during solar magnetic flux emergence, *ApJ*, **547**, 503–519, 2001.
- Manchester, W. B., T. Gombosi, I. Roussev, D. L. De Zeeuw, I. V. Sokolov, K. G. Powell, G. Tóth, and M. Opher, Three-dimensional MHD simulation of a flux rope driven CME, *J. Geophys. Res.*, **109**, A01102, 2004.
- Romashets, E. P. and M. Vandas, Interplanetary magnetic clouds of toroidal shapes, *Proc. ICS 2003 Symposium*, 535–540, 2003.
- Roussev, I. I., T. G. Forbes, T. I. Gombosi, I. V. Sokolov, D. L. DeZeeuw, and J. Birn, A three-dimensional flux rope model for coronal mass ejections based on a loss of equilibrium, *ApJ*, **588**, L45–L48, 2003.
- Titov, V. S. and P. Démoulin, Basic topology of twisted magnetic configurations in solar flares, *A&A*, **351**, 707–720, 1999.
- Wang, Y.-M. and N. R. Sheeley, Solar wind speed and coronal flux-tube expansion, *ApJ*, **355**, 726–732, 1990.
- Wu, S. T., W. P. Guo, D. J. Michels, and L. F. Burlaga, MHD description of the dynamical relationships between a flux rope, streamer, coronal mass ejection, and magnetic cloud: An analysis of the January 1997 Sun-Earth connection event, *J. Geophys. Res.*, **104**, 14789, 1999.
- Yashiro, S., N. Gopalswamy, G. Michalek, O. C. St. Cyr, S. P. Plunkett, N. B. Rich, and R. A. Howard, A catalog of white light coronal mass ejections observed by the SOHO spacecraft, *J. Geophys. Res.*, **109**, A07105, 2004.

Non-thermal electrons at the Earth's bow shock: A 'gradual' event

M. Oka¹, T. Terasawa², M. Fujimoto³, H. Matsui⁴, Y. Kasaba⁵, Y. Saito³, H. Kojima⁶, H. Matsumoto⁷, and T. Mukai⁸

¹Kwasan Observatory, Kyoto University, Yamashina-ku, Kyoto, Japan

²Tokyo Institute of Technology, Meguro-ku, Tokyo, Japan

³Institute of Space and Astronautical Science, Japan Aerospace Exploration Agency, Kanagawa, Japan

⁴University of New Hampshire, Durham, New Hampshire, USA

⁵Tohoku University, Sendai, Japan

⁶Research Institute for Sustainable Humanosphere, Kyoto University, Uji, Kyoto, Japan

⁷Kyoto University, Sakyo-ku, Kyoto, Japan

⁸Japan Aerospace Exploration Agency, Chofu, Tokyo, Japan

(Received February 18, 2008; Revised April 6, 2008; Accepted May 19, 2008; Online published May 29, 2009)

The Earth's bow shock is known to produce non-thermal electrons which are generally observed as a 'spike' in their flux profile. Here, in this paper, we present an analysis of electron and whistler wave properties for a quasi-perpendicular shock crossing that is supercritical, but subcritical to the so-called whistler critical Mach number, M_{crit}^w , above which whistler waves cannot propagate upstream. We have found that the amplitudes of whistler waves increased exponentially as a function of time prior to the shock encounter, while the suprathermal (>2 keV) electron flux similarly increased with time, although with differing e -folding time scales. Comparison of the electron energy spectrum measured within the ramp with predictions from diffusive shock acceleration theory was poor, but the variation of pitch angle distribution showed scattering of non-thermal electrons in the upstream region. While not finding a specific mechanism to account for the electron diffusion, we suggest that the whistlers seen probably account for the differences observed between this 'gradual' event and the 'spike' events seen at shocks with no upstream whistlers.

Key words: Particle acceleration, scattering, bow shock, whistlers.

1. Introduction

Energetic electrons with energies of more than 20 keV have been observed at and near the Earth's bow shock (e.g., Fan *et al.*, 1964; Frank and Van Allen, 1964; Anderson, 1969; Vandas, 1989). Since larger electron flux can be found on the interplanetary magnetic field (IMF) tangent to the bow shock (e.g., Anderson *et al.*, 1979; Kasaba *et al.*, 2000), electrons are considered to be accelerated in the quasi-perpendicular region where the shock angle θ_{Bn} is larger than 45° . Gosling *et al.* (1989) were the first to carry out comprehensive analysis of suprathermal (<20 keV) electrons across the shock front. In their quasi-perpendicular shock events, energetic electron flux was enhanced at the shock transition, and because of the localized feature, they termed their events as 'spike' events. The energy spectrum showed a power-law form with the spectrum index of 3–4. The pitch angle distribution was almost isotropic at the transition layer while it was anisotropic in both the upstream and the downstream regions. More recently, Oka *et al.* (2006) conducted a statistical analysis of the power law indices measured in the shock layers. They reported that the power-law index of electron energy spectra is regulated by the so-called whistler critical Mach number M_{crit}^w , which is defined as the critical point above which

whistler waves cannot propagate upstream.

In this paper, we report a shock crossing event that showed a 'gradual' profile of non-thermal electron flux in association with an intensification of precursor whistlers. Contrary to the spike events reported by Gosling *et al.* (1989), the electron flux increased exponentially with decreasing distance from the shock. The event has been determined to be subcritical in relation to the whistler critical Mach number M_{crit}^w . We will describe properties of the waves and discuss the origin and transport of the non-thermal electrons in this gradual event.

2. Observation

Our event is observed by Geotail at $\sim 03:10$ UT on 11 February 1995 at an inbound crossing of the bow shock near the subsolar point, i.e., at $(12.2, 4.0, 0.6)R_E$ in the GSE coordinate. Figure 1 shows the overview of main physical parameters of the gradual crossing event. The shock transition appears as an abrupt change in both the magnetic field data (MGF, Kokubun *et al.*, 1994) as well as the plasma data (LEP, Mukai *et al.*, 1994). The shock normal direction estimated by the Minimum Variance Analysis (Sonnerup and Cahill, 1967) was $(0.94, 0.31, -0.17)$, consistent with the shock normal derived from the semi-empirical bow shock model of Peredo *et al.* (1995). This model is known to give normal directions in agreement with those obtained by the timing method of multi-spacecraft (Horbury *et al.*, 2002). The upstream parameters, M_A and θ_{Bn} , were then estimated to be ~ 6.8 and $\sim 68^\circ$, respectively. (For various methods

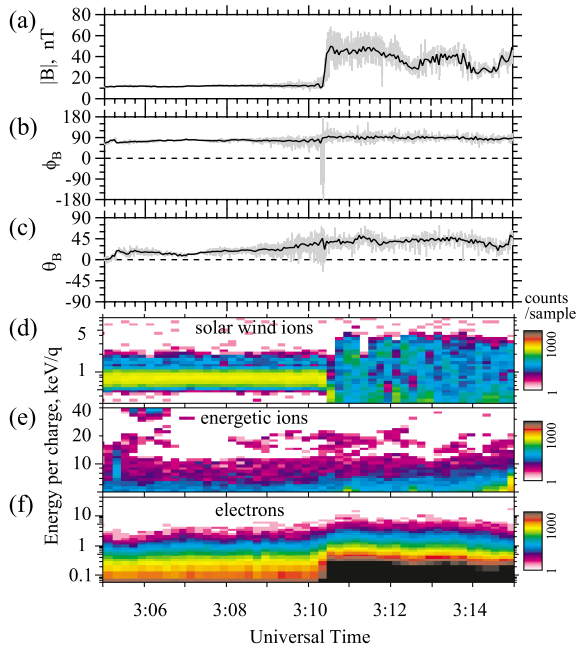


Fig. 1. From top to bottom are (a) magnitude $|B|$, (b) azimuthal ϕ_B , and (c) latitudinal θ_B component of the magnetic field (MGF) with 3 s (black line) and 1/16 s (gray line) sampling, and the energy-time (Et) diagrams of (d) solar wind ions (LEP/SWI), (e) omni-directional energetic ions (LEP/EAI), and (f) omni-directional electrons (LEP/EAE), respectively.

of shock normal determination, see, e.g., Paschmann and Daly (1998).) Noticeable in the magnetic field data in Fig. 1 are the relatively large fluctuations increasing with time (03:08–03:10 UT, $\delta B/B \sim 20\%$). Our particular interest also goes to the time profile of higher energy (>0.5 keV) electrons, as can be seen in the panel (f) as a smooth increase of count rate in the time period of 03:09–03:11 UT. It is noted that the spacecraft soon exited from the magnetosheath at 03:15 UT.

Figure 2 shows the detailed spectral properties of the waves. They are dominated by the right-hand polarized component accompanied by a frequency cut-off at around f_{LH} which threshold seems not to have been noted earlier. We speculate that this is because whistler generation concerns both ion and electron dynamics. There are tens of detailed models for whistler generation, and it is not the purpose of this letter to discuss the physical meaning of f_{LH} . From the Minimum Variance Analysis as well as the Means method (Means, 1972), the propagation angle θ_{kB} (the cone angle between the k -vector and background magnetic field) were estimated to be 20 – 40° . We also removed the 180° ambiguity of the estimated k -vector using one component of electric field (EFD) data (Matsui *et al.*, 1997). As a result, the waves with frequencies lower than ~ 10 Hz indicated propagation toward the sun, away from the shock front, consistent with a past report (Orlowski *et al.*, 1994). For higher frequencies, we could not obtain reliable results on the propagation direction, probably due to the low intensities of the waves. Note that the cone angle between the k -vector and the solar wind V_{SW} , θ_{kV} , were estimated to be 60 – 90° so that the Doppler shift was not significant. Supportingly, the spectral slope of the high-frequency range is approximately 5, consistent with past ob-

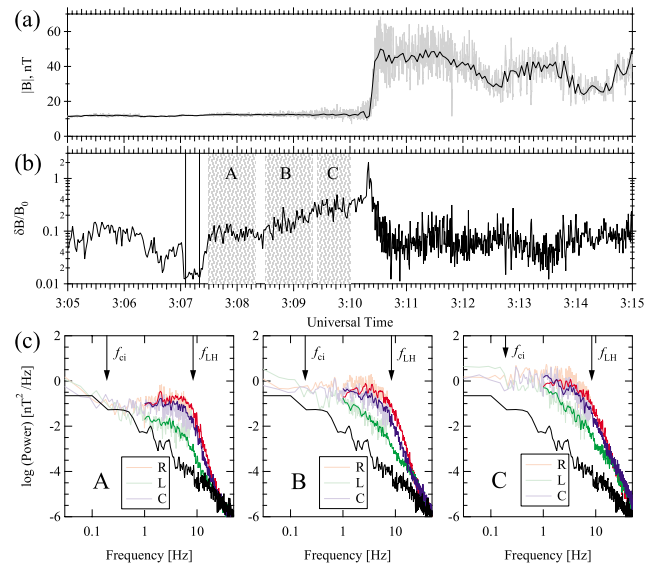


Fig. 2. From top to bottom are (a) the magnetic field magnitude (equivalent with Fig. 1(a)), (b) root mean square of band pass filtered magnetic field, (c) FFT spectra obtained at region A, B, and C indicated by the shaded regions in panel (b). The root mean square was obtained from frequency greater than fourfold the ion cyclotron frequency and has been normalized by the ambient magnetic field magnitude. Arrows in panel (c) show ion cyclotron frequency ($f_{ci} = 0.19$ Hz) and lower-hybrid frequency ($f_{LH} = \sqrt{f_{ci} f_{ce}} = 8.4$ Hz), whereas the black curve shows the background level obtained from 03:07:05–03:07:20 UT (indicated by two vertical lines). The red, green, and blue corresponds to the R, L, and C component, respectively from the fluxgate magnetometer (MGF/FX, <8 Hz, light colored) and the search coil magnetometer (MGF/SC, <32 Hz, dark colored).

servations of right-hand polarized whistler waves (Orlowski *et al.*, 1995). While traveling upwind, the waves suffered considerable (exponential) damping, as shown in the left-hand side of Fig. 3, which shows the temporal profiles of band pass-filtered magnetic field data. The characteristic time scale of the damping was calculated for each best fit model shown by the gray curves and found to be 47 s on average.

All observed features described above are well consistent with those of the so-called ‘1 Hz whistlers’ reported elsewhere (e.g., Fairfield, 1974; Sentman *et al.*, 1983; Orlowski *et al.*, 1994). From the above arguments, we conclude the observed waves to be the right-hand polarized whistler waves propagating away from the shock front.

It is to be emphasized that, while thermal electrons had been studied with respect to whistler wave generation (e.g., Tokar *et al.*, 1984; Orlowski *et al.*, 1995), non-thermal electrons, to the best of these authors’ knowledge, had never been observed in association with the upstream whistlers. Note again that the gradual profile of non-thermal electrons has not been analyzed in the past in connection with the bow shock crossing events as we will discuss below.

The right-hand side of Fig. 3 shows the time profiles of electron phase space densities (PSDs). The flux increased exponentially as the spacecraft approached the shock front. The characteristic time scale of the increase was calculated for each best fit model, shown by the red curves. Above 2 keV, the typical time scale was 24 s. During the flux increase, a pitch angle distribution also changed, as shown

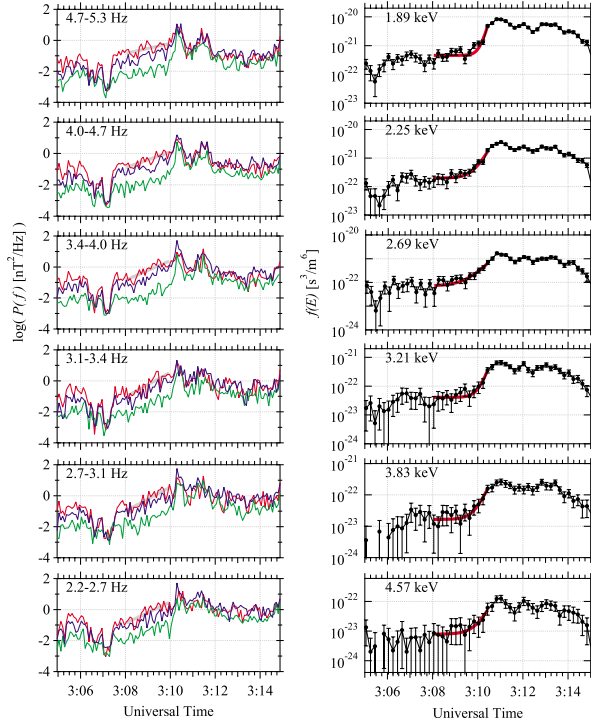


Fig. 3. (left) Temporal distributions of averaged power spectral densities (red, green, and blue for R, L, and C components) and their exponential fits (gray lines, 03:08:00–03:10:00 UT). Numbers in each panel show frequency ranges used for averaging. Frequencies are chosen so that they correspond to the resonance conditions of electrons with energy shown to the right. (right) Temporal distributions of electrons (black lines) and their exponential fits (red lines, 03:08:00–03:10:30 UT). Numbers in each panel show center energies of each energy channel.

in Fig. 4. Black symbols indicate the far upstream region of the shock, and they show strong asymmetry (i.e., larger flux in $\mu < 0$ region, where μ is the cosine of pitch angle α), indicating that electrons were streaming away from the shock front. However, substantial amount of electron counts were detected in the $\mu > 0$ region during the time interval from 03:08:30 to 03:10:00 UT, as indicated by red symbols. By this time, the spacecraft was immersed in the precursor waves. The distributions were isotropized in the immediate downstream (green and blue symbols).

Figure 5 shows the electron energy spectra. The gray line shows the spectrum obtained at 03:00 UT in the pure solar wind where there was no contamination from the bow shock. The open squares show the spectrum at 03:09:45 UT just prior to the crossing. There was a significant amount of energetic (>1 keV) electrons compared to the solar wind. The spectrum is roughly a power law. The filled squares show the spectrum at 03:10:26 UT just within the middle of the shock ramp. It now forms a complete power law above 2 keV. We then applied a chi-square fit above 2 keV with a power-law $f(E) \propto E^{-\Gamma} \exp(-E/E_{\text{roll-off}})$, where E is the electron energy as variable, $\Gamma = 4.3(\pm 0.05)$, $E_{\text{roll-off}} = 3.5(\pm 0.6)$, and the figures in the parenthesis are the 68% confidence region. The resultant $\chi^2/\text{d.o.f.}$ was 28/21, where d.o.f. is the degree of freedom and is equal to the number of data points minus the number of free parameters. A fit with the kappa distribution covering the whole energy range yielded relatively high $\chi^2/\text{d.o.f.}$. A similar

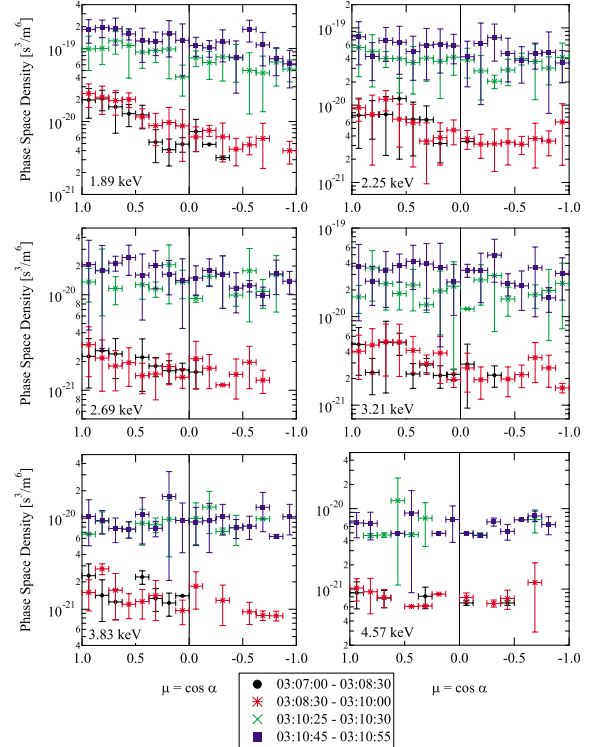


Fig. 4. Pitch angle distributions of electrons of energies 1.89, 2.25, 2.69, 3.21, 3.83, and 4.57 keV. The vertical and horizontal axes show PSDs and μ (the cosine of pitch angle α), respectively. Since the magnetic field was directed toward the sun, $\mu > 0$ corresponds to propagation away from the shock front. We have organized the obtained three-dimensional distribution function by μ , and the horizontal axis has been binned into 16 bins. The color code indicates different time intervals (in UT), as shown in the annotation.

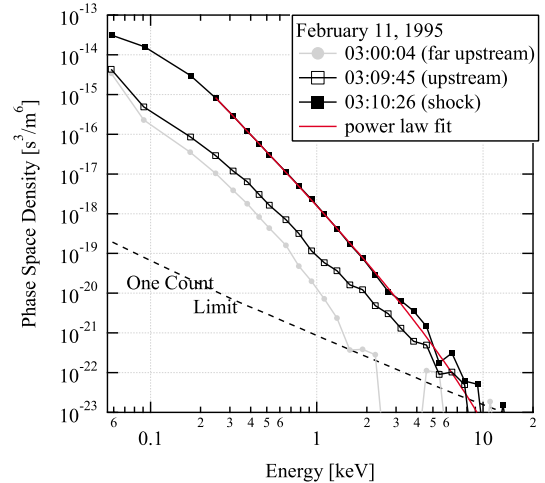


Fig. 5. Energy spectra of electrons during the bow shock transition.

spectrum was observed in the immediate downstream as well. Note that $E_{\text{roll-off}}$ was introduced to better fit the observation, but we have not succeeded in deriving information of maximum attainable energy of electrons (Oka *et al.*, 2006).

3. Discussion

The ‘gradual’ profile of electron flux, the scattering of particles, and the appearance of the power-law energy spec-

trum remind us of the diffusive shock acceleration (DSA, e.g., Blandford and Ostriker, 1978). In this process, particles are continuously scattered and move back and forth across the shock front to gain a net momentum from the velocity difference between upstream and downstream. However, there are some difficulties in the DSA to fully explain the observed features. The observed density ratio $r \sim 2.5$ ($N_1 = 21/\text{cm}^3$ for the upstream and $N_2 = 52/\text{cm}^3$ for the downstream) and the classical DSA formula $\Gamma_{\text{DSA}} = 3r/2(r-1) = 2.5$ do not reproduce the observed $\Gamma \sim 4.3$. The quantitative difference can readily be interpreted by, for instance, a free escape boundary that allows a significant number of particles to escape from the acceleration region. The discrepancy between the e -folding distances derived from wave measurements (with the resolution of 47 s) and particle measurements (with the resolution of 24 s) indicates that the waves were not generated by the non-thermal electrons and that self-scattering was weak. Therefore, we do not consider the classic DSA mechanism to be fully responsible for the generation of the observed power-law spectra.

Nevertheless, we still consider there was substantial scattering in the upstream, as is evident from Fig. 4. We have shown that the whistler waves were propagating along with the majority of the electrons. Since the direction must be opposite to that of electron streaming in order to satisfy the cyclotron resonance condition, the cyclotron resonance by the right-hand-polarized whistlers is unlikely as the physical mechanism of scattering. The observed whistlers were oblique waves ($\theta_{kB} = 20\text{--}40^\circ$), and so the left-hand-polarized component and/or electrostatic component of the waves might have been playing a role in electron scattering. It should be also mentioned that the amplitudes of the upstream waves were relatively high so that a non-linear effect should have played a role not only for the scattering but also acceleration. A recent theory indeed points out the possibility of efficient particle acceleration at a turbulent magnetic field where all scales are larger than the particle gyroradius (e.g., Giacalone, 2005; Jokipii and Giacalone, 2007). That the spectral index was relatively large also favors this theory, although the detailed comparison is left for future work.

We focus on the fact that the gradual profile was found at the shock with M_A slightly below M_{crit}^w ($M_A/M_{\text{crit}}^w \sim 0.65$ in this event). Our interpretation is as follows. In a higher M_A shock ($M_A > M_{\text{crit}}^w$), whistler waves do not propagate upstream so that any electron that escapes the shock front cannot interact with the waves and the intense flux can only be found at the shock front resulting in ‘spike’ events. On the other hand, in a much lower M_A shock ($M_A \ll M_{\text{crit}}^w$), there would be plenty of waves to scatter particles, but the number of non-thermal electrons that are subject to scattering is small. Therefore, we expect to find similar events in the Mach number range slightly below M_{crit}^w .

Unfortunately, however, the time resolution needs to be sufficiently high to resolve the decaying profile of non-thermal electrons. In the 78 events of Oka *et al.* (2006), there were a few events that seemed to be ‘gradual’, but the decaying time was of the order of the time resolution of the particle measurement (12 s), and thus we could not replicate the analysis presented in this paper. We anticipate that more

sophisticated observations of multi-spacecraft mission such as Cluster, MMS, and SCOPE/CrossScale will reveal the nature of ‘gradual’ events.

Acknowledgments. The authors are grateful to all members of the Geotail project. This work was partially supported by the Grant-in-Aid for Creative Scientific Research (17GS0208) from the MEXT, Japan. MO was supported by the Grant-in-Aid for JSPS Postdoctoral Fellows for Research Abroad.

References

- Anderson, K. A., Energetic electrons of terrestrial origin behind the bow shock and upstream in the solar wind, *J. Geophys. Res.*, **74**, 95, 1969.
- Anderson, K. A. *et al.*, Thin sheets of energetic electrons upstream from the Earth’s bow shock, *Geophys. Res. Lett.*, **6**, 401, 1979.
- Blandford, R. D. and J. P. Ostriker, Particle acceleration by astrophysical shocks, *Astrophys. J.*, **221**, L29–L32, 1978.
- Fairfield, D. H., Whistler waves observed upstream from collisionless shocks, *J. Geophys. Res.*, **79**, 1368–1378, 1974.
- Fan, C. Y. *et al.*, Evidence for $>30\text{keV}$ electrons accelerated in the shock transition region beyond the Earth’s magnetospheric boundary, *Phys. Rev. Lett.*, **13**, 149, 1964.
- Frank, L. A. and J. A. Van Allen, Measurements of energetic electrons in the vicinity of the sunward magnetospheric boundary with Explorer 14, *J. Geophys. Res.*, **69**, 4923, 1964.
- Giacalone, J., Particle acceleration at shocks moving through an irregular magnetic field, *Astrophys. J.*, **624**, 765, 2005.
- Gosling *et al.*, Suprathermal electrons at Earth’s bow shock, *J. Geophys. Res.*, **94**, 10,011–10,025, 1989.
- Horbury *et al.*, Four spacecraft measurements of the quasiperpendicular terrestrial bow shock: Orientation and motion, *J. Geophys. Res.*, **107**, 273, 2002.
- Jokipii, J. R. and J. Giacalone, Adiabatic compression acceleration of fast charged particles, *Astrophys. J.*, **660**, 336, 2007.
- Kasaba, Y. *et al.*, Statistical studies of plasma waves and backstreaming electrons in the terrestrial electron foreshock observed by Geotail, *J. Geophys. Res.*, **105**, 79–103, 2000.
- Kokubun *et al.*, The GEOTAIL magnetic-field experiment, *J. Geomag. Geoelectr.*, **46**, 7–21, 1994.
- Matsui, H. *et al.*, Long-duration whistler waves in the magnetosheath: Wave characteristics and the possible source region, *J. Geophys. Res.*, **102**, 17,583–17,593, 1997.
- Means, J. D., Use of three-dimensional covariance matrix in analyzing the polarization properties of plane waves, *J. Geophys. Res.*, **77**, 5551, 1972.
- Mukai, T. *et al.*, The Low Energy Particle (LEP) experiment onboard the GEOTAIL satellite, *J. Geomag. Geoelectr.*, **46**, 669–692, 1994.
- Oka, M. *et al.*, Whistler critical Mach number and electron acceleration at the bow shock: Geotail observation, *Geophys. Res. Lett.*, **33**, L24104, 2006.
- Orlowski, D. S. *et al.*, On the source of upstream whistlers in the Venus foreshock, in *COSPAR Colloquia, Plasma environments of non-magnetic Planets, vol. 4*, edited by T. I. Gombosi, 217–227, Pergamon Press, New York, 1994.
- Orlowski, D. S. *et al.*, Damping and spectral formation of upstream whistlers, *J. Geophys. Res.*, **100**, 17,117–17,128, 1995.
- Paschmann, G. and P. W. Daly, Analysis methods for multi-spacecraft data, *ISSI Scientific Report, SR-001*, pp. 536, 1998.
- Peredo, M. *et al.*, Three-dimensional position and shape of the bow shock and their variation with Alfvénic, sonic and magnetosonic Mach numbers and interplanetary magnetic field orientation, *J. Geophys. Res.*, **100**, 7907–7916, 1995.
- Sentman, D. D. *et al.*, The oblique whistler instability in the earths foreshock, *J. Geophys. Res.*, **88**, 2048–2056, 1983.
- Sonnerup, B. U. Ö. and L. J. Cahill Jr., Magnetopause structure and attitude from Explorer 12 observations, *J. Geophys. Res.*, **72**, 171–183, 1967.
- Tokar, R. L. *et al.*, Whistler mode turbulence generated by electron beams in the bow shock, *J. Geophys. Res.*, **89**, 105, 1984.
- Vandas, M., Acceleration of electrons by a nearly perpendicular Earth’s bow shock: A comparison between observation and theory, *Bull. Astron. Inst. Czech*, **40**, 175–188, 1989.

Influence of the foreshock of the Earth's bow shock on the interplanetary shock propagation during their mutual interaction

Lubomír Přeč, Zdeněk Němeček, and Jana Šafránková

Charles University, Faculty of Mathematics and Physics, V Holesovickach 2, 180 00 Praha 8, Czech Republic

(Received October 27, 2007; Revised April 13, 2008; Accepted April 14, 2008; Online published May 29, 2009)

Interplanetary shocks have been recognized as a very efficient source of geomagnetic disturbances. We present a short study of the propagation of one interplanetary (IP) shock observed by five spacecraft located in the solar wind far upstream of the Earth's bow shock as well as in its close vicinity. The IP shock normal was highly inclined from the Sun-Earth line and thus the IP shock-bow shock interaction started at the flank. We have found a significant evolution of IP shock parameters during its motion along the bow shock. This modification is discussed and attributed to the presence of strong fluxes of energetic particles in the foreshock.

Key words: Solar wind-magnetosphere interaction, upstream conditions, interplanetary shock, foreshock.

1. Introduction

Geospace is affected by the solar wind, a supersonic plasma stream emerging from the Sun. Besides large-scale structures (such as the interplanetary magnetic field sector and solar wind flow regime boundaries), eruptive solar events of high intensity, predominantly solar flares resulting in halo Coronal Mass Ejections (CMEs) and solar energetic particle emissions, can have a significant impact on geospace. The majority of the very intense storms were observed to be associated with interplanetary CMEs (ICMEs) and shocks passing by the Earth (Tsurutani and Gonzalez, 1997). They are an interplanetary manifestation of earthward directed CMEs. For example, interplanetary pressure events, like interplanetary (IP) shocks, compress or expand the magnetosphere and increase or decrease the magnetopause and tail currents that result in changes of other near-Earth current systems (Le *et al.*, 1998). The geoeffectiveness of the solar wind structures and discontinuities is related to their 3D geometry and orientation. Since multi-spacecraft observations are necessary for the determination of the 3D geometry and structure of shocks (and/or other structures in the solar wind) (e.g., Thomsen, 1988), not too many experimental studies have attempted to address this problem.

Several studies have been done in the recent years analyzing the solar wind interplanetary magnetic structures that can be geoeffective (e.g., review by Gonzalez *et al.*, 1999). Vennerstroem (2001) examined 30 years of satellite measurements of the solar wind during magnetic storms and he had estimated the relative importance of the ejection of magnetic structures from the Sun and the stream interaction processes during solar wind propagation in generating intense southward magnetic fields in the interplan-

etary medium. Echer *et al.* (2006) presented a statistical study of the geoeffectiveness of the solar wind magnetic interplanetary structures including magnetic clouds (MCs), corotating interaction regions (CIRs) and interplanetary (IP) shocks over a wide observational period. They observed that magnetic clouds are more efficient than shocks or CIRs in producing all geomagnetic disturbances and they have confirmed that compound structures (shocks and MCs) are more geoeffective in every type of magnetospheric activity than isolated structures. However, the application of these findings in the space weather models requires a precise forecasting of the structure arrival to the Earth that is generally a difficult task (see e.g., Fry *et al.*, 2003 or McKenna-Lawlor *et al.*, 2006).

A strong correlation between IP shocks impinging on the magnetosphere and geomagnetic disturbances has been reported by many authors (e.g., Gonzalez *et al.*, 1999). The interaction of IP shocks with the Earth's bow shock and their transmissions through the magnetosheath to the boundary of the magnetosphere has been studied mainly by a gas dynamic modeling (e.g., Dryer, 1973; Grib *et al.*, 1979; Spreiter and Stahara, 1994). Generally, it is assumed that the incoming IP shocks are planar on the scale-size of the magnetosphere in the undisturbed solar wind. Russell *et al.* (2000) analyzed a single IP shock with four solar wind spacecraft and found that normals calculated from the data of three of them were consistent with the planarity assumption (with the accuracy of the travel time estimates). On the other hand, a deviation from planarity has also been reported (e.g., Russell *et al.*, 1983; Šafránková *et al.*, 1998).

Two papers by Koval *et al.* (2005, 2006) demonstrate that the shock front in the magnetosheath is inclined and this inclination results in a delay of the shock arrival to the magnetopause. A non-planar shock propagation through the magnetosheath resulting from experimental observations has been confirmed by two numerical MHD simulation results (Koval *et al.*, 2006).

The short survey has shown that the problem of the interaction of an IP shock with the Earth's magnetosphere is not fully explained. Although MHD modeling achieved a particular success in description of the IP shock interaction with the bow shock (e.g., Zhuang *et al.*, 1981; Grib, 1982; Yan and Lee, 1996; Samsonov *et al.*, 2006), the models have two significant limitations: (1) their present codes can be applied only to the shocks perpendicular to the solar wind velocity and (2) they cannot account for foreshock effects.

In the paper, we have identified one IP shock that was registered by 5 spacecraft in the solar wind. Two of them were located far upstream and three others in a close vicinity of the bow shock in different positions with respect to the expected foreshock boundary. Moreover, the shock normal determined either by the 4-spacecraft method or from Rankine-Hugoniot relations (this method solves the full set of Rankine-Hugoniot equations according to the Vinas and Scudder (1986) paper) was declined on a large angle from the Sun-Earth line. The paper is devoted to a comprehensive study of this event and it is oriented to a preliminary analysis of the foreshock effects.

2. Observation

The IP shock (probably CIR-driven) was first observed by ACE near the L1 point at ~ 0007 UT on August 10, 1998 and about 24 minutes later by WIND at the distance about $80R_E$ from the Earth. As can be seen in Fig. 1, both spacecraft observed nearly rectangular jumps of all parameters; the solar wind speed changed from ~ 410 to ~ 440 km/s and the density from ~ 4 to ~ 9 cm $^{-3}$. These jumps suggest a rather weak IP shock but the shock parameters calculated from the WIND magnetic field and plasma data using Rankine-Hugoniot relations show that its Alfvénic Mach number is as high as 6.6 ($v_A = 54$ km/s) in the normal incidence frame. The reason is that, although the shock speed is only 355 km/s in the observer reference frame, it is largely (on $\sim 50^\circ$) declined from the Sun-Earth line because the shock normal vector is $n = [-0.53; -0.44; 0.73]$ and the shock speed in the solar wind frame is 346 km/s. The shock can be classified as quasiperpendicular, $\Theta_{BN} \approx 63^\circ$.

The same IP shock was observed later by IMP 8, Geotail, and Interball-1 in front of the bow shock. Since their locations are very important for the present study, we are bringing a sketch in Fig. 2. The spacecraft positions were rotated into one plane but it should be noted that all of them were very close to the ecliptic plane. We have used the timing of the shock observations by ACE, WIND, IMP 8, and GEOTAIL and estimated the shock parameters. These parameters are given in the captions of Fig. 2 and one can note that they are very similar to those derived from WIND measurements. This fact confirms that the shock can be considered to be planar on the scale of the spacecraft separation. The cross-section of the shock plane with the XY_{GSE} plane is shown as a dashed line in the figure.

Taking into account the shock orientation, one would expect that the shock would arrive nearly simultaneously to IMP 8 and Geotail and with a significant delay to Interball-1. We have chosen the magnetic field strength and ion flux for a comparison of observation in different points that is

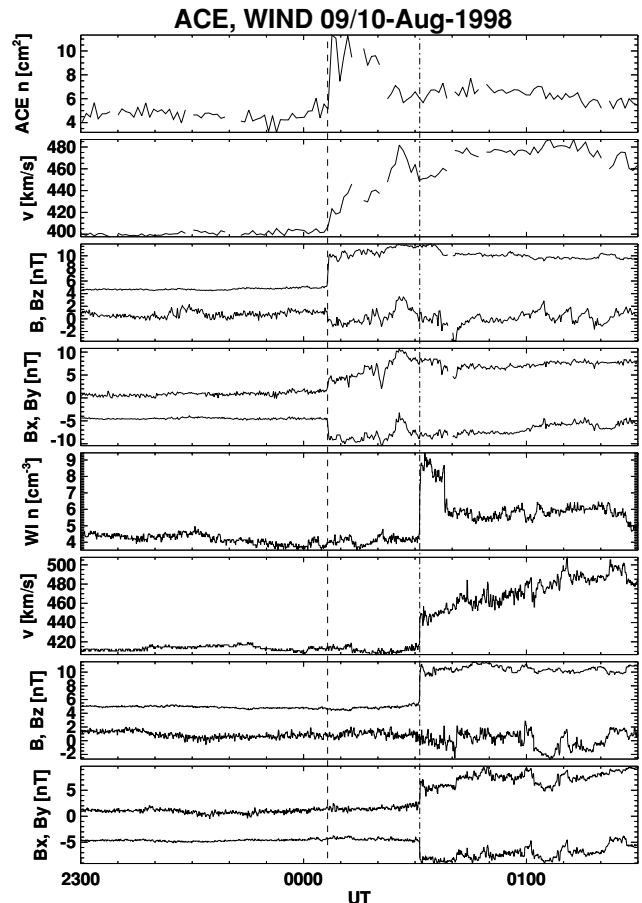


Fig. 1. Fast forward shock observed on August 10, 1998 by ACE and Wind upstream of the bow shock (thin dashed and dashed-dotted lines). From the top to bottom: ACE (first four panels) and Wind (second four panels) densities, velocities, and IMF strengths and all components.

shown in Fig. 3. The ion flux is computed as a product of the proton speed and density for all spacecraft except Interball-1 and it covers the energy range of several keV (up to ~ 25 keV) depending on a particular spacecraft. Interball-1 was equipped with a special set-up for ion flux measurements without any selection of energies. Since the contribution of high-energy ions to the total ion flux is small, we assume that the different energy ranges cannot spoil the results of our qualitative study.

The originally very steep IP shock front underwent a significant evolution. The IMP 8 observation reveals similar shock features as those observed by WIND but a strong significant modification of the shock front was observed by Geotail and no similar shock-like discontinuity was detected at the Interball-1 location. Instead, Interball-1 observed short spikes of both depicted parameters approximately at the predicted time of the IP shock arrival. These spikes are followed by a gradual rise and they reached their expected post-shock values only after 10–12 minutes.

3. Discussion and Conclusion

The shock front modification observed by Interball-1 cannot be probably attributed to a temporal evolution because the shock withstood unchanged for ~ 35 minutes from ACE to IMP 8 and the expected time lag between IMP 8

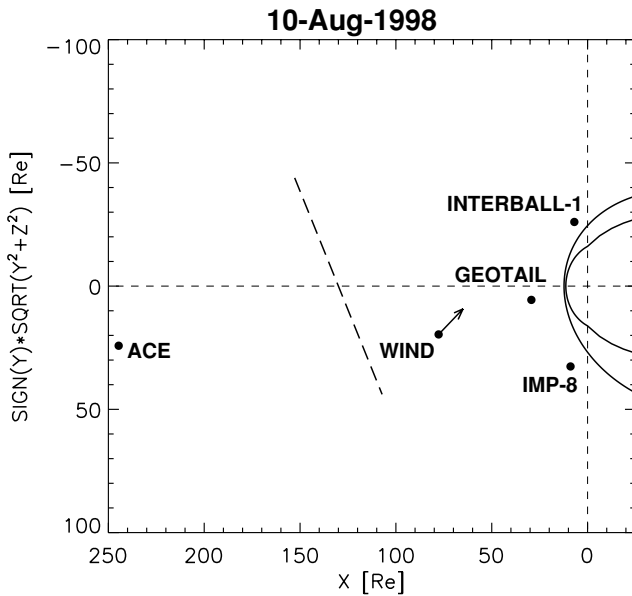


Fig. 2. Cylindrical projection of the spacecraft locations onto the equatorial plane. Jerab *et al.* (2005) and Petrinec and Russell (1996) models were applied to determine Earth's bow shock and magnetopause positions before the shock. Shock parameters computed from Rankine-Hugenoit relations from the Wind data are: $v_{sh} = 355$ km/s, and $n = [-0.53; -0.44; 0.73]$ (an arrow at the Wind location). The normal and speed computed from timing of the 4 spacecraft (Wind, ACE, Geotail, IMP 8) observations (Koval *et al.*, 2005) are: $v_{sh} = 319$ km/s, and $n = [-0.55; -0.29; 0.77]$. The dashed line shows this shock plane.

and Interball-1 is about 7 minutes, only. On the other hand, IMP 8 was orbiting in front of the quasiperpendicular bow shock, whereas Interball-1 was moving in the quasiparallel region and Geotail was probably near the ion foreshock boundary as can be seen from the schematics in Fig. 4 (note that the ion foreshock boundary lies downstream of that of electron foreshock due to a smaller ion speed). Positions of the spacecraft as well as the magnetic field vectors are projected onto the XY_{GSE} plane. The estimated location of the IP shock is shown by thin dashed lines with about two-minute spacing, the heavy dashed line stands for the electron foreshock boundary after the IP shock arrival. Both upstream and downstream IMF orientations are shown by the heavy arrows.

The main foreshock feature that can influence the propagation of the IP shock is probably a presence of energetic particles because the amplitude of ULF waves was very low in our case (see Fig. 3). For this reason, we are showing the temporal profiles of several energies measured by Geotail and Interball-1 in Fig. 5. The estimated IP shock fronts are distinguished by dashed vertical lines. The Interball-1 magnetic field profile is shown for the sake of reference. The measurements of both spacecraft are, in some sense, similar. Prior the IP shock arrival, both of them observe gradually increasing particle fluxes at all energies. Their anisotropy is very low. It is shown in the last panel for Geotail as anisotropy coefficients and it can be estimated from a (lack of) spin modulation in the F_{p2} panel of the Interball-1 data (3th panel in Fig. 5). The anisotropy coefficients, $a1$ and $a2$, are amplitudes of the first and second harmonics of

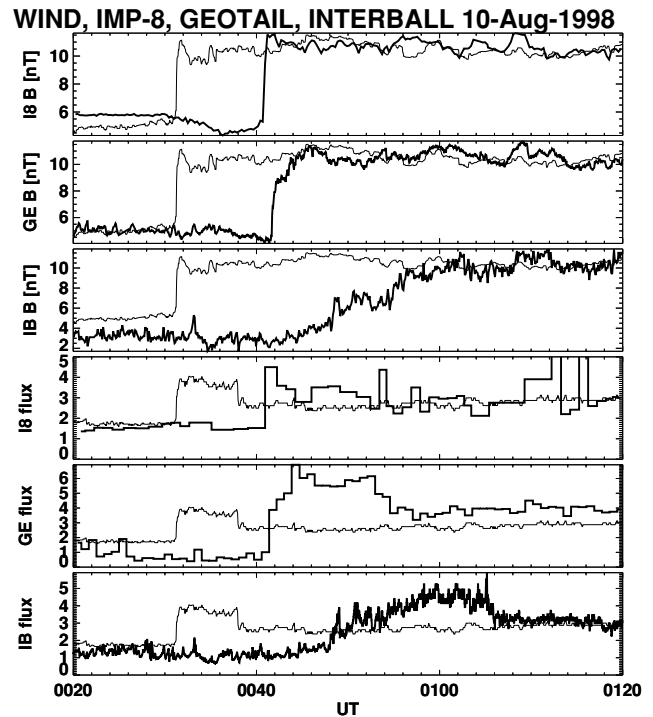


Fig. 3. IMP 8, Geotail, and Interball-1 observations of the IP shock upstream of the bow shock on August 10, 1998. From top bottom: IMF (first three panels) and ion fluxes (in units of 10^8 $cm^{-2} s^{-1}$) from IMP 8, Geotail, and Interball-1, respectively. In each panel, the IMF or ion flux from Wind (thin lines) are presented for the sake of reference.

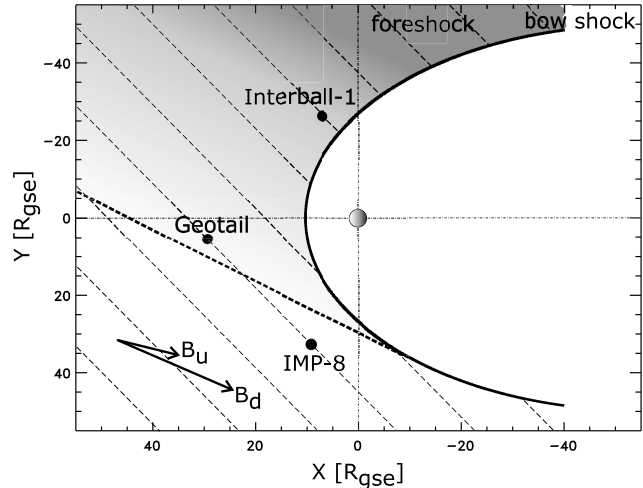


Fig. 4. The sketch of projections of spacecraft locations onto the ecliptic plane that respects their real observations in different distances from the electron foreshock boundary (heavy dashed line). The orientations of upstream (B_u) and downstream (B_d) IMF are shown by the arrows. The estimated orientation of the IP shock is depicted by thin dashed lines.

the Fourier fit to the measured ratio of parallel and perpendicular particle fluxes. The increase of the particle flux can be connected with the approaching IP shock because the flux of particles accelerated there is added to the original foreshock flux. The rise of the energetic particle flux is terminated not at but about two minutes after IP shock arrivals to both locations. After this peak, the particle flux drops down by an order of magnitude and becomes anisotropic at

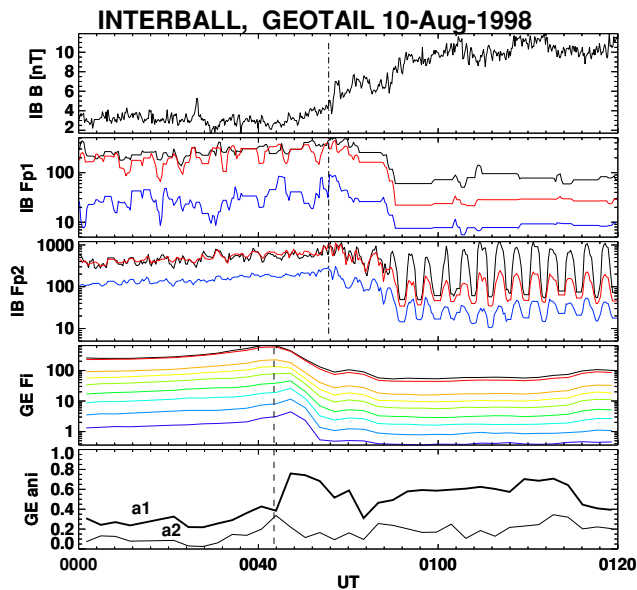


Fig. 5. The temporal profiles of energetic particles measured on Interball-1 and Geotail before and after the IP shock transition. Interball-1 (first three panels) show 3 different energies (blue line—115 keV, red—50 keV, and black—25 keV) in two directions (F_{p1} in the sunward and F_{p2} near the anti-sunward directions). Geotail panels (two bottom panels) show energetic particle fluxes (4th panel from top to bottom—the energy range from 67 to 414 keV) and anisotropy coefficients ($a1$ and $a2$ in the 5th panel).

the Geotail location. This decrease is probably connected with the Geotail exit from the ion foreshock because the IP shock (and the downstream IMF) approached the bow shock about 2 minutes after it passed Geotail (see Fig. 4). The drop of the energetic particle flux is associated with a new rise of the magnetic field toward its post-shock equilibrium value (compare Figs. 3 and 5).

The behavior of the energetic particles at the Interball-1 location is more peculiar because their flux remains nearly isotropic for about 6 minutes after the IP shock arrival and then it jumps down and a strong anisotropy appears. An analysis of pitch angles revealed that the flux at about 90° remains nearly on a previous level and only particles with low and high pitch angles disappeared. This change is accompanied with a new rise of the magnetic field strength. In this case, the delay of the change of energetic particle properties cannot be connected with reformation of the foreshock and its source is unclear.

Finally, we have presented a short case study of the IP shock propagation through the foreshock. We have shown that the profiles of basic parameters can be substantially modified, probably due to presence of energetic particles. However, the exact mechanism of this modification requires a further study that would include a modeling of particle trajectories.

Acknowledgments. The presented work was partly supported by the Research plan MSM 0021620860 that is financed by the Ministry of Education of the Czech Republic and partly by the Czech Grant Agency under Contracts 205/07/0694, and 205/06/0875. Their supports are greatly acknowledged. The authors would like to thank to teams of all spacecraft involved in this study.

References

- Dryer, M., Bow shock and its interaction with interplanetary shocks, *Radio Sci.*, **8**, 893–901, 1973.
- Echer, E., W. D. Gonzalez, and M. V. Alves, On the geomagnetic effects of solar wind interplanetary magnetic structures, *Space Weather*, **4**, S06001, doi:10.1029/2005SW002000, 2006.
- Fry, C. D., M. Dryer, Z. Smith, W. Sun, C. S. Deehr, and S.-I. Akasofu, Forecasting solar wind structures and shock arrival times using an ensemble of models, *J. Geophys. Res.*, **108**, A1070, doi:10.1029/2002JA009474, 2003.
- Gonzalez, W. D., B. T. Tsurutani, and A. L. C. De Gonzalez, Interplanetary origin of geomagnetic storms, *Space Sci. Rev.*, **88**, 529–562, 1999.
- Grib, S. A., Interaction of non-perpendicular/parallel solar wind shock waves with the Earth's magnetosphere, *Space Sci. Rev.*, **32**, 43–48, 1982.
- Grib, S. A., B. E. Brunelli, M. Dryer, and W.-W. Shen, Interaction of interplanetary shock waves with the bow shock-magnetopause system, *J. Geophys. Res.*, **84**, 5907–5921, 1979.
- Jerab, M., Z. Nemecek, J. Safrankova, K. Jelinek, and J. Merka, A study of bow shock locations, *Planet. Space Sci.*, **53**, 85–94, 2005.
- Koval, A., J. Safrankova, Z. Nemecek, and L. Prech, Deformation of interplanetary shock fronts in the magnetosheath, *Geophys. Res. Lett.*, **32**, doi:10.1029/2005GL023009, 2005.
- Koval, A., J. Safrankova, Z. Nemecek, A. A. Samsonov, L. Prech, J. D. Richardson, and M. Hayosh, Interplanetary shock in the magnetosheath: Comparison of experimental data with MHD modeling, *Geophys. Res. Lett.*, **33**, doi:10.1029/2006GL025707, 2006.
- Le, G., C. T. Russell, and J. G. Luhmann, Polar magnetic observations of the low-altitude magnetosphere during the January 1997 coronal mass ejection/magnetic cloud event, *Geophys. Res. Lett.*, **25**, 2533–2536, 1998.
- McKenna-Lawlor, S. M. P., M. Dryer, M. D. Kartalev, Z. Smith, C. D. Fry, W. Sun, C. S. Deehr, K. Kecskemeti, and K. Kudela, Near real-time predictions of the arrival at Earth of flare-related shocks during Solar Cycle 23, *J. Geophys. Res.*, **111**, A11103, doi:10.1029/2005JA011162, 2006.
- Petrinec, S. M. and C. T. Russell, Near-Earth magnetopause shape and size as determined from the magnetopause flaring angle, *J. Geophys. Res.*, **101**, 137–152, 1996.
- Russell, C. T., J. T. Gosling, R. D. Zwickl, and E. J. Smith, Multiple spacecraft observations of interplanetary shocks: ISEE three-dimensional plasma measurements, *J. Geophys. Res.*, **88**, 9941–9947, 1983.
- Russell, C. T., *et al.*, The interplanetary shock of September 24, 1998: Arrival at Earth, *J. Geophys. Res.*, **105**, 25,143–25,154, 2000.
- Safrankova, J., Z. Nemecek, L. Prech, G. Zastenker, N. Nikolaeva, M. Nozdrachev, A. Skalsky, K. Paularena, and T. Mukai, January 10–11, 1997 magnetic cloud: Multipoint measurements, *Geophys. Res. Lett.*, **25**, 2549–2552, 1998.
- Samsonov, A. A., Z. Nemecek, and J. Safrankova, Numerical MHD modeling of propagation of interplanetary shock through the magnetosheath, *J. Geophys. Res.*, **111**, A08210, doi:10.1029/2005JA011537, 2006.
- Spreiter, J. R. and S. S. Stahara, Gasdynamic and magnetohydrodynamic modeling of the magnetosheath—a tutorial, *Adv. Space Res.*, **14**(7), 5–19, 1994.
- Thomsen, M. F., Multispacecraft observations of collisionless shocks, *Adv. Space Res.*, **8**(9), 157, 1988.
- Tsurutani, B. T. and W. D. Gonzalez, The interplanetary causes of magnetic storms: a review, in *Magnetic storms*, edited by B. T. Tsurutani, W. D. Gonzalez, Y. Kamide, and J. K. Arballo, AGU Monograph 98, Washington, D.C., pp. 77–90, 1997.
- Vennerstroem, S., Interplanetary sources of magnetic storms: A statistical study, *J. Geophys. Res.*, **106**, 29,175–29,184, 2001.
- Vinas, A. F. and J. D. Scudder, Fast and optimal solution to the Rankine-Hugoniot problem, *J. Geophys. Res.*, **91**, 39–58, 1986.
- Yan, M. and L. C. Lee, Interaction of interplanetary shocks and rotational discontinuities with the Earth's bow shock, *J. Geophys. Res.*, **101**, 4835–4848, 1996.
- Zhuang, H. C., C. T. Russell, E. J. Smith, and J. T. Gosling, Three-dimensional interaction of interplanetary shock waves with the bow shock and magnetopause: A comparison of theory with ISEE observations, *J. Geophys. Res.*, **86**, 5590–5600, 1981.

Three dimensional configuration of earthward fast plasma flow in the near-Earth plasma sheet

Koji Kondoh, Masayuki Ugai, and Tohru Shimizu

Research Center for Space and Cosmic Evolution, Ehime University, Japan

(Received November 2, 2007; Accepted August 16, 2008; Online published May 29, 2009)

The earthward short-term (1-min. order) fast flow event (Flow Burst) and the long-term (10-min. order) fast flow event (Bursty Bulk Flow) observed in the near-Earth plasma sheet are examined using three dimensional MHD simulations on the basis of spontaneous fast reconnection model. It is well known that these fast flow events are closely related to the magnetic substorms. On the other hand, it is considered that these fast flow events are caused by the magnetic reconnection in the near-Earth magnetotail. The time profiles of plasma quantities in these events observed by in-situ satellites are quite different in each event. Above Flow Burst and Bursty Bulk Flow events are often examined separately due to the large difference in time scale. In this paper, these differences are interpreted by the three-dimensional position of satellite relative to the X-line and the reconnection jet channel, and the simulation results are directly compared with the results of in-situ satellite observations using the virtual satellites located in simulation domain.

Key words: Earthward flow, magnetic reconnection, near-Earth plasma sheet, three-dimensional MHD simulation.

1. Introduction

Earthward fast flows in the near-Earth plasma sheet have been observed in association with geomagnetic substorms (Angelopoulos *et al.*, 1992). It is considered that these fast flows are fast reconnection outflows. In space plasmas of extremely large magnetic Reynolds number, magnetic reconnection can convert magnetic energy to plasma energies most effectively by slow shocks. A possible fast reconnection configuration, involving standing slow shocks, was first proposed by Petschek (1964). In this respect, we have proposed the spontaneous fast reconnection model. This model predicts that the fast reconnection mechanism spontaneously develops from inside the system by the self-consistent interaction between plasma microscopic processes and macroscopic reconnection flows (Ugai, 1984, 1986). The previous MHD simulations have demonstrated that the spontaneous fast reconnection model works quite effectively even in three dimensional situations (Ugai and Kondoh, 2001; Ugai *et al.*, 2004, 2005). Once the fast reconnection builds up, an Alfvénic fast flow is caused, and if the fast flow is obstructed, the reconnected field lines are piled up, and a magnetic loop is formed. A magnetic loop in our simulation is allowed to be formed because of a wall boundary assumed at one edge of a current sheet system (Ugai *et al.*, 2003). Sergeev *et al.* (2000) showed a narrow transient flow jet using five spacecraft measurements. They showed that the $\sim 3R_e$ wide fast plasma jet propagates from $\gtrsim 40R_e$ in the midtail, and is able to reach the inner magnetosphere at $6.6R_e$ in about 10 minutes. This property

consists with the previous results of MHD simulations on the basis of spontaneous fast reconnection model (Ugai *et al.*, 2003).

Earthward fast flow events observed in the near-Earth plasma sheet have the different profiles in each event. For example, Figs. 1(a) and (b) are the different two events observed by Geotail satellite. These figures show the time profiles of the plasma bulk velocity component V_x (top panel), the magnetic field components B_x (dotted line), B_z (solid line) (middle panel), and the ion density N (bottom panel). These satellites observed at $X = -29.67R_E$, $Y = 7.50R_E$, $Z = -1.26R_E$ (a), $X = -28.31R_E$, $Y = 2.65R_E$, $Z = -2.03R_E$ (b) in GSM coordinate, respectively. In GSM coordinate system, these events were observed at very near positions. The maximum velocity of V_x is almost same, 600 km/s. As you can see, however, these two events are quite different. The duration of the enhancement of flow velocity in Fig. 1(a) (~ 7 min.) is remarkably longer than that in Fig. 1(b) (~ 1 min.). The variation of the ion density in the course of fast flow is large in Fig. 1(a), while that is little in Fig. 1(b). In this paper, we examine the earthward fast flow using three-dimensional MHD simulations on the basis of spontaneous fast reconnection model, and what causes these differences.

2. Simulation Model

The earthward fast flow is closely related to the formation of magnetic loop (or magnetic dipolarization), so that the present simulation model is similar to the one of the 3D magnetic loop dynamics (Kondoh and Ugai, 2007).

These previous magnetic loop simulations using the wall boundary showed that the fast magnetic reconnection produces fast reconnection jet, and it flows in plasma sheet and

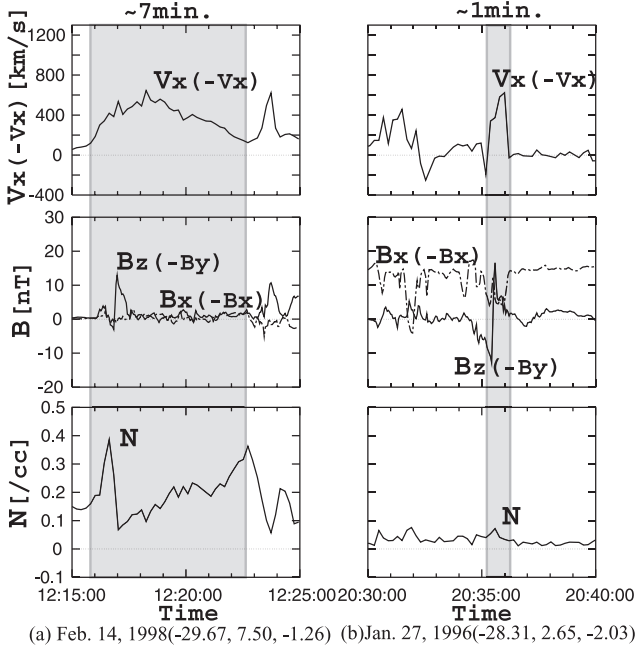


Fig. 1. Geotail observation data showing the plasma bulk velocity component (V_x), magnetic field components (B_x , B_z) and ion density (N) (12:15–12:25 UT, 14 February 1998 (a), 20:30–20:40 UT, 27 January 1996 (b)). The variables in parenthesis indicate the corresponding ones in our coordinate system.

is suddenly braked at the boundary between the dipolar and tail-like magnetic field because of the counterward pressure force, and the reconnection jet is decelerated. This situation may be consistent with the earthward fast flow, and these results are in good agreement with the situation inferred from the observation results of earthward fast flow (Shiokawa *et al.*, 1997).

2.1 Simulation modeling

As an initial configuration, the one-dimensional anti-parallel magnetic field $\mathbf{B} = [B_x(y), 0, 0]$ is assumed as: $B_x(y) = \sin(\pi y/2)$ for $0 < y < 1$; $B_x(y) = 1$ for $1 < y < Y_1$; $B_x(y) = \cos[(y - Y_1)\pi/1.2]$ for $Y_1 < y < Y_m (= Y_1 + 0.6)$; $B_x(y) = 0$ for $Y_m < y$; also, $B_x(y) = -B_x(-y)$ for $y < 0$. The plasma pressure $P(y)$ initially satisfies the pressure-balance condition, $P + B_x^2 = 1 + \beta_0$, where β_0 is the ratio of plasma pressure to the magnetic pressure in the ambient magnetic field region $1 < y < Y_1$, so that $P(y = 0) = 1 + \beta_0$ initially (in the present study, $\beta_0 = 0.15$ is taken); Initially, fluid velocity $\mathbf{u} = (0, 0, 0)$ and constant temperature $T = P/\rho = 1 + \beta_0$ is assumed, so that the plasma density ρ initially satisfies $\rho(y) = P(y)/(1 + \beta_0)$. The normalization of quantities, based on the initial quantities, is self-evident; Distances are normalized by the half-width of the current sheet d_0 , \mathbf{B} by the field strength in the magnetic field region B_{x0} , P by $B_{x0}^2/(2\mu_0)$, and ρ by $\rho_i = \rho(y = 0)$; also, \mathbf{u} by $V_{Ax0} (= B_{x0}/\sqrt{\mu_0\rho_i})$, time t by d_0/V_{Ax0} , current density \mathbf{J} by $J_0 = B_{x0}/(\mu_0 d_0)$, and so forth.

Here, the conventional symmetry boundary conditions are assumed on the (x, y) , (y, z) , and (z, x) planes. Hence, the computational region can be restricted to the first quadrant only and taken to be a rectangular box, $0 < x < L_x$,

$0 < y < L_y$, and $0 < z < L_z$; also, for simplicity, the conventional symmetry boundary condition is assumed on the outer boundary plane $x = L_x$, and on the other boundary planes ($y = L_y$ and $z = L_z$) the free boundary conditions are assumed.

As in the 2D model, a current-driven anomalous resistivity model is assumed in the form,

$$\eta(\mathbf{r}, t) = k_R [V_d(\mathbf{r}, t) - V_C] \quad \text{for } V_d > V_C, \quad (1)$$

$$= 0 \quad \text{for } V_d < V_C$$

where $V_d(\mathbf{r}, t) = |\mathbf{J}(\mathbf{r}, t)/\rho(\mathbf{r}, t)|$ is the relative electron drift velocity, and V_C may be a threshold for micro instabilities. Here, $k_R = 0.003$ and $V_C = 12$ are taken.

In order to disturb the initial static configuration, a localized resistivity model is assumed around the point $(L_x, 0, 0)$ in the 3D form,

$$\eta(\mathbf{r}) = \eta_0 \exp \left[-((x - L_x)/k_x)^2 - (|y|/k_y)^3 - (|z|/k_z)^3 \right] \quad (2)$$

Here, we take $k_x = k_y = 0.8$ and $\eta_0 = 0.02$ in the manner similar to the previous 2D simulations; also, k_z provides the 3D effects, we take $k_z = 5$ in the present study. The disturbance (2) is imposed only in the initial time range $0 < t < 4$, and the anomalous resistivity model (1) is assumed for $t \geq 4$. Hence, the fast reconnection mechanism may be triggered at $x = L_x$ in this model.

It should be noted that sufficiently small mesh sizes are required for precise computations of the spontaneous fast reconnection evolution, so that we assume $\Delta x = 0.04$, $\Delta y = 0.015$, and $\Delta z = 0.1$. Also, we take the magnetic field region size $Y_1 = 4$, and the whole computational region size is assumed to be $L_x = 10$, $L_y = 9.6$ and $L_z = 9.8$. Here, we should notice that positive x , y , z -directions in this paper correspond to tailward, southward, and eastward in usual GSM co-ordinate system, respectively.

3. Results

In this simulation model, initiated by the disturbance (2) given at $x = L_x$ in the finite extent $|z| < k_z = 5$, the current sheet thinning occurs near the $x = L_x$, giving rise to distinct enhancement of the current density. Once the drift velocity V_d exceeds the given threshold (1), fast reconnection drastically grows as nonlinear instability because of the positive feedback between the anomalous resistivity and the reconnection flow. Ahead of the Alfvénic reconnection jet flowing to negative x -direction, a large-scale 3D plasmoid is formed and propagates, and the plasmoid collides with the $x = 0$ wall boundary, giving rise to a 3D magnetic loop.

3.1 Virtual observations

In order to directly compare the simulations with the satellite observations, let us consider such a virtual satellite that is located at a spatial point (x, y, z) in the plasma sheet. For simplicity, we assume that the satellite does not move in spite of the progress of time. Then, the virtual satellite can readily detect the temporal changes of plasma quantities at its location on the basis of the simulation results. In what follows, we examine what the virtual satellite observes as the fast reconnection mechanism builds up and proceeds.

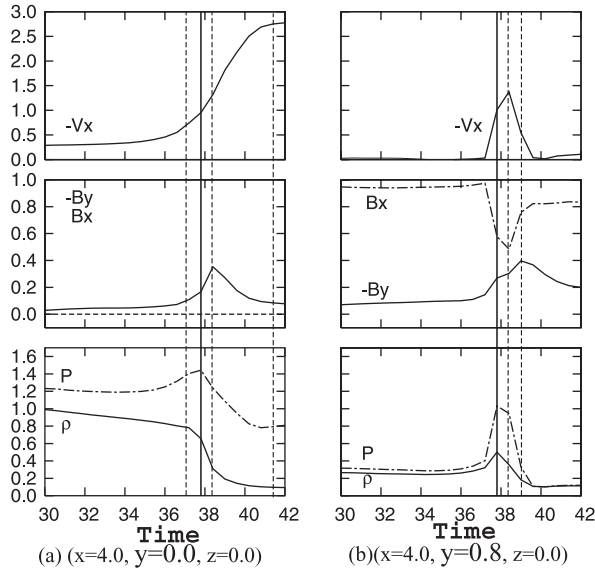


Fig. 2. Time variations of $-V_x$, B_x , $-B_y$, ρ , and P for the interval of $t = 30$ to 42 at $X = 4.0$, $Z = 0.0$, $Y = 0.0$ (a) and 0.8 (b).

At first, two virtual satellites are located at the positions $(4.0, 0.0, 0.0)$ and $(4.0, 0.8, 0.0)$ in order to examine the profiles at different y -positions. These positions correspond to them in the central plasma sheet (hereafter, call CPS) and near the plasma sheet boundary layer (hereafter, call PSBL), respectively. Figure 2 shows the temporal variations of the plasma flow velocity (top panel), magnetic field components (middle panel), plasma pressure and plasma density (bottom panel) detected by the virtual satellites located at $(4.0, 0.0, 0.0)$ (a) and $(4.0, 0.8, 0.0)$ (b). In the CPS (a), the earthward flow velocity V_x reaches Alfvén velocity. The local magnetic field dipolarizes a little. P and ρ largely decrease in the course of the fast flow, and the temperature becomes high there. On the other hand, near the PSBL (b), the enhancement of V_x is small and short, B_x largely decrease in the course of fast flow. The clear dipolarization is also detected. The durations of the variations in P and ρ are nearly same and short. The temperature in the course of the fast flow is high as well as that in the CPS. The peak times of the pressure enhancement T_P indicated by the vertical solid lines are almost same $t \sim 37.7$. The vertical dotted lines indicate the peak times of the other quantities. The earthward flow speed $|V_x|$ at T_P are almost same ~ 1.0 at both positions. The earthward flow speed in the CPS gradually increase from $t \sim 30$, whereas it near the PSBL starts to increase just before T_P . The anti-correlation between the earthward flow speed $|V_x|$ and earthward component of magnetic field B_x is clear in Fig. 2(b). This rapid increase (decrease) and decrease (increase) of $|V_x|$ (B_x) near the PSBL means that the satellite suddenly goes in the fast flow channel and suddenly goes out there.

Secondly, the other two virtual satellites are located at $(4.0, 0.4, 0.0)$ and $(4.0, 0.4, 1.2)$ in order to examine the profiles at different z -positions. These positions correspond to the those in the channel of Alfvénic fast flow (hereafter, call fast flow channel) and outside of the fast flow channel in the z -direction, respectively. In Fig. 2, the one satellite

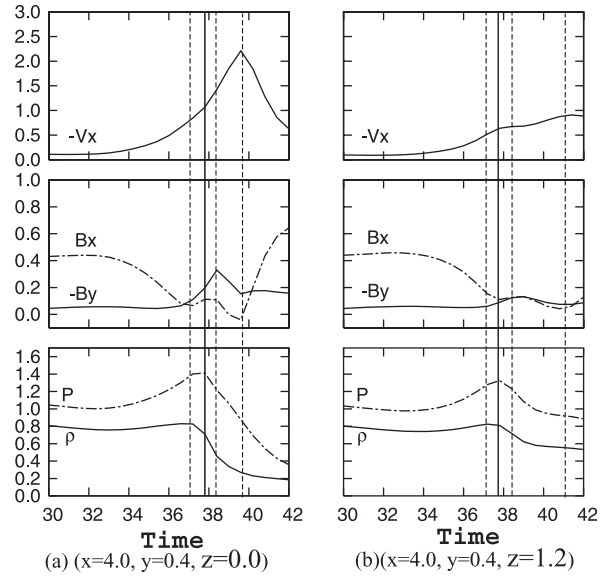


Fig. 3. Time variations of $-V_x$, B_x , $-B_y$, ρ , and P for the interval of $t = 30$ to 42 at $X = 4.0$, $Y = 0.4$, $Z = 0.0$ (a) and 1.2 (b).

was located in the $y = 0$ plane in order to examine the profiles of the satellite observations at different y -positions. However, it is rare case that the actual satellites are located in the neutral sheet, that is, they observe no B_x component. Therefore, these two virtual satellites are located in the $y = 0.4$ plane. Figure 3 shows the temporal variations of the plasma flow velocity (top panel), magnetic field components (middle panel), plasma pressure and plasma density (bottom panel) detected by the virtual satellite located at $(4.0, 0.4, 0.0)$ (a) and $(4.0, 0.4, 1.2)$ (b). In the fast flow channel (a), the enhancement of earthward flow speed is large, but the satellite goes out the fast flow channel in the y -direction at $t \sim 40$. The plasma pressure and density decrease is significantly large. On the other hand, the enhancement of earthward flow speed observed outside the fast flow (b) is small, but the duration is very long because the satellite does not go out the fast flow channel in the y -direction easily due to the calm plasma sheet thinning. The decrease of plasma pressure and density observed outside the fast flow channel is not so large.

4. Summary

In this paper, the earthward fast flow events observed in the near-Earth plasma sheet were examined using three dimensional magnetohydrodynamics simulations on the basis of the spontaneous fast reconnection model. In particular, the properties of the variation of physical quantities in each observation point relative to the X reconnection line and the narrow channel of fast reconnection jet were investigated in three dimensions. The time variations of physical quantities observed by virtual satellites were quite different between the satellite positions in central plasma sheet and near the plasma sheet boundary layer. The satellite located in central plasma sheet does not go out the narrow channel of fast flow, so that the enhancement of earthward fast flow speed is large, and the decrease of plasma pressure and density is large. On the other hand, the satellite located near the

plasma sheet boundary layer suddenly comes in the narrow channel and suddenly goes out, so that the enhancement of earthward fast flow speed is small and short, the decrease of earthward component of magnetic field is large in the course of fast flow, and the variations of plasma pressure and density are observed only in the course of fast flow. The time variations of physical quantities observed by virtual satellites were also quite different between the satellite positions in the sheet current direction. As mentioned in Introduction, the Alfvénic earthward fast jet flows in very narrow channel. In addition to this, relatively slow earthward jet (about 1/3 of Alfvén speed) flows in wider region in the sheet current direction. In that region, plasma sheet thinning is also calm, so that the satellite located in that region does not go out that region easily. Therefore, the long duration enhancement of earthward flow is observed in that region. Let us interpret the positions of the satellites which observed the sample two events shown in Introduction on the basis of these results. The properties in Fig. 1(a) were long enhancement of earthward flow speed, small variation of earthward component of magnetic field, small increase of northward component of magnetic field, and small decrease of plasma density. These properties are same as that observed in the region near the central plasma sheet and outside of the narrow channel of the Alfvénic fast flow. On the other hand, the properties in Fig. 1(b) were short enhancement of earthward flow speed, very small variation of plasma density, and large variation of earthward component of magnetic field. These were clearly same as the results observed at the near plasma sheet boundary layer. In summary, we have demonstrated that the time variation of plasma quantities in the earthward fast flow event depends on the satellite position, in particular on the position relative to narrow channel of Alfvénic fast flow.

Acknowledgments. This work was supported by Grant-in-Aids for Creative Scientific Research ‘The Basic Study of Space Weather Prediction’ (17GS0208, Head Investigator: K. Shibata)

from the Ministry of Education in Japan, Mitsubishi Foundation, RISH of Kyoto University, and Solar Terrestrial Environment Laboratory of Nagoya University. The computer program was tested and run at the Computational Centers of Nagoya and Kyoto University. Geotail magnetic field and plasma data were provided by T. Nagai and T. Mukai through DARTS at Institute of Space and Astronautical Science, JAXA in Japan.

References

- Angelopoulos, V., W. Baumjohann, C. F. Kennel, F. V. Coroniti, M. G. Kivelson, R. Pellat, R. J. Walker, H. Luhr, and G. Pashmann, Bursty bulk flows in the inner central plasma sheet, *J. Geophys. Res.*, **97**, 4027–4039, 1992.
- Kondoh, K. and M. Ugai, Study of three dimensional structure of the fast convection flow in the plasma sheet by MHD simulations on the basis of spontaneous fast reconnection model, *Adv. Space Res.*, **39**, 1378–1381, 2007.
- Petschek, H. E., Magnetic field annihilation, *Magnetic Field Annihilation, NASA Spec. Publ. SP-50*, 425–439, 1964.
- Sergeev, V. A., J.-A. Sauvaud, D. Popescu, R. A. Kovrazhkin, K. Liou, P. T. Newell, M. Brittnacher, G. Parks, R. Nakamura, T. Mukai, and G. D. Reeves, Multiple-spacecraft observation of a narrow transient plasma jet in the Earth’s plasma sheet, *Geophys. Res. Lett.*, **27**, 851–854, 2000.
- Shiokawa, K. *et al.*, Braking of high-speed flows in the near-Earth tail, *Geophys. Res. Lett.*, **24**, 1179–1182, 1997.
- Ugai, M., Self-consistent development of fast magnetic reconnection with anomalous plasma resistivity, *Plasma Phys. Controlled Fusion*, **26**, 1,549–1,563, 1984.
- Ugai, M., Global dynamics and rapid collapse of an isolated current-sheet system enclosed by free boundaries, *Phys. Fluids*, **29**, 3,659–3,667, 1986.
- Ugai, M. and K. Kondoh, Computer studies on the spontaneous fast reconnection evolution in various physical situations, *Phys. Plasmas*, **8**, 1,545–1,552, 2001.
- Ugai, M., K. Kondoh, and T. Shimizu, Computer simulations on three-dimensional magnetic loop dynamics by the spontaneous fast reconnection model, *Phys. Plasmas*, **10**, 357–363, 2003.
- Ugai, M., K. Kondoh, and T. Shimizu, Computer studies on the three-dimensional spontaneous fast reconnection model as a nonlinear instability, *Phys. Plasmas*, **11**, 1,416–1,423, 2004.
- Ugai, M., K. Kondoh, and T. Shimizu, Spontaneous fast reconnection model in three dimensions, *Phys. Plasmas*, **12**, 042903, 2005.

K. Kondoh (e-mail: kondo@cs.ehime-u.ac.jp), M. Ugai, and T. Shimizu

Timing of substorm related auroral oscillations

P. Martin¹, N. E. Turner¹, and J. Wanliss²

¹Florida Institute of Technology

²Presbyterian College

(Received October 26, 2007; Accepted August 16, 2008; Online published May 29, 2009)

Previous studies have shown that auroral luminosity oscillations are often associated with substorms. Here we examine photometer data for the magnetospheric substorm on April 1, 2000 (expansive phase onset at 0525 UT) to study the detailed timing of the auroral oscillations relative to onset. Accurate timing information for the periodicities in the photometer data were determined using the wavelet transform. We find that the oscillations occur primarily during the recovery phase.

Key words: Aurora, substorm, wavelet, CANOPUS.

1. Introduction

Magnetospheric substorms are among the more consequential space weather effects, second in importance only to the massive and global space storms. Several studies have considered the effects of magnetohydrodynamic (MHD) waves on particle precipitation in the ionosphere (Berger, 1963; Davidson, 1990; Milan *et al.*, 2001), and a strong link has been suggested between discrete auroral arcs and MHD waves (Samson *et al.*, 1996; Wanliss and Rankin, 2002; Wanliss *et al.*, 2002). MHD field line resonances (FLRs) are formed through wave coupling of compressional and shear Alfvén waves. The local compression of the magnetosphere at substorm expansive phase onset generates compressional MHD waves that encounter positive gradients in the Alfvén velocity leading to the excitation of shear Alfvén waves on the magnetic shells distant from the source of the onset. Because of the coupling of energy at spatially different locations, auroral activity is expected to occur at high and low latitudes. Theory predicts that the high latitude activity will feature a poleward phase shift of 180 degrees across the belt of auroral oscillation (Hughes, 1983; Liu *et al.*, 1995). Similarly, the low latitude activity should exhibit a 180 degree equatorward phase shift and a temporarily varying parallel electric field will be established along the resonant field line (Block and Fälthammer, 1990; Liu *et al.*, 1995). A consequence of this parallel electric field is the periodicities of the precipitating protons and electrons are anti-correlated. If there were no parallel electric field there should be no such phase difference and the precipitation of protons and electrons would likely be similarly modulated (Liu *et al.*, 1995).

In this study we examine the timing of substorm associated auroral oscillations in order to determine which substorm phase they are associated with. The data are for the substorm on April 1, 2000 previously studied in detail by

Wanliss and Rankin (2002). They found 2.2 mHz pulsations in magnetometer and photometer data. The proton and electron auroras were found to oscillate essentially out of phase, and the variation of phase across the peak in the luminosity resonance followed the pattern expected for the coupling of resonant Alfvén modes by normal compressional modes in the magnetotail. The previous work established accurate frequency information, but here we wish to establish detailed timing of the oscillations, a task for which the multiple filters of the wavelet transform are best suited.

2. Data Description

Wanliss and Rankin (2002) used photometer data from the Gillam meridian scanning photometer in northern Canada and found luminosity oscillations associated with magnetospheric substorms. They examined photometer and magnetometer data of a magnetospheric substorm on April 1, 2000 which had its expansive phase onset at 0525 UT. They examined the proton (486.1 nm) and electron (557.7 nm, 630.0 nm) auroras. The 486.1 nm ($H\beta$) emission is caused by precipitation of protons of tens of keV, 557.7 nm from hot electrons of several keV, and 630.0 nm from warm electrons of a few hundred eV. This particular substorm occurred during a moderate space storm recovery phase with minimum $D_{st} = -60$ nT. Figure 1 shows the 557.7 nm photometer data from the Gillam station (GILL). The data show brightness (Rayleighs) as a function of latitude and time. Each meridian scan takes one minute to complete, and data are organized into 17 latitudinal bins. The substorm growth phase is indicated by the steady equatorward motion of the auroras prior to 0525 UT, indicative of stretching of the inner magnetotail (Wanliss *et al.*, 2000). At this time the emissions brighten and begin to move poleward, indicative of dipolarization of the previously stretched field lines.

A Fourier spectrogram of each wavelength revealed a peak around 2.2 mHz (Wanliss and Rankin, 2002). The 630.0 nm wavelength also showed peaks at 2.9 and 3.8 mHz. Using CANOPUS magnetometer data the Pi2

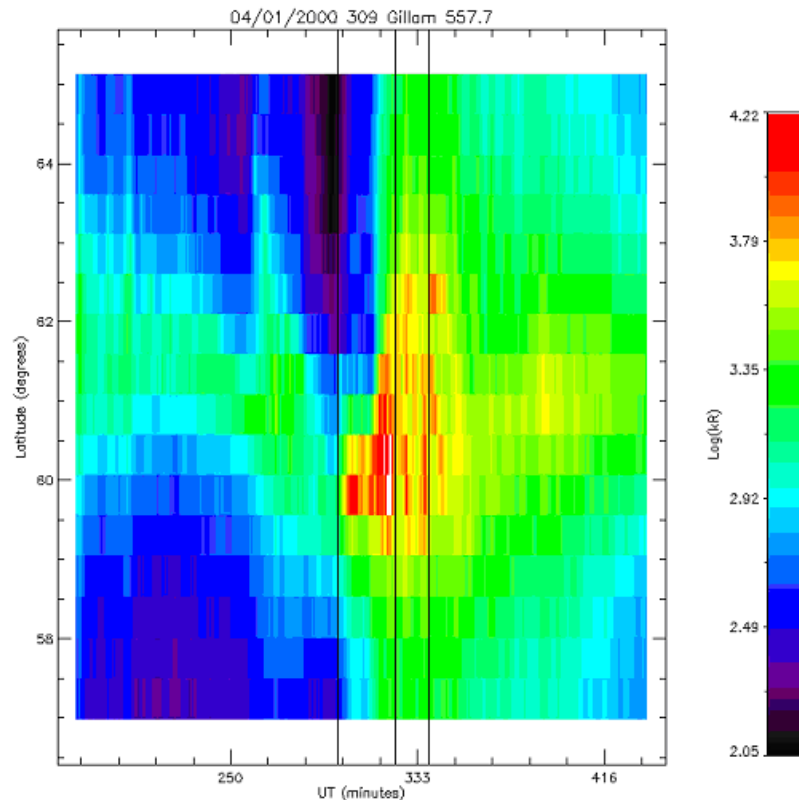


Fig. 1. Photometer data (557.7 nm) from the Gillam station for April 1, 2000 where substorm onset begins at the 309th minute of the day. The first vertical line indicates substorm onset and the two other lines indicate an equatorward intensification of the aurora.

pulsation was found to be localized between 67.4 and 69.7 degrees geomagnetic latitude. A phase correlation analysis was performed to determine if the spectral peaks might be related to field line resonances (FLR). The signals at 66.6, 66.1, and 65.6 degrees magnetic latitude, were anti-correlated which is consistent with a FLR and a parallel electric field. The phase shift around 2.2 mHz showed a 120 degree phase shift at ~ 66 degrees for the 557.7 nm line which is lower than the theoretically required 180 degrees expected for a FLR (Chen and Hasegawa, 1974). For the 630.0 nm emission there was a 100 degree phase change which is qualitatively consistent but not quantitatively consistent with the FLR theory.

3. Wavelet Analysis Method

As with our previous work we produce a spectrogram of the photometer data for the substorm on April, 1 2000. Spectral analysis yields excellent frequency resolution for the peaks in the spectrogram, but poor timing information. In this study we seek good timing and frequency information, thus the wavelet transform is used to identify significant spectral power in frequency/time space. The varying size of the frequency/time bins makes it easier to identify wave power in time compared to the fixed size of the frequency/time bins in the windowed Fourier transform. Obviously, good time information results in decreased frequency resolution.

The output of the wavelet transform is both time and frequency dependent which is similar to the windowed Fourier transform. However, one obvious difference is the variable

time length of the wavelet which results in a variable scale size or frequency band. The user does not need to know the frequency band to be searched for significant waves. The time span of the wavelet determines the frequency of the band in the spectrum. The wavelet makes multiple passes through the time series, adjusting its size for each pass. This is necessary to guarantee a complete period will fit in the wavelet and be recognized as a true wave, not a discontinuity. The resulting wave power is distributed in frequency and time. The highest possible frequency of the wavelet transform is the Nyquist frequency which is determined by the sampling rate. The lowest possible frequency is determined by the time length of the time series. The version of the wavelet transform used in this study, required a minimum of eight complete wavelets to fit in the time series. The time length of the wavelet determines the lowest possible frequency. The multiple scale sizes also provide an advantage, in terms of timing issues, over the windowed Fourier transform. There is little power leakage along the time axis.

The power element of the wavelet transform represents the variance of the original time series at a specific range of time and frequency. Percival and Walden (1993, 2000) and Torrence and Compo (1998) showed the distribution of the power elements of the windowed Fourier and wavelet spectrums are similar to a chi-square distribution with 2 degrees of freedom. Therefore, analysis of variance (ANOVA) can be performed on the output to determine an accurate estimate of the frequency/time spectrum of the time series or the power spectral density (PSD).

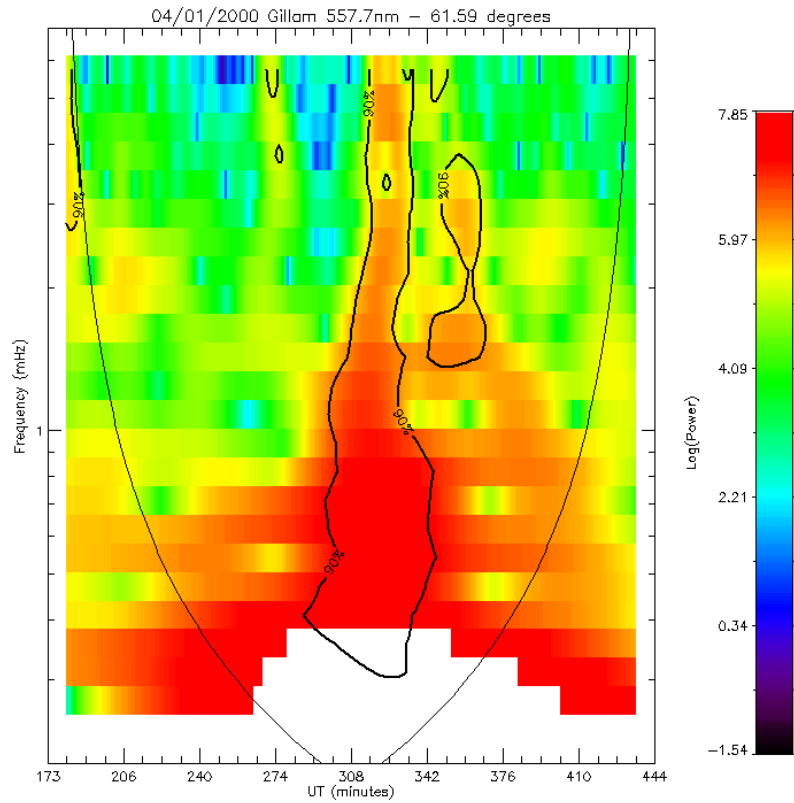


Fig. 2. The wavelet spectrum of the 557.7 nm photometer data measured at 61.6 degrees latitude. The regions outlined highlight significant spectral power.

486.1 nm

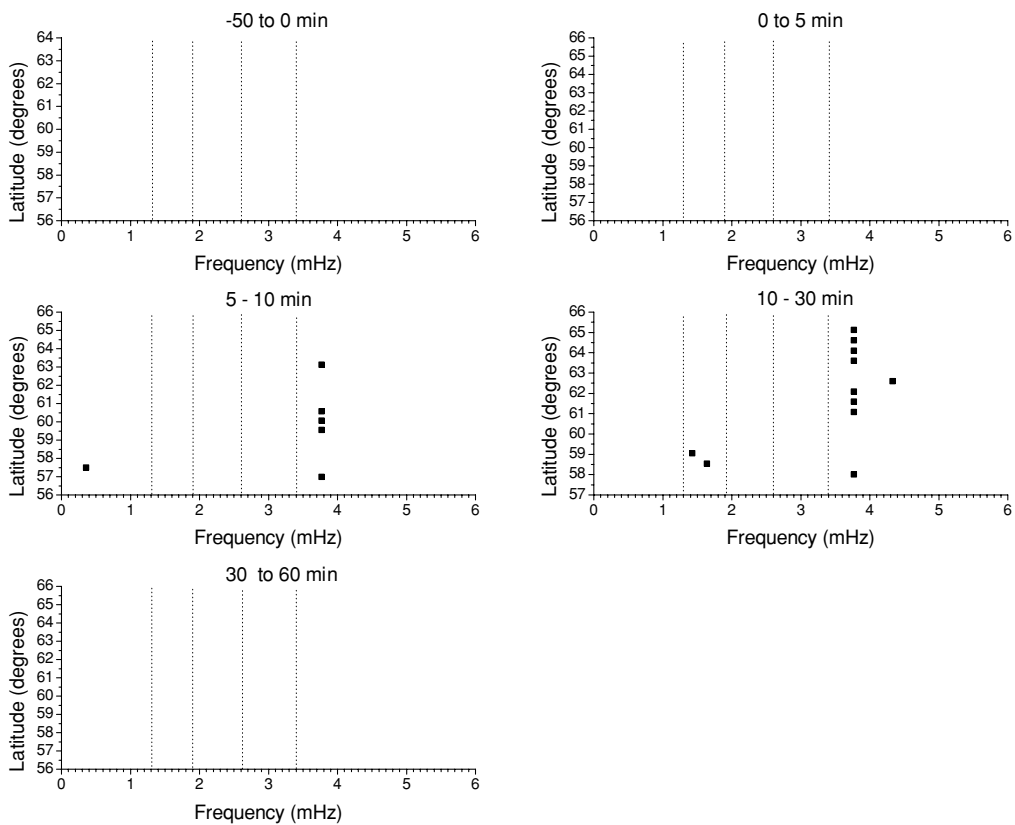


Fig. 3. The significant peaks in the 486.1 nm photometer spectra based on measurements at different latitudes. The data are divided into time intervals which represent the phases of the substorm. The vertical dashed lines mark the CMS frequencies greater than 1 mHz.

557.7 nm

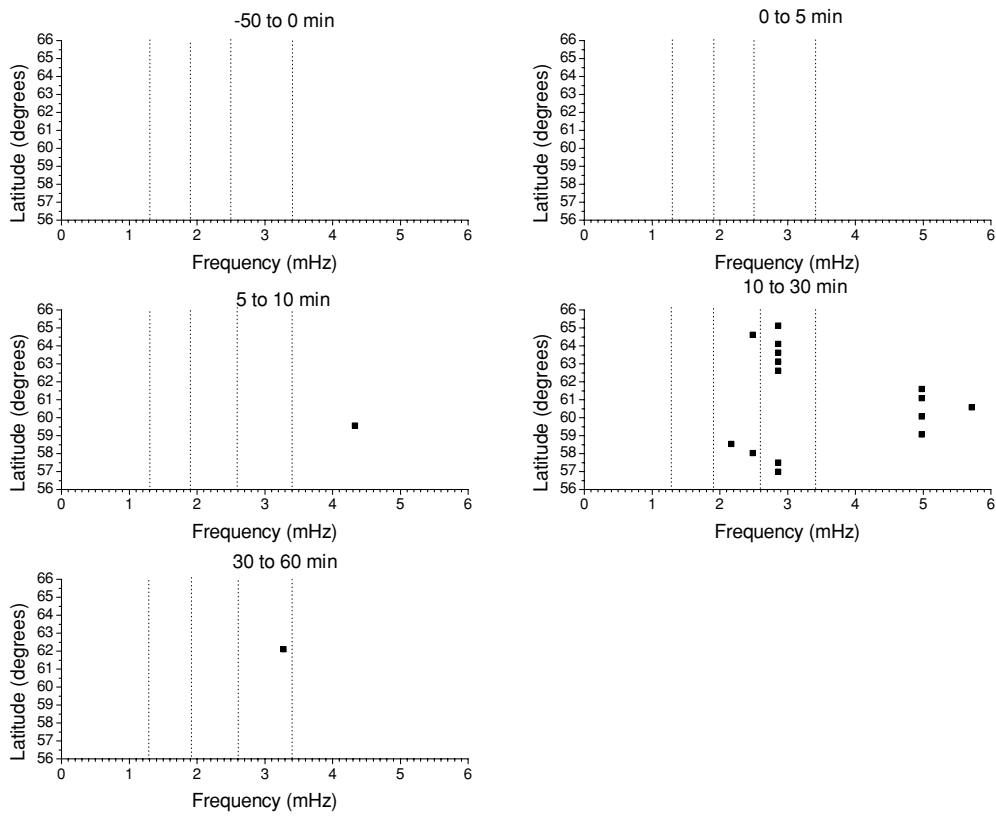


Fig. 4. The significant peaks in the 557.7 nm photometer spectra based on measurements at different latitudes.

630.0 nm

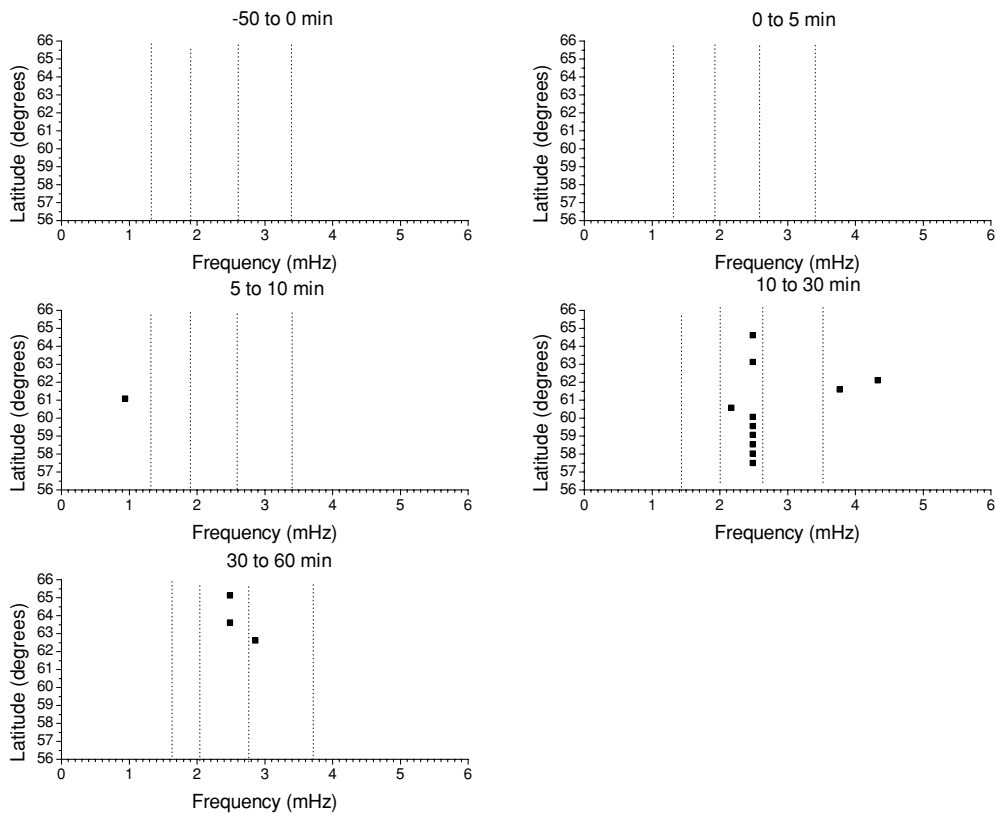


Fig. 5. The significant peaks in the 630.0 nm photometer spectra based on measurements at different latitudes.

The power spectrum is determined from the baseline power level for each frequency band from which wave amplitudes can be measured (Percival and Walden, 1993, 2000; Torrence and Compo, 1998). The process of analysis of variance for the wavelet power spectrum assumes the time series has a mean power spectrum (Torrence and Compo, 1998). If a peak in the spectrum is significantly above the background then it can be assumed to be a true feature with a particular percent confidence (Torrence and Compo, 1998). A 90% confidence level was calculated for each scale which spans the entire length of the time series (256 minutes). Any random power variable with a value less than the 90% confidence level has a 90% probability of being the true mean and was considered to be part of the background. A power value greater than the confidence level is considered extraordinary and therefore significant. Any significant power value is considered to be a real peak in the spectral estimate.

We have used the complex valued Morlet wavelet over a 256 minute interval (± 128 minutes from substorm onset). The time resolution of the continuous wavelet transform (CWT) increases at higher frequencies where the bandwidth gets larger (Press *et al.*, 1992; Percival and Walden, 2000). For this analysis, the transform is set up for 56 scales or frequency bins; there are 5 subscales for every scale and there are 11 scales. These scales span 0.47 mHz to 500 mHz which is the Nyquist frequency. The first 18 scales (0.47 to 5.73 mHz) were used for this analysis. Figure 2 shows the spectrogram for the 557.7 nm data with the 90% confidence level indicated.

4. Results

The significant peaks from the seventeen latitudes for each of the three auroral wavelengths are combined to create Figs. 3 through 5. The spectra are summarized according to latitude and frequency across the entire 256 minute interval around the substorm onset which is marked as time equal to zero. The error bars indicate the bandwidth of the peaks. The error bar range marks high and low frequencies where the signal/noise drops below a value of 1. The vertical dashed lines mark the CMS frequencies greater than 1 mHz as identified by Samson *et al.* (1991) (1.3, 1.9, 2.7 and 3.3 mHz).

We find that spectral peaks in the 3 observed auroral wavelengths (486.1, 557.7, and 630.0 nm) have a North-South alignment during the expansion phase of the substorm. The North-South arrangement is a result of the spectral peaks from the 17 different latitudes possessing the same frequency. In each of the three studied auroral wavelengths no significant wave activity is observed during the growth and early expansive phases of the substorm (-50 to 0 min, and 0 to 5 min). Figures 3 through 5 show that the peaks in the spectrum form a North-South arrangement near one of the CMS frequencies, with most significant activity occurring from 10 to 30 minutes after substorm onset when the expansion phase is well developed.

5. Discussion

The study by Wanliss and Rankin (2002) showed how oscillations in the aurora were tied to substorm initiated, field line resonances. Here we have considered the timing of the FLR. Whereas the previous study accurately determined the frequency of the auroral oscillations, here we have utilized the wavelet transform to achieve accurate and quantitative isolation of the timing of *significant* oscillations. We find that the auroral oscillations for both electron and proton auroras do not begin at substorm expansion phase onset, but several minutes after the identified onset, and at a relatively localized latitude range. The oscillations intensify throughout the rest of the expansion phase across a wide range of latitudes, before dying down during the substorm recovery phase.

Acknowledgments. The Gillam meridian scanning photometer is owned and operated by the Canadian Space Agency. Work on this project by PM and NT was supported by NSF grant #0454685.

References

- Berger, S., Giant pulsations in the magnetic field and pulsating aurora, *Planet. Space Sci.*, **11**, 867, 1963.
- Block, L. and C.-G. Fälthammar, The role of magnetic-field-aligned electric fields in auroral acceleration, *J. Geophys. Res.*, **95**(A5), 5877–5888, 1990.
- Chen, L. and A. Hasegawa, A theory of long-period magnetic pulsations, I, Steady excitation of field line resonances, *J. Geophys. Res.*, **79**, 1024, 1974.
- Davidson, G. T., Pitch-angle diffusion and the origin of temporal and spatial structures in morningside aurorae, *Space Sci. Rev.*, **53**, 45, 1990.
- Hughes, W., Waves in magnetospheric plasmas: Editorial, *Geophys. Res. Lett.*, **10**(8), 601–602, 1983.
- Liu, W. W. *et al.*, Theory and observation of auroral substorms: a magnetohydrodynamic approach, *J. Geophys. Res.*, **100**, 79, 1995.
- Milan, S. E. *et al.*, Auroral forms and the field-aligned current structure associated with field line resonances, *J. Geophys. Res.*, **106**, 25825, 2001.
- Percival, D. B. and A. T. Walden, *Spectral Analysis for Physical Applications*, pp. 196–258, Cambridge University Press, 1993.
- Percival, D. B. and A. T. Walden, *Wavelet Methods for Time Series Analysis*, pp. 56–145, Cambridge University Press, 2000.
- Press, W. H., S. A. Teukolsky, W. T. Vetterling, and B. P. Flannery, *Numerical Recipes in C*, pp. 496–608, Cambridge University Press, 1992.
- Samson, J. C., R. A. Greenwald, J. M. Ruohoniemi, T. J. Hughes, and D. D. Wallis, Magnetometer and radar observations of magnetohydrodynamic cavity modes in the Earth's magnetosphere, *Can. J. Phys.*, **69**, 928, 1991.
- Samson, J. C. *et al.*, Observations of field line resonances, auroral arcs, and auroral vortex structure, *J. Geophys. Res.*, **101**, 17373–17383, 1996.
- Torrence, C. and G. P. Compo, A practical guide to wavelet analysis, *Bull. Am. Meteor. Soc.*, **79**(1), 61–78, 1998.
- Wanliss, J. A. and R. Rankin, Auroral substorm dynamics and field line resonances, *Earth Planets Space*, **54**, 927, 2002.
- Wanliss, J. A., J. C. Samson, and E. Friedrich, On the use of photometer data to map dynamics of the magnetotail current sheet during substorm growth phase, *J. Geophys. Res.*, **105**, 27673–27684, 2000.
- Wanliss, J. A., R. Rankin, J. C. Samson, and V. T. Tikhonchuk, Field line resonances in a stretched magnetotail: CANOPUS optical and magnetometer observations, *J. Geophys. Res.*, **107**(0), 10.1029/2001JA000257, 2002.

Statistically predicting Dst without satellite data

A. S. Parnowski

Space Research Institute NASU & NSAU, 40 prosp. Akad. Glushkova, Kyiv-187, 03680 MSP, Ukraine

(Received August 14, 2007; Revised September 16, 2007; Accepted September 23, 2007; Online published May 29, 2009)

In this paper we construct a regression relationship for predicting Dst 1 hour ahead. Our model uses only previous Dst values. This regression is totally unbiased and does not rely on any physical model, except for the fact that Dst somehow contains the information on the recurrent geomagnetic storms. This regression has the prediction efficiency of 0.964, linear correlation with official Dst index of 0.982, and RMS of 4.52 nT. These characteristics are inferior only to our other model, which uses satellite data and provides the prediction efficiency of 0.975, linear correlation with official Dst index of 0.986, and RMS of 3.76 nT. This makes it quite suitable for prediction purposes when satellite data are not available.

Key words: Space weather, statistical model, Dst prediction.

1. Introduction

Space weather prediction is one of the main tasks of modern space research. The necessity of such activities was well understood for a long time (Marubashi, 1989). Space weather prediction activities divide into two large categories: prediction of space weather directly in space, and prediction of space weather manifestations on the Earth. The first category is mostly important for planning of space missions, predicting and evading hardware failures of spacecraft due to arcing in electronic components, and assuring astronaut safety with respect to radiation hazard. These tasks mainly require prediction of energetic particle fluxes. The second category deals with influence of space weather on power grid operation, radio communications, and health of people, especially those with cardiovascular diseases. These tasks mainly require prediction of geomagnetic disturbances. This article will focus on space weather prediction on the Earth.

There are many quantitative indices of geomagnetic activity. The most widely used of them are storm-time disturbance Dst and planetary geomagnetic activity index Kp. Dst is more convenient for prediction purposes, because it directly equals the disturbance of H -component on the Earth measured in gammas ($1\gamma = 10^{-4}\text{Gs} = 1\text{nT}$). It is averaged over several low- and mid-latitude magnetometer stations and is usually associated with the westward ring current, which appears during the storm at $4\text{--}8R_E$, although this association was strongly criticized by e.g. Campbell (1996). At the same time, Kp is an integral and more artificial characteristic of the overall level of geomagnetic disturbance. In this paper Dst is used for space weather prediction.

Space weather prediction is a challenging and nontrivial activity (Joselyn, 1995; Li *et al.*, 2003). Since Burton *et al.*

(1975) published their pioneering work, many authors tried to forecast space weather indices. Papers (Kugblenu *et al.*, 1999; Watanabe *et al.*, 2002; Wing *et al.*, 2005; Palloccchia *et al.*, 2006) featured neural network approach; papers (Zhou and Wei, 1998; Balikhin *et al.*, 2001; Harrison and Drezet, 2001) incorporated adaptive filtering; papers (Rangarajan and Barreto, 1999; Oh and Yi, 2004; Wei *et al.*, 2004; Johnson and Wing, 2004) applied statistical methods; papers (Burton *et al.*, 1975; Valdivia *et al.*, 1996; O'Brien and McPherron, 2000a, b; Temerin and Li, 2002; Ballatore and Gonzales, 2003; Cid *et al.*, 2005; Siscoe *et al.*, 2005; Temerin and Li, 2006) used empirical models; and papers (Dryer *et al.*, 1984; Raeder *et al.*, 2001) developed global MHD simulations.

The best results for 1-hour prediction were achieved by Temerin and Li (2002, 2006), who used an empirical model. They achieved the prediction efficiency of 0.91, linear correlation of 0.95 and RMS of 6.4 nT. Neural network approach provides short-term predictions up to 4 hours in the paper (Wing *et al.*, 2005). It experiences significant difficulties predicting geomagnetic storms with $Kp > 5$, though. Adaptive filtering seems more successful being able to provide 8-hour predictions in the paper (Harrison and Drezet, 2001). However, in the papers, which incorporate adaptive filtering, the volume of the dataset usually does not exceed 6 months of data (4380 points), which is not enough to correctly describe long-time variations in geomagnetic activity, caused, e.g., by 11-year solar cycle. Statistical methods give interesting results, but were rarely used for prediction, and much more often for developing and constraining empirical models (Johnson and Wing, 2004). Empirical models were the most often used, and provided some of the best 1-hour predictions. Most of them are improvements of the empirical relationship proposed in a pioneering paper by Burton *et al.* (1975), who analysed the ring current injection and decay. However, their model suffered from the lack of solar wind data and poor physical understanding of solar wind-magnetosphere interaction at that time. Global MHD simu-

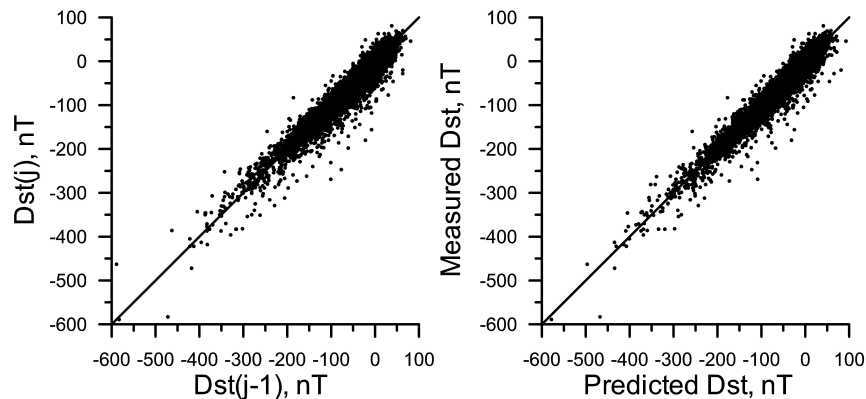


Fig. 1. Scatter plots of measured Dst versus Dst 1 hour ago (on the left) and versus predicted Dst (on the right).

lations give the longest prediction times but fail to correctly describe kinetics in boundary layers and ballooning instabilities, which are believed to be responsible for the sub-storm onset.

Here we use the same method as in our other article (Parnowski, 2008), which combines statistical and empirical approaches. We payed attention mostly to 1-hour prediction, though we obtained a 9-hour prediction as well. We predicted Dst 1 hour ahead because the temporal resolution of the dataset was 1 hour, so we just predicted the next value in the series. Besides, longer prediction times resulted in predicted value being shifted in time. For prediction we use only that information, which is available at the moment when prediction is made, i.e. 1 hour prior to the predicted value. We will reference to this value as “1 hour ago”. We determine the quality of prediction by 3 values: residual mean square (RMS), prediction efficiency (PE), defined as $[1 - (\text{mean squared residual})/(\text{variance of data})]$ (Temerin and Li, 2002), and the linear correlation coefficient (LC) between the prediction and Dst. In the article (Parnowski, 2008) we constructed a regression relationship, which provides $PE = 0.975$, $LC = 0.986$, and $RMS = 3.76$ nT.

However, this relationship requires satellite data to be continuous for the previous 20 hours. Thus, when the data contain a gap for some reason, we are unable to predict Dst for the next 20 hours. For this reason, we need an ‘emergency’ regression, which would operate without satellite data. Besides, satellite data are often missing during very strong geomagnetic storms, which are the most interesting events. Such a regression will be constructed in this article.

2. Data, Routine and Results

We used the OMNI 2 database, available at NSSDC (<http://nssdc.gsfc.nasa.gov/omniweb/>). It contains IMF, solar wind and geomagnetic data, averaged over 1-hour intervals (49 parameters in total, starting from Jan 1, 1963). The complete 43-year Dst time series given therein is continuous and features an eye-visible 27-day and 11-year periodicity, which hints for strong dependence on solar activity.

We seek Dst in a regression form

$$\text{Dst}(j) = \sum_i C_i x_i,$$

where j is the current step (number of hours since Jan 1,

1963), C_i are the regression coefficients, and x_i are the regressors, which are functions of input quantities and their combinations. Values of C_i are determined by the least square method with equal statistical weights of all points, and the statistical significance of the regressors—by Fisher test (Fisher, 1954; Hudson, 1964).

The initial number of regressors was deliberately excessive to let Fisher test select the most statistically significant of them. This was done in the following way. After processing the data with the least square method, Fisher significance parameter F was determined for each regressor. All F values were compared to the values 2.7055, 3.84, 5.02, 6.635, 7.879, 10.83 and 12.1, which correspond to statistical significance of 90, 95, 97.5, 99, 99.5, 99.9 and 99.95% respectively. Then, insignificant regressors were rejected and the routine was repeated until all the regressors were significant. We chose the minimal significance level of 90%. In contrast to empirical models we do not add fitting parameters and all the regressors have obvious physical meaning. The described routine was applied to the complete 43-year dataset sans rejects. More details on the routine can be found in the paper (Parnowski, 2008).

First, we determined which previous Dst values are statistically significant. For this purpose, we constructed a regression

$$\text{Dst}(j) = C_0 + \sum_{i=1}^N C_i \text{Dst}(j-i),$$

where N is the oldest Dst value; we reached the value $N = 900$. We found that there are statistically significant values as far as 801 hours ago (33 days and 9 hours). The statistical significance of this oldest value is over 99.9%. However, it is possible that there are even older statistically significant values. A similar situation was reported by Johnson and Wing (2004) regarding Kp: “the significance is often quite large for extended periods of time (10–20 days)”. This might be related in some way to recurrent geomagnetic storms, but some additional research is required before final explanation could be given to this phenomenon. This will be done in a future article.

After determining which previous Dst values are statistically significant, we added nonlinear terms. We tried different powers of the most significant terms and their products.

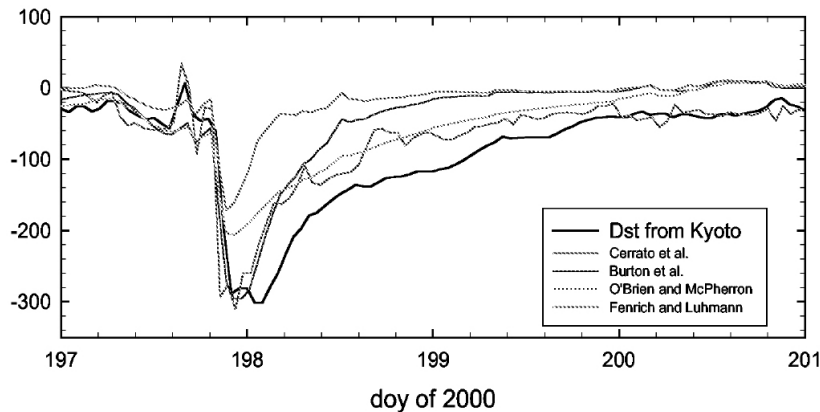


Fig. 2. Experimental Dst index data and theoretical predictions from several models. Reprinted from (Cid *et al.*, 2005). “Dst from Kyoto” stands for the official Dst index from WDC-B.

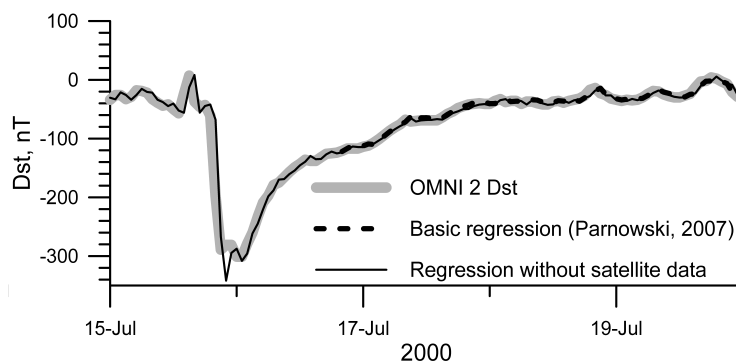


Fig. 3. Our prediction for the same period of time as on Fig. 2. Satellite data is missing in the left part of the plot.

Thus, we constructed a regression, which consisted only of Dst terms and a constant regressor. Its characteristics are: $PE = 0.964$, $LC = 0.982$, $RMS = 4.53$ nT.

To illustrate predictive capabilities of our model we present several figures: Fig. 1 shows scatter plots of measured Dst versus Dst 1 hour ago (it is the simplest possible prediction model) on the left and versus prediction on the right; Fig. 2 shows predictions by Cerrato *et al.* (2004), Fenrich and Luhmann (1998), O’Brien and McPherron (2000b), and Burton *et al.* (1975) for Jul 15–19, 2000; Fig. 3 shows our prediction for the same period of time.

More comparison with other models can be found in the paper (Parnowski, 2008).

3. Conclusion

It appeared possible to predict Dst 1 hour ahead using only its previous values. This hints for recurrent behaviour of geomagnetic activity. In terms of prediction efficiency and linear correlation with the official Dst index this model is inferior to the model, which uses satellite solar wind data. However, satellite data is often missing during strong geomagnetic storms and this model can be used to fill the gap in predicted Dst time series. Thus, a combination of a regression model using satellite data with the model obtained in this article can provide accurate on-line operational Dst forecast.

Of course, larger prediction times are desirable, but 1-hour prediction is still useful. For example, magnetometers

can be switched to high temporal resolution mode, sensitive equipment can be turned off, etc.

4. Summary

In this article we obtained the following results:

1. We derived a regression, which relies only on previous Dst values.
2. It allows predicting Dst 1 hour ahead with $PE = 0.964$, $LC = 0.982$ and $RMS = 4.53$ nT. Thus, it is very convenient for on-line Dst prediction when satellite data are not available.
3. Previous Dst values are statistically significant up to 801 hours ago and possibly more.
4. Nonlinear terms appeared to be very significant.

Acknowledgments. Author is grateful to the National Space Science Data Center for the OMNI 2 database.

References

- Balikhin, M. A., O. M. Boaghe, S. A. Billings, and H. St. C. K. Alleyne, Terrestrial magnetosphere as a nonlinear resonator, *Geophys. Res. Lett.*, **28**, 1123–1126, 2001.
- Ballatore, P. and W. D. Gonzalez, On the estimates of the ring current injection and decay, *Earth Planets Space*, **55**, 427–435, 2003.
- Burton, R. K., R. L. McPherron, and C. T. Russell, An empirical relationship between interplanetary conditions and Dst, *J. Geophys. Res.*, **80**, 4204–4214, 1975.
- Campbell, W. H., Geomagnetic storms, the Dst ring-current myth and lognormal distributions, *J. Atm. Terr. Phys.*, **58**, 1171–1187, 1996.

- Cerrato, Y., E. Saiz, C. Cid, and M. A. Hidalgo, Geomagnetic storms: their sources and a model to forecast Dst index, in *Lecture notes and essays in Astrophysics*, pp. 131–142, 2004.
- Cid, C., E. Saiz, and Y. Cerrato, Physical models to forecast the Dst index: comparison of results, *Proc. Solar Wind 11—SOHO 16 “Connecting Sun and Heliosphere”*, Whistler, Canada 12–17 June 2005 (ESA SP-592, September 2005), 116–119, 2005.
- Dryer, M., S. T. Wu, G. Gislason, S. M. Han, Z. K. Smith, J. F. Wang, D. F. Smart, and M. A. Shea, Magneto-hydrodynamic modelling of interplanetary disturbances between the Sun and Earth, *Astrophys. Space Sci.*, **105**, 187–208, 1984.
- Fenrich, R. R. and J. G. Luhmann, Geomagnetic response to magnetic clouds of different polarity, *Geophys. Res. Lett.*, **25**, 2999, 1998.
- Fisher, R. A., *Statistical methods for research workers*, Tweleventh edition, London, Oliver and Boyd, 1954.
- Harrison, R. F. and P. M. Drezet, The application of an adaptive non-linear systems identification technique to the on-line forecast of Dst index, *Proc. Les Woolliscroft memorial Conf. / Sheffield Space Plasma Meeting: Multipoint measurements versus theory*, Sheffield, UK, Apr 24–26, 2001 (ESA SP-492), 141–146, 2001.
- Hudson, D. J., *Statistics Lectures on Elementary Statistics and Probability*, Geneva, CERN, 1964.
- Johnson, J. R. and S. Wing, A cumulant-based analysis of nonlinear magnetospheric dynamics, *Report PPPL-3919rev*, http://www.pppl.gov/pub_report/2004/PPPL-3919rev.pdf, 2004.
- Joselyn, J. A., Geomagnetic activity forecasting—the state-of-the-art, *Rev. Geophys.*, **33**, 383–401, 1995.
- Kugblenu, S., S. Taguchi, and T. Okuzawa, Prediction of the geomagnetic storm associated Dst index using an artificial neural network algorithm, *Earth Planets Space*, **51**, 307–313, 1999.
- Li, X., M. Temerin, D. N. Baker, G. D. Reeves, D. Larson, and S. G. Kanekal, The predictability of the magnetosphere and space weather, *EOS*, **84**, 2003.
- Marubashi, K., The space weather forecast program, *Space Sci. Rev.*, **51**, 197–214, 1989.
- O’Brien, T. P. and R. L. McPherron, Forecasting the ring current index Dst in real time, *J. Atm. Sol.-Terr. Phys.*, **62**, 1295–1299, 2000a.
- O’Brien, T. P. and R. L. McPherron, An empirical phase-space analysis of ring current dynamics: Solar wind control of injection and decay, *J. Geophys. Res.*, **105**, 7707, 2000b.
- Oh, S. Y. and Y. Yi, Relationships of the solar wind parameters with the magnetic storm magnitude and their association with the interplanetary shock, *J. Korean Astron. Soc.*, **37**, 151–157, 2004.
- Palloccchia, G., E. Amata, G. Consolini, M. F. Marcucci, and I. Bertello, ANN prediction of the Dst index, *Mem. S.A.It. Suppl.*, **9**, 120–122, 2006.
- Parnowski, A. S., Dst prediction using the linear regression analysis, *Kosmichna Nauka i Tekhnologiya*, 2008 (accepted, in Russian).
- Raeder, J. *et al.*, Global simulation of the Geospace Environment Modeling substorm challenge event, *J. Geophys. Res.*, **106**, 381–396, 2001.
- Rangarajan, G. K. and L. M. Barreto, Use of Kp index of geomagnetic activity in the forecast of solar activity, *Earth Planets Space*, **51**, 363–372, 1999.
- Siscoe, G., R. L. McPherron, M. W. Liemohn, A. J. Ridley, and G. Lu, Reconciling prediction algorithms for Dst, *J. Geophys. Res.*, **110**, A02215, doi:10.1029/2004JA010465, 2005.
- Temerin, M. and X. Li, A new model for the prediction of Dst on the basis of the solar wind, *J. Geophys. Res.*, **107**, 1472, doi:10.1029/2001JA007532, 2002.
- Temerin, M. and X. Li, Dst model for 1995–2002, *J. Geophys. Res.*, **111**, A04221, doi:10.1029/2005JA011257, 2006.
- Valdivia, J. A., A. S. Sharma, and K. Papadopoulos, Prediction of magnetic storms by nonlinear models, *Geophys. Res. Lett.*, **23**, 2899–2902, 1996.
- Watanabe, S., E. Sagawa, K. Ohtaka, and H. Shimazu, Prediction of the Dst index from solar wind parameters by a neural network method, *Earth Planets Space*, **54**, 1263–1275, 2002.
- Wei, H. L., S. A. Billings, and M. A. Balikhin, Analysis of the geomagnetic activity of the Dst index and self-affine fractals using wavelet transforms, *Nonlinear Process. Geophys.*, **11**, 303–312, 2004.
- Wing, S., J. R. Johnson, J. Jen, C.-I. Meng, D. G. Sibeck, K. Bechtold, J. Freeman, K. Costello, M. Balikhin, and K. Takahashi, Kp forecast models, *J. Geophys. Res.*, **110**, A04203, doi:10.1029/2004JA010500, 2005.
- Zhou, X.-Y. and F.-S. Wei, Prediction of recurrent geomagnetic disturbances by using adaptive filtering, *Earth Planets Space*, **50**, 839–845, 1998.

A. S. Parnowski (e-mail: dyx@ikd.kiev.ua)

Properties of dayside nonlinear rising tone chorus emissions at large L observed by GEOTAIL

Olga P. Verkhoglyadova^{1,2}, Bruce T. Tsurutani³, Y. Omura², and S. Yagitani⁴

¹University of California, Riverside, USA

²RISH, Kyoto University, Uji, Kyoto, Japan

³Jet Propulsion Laboratory, CalTech, Pasadena, USA

⁴Kanazawa University, Kanazawa, Japan

(Received September 10, 2007; Revised November 11, 2007; Accepted December 20, 2007; Online published May 29, 2009)

This paper studies some wave properties of nonlinear rising tone chorus emissions in the outer regions of the dayside equatorial magnetosphere at $\sim(6.3, -4.7, 0.7R_E)$ in GSE coordinates. We analyze data obtained with the PWI and WFC receivers on GEOTAIL associated with a substorm on April 29, 1993. Fine structure of the chorus elements and inter-element spacings are shown. Directions of propagation of the chorus elements relative to the local magnetic field lines are analyzed. Wave polarizations, intensities and spectral properties of chorus in the equatorial Earth's magnetosphere are discussed.

Key words: Chorus emissions, wave-particle interactions, electron acceleration.

1. Introduction

Major chorus statistical properties have been presented in Tsurutani and Smith (1974, 1977), Nagano *et al.* (1996) and Meredith *et al.* (2001, 2003). Recently, progress has been made in studies of wave properties in the generation region, such as fine structure and propagation of chorus (Santolik *et al.*, 2003, 2004) using multipoint Cluster measurements. We will summarize some relevant chorus characteristics below.

Chorus ELF waves are observed in the outer magnetosphere at $L > 5R_E$ primarily in two latitude regions, and have been classified into equatorial and high-latitude chorus (Tsurutani and Smith, 1977). Equatorial chorus ($MLAT < 15^\circ$) occurs during substorms with the peak intensity near the magnetic equator. These waves are believed to be generated by trapped substorm electrons via a cyclotron resonance instability (see also Lauben *et al.*, 2002). High-latitude chorus is detected near the magnetopause and has little apparent connection with substorm activity. Our study is focused on the near-equatorial dayside chorus waves.

Equatorial chorus is an electromagnetic whistler mode wave observed as two distinct bands, one above and one below 0.5 of the local electron gyrofrequency, ν_{ce} (Tsurutani and Smith, 1974). The wave absence at $0.5\nu_{ce}$ can be explained by Landau damping. Chorus is often composed of ~ 0.5 sec elements. There are several types of frequency-time chorus structures: rising and falling tones, and narrow-band (structureless) chorus. Chorus is a nonlinear emission. Its elements are composed of sub-elements or wave packets separated by intervals of noise (Santolik *et al.*, 2003). Chorus plays an important role in wave-particle interac-

tions in the outer magnetosphere (Tsurutani and Lakhina, 1997; Horne *et al.*, 2005). An up-to-date review of the chorus-driven electron acceleration based on CRRES observations was made by Meredith *et al.* (2001, 2003). Computer modeling results on relativistic electron interaction with whistler mode waves were reported by Omura and Summers (2004). In the case of a chorus element, contribution to the pitch-angle diffusion from a nearly monochromatic large-amplitude sub-element(s) can be much larger than from an average wave field of the whole element. The main focus of this study is on properties of nonlinear chorus emissions which could be important for wave-particle interactions, i.e., fine structure of the chorus waves, direction of propagation, polarization and magnitudes of the magnetic field disturbances.

2. Analysis of the GEOTAIL Data

We present first results on four time intervals of wave activity during a substorm interval starting at ~ 2307 UT of April 29, 1993. A major negative excursion of the AL index started at ~ 2100 UT. Assuming chorus wave generation by gradient-drifting of 10–40 keV electrons, a delay time between the onset of chorus and a substorm is estimated as ~ 2 hrs (Tsurutani and Smith, 1974). Equatorial daytime chorus is expected to have maximum intensity at ~ 1000 LT due to the dayside maximum of energetic electron precipitation. This timing agrees with the beginning of rising tone chorus observations by GEOTAIL around ~ 930 LT. The satellite was located in the near-equatorial magnetosphere at $\sim(6.3, -4.7, 0.7R_E)$ (in GSE coordinates) and the geocentric distance of $\simeq 7.9R_E$ at the time of these observations. Intense chorus emissions were observed with the PWI and WFC instruments (Matsumoto *et al.*, 1993; Nagano *et al.*, 1996) onboard GEOTAIL. The PWI (plasma wave instrument) consists of a 3-component search-coil and 2 wire (elec-

Table 1. Properties of rising tone elements (see text for details).

Start time	Δt , sec	$\nu_{1,2}$, kHz	$\Delta\nu$, Hz	ν_0 , kHz	ν_{ce} , kHz	B_{max} , pT	θ , °	θ_G , °	θ_r , °
2306:55	0.3	0.9, 0.5	220	0.8	3.44	80	11	62	77
2306:55	0.15	0.75, 0.62	130	0.7	3.44	70	29	66	78
2311:39	0.3	0.95, 0.55	400	0.75	3.51	200	17	65	78
2321:07	0.68	1.1, 0.65	450	0.875	3.50	300	42	60	76
2349:31	0.7	1.1, 0.65	450	0.875	3.03	100	22	55	73
2349:31	0.6	1, 0.6	400	0.8	3.03	100	22	58	75

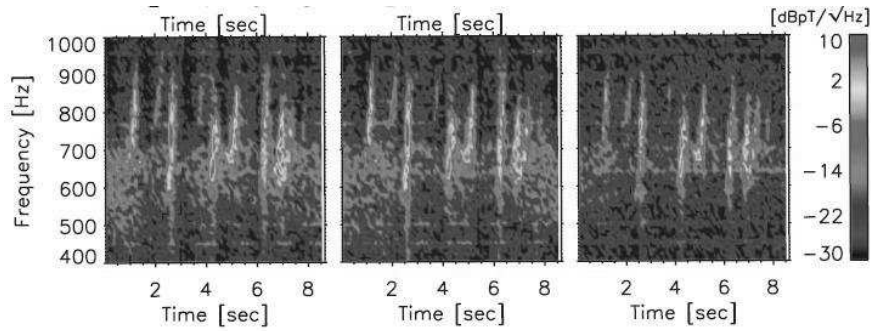


Fig. 1. Time-frequency power spectra of three magnetic field components in GSM coordinates derived from WFC measurements onboard GEOTAIL. The beginning of the interval corresponds to 2306:55 UT of April 29, 1993. The left, central and right panels correspond to B_x , B_y and B_z components.

tric) antennas with sensitivity of 1.5×10^{-5} nT/Hz $^{1/2}$ for the magnetic field and 8.0×10^{-9} V/(m Hz $^{1/2}$) for the electric field, respectively. The WFC (wave form capture) receiver samples 8.7 sec snapshots every 5 min between 10 Hz and 4 kHz. For each of the four time intervals of ~ 8.7 sec duration we select several distinct rising tone chorus elements. Properties of 6 such elements are summarized in Table 1. The following parameters were estimated: Δt is the duration of a rising tone element, $\nu_{1,2}$ are the maximum and minimum frequencies within the element, $\Delta\nu$ is the frequency band (bandwidth at half-maximum), ν_0 —average frequency of the tone, B_{max} —the maximum magnitude of magnetic field disturbance in the chorus, θ —the propagation angle to the local magnetic field line, θ_G —the local Gendrin angle calculated for ν_0 , and θ_r is the resonance angle. Average magnetic field components measured at $\sim 2306:55$ UT were (26.1, 52.1, 108.2 nT) in GSE coordinate system. An example of chorus is shown in Fig 1.

We process magnetic field waveforms in the principal or the minimum variance analysis (MVA) frame to find direction of propagation of the waves (Tsurutani and Smith, 1977), which corresponds to a direction of minimum variation. As it follows from the chorus generation mechanism, the most intense elements correspond to waves generated locally and propagating under small angles θ to the local magnetic fieldline (see also Goldstein and Tsurutani, 1984). Whereas waves generated far away have smaller magnitudes (due to Landau damping) and may be propagating obliquely to the local magnetic field line. Our results in Table 1 show that observed intense chorus emissions propagate under relatively small angles to the local magnetic field line. We found that chorus sub-elements sometimes have different directions of propagation relative to the background magnetic field.

The maximum angle of electromagnetic wave propaga-

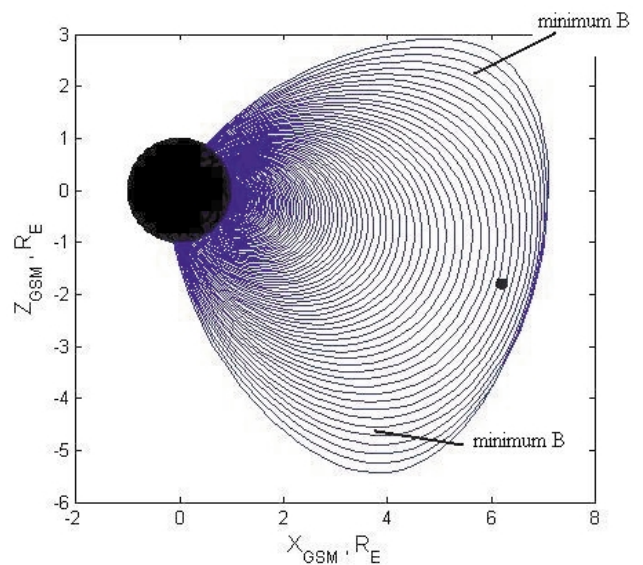


Fig. 2. A schematic view of the inner magnetosphere distorted by the solar wind compression obtained with the Tsyganenko model (Tsyganenko, 2002). A projection into noon local time plane is shown. The projection of the GEOTAIL spacecraft position into the (XZ) plane is indicated by a small dot. “Minimum B pockets” are shown.

tion relative to the magnetic field line is the resonance angle, $\cos(\theta_r) = \nu/\nu_{ce}$ (Goldstein and Tsurutani, 1984), presented in the last column of Table 1. The “Gendrin” angle, shown in the next to the last column of Table 1, is defined in linear plasma theory and corresponds to a minimum value of the refractive index parallel to the magnetic field line and is defined locally as $\cos(\theta_G) = 2\nu/\nu_{ce}$ (Gendrin, 1961). At the same time, the Gendrin angle is the upper limit for the angle θ . The condition for angular region $\theta = \pm\theta_G$ indicates a proximity to wave generation region for the lower-band

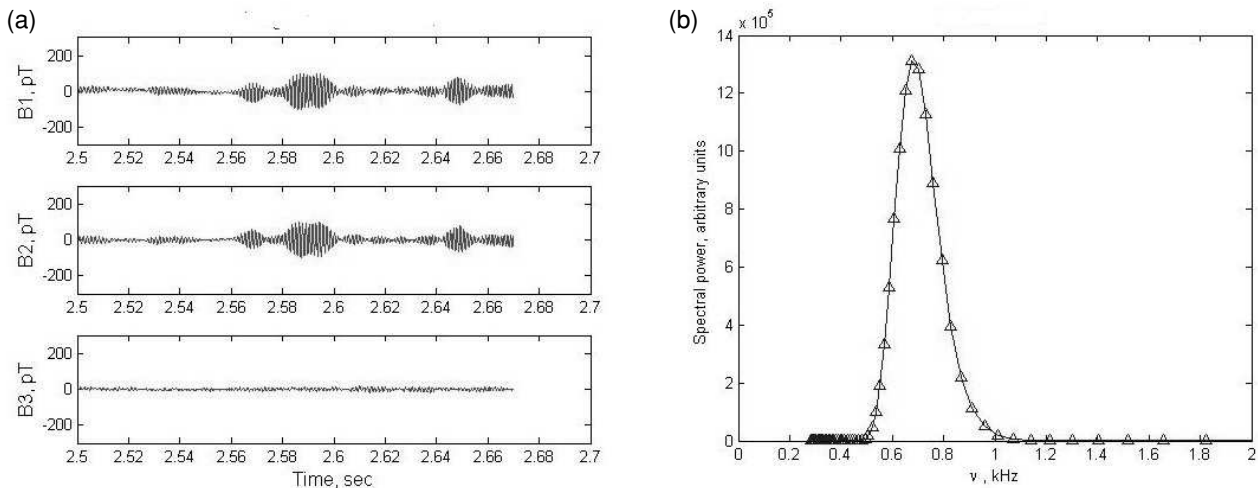


Fig. 3. (a) Example of magnetic field waveform of a chorus element shown in the principal frame. B_1 , B_2 and B_3 denote the maximum, intermediate and minimum variance directions, respectively. Notice sub-elements separated by intervals of noise. (b) Instantaneous spectrum of the chorus sub-element at $t \simeq 2.585$ sec obtained by using Morlet wavelet.

chorus ($\nu_0 < 0.5\nu_{ce}$) (Lauben *et al.*, 2002). The estimated θ_G in the Table 1 are quite large and are not close to $\pm\theta$.

By the definition and given constant wave frequency, θ_G is larger in the areas of large background magnetic field, B_0 , and smaller in the “minimum B pockets” (Tsurutani and Smith, 1977). What was the Geotail position in the dipole magnetic field? Figure 2 presents schematic view of the noon local time cross-section of the inner magnetosphere in the GSM coordinates. This sketch was produced with the Tsyganenko model (Tsyganenko, 2002) under undisturbed conditions. The beginning of the interval of Geotail observations was characterized by a very quiet ring current with minimum SYM-H $\simeq -10$ nT. For this model application we choose Dst = 0, IMF $B_z = 0$ and $B_y = 0$ (in GSM) and the solar wind dynamical pressure equal to 6 nPa. The magnetic dipole axis is tilted towards the X -axis of the GSM coordinate system.

A distortion (compression) of the outer dayside magnetosphere field lines as compared to a dipole field is clearly shown. Areas of minimum B_0 are situated at high magnetic latitudes and at large L ($r > 6R_E$). This sketch is similar to that in Tsurutani and Smith (1977). The small dot on the right side of the plot is the GEOTAIL position in the (XZ) plane. The GEOTAIL GSM coordinates were $\sim(6.3, -4.4, -1.7R_E)$. Thus, the satellite at the time of chorus measurements was located at the magnetic equator and away from the “minimum B pockets”.

We use FFT and Morlet wavelet analyses to study spectral properties of the chorus. The wavelet analysis is often applied to study spectral characteristics of a signal with varying time frequencies (Torrence and Compo, 1998). We use the Morlet wavelet with adjustable resolution in time and frequency to calculate instantaneous spectra of chorus elements as well as standard wave spectra in the time-frequency variables. Distinct spectral features within chorus elements corresponding to sub-elements or wave packets were detected. Similar analysis was performed by Santolik *et al.* (2003, 2004) based on Cluster data. The peak frequency in our study corresponds to about $(0.15-0.4)\nu_{ce}$

(see Table 1). Thus, only the lower-band chorus elements ($\nu_0 < 0.5\nu_{ce}$) were analyzed. Figure 3(a) shows an example of one chorus element in the MVA frame consisting of wave packets or sub-elements. One can notice that the wave is circularly polarized. The spectrum of a chorus sub-element is a narrow-band signal (Fig. 3(b)). Bandwidths at half-maxima for the chorus elements are presented in Table 1. The spectra of wave packets are narrower, and correspond to only a part of the riser element. Wavelet analysis revealed that the wave packet intervals showed small changes in phase, and noise intervals showed large changes in phase. The latter can be explained by random character of disturbances in noise intervals and corresponding rotations of the polarization plane.

We estimate spectral wave intensities for a sub-element and for the whole element presented in the first line of Table 1. Wave intensity of the wave packet is $\sim 5.7 \cdot 10^{-3}$ nT² compared to $\sim 7.4 \cdot 10^{-4}$ nT² average over the whole element, showing increase by the factor of about 8. The ratio of the wave packet intensity to intensity of the inter-element spacing ($\sim 6 \cdot 10^{-5}$ nT²) is thus about two orders of magnitude.

3. Conclusions

The study addresses some properties of the rising tone chorus emissions observed with PWI and WFC instruments onboard GEOTAIL during a substorm of April 29, 1993. Most of the chorus waves were found to propagate under small angles ($\sim 11^\circ-22^\circ$) relative to the ambient magnetic field lines. The waves were not propagating at the Gendrin angles. GEOTAIL was located near the magnetic equator and away from the “minimum B pockets” (Tsurutani and Smith, 1977). We use the Tsyganenko model to illustrate that the outer magnetosphere was compressed, even under very quiet conditions. Correct interplanetary data are needed to map the “minimum B pockets” more accurately.

These waves are nearly parallel propagating and are presumably generated close to the GEOTAIL location at large L in the vicinity of the near-equatorial magnetopause. Tim-

ing of the chorus observation correspond roughly to time delays of substorm electrons drifting from the midnight sector. There is a possibility that magnetospheric compression due to the solar wind ram pressure enhances chorus generation at large L -shells (Zhou *et al.*, 2003). Chorus can be intensified by drift-shell splitting. These mechanisms require further studies.

Chorus emissions show distinct fine structure with wave packets separated by intervals of noise (Santolik *et al.*, 2003). We apply FFT and Morlet wavelet transforms to estimate spectral wave intensities for a wave packet or sub-element and the whole element. It is shown that the chorus emissions have higher intensities ($>10^{-3}$ nT²) inside sub-elements compared to the average intensity of the whole element by the factor of ~ 8 .

Acknowledgments. Work of O.V. at RISH, Kyoto University was supported by JSPS Fellowship.

References

- Gendrin, R., Le guidage des whistlers par le champ magnetique, *Planet. Space Sci.*, **5**, 274, 1961.
- Goldstein, B. E. and B. T. Tsurutani, Wave normal directions of chorus near the equatorial source region, *J. Geophys. Res.*, **89**(A5), 2789, 1984.
- Horne, R. B., R. M. Thorne, Yu. Y. Sprits *et al.*, Wave acceleration of electrons in the Van Allen radiation belts, *Nature*, **437**(7056), 227, 2005.
- Lauben, D. S., U. S. Inan, T. F. Bell, and D. A. Gurnett, Source characteristics of ELF/VLF chorus, *J. Geophys. Res.*, **107**(A12), 1429, doi:10.1029/2000JA003019, 2002.
- Matsumoto, H., I. Nagano, R. R. Anderson *et al.*, Plasma wave observations with GEOTAIL spacecraft, *J. Geomag. Geoelectr.*, **46**, 59, 1993.
- Meredith, N. P., R. B. Horne, and R. R. Anderson, Substorm dependence of chorus amplitudes: implications for the acceleration of electrons to relativistic energies, *J. Geophys. Res.*, **106**(A7), 13,165, 2001.
- Meredith, N. P., M. Cain, R. B. Horne, and D. Summers, Evidence for chorus-driven electron acceleration to relativistic energies from a survey of geomagnetically disturbed periods, *J. Geophys. Res.*, **108**(A6), 1248, doi:10.1029/2002JA009764, 2003.
- Nagano, I., S. Yagitani, H. Kojima, and H. Matsumoto, Analysis of wave normal and Poynting vector of the chorus emissions observed by GEOTAIL, *J. Geomag. Geoelectr.*, **48**, 299, 1996.
- Omura, Y. and D. Summers, Computer simulations of relativistic whistler-mode wave-particle interactions, *Phys. Plasmas*, **11**(7), 3530, 2004.
- Santolik, O., D. A. Gurnett, J. S. Pickett, M. Parrot, and M. Comilleau-Wehrlin, Spatio-temporal structure of storm-time chorus, *J. Geophys. Res.*, **108**(A7), 1278, 2003.
- Santolik, O., D. A. Gurnett, J. S. Pickett, M. Parrot, and M. Comilleau-Wehrlin, A microscopic and nanoscopic view of storm-time chorus on 31 March 2001, *Geophys. Res. Lett.*, **31**, L02801, doi:10.1029/2003GL018757, 2004.
- Torrence, C. and G. P. Compo, A practical guide to wavelet analysis, *Bull. Am. Met. Soc.*, **79**(1), 61, 1998.
- Tsurutani, B. T. and E. J. Smith, Postmidnight chorus: A substorm phenomenon, *J. Geophys. Res.*, **79**(1), 118, 1974.
- Tsurutani, B. T. and E. J. Smith, Two types of magnetospheric ELF chorus and their substorm dependencies, *J. Geophys. Res.*, **82**, 5112, 1977.
- Tsurutani, B. T. and G. Lakhina, Some basic concepts of wave-particle interactions in collisionless plasma, *Rev. Geophys.*, **35**(4), 491, 1997.
- Tsyganenko, N., A model of the near magnetosphere with a dawn-dusk asymmetry. 1. Mathematical structure, *J. Geophys. Res.*, **107**(A8), 1179, doi:10.1029/2001JA000219, 2002.
- Zhou, X.-Y., R. J. Strangeway, P. C. Anderson, D. G. Sibeck, B. T. Tsurutani, G. Haerendel, H. U. Frey, and J. K. Arballo, Shock aurora: FAST and DMSP observations, *J. Geophys. Res.*, **108**(A4), doi:10.1029/2002JA009701, 2003.

O. P. Verkhoglyadova (e-mail: olgav@ucr.edu), B. T. Tsurutani, Y. Omura, and S. Yagitani

Proxy for the ionospheric peak plasma density reduced by the solar zenith angle

T. L. Gulyaeva^{1,2}

¹IZMIRAN, 142190 Troitsk, Moscow Region, Russia

²Space Research Centre PAS, Bartycka 18-A, 00-716 Warsaw, Poland

(Received October 17, 2007; Revised January 25, 2008; Accepted March 19, 2008; Online published May 29, 2009)

The F_2 layer peak plasma density $N_m F_2$ is reduced by the factor constructed from the relative changes in the Sun's zenith angle χ for a particular local time and the local noon value χ_0 . Proposed transformation yields a proxy for the peak plasma density which coincides with the source observation at noon but apart from the latter is gradually reduced towards the night. Hourly observations at 8 ground based ionosondes for the solar maximum (2000) and minimum (2006) are analyzed for inter-stations and inter-seasonal correlation of the peak plasma density and the proxy values. The proxy values show improved correlation between the data at different locations and improved inter-seasonal correlations for a particular location due to greater homogeneity of results throughout the year contributing to improved evaluation of the ionospheric weather indices.

Key words: Ionosphere, plasma density, solar zenith angle.

1. Introduction

Diurnal and seasonal changes of the plasma density and temperature in the ionosphere depend directly on the illumination of the upper atmosphere by the Sun. The features of the peak plasma density, $N_m F_2$, m^{-3} , proportional to square of the ionospheric critical frequency $f_o F_2$ can be made more uniform if the effect of the solar grazing incidence on the plasma density in the F region could be reduced with a proper transformation.

Earlier, the relevant relations of the noon F_2 layer critical frequency have been investigated for the magnetic conjugate locations at the ends of the magnetic line of force assuming that daytime temperature of the neutral gas is proportional to the cosine of the Sun's zenith angle at local noon (Rotwell, 1962). The correction factor deduced for such relation, so called "M-factor" has been used for constructing the global model of the noon $f_o F_2$ critical frequency from the data of global network of ionosondes (Besprouzannaja, 1970, 1987) and the monthly ionospheric index $M F_2$ (Mikhailov and Mikhailov, 1995). However, this approach is valid only for the local noon while relevant transformation for all times throughout the day is required.

The solar zenith angle determines proportions of daytime and nighttime conditions in the ionosphere at different altitudes over the Earth (Gulyaev and Gulyaeva, 1984) with relevant plasma density and temperature controlled by the energy transmitted from the Sun in the form of an electromagnetic wave radiation in the UV/EUV ranges to the upper atmosphere (Chapman, 1931). The solar zenith angle dependence as predicted by the Chapman ionization theory cannot thoroughly explain spatial and temporal variations

of the ion density by the factors such as plasma production due to UV/EUV alone, differential loss due to varying recombination rate, transport, neutral winds, atmospheric composition. The energy input from the magnetosphere in the form of electric fields and charged particle precipitation due to the solar wind also contributes significantly to the changes of the peak plasma density (Lal, 1997). If the dominant effect of the solar zenith angle on the ionospheric plasma density could be reduced by a proper transformation, an improved metric of the solar-controlled behaviour of the plasma around the peak of the F_2 layer can be obtained.

In the present paper, the variations in the Sun's zenith angle are used to produce a proxy for the peak plasma density, $N_p F_2$, by multiplying the observed peak plasma density $N_m F_2$ by a factor related with the solar zenith angle χ at a particular time and the local noon value χ_0 . This process is evaluated with the data of eight ground based ionosondes at solar minimum (2006) and maximum (2000) to illustrate the advantages of the reduced peak plasma density as compared with the source observations that will be useful for applications in the ionosphere modeling and forecasting.

2. Technique of Inversion of the F_2 Layer Critical Frequency by the Solar Zenith Angle

The solar zenith angle χ reaches peak at the local midnight tending to a minimum at the local noon. Impact of the local conditions of the Sun's illumination can be excluded by normalizing the peak plasma density $N_m F_2$ by the solar zenith angle χ in radians. Change of the normalizing factor $1/\chi$ from day to night is shown by the dashed line with triangles in Fig. 1.

The multiplier $1/\chi$ is larger when the solar zenith angle gets smaller and in the limit of noon between the north and south tropics as χ approaches zero, $1/\chi$ tends to infinity.

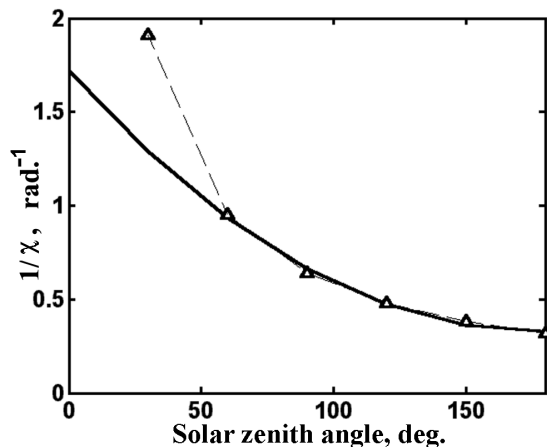


Fig. 1. Correction factor deduced from the solar zenith angle.

To avoid this singularity, we introduce the second order polynomial approximation of the best least square fit to $1/\chi$ for the angles of $\chi > 1$ rad. as follows:

$$z(\chi) = \gamma(x^2 - \beta x + \alpha) \quad (1)$$

where $x = \chi^\circ/100$, $\alpha = 3.8749$, $\beta = 3.5402$, and $\gamma = 0.4444$ and $z(\chi)$ is given in solid line in Fig. 1.

Multiplying $N_m F_2$ by the coefficient $z(\chi)$ yields reduced nighttime and sunrise/sunset values but tends to increase the daytime values, particularly in summer towards the equator when $z \gg 1$. To equilibrate such opposite effects for day and night we replace multiplier in Eq. (1) by the normalizing factor $C(\chi, \chi_0)$ equal to the ratio of the coefficient of Eq. (1) for given local time to the value for local noon:

$$C(\chi, \chi_0) = z(\chi)/z(\chi_0). \quad (2)$$

With the normalizing factor defined in terms of coefficients α and β we obtain the proxy $N_p F_2$ for the peak plasma density $N_m F_2$ by multiplying the latter by $C(\chi, \chi_0)$:

$$N_p F_2 = C(\chi, \chi_0) \times N_m F_2. \quad (3)$$

The resultant $N_p F_2$ coincides with the source value $N_m F_2$ at noon ($C_0 = 1$) but it is essentially reduced towards the night when coefficient $C(\chi, \chi_0)$ tends to zero depicting a reduced maintenance of nighttime ionization compared with its noon value. Thus, all regularities of the noon peak plasma density $N_m F_2$ (Besprozvannaja, 1987; Willisroft and Poole, 1996) are valid for $N_p F_2$. However the reduced values of $N_p F_2$ at other times are significantly changed.

3. Validation of the Proxy for the Peak Plasma Density with Ground Based Ionosonde Data

The above transformation is applied to daily-hourly observations at 8 ionospheric stations listed in Table 1 for the solar maximum (2000) and minimum (2006). The solar zenith angle was calculated for given day of year, geodetic coordinates of ionosonde site and local time with the standard subroutine SOCO (McNamara, 1986) of the International Reference Ionosphere code (Bilitza, 2001).

Figure 2 shows the monthly median at Chilton for the source $N_m F_2$ and reduced $N_p F_2$ for 4 seasons during the

Table 1. Geodetic and geomagnetic coordinates (latitude and longitude) of the ionosonde stations providing data used in the present paper.

Station	Geodetic		Magnetic	
	Lat °N	Lon °E	Lat °N	Lon °E
Sodankyla	67.4	026.6	63.6	120.8
Julius-Rugen	54.6	013.4	54.3	099.7
Chilton	51.6	358.7	54.1	083.2
Moscow	55.5	037.3	50.4	123.2
Tortosa	40.4	000.3	43.6	080.9
Rome	41.8	012.5	42.3	093.2
El Arenosillo	37.1	353.3	41.4	072.3
Wakkanai	45.4	141.7	35.5	207.3

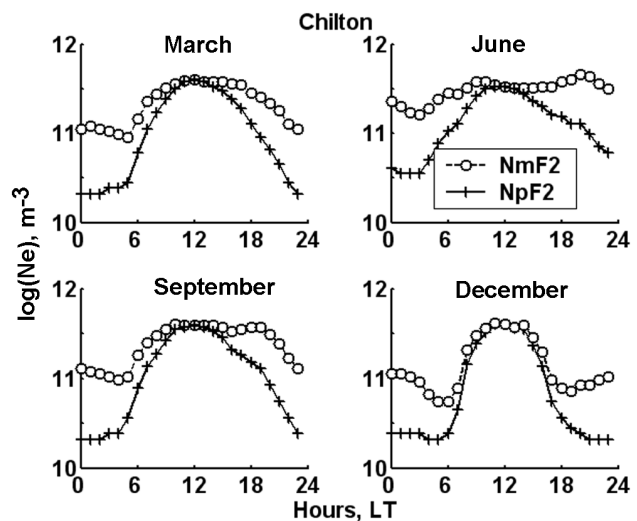


Fig. 2. Monthly median of observed peak plasma density $N_m F_2$ at Chilton and proxy $N_p F_2$ reduced by the solar zenith angle for four seasons at the solar minimum 2006.

solar minimum: spring (March), summer (June), autumn (September) and winter (December) 2006. The source median and the proxy median coincide at noon. The diurnal curve of $N_p F_2$ become rather uniform throughout the year gradually reduced from day to night which corresponds to reduced income of the ionizing radiation from the Sun (Gulyaev and Gulyaeva, 1984). The sunrise minimum of $N_m F_2$ is smoothed in the diurnal change of $N_p F_2$. The diurnal variation is particularly improved at summer when it became similar to $N_p F_2$ variation for other seasons.

The hourly values of $N_m F_2$ and $N_p F_2$ for four seasons are used for each pair of stations of Table 1 and the mean of all correlation coefficients are computed. In Table 2, the interlocation correlation coefficient r_2 is presented for selected months at solar maximum (2000) and minimum (2006). Improved correlation between the stations data is obtained with the proxy values in all cases. The most appreciable improvement of r_2 is obtained for the summer solstice when the dominant is daytime process of the ion production due to solar illumination during the day.

While the improvement in the correlation of the data from different stations has been the primary goal of implementation of Eq. (3), the results reveal also an improved the interseasonal correlation coefficient r_1 for each station in Ta-

Table 2. Mean inter-station correlation coefficient for observed $N_m F_2$ and proxy $N_p F_2$ for the peak plasma density at solar maximum and minimum for four seasons/months.

Year	2000		2006	
Month	$N_m F_2$	$N_p F_2$	$N_m F_2$	$N_p F_2$
03	0.841	0.906	0.801	0.888
06	0.521	0.834	0.478	0.802
09	0.653	0.814	0.771	0.883
12	0.827	0.881	0.756	0.856

Table 3. Inter-seasonal correlation coefficient averaged for all stations for $N_m F_2$ and $N_p F_2$ at solar maximum (2000) and solar minimum (2006) for two pairs of months.

Year	2000		2006	
Months	$N_m F_2$	$N_p F_2$	$N_m F_2$	$N_p F_2$
03~12	0.824	0.938	0.641	0.880
06~09	0.298	0.858	0.528	0.885

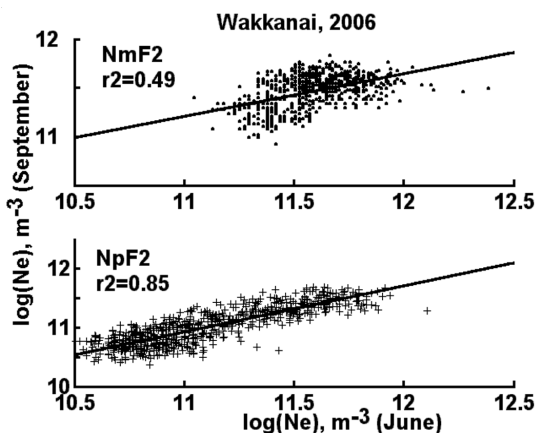


Fig. 3. Inter-seasonal relation for September versus June 2006 for observed peak plasma density $N_m F_2$ (upper panel) and for proxy $N_p F_2$ (lower panel) at Wakkanai.

ble 1. The averages of the correlation coefficients r_1 are provided in Table 3 for all stations referring to selected months of March–December and June–September at the solar maximum and minimum. The proposed technique brings improved inter-seasonal correlations for $N_p F_2$ as compared with $N_m F_2$, particularly, for the June–September pair of months due to the most appreciable changes in $N_p F_2$ for the summer solstice.

Figure 3 illustrates inter-seasonal relation for June–September at Wakkanai between the hourly values of $N_m F_2$ (upper panel) and $N_p F_2$ (lower panel) at solar minimum, 2006. It is evident that regression between the data for 2 different seasons (summer and equinox) is improved in the proxy data set as compared with the observed $N_m F_2$. It is expected that proposed transformation of the F_2 layer peak density depicting more uniform daily/seasonal variation as compared with the observations would be helpful for the modelling and forecasting purposes than the more sophisticated day-to-day and hour-to-hour changes of the source $N_m F_2$ data.

The advantages of the proposed approach proved to be useful for reconstruction of missed ionosonde observations of the critical frequency $f_o F_2$ with the data of another station using the cloning technique discussed in (Gulyaeva *et al.*, 2008) so that the complete daily/hourly data sets for selected location/season/month are available for derivation of the ionospheric weather indices.

4. Conclusion

In this study, a new technique for obtaining a proxy for the ionospheric peak plasma density is proposed. The correction factor depends on ratio of the solar zenith angle at the time of observation to its local noon value. The noon values of the normalized peak plasma density coincide with observations of $N_m F_2$ but $N_p F_2$ is gradually reduced from day to night throughout the year for all observations analyzed at eight ionospheric stations for the maximum and minimum of solar activity. The normalization of the peak plasma density improves not only the correlation coefficient between the data of different stations but also the inter-seasonal correlation for the data of a particular station.

The proposed technique of inversion of the peak plasma density by the solar zenith angle presents physically justified replacement of the variable by a proxy value of significantly improved characteristics. The proposed proxy parameter exhibits diurnal/seasonal homogeneity of the peak electron density which is one of the key parameters of modern ionospheric models.

Acknowledgments. The ionospheric data used in the present study are provided via internet from WDC A for STP, Boulder, CO, USA; WDC C1, Oxford, UK; IZMIRAN, Moscow, Russia; SGO, Sodankyla, Finland; WDC for Ionosphere, NICT, Tokyo, Japan. The author thanks two anonymous referees for useful comments. The author is grateful to Feza Arican for her comments and assistance in improvements to the paper.

References

- Besprozvannaja, A. S., On a nature of the seasonal anomaly of the F2 layer noon ionization, *Geomagn. Aeronomy*, **10**, 986–992, 1970.
- Besprozvannaja, A. S., Peculiarities of the regular F2 layers, *Geomagn. Aeronomy*, **27**, 728–734, 1987.
- Bilitza, D., International Reference Ionosphere 2000, *Radio Sci.*, **36**(2), 261–275, 2001.
- Chapman, S., Absorption and dissociative or ionizing effect of monochromatic radiation in an atmosphere on a rotating earth, *Proc. Phys. Soc., London*, **43**, 26–45, 1931.
- Gulyaev, R. A. and T. L. Gulyaeva, On illuminating the ionosphere by sunlight during nighttime, *Geomagn. Aeronomy*, **24**, 347–348, 1984.
- Gulyaeva, T. L., I. Stanislawski, and M. Tomasik, Ionospheric weather: Cloning missed foF2 observations for derivation of variability index, *Ann. Geophys.*, **26**, 315–321, 2008.
- Lal, C., Contribution to F2 layer ionization due to the solar wind, *J. Atmos. Solar-Terr. Phys.*, **59**(17), 2203–2211, 1997.
- McNamara, L., Private communication, 1986.
- Mikhailov, A. V. and V. V. Mikhailov, A new ionospheric index MF2, *Adv. Space Res.*, **15**(2), 93–97, 1995.
- Rotwell, P., Charged particles in the Earth's magnetic field and the ionospheric F2-layer, *J. Phys. Soc. Japan*, **17**, Suppl. 1, 263–267, 1962.
- Williscroft, L.-A. and A. W. V. Poole, Neural networks, foF2, sunspot number and magnetic activity, *Geophys. Res. Lett.*, **23**(24), 3659–3662, 1996.

Investigation of ionospheric gradients for GAGAN application

K. Ravi Chandra, V. Satya Srinivas, and A. D. Sarma

Research and Training Unit for Navigational Electronics, Osmania University, Hyderabad, India

(Received October 29, 2007; Revised July 21, 2008; Accepted September 28, 2008; Online published May 29, 2009)

To cater to the needs of aviation applications, GPS Aided GEO Augmented Navigation (GAGAN) system is being implemented over the Indian region. The most prominent parameter affecting the navigation accuracy of GAGAN is ionospheric delay which is a function of TEC. In the equatorial and low latitude regions such as India, TEC is often quite high with large spatial gradients. Carrier phase data from the GAGAN network of Indian TEC Stations is used for estimating ionospheric gradients in multiple viewing directions. Rate of TEC (ROT) and Rate of TEC Index (ROTI) are calculated to identify the ionospheric gradients. Among the satellite signals arriving in multiple directions, the signals which suffer from severe ionospheric gradients are identified and avoided for improving GAGAN positional accuracy. The outcome of this paper will be helpful for improving GAGAN system performance.

Key words: GAGAN, ionospheric gradients, ROT, ROTI.

1. Introduction

The Global Positioning System (GPS) is a navigation system which provides continuous positioning and timing information under all weather conditions. As the accuracy of the stand alone GPS is not sufficient for category I (CAT-I) precision approach, Space Based Augmentation Systems (SBAS) are evolved to cater to the needs of aviation applications. GPS Aided GEO Augmented Navigation (GAGAN) is one such system planned in India. The most prominent error affecting the accuracy of GAGAN is the ionospheric delay. The ionosphere is decorrelated with distance and as well as with time causing anomalies. For reliable communication, navigation and surveillance systems, ionospheric gradients need to be thoroughly investigated for improving the performance. The purpose of the gradients is to identify the satellite signals, which are gradient-free in their direction of propagation. As a result, precise TEC data can be obtained from among the visible satellites in multiple directions. To achieve this objective, initially the satellite signals which do not severely suffer from the gradient effects are identified. Subsequently, among the identified satellite signals the best four are considered for accurate positional information using the Dilution of Precision (DOP) approach (Parkinson *et al.*, 1996). Jean-Marie (2006) referred DOP as the effect of ‘geometry of satellites’ on measurement accuracy. Gang *et al.* (2003) have proposed a new method ‘Cumulative sum’, which quickly and reliably detects small but hazardous gradients for Local Area Augmentation System (LAAS) scenario. Walter *et al.* (2004) reported the effects of large ionospheric gradients on single frequency airborne smoothing filters for Wide Area Augmentation System (WAAS) and LAAS, and also their mitigation tech-

niques. Warnant and Pottiaux (2000) also made an attempt to identify possible correlations between the ionospheric activity and unidentified problems in GPS data processing by duly detecting the travelling ionospheric disturbances. In this paper the estimated ROT and ROTI (TECu/min) of all visible satellites are used to identify signals which suffer from severe ionospheric gradients.

2. Results and Discussion

In the GAGAN network 20 TEC stations are installed to monitor the ionospheric behavior. The data from one of these TEC stations (Lucknow, Lat. 26.76°N, Long. 80.88°E) is used for this analysis. The processed GPS data contains 23 parameters. Out of these only seven parameters, namely user position, PRN number of satellite, GPS week number, GPS seconds of the week, elevation angle, azimuth angle and TEC are used in the analysis.

Several days of data corresponding to both quiet and disturbed days are analyzed. However, in this paper the data from various visible Satellite Vehicles (SVs) corresponding to a typical disturbed ($7 < K_p < 8$) day (25th July, 2004) is processed and analyzed for identifying the ionospheric gradients. The sampling rate of data is 1 minute.

The rate of change of the ionospheric delay (ROT) due to satellite signals received at the receiver is given as (Warnant and Pottiaux, 2000)

$$\text{ROT}_u^k(t_i) = \frac{\text{TEC}_u^k(t_i) - \text{TEC}_u^k(t_{i-1})}{t_i - t_{i-1}} \text{ (TECu/min)}. \quad (1)$$

Where $\text{ROT}_u^k(t_i)$ = Rate of TEC estimated at time epoch t_i by receiver (u) on satellite (k), $\text{TEC}_u^k(t_i)$ and $\text{TEC}_u^k(t_{i-1})$ = Total Electron Content measured by receiver (u) on satellite (k) at epoch t_i and epoch t_{i-1} respectively.

ROT is a function of K_p , viewing direction and magnetic activity. Secondly, these ROT values are converted from slant to vertical using a standard mapping function $M(E)$

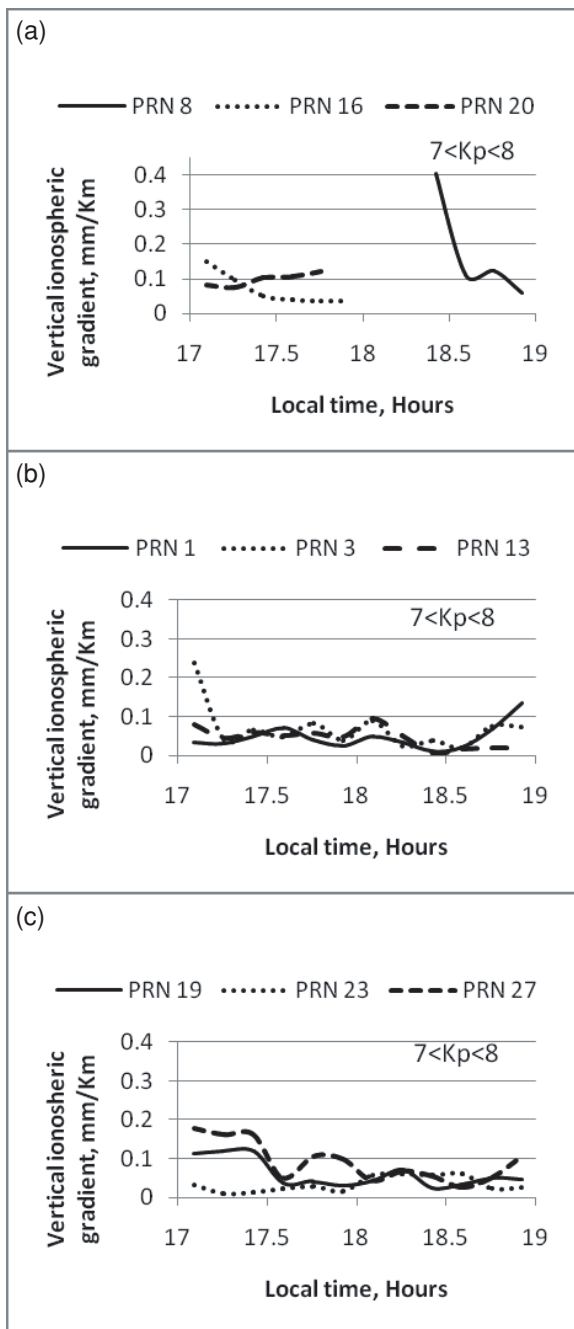


Fig. 1. Variation of vertical ionospheric gradient for all visible multiple viewing satellites based on Lucknow GAGAN network TEC stations (25th July, 2004) over a local time period (17:00–19:00 Hrs).

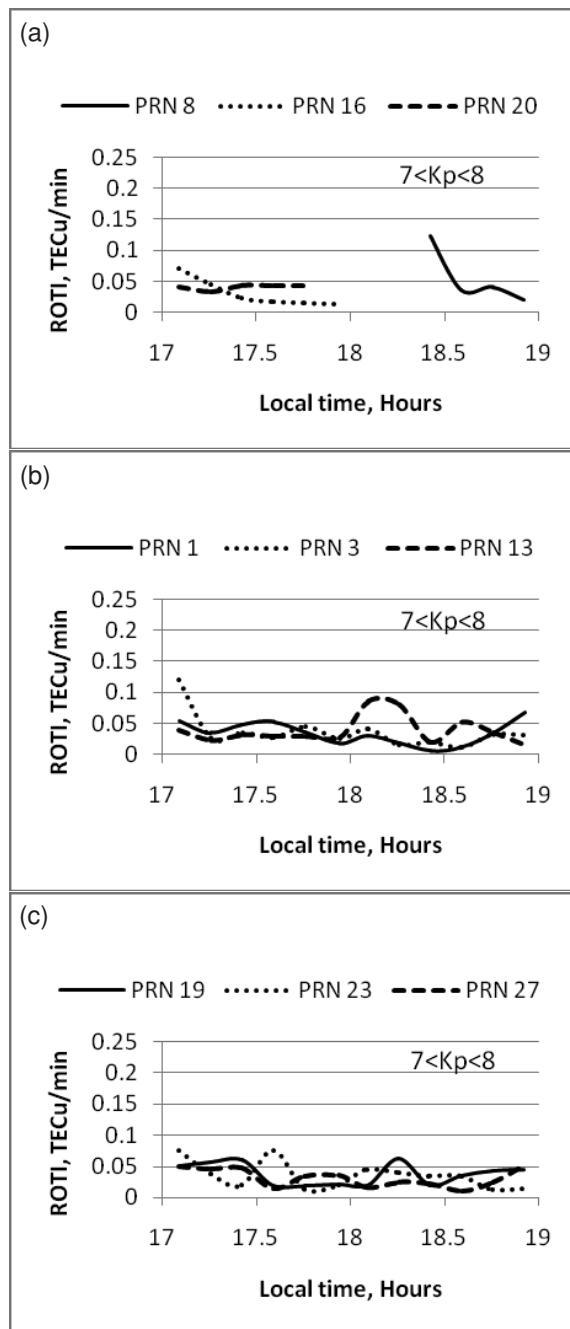


Fig. 2. Variation of ROTI for all visible multiple viewing satellites based on Lucknow GAGAN network TEC stations (25th July, 2004) over a local time period (17:00–19:00 Hrs).

(Guochang, 2003)

$$M(E) = \left\{ 1 - \left(\frac{R_E}{R_E + h} \right)^2 \cos^2 E \right\}^{1/2} \quad (2)$$

Where E = Elevation angle at the reference station (in degrees),
 h = Altitude of the ionospheric shell above the surface of the Earth (350 Km)
 R_E = Earth radius (6378 Km).

The slant ROT is averaged over 10 minutes to obtain

$\langle \text{ROT} \rangle$. ROTI is standard deviation of ROT and is given as (Krankowski *et al.*, 2005)

$$\text{ROTI} = \sqrt{\langle \text{ROT}^2 \rangle - \langle \text{ROT} \rangle^2} \text{ (TECu/min)} \quad (3)$$

ROTI measurements can be used to predict the presence of ionospheric scintillation also (Basu *et al.*, 1999). Its values signify the presence of only temporal gradients. In order to identify spatial gradients, Jiyun *et al.* (2006) proposed a ‘Time step method’. By considering the distance between the Ionospheric Pierce Point (IPP) at epoch t_i and IPP at epoch t_{i-1} , the vertical ionospheric gradient (σ_{VIG}) is esti-

mated as

$$\sigma_{u\text{VIG}}^k(t_i) = \frac{\text{TEC}_u^k(t_i) - \text{TEC}_u^k(t_{i-1})}{D_{t_i, t_{i-1}}} \text{ (mm/Km)}. \quad (4)$$

Where $D_{t_i, t_{i-1}}$ = Distance between the IPPs corresponding to time epochs t_i and t_{i-1} .

As the delays due to different epochs were considered and divided by the corresponding separation, the estimated σ_{VIG} is a combination of both temporal and spatial gradients.

The typical data from various visible satellites corresponding to two hours (Local time: 17:00–19:00 Hrs) are processed and analyzed. Variations of σ_{VIG} with respect to local time are presented for selected visible satellites (Fig. 1). At 17.08 Hrs, eight satellites are visible. After about 17.74 Hrs, SV 20 and after 17.91 Hrs, SV 16 have gone out of sight and only six satellites are visible. After about 18.24 hours, the SV 8 has come in to line of sight to reference station. Hence, there exists a corresponding trace of ROTI curve after 18.24 hour onwards. From the data, it is evident that, at any point of time GPS receiver is in line of sight with a minimum six and a maximum eight satellites. To investigate the effect due to temporal gradients, variation of ROTI with respect to local time is presented for all visible satellites (Fig. 2). It is shown that for the entire time period ROTI and σ_{VIG} for SVs 1, 13, 16, 19, 20, 23 and 27 has not exceeded the maximum values of 0.085 TECu/min (PRN 16) and 0.177 mm/Km (PRN 27) respectively. Further, there are no abrupt changes in the plots. It signifies that impact of ionospheric anomalous activity ($7 < K_p < 8$) on different viewing SVs has the similar effect. Except for a few epochs, SVs 3 and 8 also show similar trend. At local time of 18.41 Hrs, both ROTI (0.1238 TECu/min) and σ_{VIG} (0.4047 mm/Km) are identified to be the maximum due to PRN 8. From both Figs. 1 and 2, it is observed that, the plots exhibit similar trend. It signifies that even though σ_{VIG} is a combination of both temporal and spatial gradients, the role of temporal gradients seem to be predominant. The reason for this could be less spatial variation between the successive IPPs. This is in turn based upon the radial movement of satellite (angular velocity of approx. 3.9 Km/sec) and user.

On estimation of gradients an attempt is made to improve the accuracy and integrity of user position. As example estimation, a time epoch of 17.08 Hrs is considered. Out of all the visible satellites, σ_{VIG} values of SV 3 (0.2378 mm/Km) and SV 27 (0.1777 mm/Km) are found to be relatively higher than the rest of the SVs. Therefore, the signals from these two SVs are avoided. Consequently, among the available SVs, only six will remain. Among these six SVs, the best four are chosen, based on DOP geometry for accurate position estimation. Since there are six visible satellites DOP geometry is to be checked only for 15 combinations

of four satellites. In this way we are able to avoid the signals affected by ionospheric gradients and also minimize the DOP computations from 70 to 15 for selection of the best 4 SVs.

3. Conclusions

In order to provide accurate position as well as integrity information, investigation of ionospheric gradients is necessary for GAGAN applications. The outcome of this work can be extended for the LAAS system for improving performance of Required Navigation Performance (RNP) parameters viz. accuracy, availability, integrity and continuity to achieve CAT II accuracy requirement of civil aviation applications. This paper emphasizes that, precise estimation and identification of ionospheric gradients over a low latitude region is necessary to achieve better accuracies. This will help to identify relatively gradient-free propagation paths, among the multiple viewing directions of satellites. Subsequently, among the available satellite signals the best four can be chosen to achieve best DOP value for improving positional and integrity information.

Acknowledgments. The research work presented in this paper has been carried out under the project entitled “Analysis and modeling of Indian Ionospheric Electron Content for GPS Applications” funded by ISRO, Bangalore, Vide Order No. CAWSES:05, Dated: 28th December, 2005.

References

- Basu, S., K. M. Groves, J. M. Quinn, and P. Doherty, A comparison of TEC fluctuation and scintillation at Ascension Island, *J. Atmos. Sol. Terr. Phys.*, **61**, 1219–1226, 1999.
- Gang, X., S. Pullen, M. Luo, and P. Enge, *Detecting Ionospheric Gradients with Cumulative Sum (CUSUM) Method*, American Institute of Aeronautics and Astronautics, Inc. (AIAA 2003-2415), 2003.
- Guochang, Xu., *GPS Theory, Algorithms and Applications*, Springer-Verlog, Berlin, Germany, 2003.
- Jean-Marie, Z., *Essentials of Satellite Navigation*, Ublox compendium, GPS-X-02007-C, 2006.
- Jiyun, L., S. Pullen, S. Datta-Barua, and P. Enge, *Assessment of Nominal Ionosphere Spatial Decorrelation for LAAS*, IEEE/ION PLANS 2006, pp. 506–514, 2006.
- Krankowski, A., I. I. Shagimuratov, Lubomir, W. Baran, and I. I. EphishoV, Study of TEC fluctuations in Antarctic Ionosphere during storm using GPS observations, *Acta Geophysic Apolonica*, **53**(2), 205–218, 2005.
- Parkinson, B. W., *GPS Theory and Applications*, pp. 81–114, American Institute of Aeronautics and Astronautics, Inc, Volume I, Washington, 1996.
- Walter, T., S. Datta-Barua, J. Blanch, and P. Enge, *The Effects of Large Ionospheric Gradients on Single Frequency Airborne Smoothing Filters for WAAS and LAAS*, Institute of Navigation’s National Technical Meeting, San Diego CA, January 2004.
- Warnant, R. and E. Pottiaux, The increase of the ionospheric activity as measured by GPS, *Earth Planets Space*, **52**, 1055–1060, 2000.

K. Ravi Chandra, V. Satya Srinivas, and A. D. Sarma (e-mail: ad_sarma@yahoo.com)

The total failures of GPS functioning caused by the powerful solar radio burst on December 13, 2006

E. L. Afraimovich, V. V. Demyanov, and G. Ya. Smolkov

Institute of Solar-Terrestrial Physics, the Russian Academy of Sciences, the Siberian Branch, 664033, Irkutsk, Russia

(Received October 23, 2007; Revised July 6, 2008; Accepted August 21, 2008; Online published May 29, 2009)

We investigated failures in the GPS performance produced by extremely dense solar radio burst fluxes associated with the intense (X3.4 in GOES classification) solar flare and Halo CME recorded by SOHO/LASCO on December 13, 2006. According to substantial experimental evidence, high-precision GPS positioning on the entire sunlit side of the Earth was partially disrupted for more than 12–15 min; the high level of GPS slips resulted from the wideband solar radio noise emission. Our results are in agreement with the data obtained recently for the extreme solar radio burst on December 6, 2006, and provide a sound basis for revising the role of space weather factors in the functioning of state-of-the-art satellite systems and for taking a more thorough account of these factors in their development and operation.

Key words: Solar flares, solar radio emission, GPS, GLONASS, GALILEO.

1. Introduction

Strong solar activity observed on December 6 and 13, 2006; i.e., during the solar cycle 23 minimum, was absolutely unexpected. Its study and analyses of the consequences for the space environment are not complete yet. This kind of solar activity is of great interest not only to astronomers and radio astronomers, but to other scientists and engineers, as well. The broadband solar radio emission following the flare exceeded powerful solar radio bursts in all known flares by at least two orders of magnitude (Cerruti *et al.*, 2006a, b; Carrano *et al.*, 2007; Carrano and Bridgwood, 2008; Gary, 2008).

The powerful solar radio burst (SRB) on December 6, 2006, led to failures in the functioning of wideband satellite radio systems including the GPS. The functioning failures and deep damping of GPS signals were registered at certain standard GPS receivers and specialized monitors of ionospheric scintillations in the L range (Cerruti *et al.*, 2006a, b; Carrano *et al.*, 2007; Carrano and Bridgwood, 2008; Kintner, 2008). However, worldwide failures of the GPS due to extreme solar activity in December 2006 are still a matter of debate. Meanwhile, this problem is of doubtless scientific and practical interest as regards to the estimation of the space weather effect on the functioning of one of the most powerful and reliable satellite systems considered practically impregnable. Using data from the global network of dual-frequency GPS receivers, Afraimovich *et al.* (2007) found significant evidence that the high-precision GPS positioning on the entire sunlit side of the Earth was paralyzed for more than 10 minutes on December 6, 2006.

There are many published papers regarding the GPS fail-

ure during the 2006 December 6 SRB (see References). But we do not know any publications on the GPS failure during the 2006 December 13 powerful SRB, although the radio flux $F(t)$ was strong enough for both bursts. In this study, we investigate global failures of the GPS performance due to the 2006 December 13 SRB.

2. The Solar Radio Bursts on 13 December 2006 (Concise Description)

Complex, and especially large, microwave bursts were recorded from 02:21 to 04:37 UT, exhibiting weakening with time. A type II burst (02:27–02:44 UT) was followed by a type IV radio burst that ended at 10:12 UT (signatures of wideband solar radio noise emission and disturbances of the solar corona). This radio emission is associated with X-type flare and Halo CME. The latter commenced at 02:18:30 UT (first seen by the LASCO C2 at 02:54 UT and by the LASCO C3 at 03:18 UT; the C3 occulting disk was fully surrounded by 03:42 UT, the mean plane-of-the-sky speed was ~ 1440 – 1800 km/sec). The events with MHD fast-mode shock wave (type II) and plasmoid ejection (Halo CME) are confirmed by observations with the EUV Imaging Spectrometer on-board the Hinode satellite (Asai *et al.*, 2008). Such radio emission was associated with an X-type flare, proton storms, and Halo CME. The said events started and developed at different time intervals and stages of the flare and at different heights in the solar atmosphere.

The flare occurred at the apparent collision site between the large opposite polarities of the umbral magnetic field of AR 10930. The polarity inversion line at the collision site became very complicated and unsteady due to highly sheared magnetic fields caused by the rotation and W-to-E motion of emerging fluxes. The fine structure of magnetic fields at the flare site changed with time: some parts of the complicated polarity inversion line disappeared, and then the azimuthal angle of the magnetic fields changed

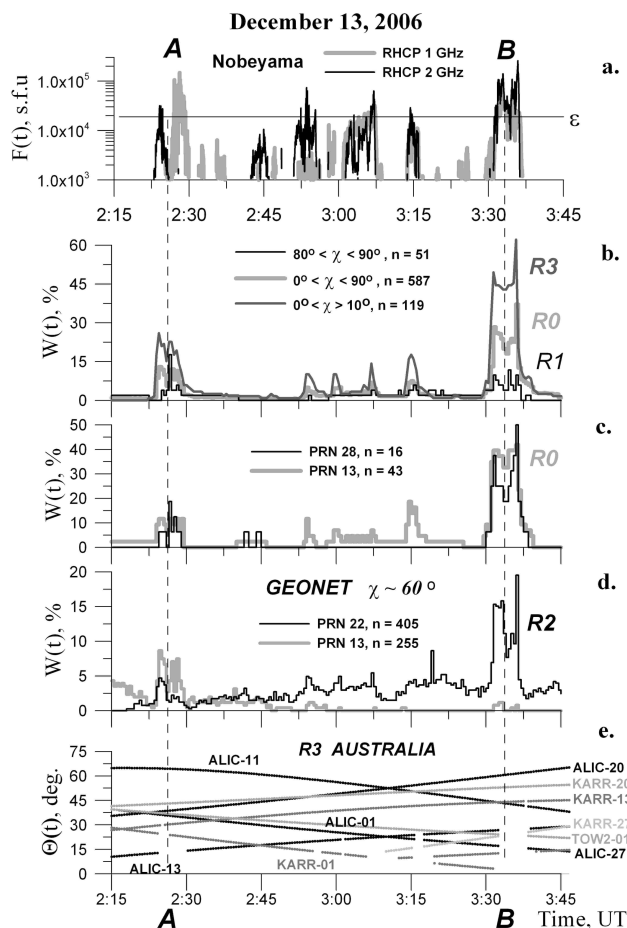


Fig. 1. The relative number of GPS sites $W(t)$ where the 30-s count omissions were observed during December 13, 2006, solar radio bursts: (a) the flux $F(t)$ of the RHCP radio emission observed by the Nobeyama Radio Polarimeters at 1 GHz and at 2 GHz; thick gray line and black line, respectively; logarithmic scale. The vertical dashed lines correspond to the centre of time intervals **A** and **B**. About the marks **A** and **B** look in the text. (b) region R_3 , Australia; region R_0 , GPS world network, and region R_1 , Western Asia, gray line, thick gray line and black line, respectively, all PRN; (c) region R_0 , GPS world network, PRN 13 and 28, thick gray line and black line, respectively; (d) region R_2 , GEONET, PRN 13 and 22, thick gray line and black line, respectively; (e) time dependences of elevation angle $\theta(t)$ for different PRN and selected GPS sites KARR, ALIC, TOW2, region R_3 , Australia (dots); empty time intervals correspond to the count omissions.

by $\sim 90^\circ$ in those areas, becoming more spatially uniform within the collision site (Kubo *et al.*, 2007; Su *et al.*, 2007). In such circumstances the Right Hand Circular Polarization (RHCP) of microwave bursts can only be registered in certain intervals of the flare time. This was clearly confirmed by observations of total fluxes and circular polarity at the Nobeyama Radio Polarimeters (see Fig. 1(a)) and fixed-frequency observations of total fluxes in other observatories (RSTN Learmonth, Palehua, <http://www.ngdc.noaa.gov/stp/SOLAR/ftpsolarradio.html>). Moreover, the circular polarity of microwave bursts during the X3.4 flare in December 2006 could also change due to the reversal of the circular polarity sign when the radio emission was propagating across a fragmented magnetic field.

This study is focused on the microwave band of two

GPS frequencies ($f_1 = 1575.42$ MHz and $f_2 = 1227.60$ MHz) at 2:20–2:28 UT (corresponding to the type II radio burst) and 3:30–3:38 UT (corresponding to the type IV radio burst). Klobuchar *et al.* (1999) predicted that solar radio bursts could affect GPS performance if a solar flux was sufficiently large in the L band frequency range and had a RHCP—to which polarization GPS antennas are receptive. Therefore it is important first to know data of solar radio flux with RHCP, especially near the auxiliary GPS frequency f_2 (see below Section 5.2).

Data from the Nobeyama Radio Polarimeters (http://solar.nro.nao.ac.jp/norp/html/event/20061213_0247/) show that the RHCP solar radio emission on December 13, 2006 exceeded $1.47 \cdot 10^5$ sfu at 1 GHz at 02:28:09 UT, exceeding $2.57 \cdot 10^5$ sfu at 2 GHz at 03:35:51 UT (Fig. 1(a), thick gray line and black line, respectively). The sharp impulses of the solar radio flux can be noted in the first interval, 02:20 to 02:28 UT (symbol **A**), and in the second interval, 03:30 to 03:38 UT (symbol **B**). The vertical dashed lines correspond to the centre of time intervals **A** and **B**.

3. Method for GPS Data Processing

We use the GLOBDET software developed at the ISTEP SB RAS to treat GPS data from the global network of dual-frequency receivers (Afraimovich *et al.*, 2000; Afraimovich, 2000). Our database of the GPS network's RINEX files includes data from over 1500 GPS sites (<http://sopac.ucsd.edu/other/services.html>). We also complement data from the Japanese GPS network GEONET (about 1225 sites in all) (ftp://terras.gsi.go.jp/data/GPS_products/). At present, it is the largest regional GPS network in the world.

Figure 2 presents the geometry of the global network of GPS receivers in the Earth sunlit side ((a), (b), gray circles) and GEONET geometry ((b), black triangles) on December 13, 2006. The names of the sites are not given, for reasons of space. It is clear that the level of solar noise interference depends on the Sun zenith angle χ (Carrano *et al.*, 2007). We have examined this dependence. The rectangles mark different regions (R_0 – R_3) with different zenith angles χ . Asterisks show the location of sunlit points for December 13, 2006, at 02:30 and 03:30 UT. The bold triangles on Fig. 2 (region R_3 , Australia) mark selected GPS sites KARR, ALIC, TOW2.

In order to estimate the GPS performance we used different methods for processing RINEX files described by Afraimovich *et al.* (2002). For all n lines of sight (LOS) between the GPS world network receivers and satellites we calculate the relative number of GPS sites $W(t)\%$, where the 30-s count omission for GPS satellites with their pseudo random noise (PRN) code number (Hofmann-Wellenhof *et al.*, 1992) was simultaneously observed at two GPS frequencies f_1 and f_2 .

In addition, for all LOSs between GEONET/GPS receivers and PRN, we calculated the relative density $Q(t)\%$ of measurement slips of main GPS-signal parameters: L_1 , L_2 are the phase delay, and P_1 , P_2 the group delay for f_1 and f_2 , respectively. A measurement slip was registered when the current 30-s count of corresponding GPS parameters equaled zero or the current 30-s count of all parameters

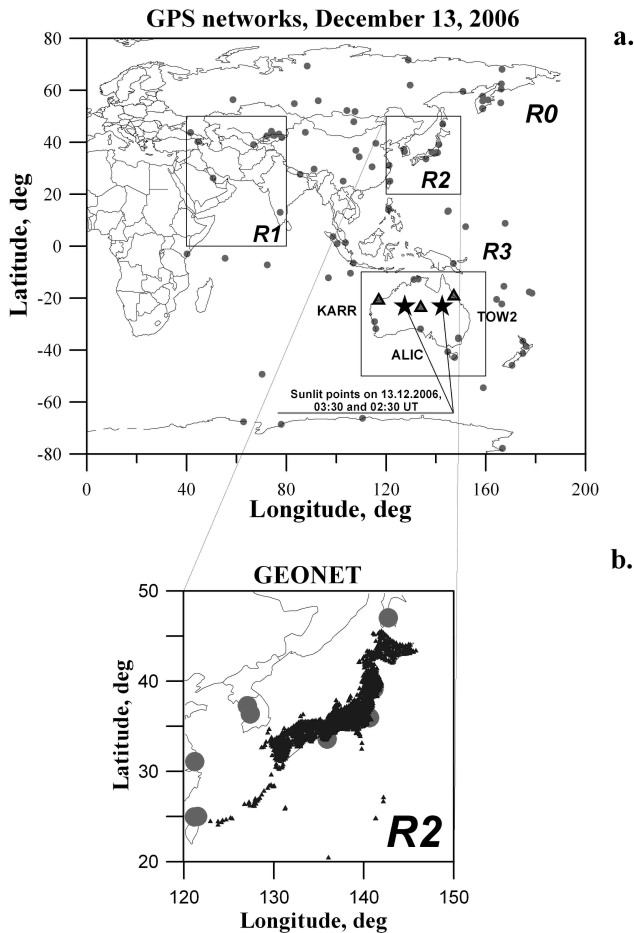


Fig. 2. The geometry of global network of GPS receivers in sunlit side of the Earth ((a), (b), gray circles) and GEONET geometry in Japan ((b), black triangles). The names of the sites are not given for reasons of space. The rectangles mark different region (R_0 – R_3) with different Sun zenith angles χ . Stars at Australia map R_3 show the location of the sunlit points for December 13, 2006, on 02:30 and 03:30 UT; the bold triangles mark selected GPS sites KARR, ALIC, TOW2.

was entirely absent. The measurement slip of L_2 and P_2 implies an impossibility of precise positioning in the dual-frequency mode; hence an incorrect determination of coordinates is possible in single-frequency mode. However, positioning in general is impossible if the signal at one of the GPS frequencies is not registered at all (Hofmann-Wellenhof *et al.*, 1992).

We also defined the corresponding maximum values $W_{\max}\%$ and $Q_{\max}\%$. The time resolution of the $W(t)$ dependence, 30 s, allowed us to compare in detail the $W(t)$ and $Q(t)$ values with those of the solar radio emission flux. We obtained data for all LOSs with an elevation angle θ between the direction along the LOS and terrestrial surface at the reception site of over 5° .

4. Results

Figure 1(e) illustrates the process of registering the 30-s count omission for different PRN and selected GPS sites—KARR, ALIC, TOW2—located near sunlit points corresponding to 02:30 and 03:30 UT (Fig. 2, region R_3 , Australia). Each time dependence of the elevation angle $\theta(t)$ is labeled with the GPS site and PRN name; empty time

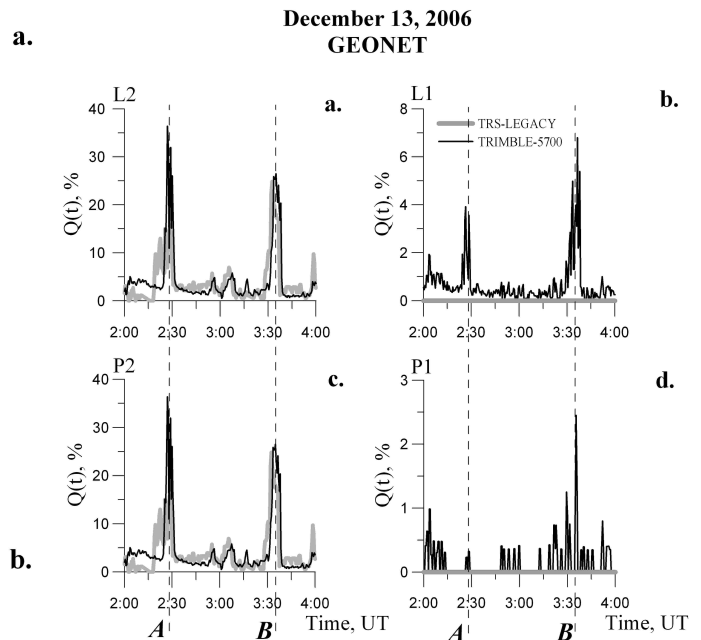


Fig. 3. The relative density of slips of phase (L) and group (P) GPS delay measurements $Q(t)$ during the solar radio burst on December 13, 2006; GEONET, Japan; L_1 , L_2 —(b), (a); and P_1 , P_2 —(d), (c), respectively. GPS signal parameters registered by TRIMBLE-5700 receivers (thin black lines) and by TRS-LEGACY receivers (thick gray lines). For TRS-LEGACY parameters L_1 and P_1 number of slips $Q(t) = 0$ during whole duration of radio burst.

intervals correspond to count omissions.

One can see that for a low elevation angle $\theta < 30^\circ$ the count omissions coincide with the impulse SRB during periods A and B (ALIC-01, ALIC-13, ALIC-27, KARR-13, KARR-27, TOW2-01). There are no count omissions for a high elevation angle θ (ALIC-20, KARR-20).

Figure 1 shows the dependence of count omissions in GPS measurements upon the Sun zenith angle χ during the 2006 December 13 SRB. The total count omissions $W(t)$ for all registered PRN are presented in panel (b) for region R_1 (black line, $80^\circ > \chi > 90^\circ$; $n = 51$), for region R_0 (thick gray line, $0^\circ > \chi > 90^\circ$; $n = 587$ GPS sites), and for region R_3 (gray line, $0^\circ > \chi > 10^\circ$; $n = 119$). The maximum W_{\max} values of over 62% and 18% were recorded for $0^\circ > \chi > 10^\circ$, and $80^\circ > \chi > 90^\circ$, respectively. There was a wide range of zenith angles χ for the entire region R_0 , but even for this region the maximum W_{\max} values exceeded 37%, since the zenith angle χ did not exceed 50° for most of the GPS world network sites.

Figure 1(c) and (d) give the $W(t)$ time-dependences for satellites with selected PRN registered from 02:15 to 03:45 UT. Maximum W_{\max} values for region R_0 can be as high as 50% (panel (c)) and 48% (PRN28, $n = 16$; and PRN13, $n = 43$, respectively). In region R_2 (panel (d), $\chi \sim 60^\circ$), W_{\max} is 19% and 8% (PRN22, $n = 405$; and PRN13, $n = 255$, respectively).

A sharp increase in count omissions completely coincides with the impulse SRB not only during periods A and B , but also, to a lesser extent, at 02:45–03:20 UT (Fig. 1). Comparison of the time dependence of count omissions $W(t)$ for the high zenith angle $0^\circ > \chi > 10^\circ$ to that for

the intensity of RHCP radio emission $F(t)$ at frequencies 1 GHz and 2 GHz demonstrate a close similarity between these dependences (Fig. 1(a, b)). It is also necessary to note that the threshold ε , at which GPS receiver failures occur at high zenith angle, does not exceed 20,000 sfu (as indicated by a horizontal line in panel (a)).

A comparison between different types of GPS receivers' response to wideband solar radio emission impact is of great interest. The dense network of GEONET GPS receivers, equipped with 1200 TRIMBLE-5700 and 25 TRS-LEGACY receivers, is best suited for this purpose. Since the entire network is expanded over a rather small area, all the receivers were under similar influence of the solar radio noise emission during the extreme solar activity on December 13, 2006. Figure 3 presents the relative density $Q(t)$ of measurement slips for the L_1 , P_1 , L_2 , P_2 parameters registered by TRIMBLE-5700 (black lines) and TRS-LEGACY receivers (thick gray lines) on December 13, 2006. It is obvious that significant measurement slips for the main GPS signal parameters were registered by TRIMBLE-5700 receivers not only at the auxiliary frequency $f_2(L_2)$, but at the basic GPS frequency $f_1(L_1)$ as well. Nevertheless, significant measurement slips for the main parameters were detected by TRS-LEGACY receivers at the auxiliary frequency f_2 only. For TRS-LEGACY, the number of L_1 and P_1 slips was nil during the entire radio burst.

5. Discussion

There are some peculiarities in the time dependencies of count omissions and measurement slips for GPS-signal parameters we obtained:

5.1. Count omissions in GPS measurements increase as the line-of-sight elevation angle decreases. A monotonous reduction in signal level is associated with increasing satellite-to-receiver distance. Under usual conditions, additive noise in ~ 40 dB is below the level of signals, as a result of correlation processing of broadband signal in the receiver (Hofmann-Wellenhof *et al.*, 1992; ICD-200c). During powerful solar radio bursts, noise level at low elevation is higher than the signal, which causes failures in phase tracking of the GPS signal. Besides, according to the said mechanism, the dependence of density of the maximum count omissions is not proportional to the maximum radio emission power. It is likely to be determined by the signal-to-noise ratio threshold that may differ for different GPS receivers.

5.2. The GPS measurement count omissions at the auxiliary frequency f_2 essentially exceed those for the basic GPS frequency f_1 . A lower signal/noise ratio at f_2 is primarily due to the fact that the f_2 power at the GPS satellite transmitter output is 6 dB less than that of the basic frequency f_1 with the C/A code (ICD-200c). Similar correlations of the effective radiated power of f_1 (30 watt) and f_2 (21 watt) signals are also typical of the Russian GLONASS system (Perov and Kharisov, 2005).

Phase tracking slips of the f_2 GPS signal may also be caused by lower signal/noise ratio when we use commercial noncoded receivers for f_2 installed at the global GPS network stations. These receivers have no access to the military "Y" code, and have to use the noncoded or semi-noncoded mode of reception. As a result, the signal/noise

ratio at f_2 is, at best, 13 dB lower than the mode of fully coded reception. Thus, the difference in signal powers at f_1 and f_2 for commercial receivers may exceed 10 dB, which may lead to a slip density increase at f_2 owing to the influence of additive interference, but different types of GPS receivers respond differently to this interference.

5.3. The maximum values of $W(t)$ for the time interval **A** are lower than those for **B**, while the radio flux $F(t)$ is also strong enough for both. It is quite natural, since strong bursts of solar radio emission at two GPS frequencies occurred simultaneously only during the time interval **B**, not **A** (Fig. 1(a)). Therefore the probability of the GPS count omissions is higher for the time interval **B** than for **A** (see Section 2).

5.4. The maximum values of $Q_{\max}\%$ for L_2 and P_2 for TRIMBLE-5700 receivers for the time interval **A** are higher than those for **B**, while the opposite is true for the L_1 and P_1 parameters. On the other hand, the maximum values of L_2 and P_2 TRS-LEGACY receivers for the time interval **A** are lower than those for **B**. The main reason for this discrepancy are different characteristics of hardware and software components in different GPS receivers.

5.5. Besides, the maximum values $Q_{\max}\%$ of all L_1 , P_1 , L_2 , P_2 parameters are higher than those of count omissions $W_{\max}\%$. It is quite natural, since $W(t)$ is registered for the count omission only, whereas $Q(t)$ includes not only the count omission, but also the measurement slips of each of the L_1 , P_1 , L_2 , P_2 parameters (Section 2).

6. Conclusion

We found that high-precision GPS positioning on the entire sunlit side of the Earth was partially disrupted during the extreme solar-radio burst on December 13, 2006, for more than 12–15 min; a high level of GPS slips resulted from wideband solar radio noise emission. Our results agree with data obtained recently for the extreme solar radio burst on December 6, 2006 (Cerruti *et al.*, 2006a, b; Afraimovich *et al.*, 2007; Carrano *et al.*, 2007; Carrano and Bridgwood, 2008; Kintner, 2008).

We confirmed the results obtained by Carrano *et al.* (2007) in that GPS failure does depend on Sun zenith angle χ . An increase in count omissions at high zenith angles χ (Fig. 1) testifies to the solar origin of interference (noise) at two GPS frequencies. A growing number of failures with increasing zenith angle is caused by an increase in atmospheric losses.

We agree also with the conclusion by Chen *et al.* (2005). Direct interference from SRB is not usually considered as a potential threat to GPS signal tracing, since the flux density of most bursts is below the GPS f_1 frequency threat threshold of 40,000 sfu, proposed by Klobuchar *et al.* (1999). However, analysis by Chen *et al.* (2005) revealed that a much lower threshold (4,000–12,000 sfu) should be adopted for codeless or semicodeless dual-frequency GPS receivers. For SRB on December 13, 2006, the threshold ε , at which GPS receiver failures occur at high zenith angle, does not exceed 20,000 sfu (as indicated by a horizontal line on Fig. 1(a)).

A more detailed analysis of space distribution of GPS performance slips caused by strong solar radio bursts will

be the subject of our future works. There are other dense GPS networks, for example, the permanent Korean GPS Network, KGN (Jin and Park, 2007). The accurately unified national GPS network with more than 2500 stations, named “National 2000’ GPS Control Network”, has been established by integrating the existing six nationwide GPS networks of China (Yuanxi *et al.*, 2007). A similar analysis should be made for GPS failures during the 2006 December 13 powerful solar radio burst in the said regions.

Our results provide a serious basis for revising the role of space weather factors in the functioning of modern satellite systems and for taking a more thorough account of these factors, in practice. Similar failures in the functioning of satellite navigation systems (GPS, GLONASS, European system GALILEO) may be fatal to operating safety systems as a whole, leading to great financial losses. Another important conclusion of our investigation is that continuous calibrated monitoring of the solar radio emission flux level by a large number of solar radio spectrographs allows solar radio noise level in the range of GPS-GLONASS-GALILEO frequencies to be estimated. Indeed, strong solar radio bursts can be applied as a global and free tool for testing satellite broadband radio systems including GPS. We agree with this conclusion by Gary (2008): “As our society becomes ever more dependent on wireless technology, the effects of solar radio bursts can be expected to appear more often. Mission-critical systems should be designed with solar radio emission in mind. A warning system based on an improved set of world-wide instrumentation could be implemented at relatively low cost, taking advantage of new technology that allows broadband digital signal measurements. Ultimately, such extreme flux density bursts need to be studied at high spatial resolution in order to better understand the conditions leading to their occurrence, and ultimately to be able to predict such events”.

Acknowledgments. Authors express profound gratitude to Prof. G. A. Zherebtsov for his support and interest in this investigation; to S. V. Voeykov and A. B. Ishin for their help in data and manuscript preparation, to Dr. V. V. Grechnev for his help in using the 1 GHz and 2 GHz data of the Nobeyama Radio Polarimeters; to colleagues from the Nobeyama Radio Observatory, for solar radio emission data on December 13, 2006; the the IGS center (<http://lox.ucsd.edu/cgi-bin/al-ICoords.cgi?>) and GEONET (ftp://terras.gsi.go.jp/data/GPS_products/) for RINEX data from GPS receiver networks. The work is supported by the Siberian Branch of the Russian Academy of Sciences; the Program of basic research of the Presidium of the Russian Academy of Sciences 30 “Solar activity and physical processes in the Sun-Earth system”. Finally, the authors wish to thank the referees for valuable suggestions which greatly improved the presentation of this paper.

References

Afraimovich, E. L., GPS global detection of the ionospheric response to solar flares, *Radio Sci.*, **35**(6), 1417–1424, 2000.

- Afraimovich, E. L., E. A. Kosogorov, and L. A. Leonovich, The use of the international GPS network as the global detector (GLOBDET) simultaneously observing sudden ionospheric disturbances, *Earth Planets Space*, **52**(11), 1077–1082, 2000.
- Afraimovich, E. L., O. S. Lesyuta, I. I. Ushakov, and S. V. Voeykov, Geomagnetic storms and the occurrence of phase slips in the reception of GPS signals, *Ann. Geophys.*, **45**(1), 55–71, 2002.
- Afraimovich, E. L., G. A. Zherebtsov, and G. Ya. Smolkov, Total failure of GPS during a solar flare on December 6, 2006, *Doklady Earth Sci.*, **417**(8), 1231–1235, 2007.
- Asai, A., H. Hara, T. Watanabe, Sh. Imada, T. Sakao, N. Narukage, J. L. Culhane, and G. A. Doschek, Strongly blueshifted phenomena observed with Hinode/EIS in the 2006 December 13 solar flare, *Astrophys. J.*, **684**, 2008 (in press). <http://solar.physics.montana.edu/cgi-bin/eprint/index.pl?entry=7249>, 2008-06-05 23:36 (submitted).
- Carrano, C. S. and C. T. Bridgwood, Impacts of the December 2006 solar radio bursts on the performance of GPS, *Presented at the 12th International Ionosphere Effects Symposium*, Alexandria, VA, May 13–15, 2008.
- Carrano, C. S., K. M. Groves, and C. T. Bridgwood, Effects of the December 2006 solar radio bursts on the GPS receivers of the AFRL-SCINDA network, *Proceedings of the International Beacon Satellite Symposium*, edited by P. H. Doherty, Boston College, June 11–15, 2007.
- Cerruti, A. P., P. M. Kintner, D. E. Gary, L. J. Lanzerotti, E. R. de Paula, and H. B. Vo, Observed solar radio burst effects on GPS/WAAS carrier-to-noise ration, *Space Weather* **4**, S10006, doi:10.1029/2006SW000254, <http://gps.ece.cornell.edu/>, 2006a.
- Cerruti, A. P., P. M. Kintner, D. E. Gary, and L. J. Lanzerotti, Direct observations of GPS L1 signal-to-noise degradation due to solar radio bursts, *Eos Trans. AGU*, **87**(36), Jt. Assem. Suppl., 2006b.
- Chen, Z., Y. Gao, and Z. Liu, Evaluation of solar radio bursts’ effect on GPS receiver signal tracking within International GPS Service network, *Radio Sci.*, **40**, RS3012, doi:10.1029/2004RS003066, 2005.
- Gary, D. E., Cause and extent of the extreme radio flux density reached by the solar flare of 2006 December 06, presented at the *12th International Ionosphere Effects Symposium*, Alexandria, VA, May 13–15, 2008.
- Hofmann-Wellenhof, B., H. Lichtenegger, and J. Collins, *Global Positioning System: Theory and Practice*, 327 p., Springer-Verlag Wien, New York, 1992.
- Interface Control Document: ICD-200c, <http://www.navcen.uscg.mil/pubs/gps/icd200/>.
- Jin, S. and J.-U. Park, GPS ionospheric tomography: A comparison with the IRI-2001 model over South Korea, *Earth Planets Space*, **59**(4), 287–292, 2007.
- Kintner, P. M., An overview of solar radio bursts and GPS, IES 2008, presented at the *12th International Ionosphere Effects Symposium*, Alexandria, VA, May 13–15, 2008.
- Klobuchar, J. A., J. M. Kunches, and A. J. Van Dierendonck, Eye on the ionosphere: Potential solar radio burst effects on GPS signal to noise, *GPS Solutions*, **3**(2), 69–71, 1999.
- Kubo, M., T. Yokoyama, Yu. Katsukawa *et al.*, Hinode observations of a vector magnetic field change associated with a flare on 2006 December 13, *Publ. Soc. Jpn.*, **59**, S779–S784, 2007.
- Perov, A. I. and V. N. Kharisov, *GLONASS: principles of construction and functioning*, 720 p., Moscow, 2005 (in Russian).
- Su, Yu., L. Golub, A. Van Ballegoijen *et al.*, Evolution of the sheared magnetic field of two X-class flares observed by Hinode/XRT, *Publ. Soc. Jpn.*, **59**, S785–S791, 2007.
- Yuanxi, Y., T. Yingzhe, C. Chuanlu, W. Min, Z. Peng, W. Xiaorui, S. Lijie, and Z. Zusheng, National 2000’ GPS control network of China, *Prog. Nat. Sci.*, **17**(8), 983–987, 2007.

E. L. Afraimovich (e-mail: afra@iszf.irk.ru), V. V. Demyanov, and G. Ya. Smolkov

Aeronomical effects of the solar flares in the topside ionosphere

L. A. Leonovich and A. V. Tschilin

Institute of Solar-Terrestrial Physics, Russian Academy of Sciences SB RAS, 664033 p/o box 4026, Irkutsk, Russia

(Received October 23, 2007; Revised February 22, 2008; Accepted March 20, 2008; Online published May 29, 2009)

We obtained that according to the GPS data at altitudes of the topside ionosphere ($h > 300$ km) a flare is able to cause a decrease of the electron content. Using the theoretical model it is shown that the intense transport of O^+ ions into the above-situated plasma caused by a sharp increase in the ion production rate and thermal expansion of the ionospheric plasma is a cause of the formation of the negative disturbance in the electron concentration in the topside ionosphere.

Key words: Solar flares, disturbances, ionosphere, GPS, modeling.

1. Observations of the TEC Variations during a Powerful Flare on 14 July 2000

Phase measurements of GPS signals make it possible to obtain variations of TEC along the receiver-satellite path, Fitzgerald (1997), Hoffmann-Wellenhof *et al.* (1992), Klobuchar (1986). Knowing variations in TEC, one is able to evaluate the changes in the total electron content above some given level, using the method based on the effects of partial “shadowing” of the atmosphere by the globe, Leonovich *et al.* (2002).

Now we consider the results of application of the method fore-quoted to studies of the ionospheric effects of the powerful solar flare X5.7/3B registered on 14 July 2000 at 1024 UT (N22W07) on the background of quiet geomagnetic situation ($D_{st} = -10$ nT). Figure 1(a) shows the time behavior of the energy flux of the soft X rays in the 0.1–0.8 nm range (the data from the GOES 10 satellite) for the flare in consideration. Vertical dashed lines show the beginning of the flare and the time when the X-ray flux was maximal. The corresponding variations in TEC along rays directed to the GPS satellites and crossing the shadow boundary at various heights h_0 during the flare are shown in Figs. 1(b)–1(f).

One can see in Fig. 1(b) that the total electron content within the entire ionosphere ($h_0 = 0$) for the IRKT station located in the sunlit hemisphere starts to grow from the moment of the flare beginning (1012 UT) and lasts till 1036 UT. At the ray crossing the shadow region at a height of 240 km (Fig. 1(c)), the TEC grow begins some time after the flare beginning in the soft X-ray range. Similar picture is seen at other rays satisfying the condition $h_0 < 380$ km. At the same time, for the rays with $h_0 \geq 380$ km (Figs. 1(d)–1(e)) a decrease in the electron content above the h_0 level occurs after the flare beginning (1012 UT) and lasts till 1024 UT, i.e., till the moment of the flare maximum in the soft X-ray range.

Similar decrease in the electron content after the beginning of a solar flare was detected in ionospheric observations using the incoherent scatter radar at Arecibo, Thome and Wagner (1981). During two solar flares on 21 and 23 May 1967, negative disturbances of the electron concentration with an amplitude from 3% to 10% were registered within the height interval 280–600 km. The goal of this paper is studying mechanism of electron concentration negative disturbances in the topside ionosphere caused by solar flares.

2. Results of the Model Calculations of the Ionosphere Behavior during a Solar Flare

For studying physical processes governing ionospheric effects of solar flares, we used the model of the ionosphere-plasmasphere interaction, Krinberg and Tschilin (1984). The model makes it possible to calculate time variations of the ion composition, temperature, and also of the fluxes of particles and heat in the conjugated ionospheres. The model is based on numerical solution of the nonstationary equations of the balance of particles and energy of the thermal plasma within closed magnetic field tubes, their bases lying at a height $h = 100$ km. It is assumed that the ionospheric plasma consists of electrons and atomic ions H^+ and O^+ , and also of molecular ions NO^+ , N_2^+ , and O_2^+ . The UV-radiation spectrum by Richards *et al.* (1994) and the X-ray radiation spectrum by Nusinov (1992) were used for the calculation of the photoionization rates of the thermospheric constituents O, O_2 , and N_2 and energetic spectra of the primary photoelectrons in undisturbed conditions (without a flare). The MSIS 86, Hedin *et al.* (1991), global empirical model of the thermosphere was used for the description of the spatial-time variations of the atmospheric temperature and concentrations of the neutral components O, O_2 , N_2 , and H.

For studying the flare effects, a disturbed model of the solar radiation spectrum in the X-ray and UV ranges was created. According to the existence of the pulse and slow phases of a flare, we assumed that the spectrum within the wavelength interval 0.1–10 nm stays disturbed during 36

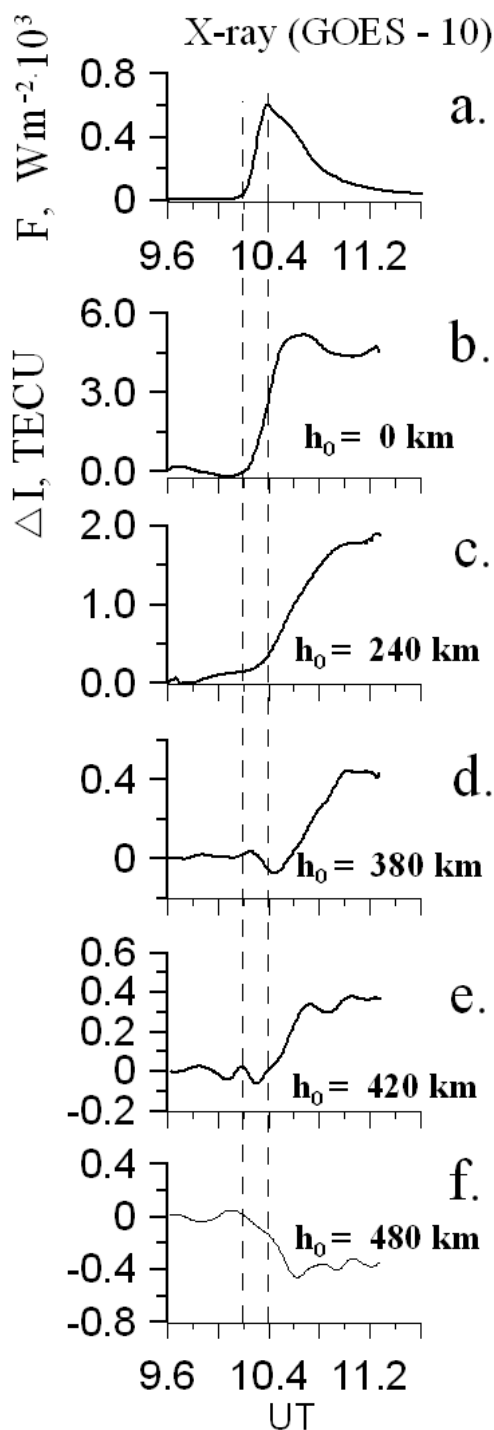


Fig. 1. Results of the TEC response according to the GPS measurements. Time profiles of the soft X-ray radiation within the 1–8 Å range (the data of the GOES 10 satellite) during the solar flare on 14 July 2000 (a). Examples of the TEC responses to the solar flare measured at the rays (between ground-based stations and GPS satellite) crossing the boundary of the Earth's shadow cone at different altitudes h_0 (b–f).

minutes (the slow phase), whereas the pulse phase (for the 10–105 nm interval) lasts during 15 minutes. We also assumed that the spectrum is disturbed instantly and stays constant during the above indicated time intervals, switching off instantly after that. To give the value of the disturbance of the solar energy flux, the entire wavelength in-

Table 1. Increase in the solar radiation intensity for particular spectral intervals during the flare.

Intervals, nm	0.1–0.8	0.8–2	2–4	4–6	6–10	10–105
Intensity factor	1000	100	50	20	4	1.3

terval was split to 6 parts. For each part the most typical value of the intensity factor, Avakyan *et al.* (1994), Horan and Kreplin (1981), Korenkov and Namgaladze (1977), was found. The value was determined as the ratio of the energy flux during the flare to the radiation flux of the quiet Sun. Table 1 shows values of the flare intensity factors for each spectral interval.

The reaction of the midlatitude ionosphere to a considered solar flare was simulated by calculating the variations of plasma parameters within the geomagnetic field tube. The calculation was performed for the period 10–15 July 2000, using arbitrary initial conditions corresponding to low content of the thermal plasma in the tube. The considered time period was characterized by high level of solar activity ($F_{10.7} \approx 210$). The model calculation results of height-time variations of the electron concentration for different conditions of solar irradiating intensity are shown in Figs. 2, (2(a)–2(f))—for the terminator area and (2(g)–2(l))—for the local noon. The moment of a solar flare beginning is shown by vertical dashed lines.

The character of the time behavior of N_e changes principally above the F_2 layer. One can see in Figs. 2(d)–2(f) and 2(j)–2(l) that within the height interval 380–600 km instead of the electron concentration increase after the flare beginning, a trough is formed in the time behavior of N_e . The value of the N_e decrease amplitude lies within 1–5%. It should be noted that the obtained in the calculations negative disturbance of the electron concentration in the topside ionosphere agrees well to the presented above TEC variations obtained as a result of processing of GPS signals and in observations at the Arecibo incoherent scatter radar Thome and Wagner (1981). Thus, one can conclude that the conditions during a solar flare could be such that an increase of the electron concentration occurs in the lower ionosphere, but in the topside ionosphere N_e decreases.

3. Discussion of the Modeling Results

In order to find the causes of formation of the electron concentration negative disturbance in the topside ionosphere, we assumed that the N_e decrease is related to inhomogeneous variations of the ultraviolet radiation in various parts of the spectrum during a flare. On the basis of this assumption, the UV-radiation spectrum within the 10–105 nm range was split to 19 equal intervals. Then, for each interval in turn, the factor of flare radiation intensity was varied from 1.3 to 10, whereas for the other intervals it stayed equal to 1.3. The calculations showed that the effect of N_e decrease after the beginning of a flare is pronounced best at the increase of the intensity factor in three following spectral intervals: 15–20 nm, 30–35 nm, and 35–40 nm.

In order to understand the physical causes of the electron concentration depletion at altitudes of the topside ionosphere, we consider the continuity equation for the iono-

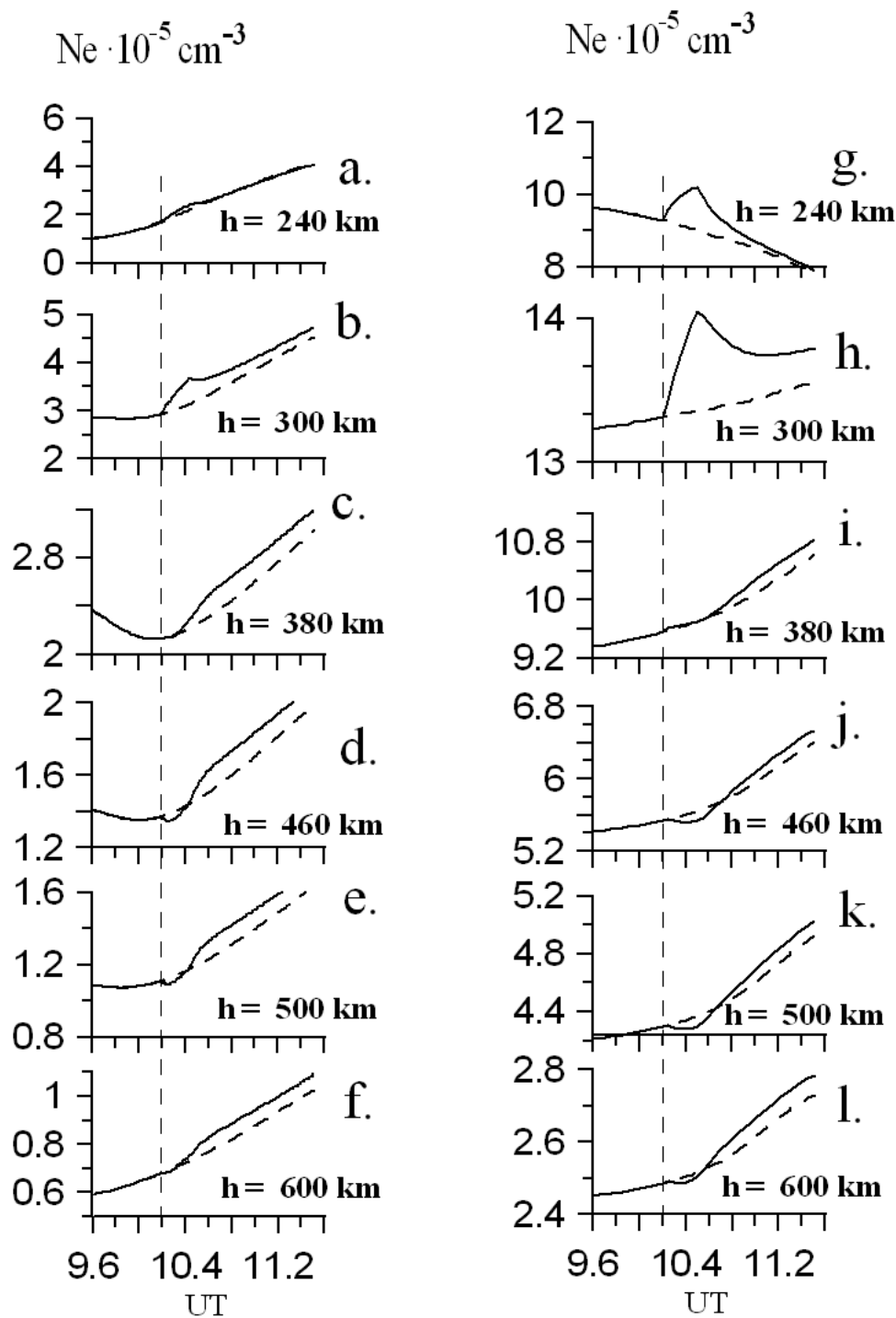


Fig. 2. The model calculation results of the height-time variations of the electron concentration for different conditions of solar irradiating intensity, (2(a)–2(f))—for the terminator area and (2(g)–2(l))—for the local noon. The dashed lines show variations of the electron concentration when solar flare misses. The moment of a solar flare beginning is shown by vertical dashed lines.

spheric plasma written in the form:

$$\frac{\partial N_e}{\partial t} = q - l_n - \text{div}(\mathbf{W}), \quad (1)$$

where q is the ion production rate; l_n is the loss rate of electron-ion pairs in chemical reactions; and \mathbf{W} is the total ion flux along a geomagnetic field line. It follows from (1) that the sign of the N_e changes is determined by the

total balance of the terms in the right-hand side and that a negative disturbance to be formed the right-hand side of (1) should be negative during the flare. The results of the modeling make it possible to determine the processes providing realization of such situation.

Figure 3 shows the time variations of the electron concentration and particular terms of the right-hand side of Eq. (1) at a height of the F_2 layer (300 km) and in the topside iono-

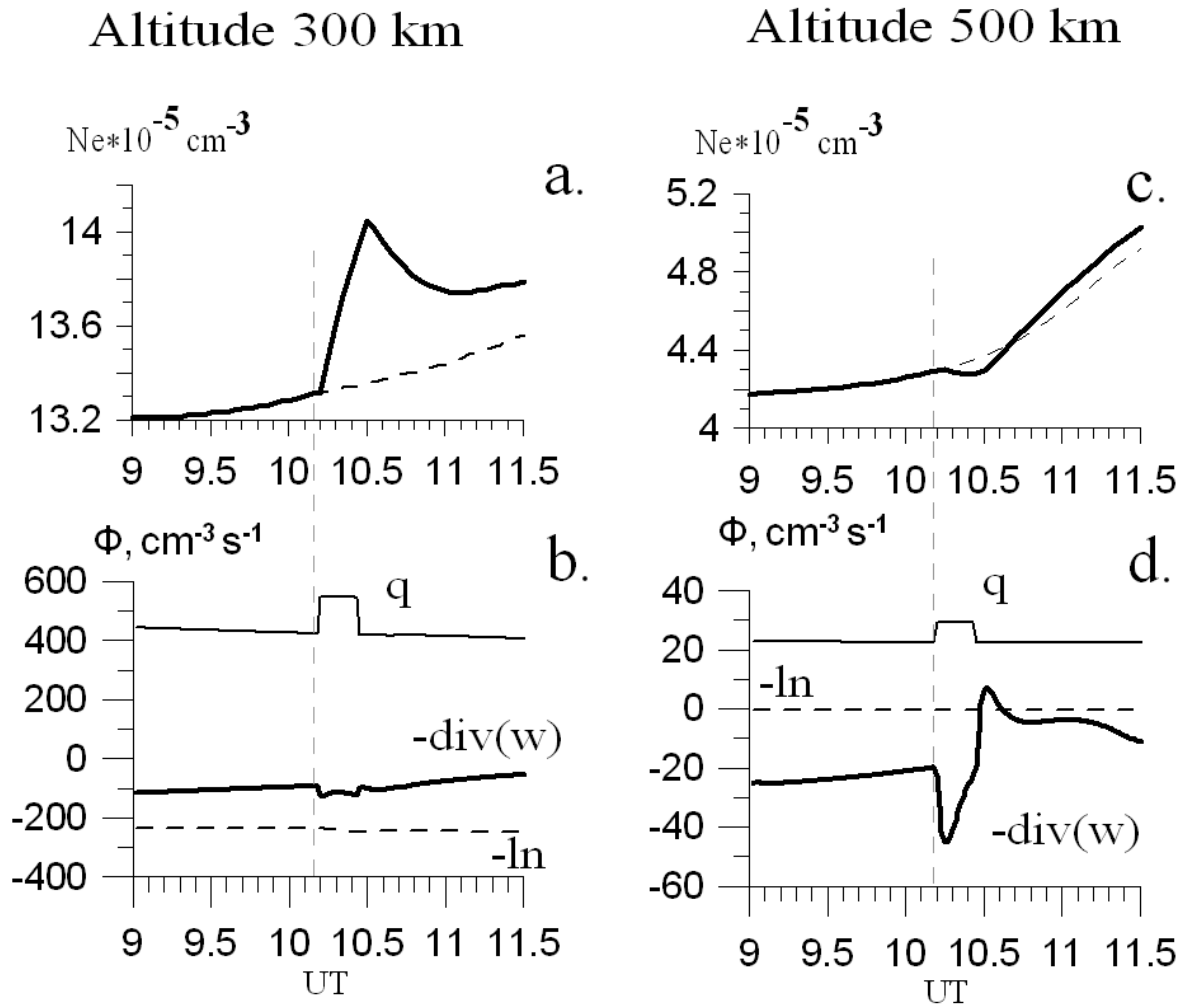


Fig. 3. Analysis of the effect of the decrease in the electron concentration during the solar flare. Thick lines show the time variations of the electron concentration during a solar flare at heights of 300 km (a) and 500 km (c), diamonds show the time variations of the electron concentration in the absence of the flare. The time variations of the terms in the continuity equation calculated for height 300 km (b) where the effect of the electron concentration depletion during the flare is not observed and 500 km (d) where the effect is clearly pronounced are also shown in the bottom panels.

sphere (500 km). It should be noted that within this height interval ions of the atomic oxygen prevail and so Eq. (1) actually describe the balance of O^+ ions. It follows from Fig. 3(b) that at a level of 300 km the value of ion production rate exceeds considerably the loss of charged particles due to the recombination I_n and transport of O^+ ions along the field lines ($\text{div}W > 0$). As a result, there occurs a monotonous increase in N_e during a flare. After the end of the flare, the photoionization rate decreases sharply. Due to that, the electron concentration at first decreases sharply and then is stabilized at some level, the latter being determined by the balance between the photoionization, input of the O^+ ions from the above-located plasmasphere, and chemical loss.

At altitudes of the topside ionosphere (500 km), the relation between particular terms of the right-hand side of (1) changes. First, a decrease with height in the absolute values of the ion production rates and recombination occurs, and, second, the role of the diffuse transport of ions in the ionization balance grows. Figure 3(d) shows that the values of the divergence of ion flux rapidly increases on an absolute value with the beginning of the flare and becomes a

predominating term in the right-hand side of Eq. (1). This happens due to the reformation of the vertical profile of the ion flux above the F_2 -layer maximum with the beginning of the flare. After the sharp increase in the initial moment of the flare, the absolute value of the flux divergence decreases reaching the pre-flare value at the end of the pulse phase (Fig. 3(d)). Then a reversal of the flux divergence sign to the opposite one occurs accompanied by an increase of the electron concentration.

Figure 4 shows the vertical profiles of the ion flux before the flare and in the maximal phase of the flare. One can see that under undisturbed conditions ions O^+ are transported from the topside ionosphere through the F_2 layer into the lower ionosphere. During the maximal phase of the flare, the plasma pressure in the F_2 layer increases sharply and above ~ 380 km an intense upward flux of O^+ ions into the plasmasphere is formed. As a result, at altitudes above ~ 380 km the divergence of the ion flux is positive and considerable on quantity, that specifies on essential upward of plasma from the ionosphere to the plasmasphere.

Thus, one can conclude that the decrease of the electron concentration in the topside ionosphere is due to the bring-

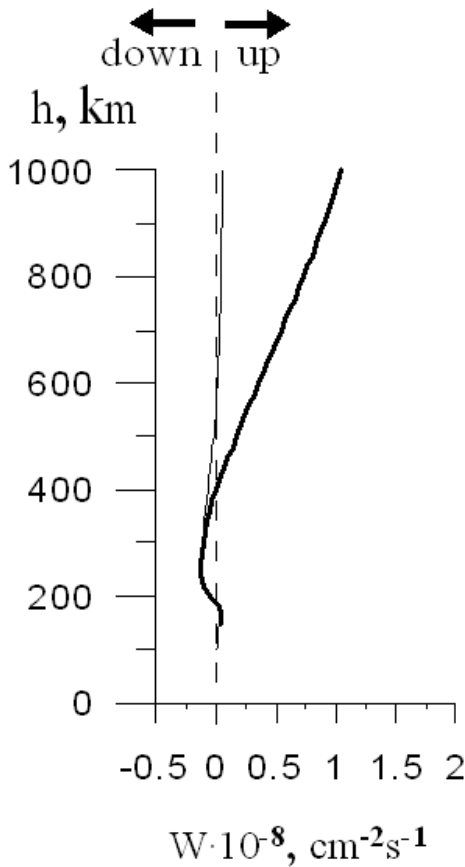


Fig. 4. Vertical profile of the flux W . Thin line shows the flux behavior before the flare. Thick line shows the flux behavior during the flare.

ing out to the plasmasphere of O^+ ions. After “switching off” the flare, the plasma pressure in the F_2 layer decreases quickly down to the level at which the difference in the pressure between the upper and lower parts of the ionosphere

can not any more support the upward flux of O^+ ions, and the ionosphere relaxes to the undisturbed state.

Now we consider the problem of length of the height interval in which the conditions needed to formation of the negative disturbance in N_e are fulfilled. Figure 5 shows the vertical profiles of the particular terms in the right-hand side of Eq. (1) before a flare (Fig. 5(a)) and during the flare (Fig. 5(b)). In the same figures, the summated profile of all terms in the right-hand side of Eq. (1) is shown by triangles. One can see that in the absence of a solar flare in the daytime the resulting curve is positive at $h < 400$ km and is close to zero above 400 km, that is, in the topside ionosphere the condition $\partial N_e / \partial t \geq 0$ is fulfilled everywhere. During a flare the right-hand side of Eq. (1) takes negative values in the 380–600 km altitude range (is shown by horizontal dashed lines in Fig. 5). So it follows that a negative disturbance of the electron concentration during a flare can cover almost the entire topside ionosphere.

4. Conclusions

The response of the ionosphere to a solar flare is studied on the basis of the observational data and results of theoretical modeling. The analysis of the results obtained made it possible to draw the following conclusions:

1. According to the observations of the variations in TEC and electron concentration at the GPS receivers network and at the IS installation at Arecibo, negative disturbances of the electron concentration can be formed in the topside ionosphere during solar flares.
2. It is found in the model simulations that the most significant effect of the N_e depletion is seen during the flares with a strong increase in the solar radiation within the following spectral intervals: 15–20 nm and 30–40 nm.
3. The intense transporting of O^+ ions up into the above-located plasmasphere is a cause of the formation of the

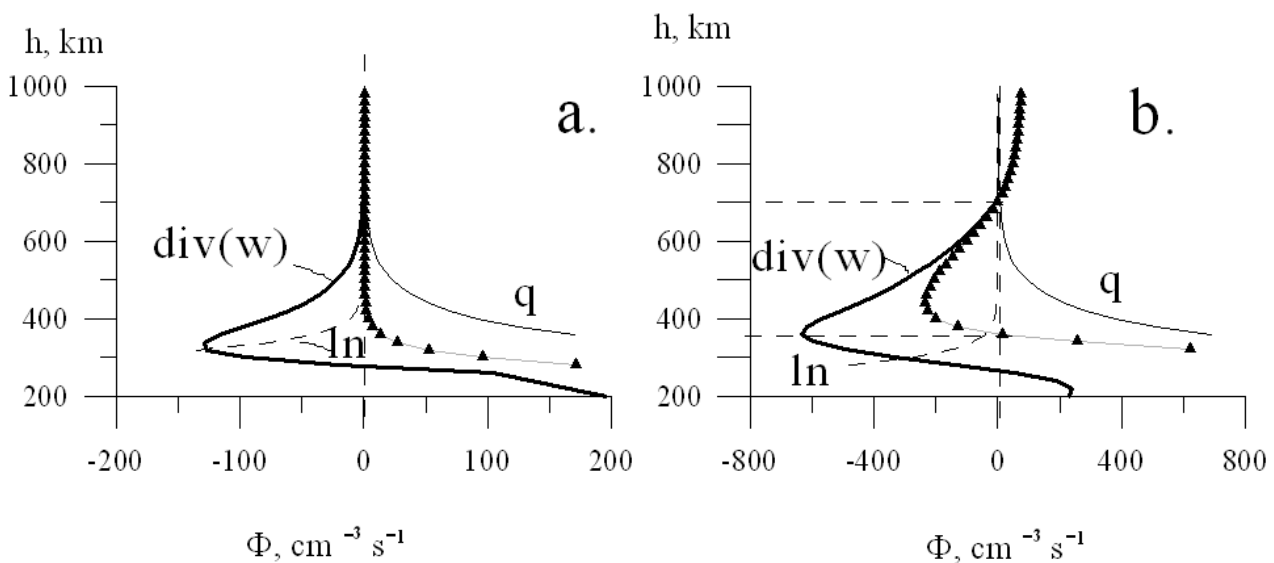


Fig. 5. Analysis of the continuity equation. Vertical profiles of the terms of the continuity equation before the flare (a) and during the flare (b). Thin curves show the electron formation rate q ; dashed curves show the electron loss rate l_n ; thick lines show the flux divergence $\text{div}(W)$. The data for the loss rate and flux divergence are shown with negative signs as they enter to the considered equation. The curve with triangles is a resulting curve.

negative disturbance in N_e in the topside ionosphere. The transporting is caused by the sharp increase in the ion production rate and in the thermal expansion of the ionospheric plasma.

Acknowledgments. The GPS data on the 14 July 2000 flare were kindly provided by E. L. Afraimovich and S. V. Voeikov. E. B. Romanova helped considerably in model simulations. We sincerely thank them all.

References

- Avakyan, S. V., A. I. Vdovin, and V. F. Pustarnakov, *Ionizing and Penetrating Radiation in the Near-Earth Space Environment*, 500 pp., Hydrometeoizdat, St.-Petersburg, 1994.
- Fitzgerald, T. J., Observations of total electron content perturbations on GPS signals caused by a ground level explosion, *J. Atmos. Sol.-Terr. Phys.*, **59**, 829, 1997.
- Hedin, A. E. *et al.*, Revised global model of thermosphere winds using satellite and ground-based observations, *J. Geophys. Res.*, **96**(5), 7657, 1991.
- Hoffmann-Wellenhof, B., H. Lichtenegger, and J. Collins, *Global Positioning System: Theory and Practice*, Springer-Verlag, Wien, 1992.
- Horan, D. M. and R. W. Kreplin, Simultaneous measurements of EUV and soft X-ray solar flare emission, *Sol. Phys.*, **74**(1), 265, doi:10.1007/BF00151295, 1981.
- Klobuchar, J. A., Ionospheric time-delay algorithm for single-frequency GPS users, *IEEE Trans. Aero. Electron. Sys.*, **23**(3), 325, 1986.
- Korenkov, Yu. N. and A. A. Namgaladze, Modelling of the ionospheric effects of the solar flares, in *Ionospheric disturbances and forecast methods*, edited by L. N. Lyhova and L. A. Yudovich, 228 pp., Moscow, Publ. House "Nauka", 1977.
- Krinberg, I. A. and A. V. Tashilin, *Ionosphere and Plasmasphere*, Nauka, Moscow, 1984.
- Leonovich, L. A., E. L. Afraimovich, E. B. Romanova, and A. V. Tashilin, Estimating the contribution from different ionospheric regions to the TEC response to the solar flares using data from the international GPS network, *Ann. Geophys.*, **20**, 1935, 2002.
- Nusinov, A. A., Models for prediction of EUV and X ray solar radiation based on 10.7-cm radio emission, in *Proc. Workshop on Solar Electromagnetic Radiation for Solar Cycle 22*, Boulder, Colo., July 1992, edited by R. F. Donnelly, NOAA ERL, Boulder, Colo., USA, 354, 1992.
- Richards, P. G., J. A. Fennelly, and D. G. Tor, EUVAC: A solar EUV flux model for aeronomic calculations, *J. Geophys. Res.*, **99**, 8981, doi:10.1029/94JA00518, 1994.
- Thome, G. D. and L. S. Wagner, Electron density enhancements in the E and F regions of the ionosphere during solar flares, *J. Geophys. Res.*, **76**, 6883, 1981.

L. A. Leonovich (e-mail: lal@iszf.irk.ru) and A. V. Tashilin